Negative and Zero Poisson's Ratio Cellular Metamaterials with Enhanced Mechanical Properties

A thesis submitted in partial fulfilment of the requirement for the degree of

Doctor of Philosophy

by

Bikram Jyoti Sahariah

Roll No.– 186103010

under the guidance of

Dr. Prasenjit Khanikar

Assistant Professor

Department of Mechanical Engineering

Indian Institute of Technology Guwahati

Guwahati- 781039, Assam, India

April 2024

Department of Mechanical Engineering

Indian Institute of Technology Guwahati

Guwahati- 781039, India

CERTIFICATE

It is certified that the work contained in this doctoral thesis titled "Negative and Zero Poisson's Ratio Cellular Metamaterials with Enhanced Mechanical Properties" submitted by Mr. Bikram Jyoti Sahariah to the Indian Institute of Technology Guwahati for the award of the degree of Doctor of Philosophy has been carried out under my supervision in the Department of Mechanical Engineering.

This work has not been submitted elsewhere for the award of any other degree or diploma. This thesis, in my opinion, has reached the standard fulfilling the requirements for the award of the degree of Doctor of Philosophy in accordance with the regulations of the institute.

Dr. Prasenjit Khanikar

Assistant Professor

Department of Mechanical Engineering

Indian Institute of Technology Guwahati

Guwahati- 781039, India

Department of Mechanical Engineering

Indian Institute of Technology Guwahati

Guwahati- 781039, India

SELF-DECLARATION STATEMENT

I, Bikram Jyoti Sahariah, hereby declare that the thesis titled "Negative and Zero Poisson's Ratio Cellular Metamaterials with Enhanced Mechanical Properties" represents my original work under the Supervision of Dr. Prasenjit Khanikar, for the degree of Ph.D. in Mechanical Engineering, at Indian Institute of Technology Guwahati.

I affirm that this thesis has not been submitted, in whole or in part, for any other academic qualification at any other institution.

All external sources of information used have been duly acknowledged and referenced following the academic guidelines. Throughout this research journey, I have maintained the highest standards of academic integrity, ensuring that this work is free from any form of plagiarism or misrepresentation.

Bikram Jyoti Sahariah

Roll No. 186103010

Department of Mechanical Engineering

Indian Institute of Technology Guwahati

ACKNOWLEDGMENT

I would like to take this opportunity to express my sincere gratitude to all who supported me to complete this thesis work.

First and foremost, I am grateful to my supervisor Dr. Prasenjit Khanikar for agreeing to be my mentor, and for his wisdom in selecting a very interesting topic for my research. It was his patient guidance, constant motivation, prompt response and positive outlook that helped me continue my progress. It was an honor to be a student of Dr. Prasenjit Khanikar, and his meticulous approach have had a positive impact that will be beneficial for the rest of my life. I would also like to thank my doctoral committee members, Prof. D. Chakraborty, Prof. R. Ganesh Narayanan and Dr. H. Sharma for their constructive comments and suggestions on the research work.

Secondly, I would like to thank Prof. S.K. Dwivedy, Prof. S. Senthilvelan and Prof. K.S.R. Krishna Murthy, the Head of the Department of Mechanical Engineering, Indian Institute of Technology (IIT) Guwahati, during the period July 2018- June 2023, for proving the laboratory facilities to carry out my thesis work. I would like to sincerely appreciate Prof. P. Venkitanarayanan, Department of Mechanical Engineering, IIT Kanpur, for providing me the opportunity to use his laboratory to carry out a part of my thesis work. I am thankful to the Central Workshop and the Central Instruments Facilities (CIF), IIT Guwahati, for allowing me to use the required facilities for my research. I am also grateful to the DST-FIST funded (Sanction No. SR/FST/ET-II/2017/111) Universal Testing Machine (UTM) facility at the Department of Mechanical Engineering, IIT Guwahati.

Thirdly, I am very grateful to my lab-mates in the Computational Mechanics and Optimization Lab, specially Mr. Akshay Namdeo, Mr. Manash Jyoti Baishya, Mr. Manish Dalakoti, Mr. Samrat Tamuly and Mr. Hritaban Acharya for their significant support and motivation. I would also appreciate my batch-mates, Mr. Tanuj Srivastava, Mr. Santanu Kumar Das, Mr. Chandan Nashine, Mr. Rohit Kumar, Mr. Brijesh Kumar Singh, Mr. Niraj Kumar Prasad and Mr. Rishabh Saxena for their company and the unforgettable memories during my PhD journey.

Last but not the least, I would like to express my deepest gratitude to my parents, my wife and my brother for their constant support, love and care. Their selfless love and encouragement have helped me complete this thesis.

Bikram Jyoti Sahariah

ABSTRACT

Cellular metamaterials are man-made structures that have unusual mechanical properties. Lattice structures belong to a category of cellular metamaterials formed by periodic arrangement of interconnected struts or plates. With a change in the arrangement of struts, the lattice structures can be made to exhibit positive, negative, or zero Poisson's ratio. In contrast to the extensive research focusing on positive Poisson's ratio lattices, only a few studies focus on enhancing the mechanical properties of lattice structures exhibiting negative Poisson's ratio (NPR) or zero Poisson's ratio (ZPR). These negative or zero Poisson's ratio lattices can find potential applications in different industries, including automobile, defense, aerospace, bio-medical, and sports. This thesis demonstrates different techniques, such as unit cell topology modification, design of dual-phase lattices, and tapered-strut lattices to enhance the mechanical properties of the NPR and ZPR lattices. The NPR lattices made of AlSi10Mg and polyamide 12 (PA12), and the ZPR lattices made of PA12 were fabricated using two different additive manufacturing techniques. Uniaxial compression tests were performed to understand the mechanical behavior of the lattices. The mechanical properties of the metallic lattices were studied under quasi-static and high-strain rate loading conditions, while the mechanical properties of the polymeric lattices were studied under only quasi-static loading conditions. The quasi-static tests were conducted using the universal testing machine, and the high-strain rate tests were conducted using a split Hopkinson pressure bar. Finite element simulations were performed to study the deformation modes and mechanical performance of the lattice structures, which were corroborated by the experiments. The compressive strength, Young's modulus, and energy absorption ability of the proposed NPR and ZPR lattices were compared with the commonly studied NPR or ZPR lattices. Moreover, the effect of unit-cell geometric parameters of the lattices on the mechanical properties was also investigated. The novel dual-phase lattices inspired by composite materials exhibited enhanced properties. Furthermore, this thesis work demonstrated that the conventional composite rule of mixture can predict Young's modulus and Poisson's ratio of the dual-phase lattices. In addition, modifying the existing unit cells by using additional struts or by replacing uniform cross-section struts with tapered struts proved promising to enhance the mechanical properties. Zero Poisson's ratio tubular lattices were also designed, and the effect of unit-cell parameters was studied by the Design of Experiments (DoE) technique with Analysis of Variance (ANOVA). The tubular lattices were optimized for high-energy absorption or high-strength-stiffness applications

TABLE OF CONTENTS

LIST OF FIGURES

LIST OF TABLES

CHAPTER 1. INTRODUCTION

1.1 Background

'Cellular solids' refer to the class of materials or structures made up of interconnected network of struts or plates in a periodic or random order [1]. The cellular structures are found in nature in the form of bone, cork, honeybee-hive, wood, fungi mushroom etc. Some examples of naturally occurring cellular structures are shown in Figure 1.1. A high strength-to-weight ratio is the most important property of cellular structures. Bone is a natural cellular structure considered an engineering marvel because it has the same strength as cast iron and weighs as light as wood [2]. Cork is another excellent example of cellular material with an outstanding combination of properties. It is chemically stable, has a high co-efficient of friction, is fire resistant, can absorb energy during impact, and is very light in weight [2]. The most crucial characteristic of a cellular structure is the 'relative density', which is defined as the ratio of the density of the cellular material (ρ) to the density of the solid material from which the cellular material is made (ρ_s) [1]. It is given as

$$\rho_r = \frac{\rho}{\rho_s} \tag{1.1}$$

where, ρ_r is the relative density of the cellular structure.

Inspired by the cellular materials found in nature, the researchers developed 'cellular metamaterials' with excellent properties. 'Metamaterials' are artificially designed structures that may possess various properties based on the application. Foams, 2D honeycombs and lattices are some examples of cellular metamaterials. Foams are classified as open-cell or closed-cell structures in which the unit cells are arranged randomly [1]. Open-cell foams have only solid edges, while closed-cell foams have solid edges and faces. On the other hand, honeycombs and lattices are made up of an array of struts or plates connected in a definite order [3]. The properties of cellular metamaterials are inherited from: (i) the material from which they are made, (ii) geometric design and (iii) relative density [3].

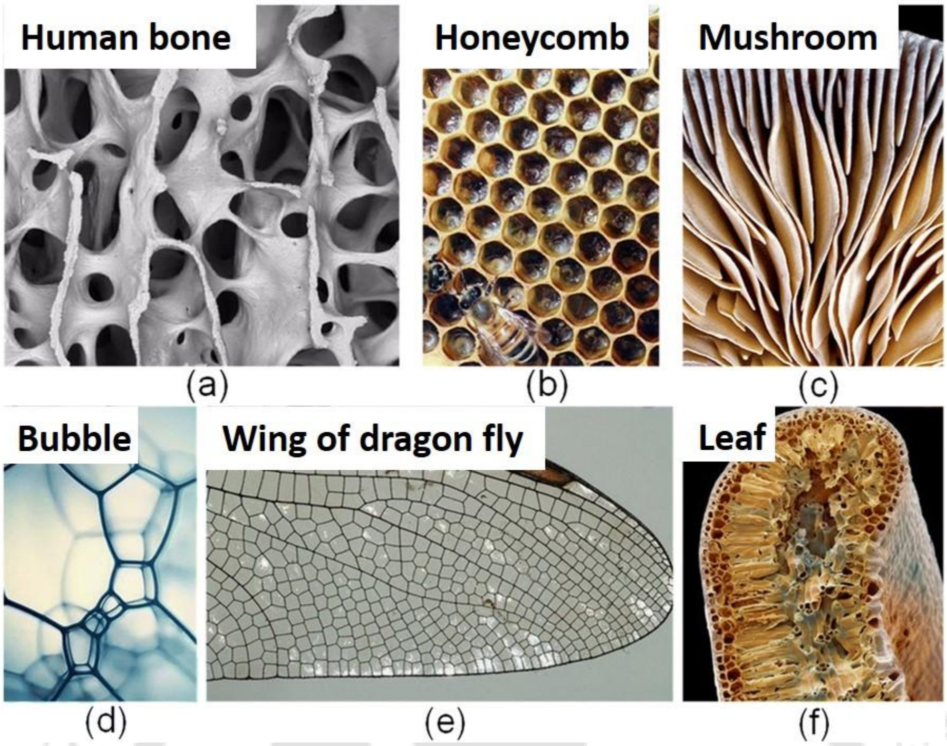

Figure 1.1. Some examples of cellular structures found in nature (Reproduced with permission from [2]).

Cellular metamaterials have gained enormous attention due to their high strength-to-weight ratio and high energy absorption ability [4]. During compressive loading, the cellular metamaterials can absorb a large amount of energy by deforming continuously at nearly constant stress [1]. Figure 1.2 shows compressive stress-strain curves of foams with elastic-plastic and elastic-brittle behaviour. The stress-strain plot for a cellular metamaterial can be divided into three regions: (i) elastic region (ii) plateau region and (iii) densification region [5]. The structure follows linear elasticity in the elastic region, and the stress is directly proportional to strain. In the plateau region, the structure can deform by elastic buckling, plastic hinging or brittle crushing, depending on the ductile or brittle behaviour of the parent material [1]. The cellular structure absorbs the maximum amount of energy during the plateau region. After the structure has completely collapsed, with a further increase in strain, the struts or plates of the opposing unit cells of the cellular structure touch each that causes the densification of the structure, and the stress increases rapidly with an increase in strain (Figure 1.2). The cellular structures with a constant plateau stress and a large densification strain are ideal for energy-absorbing applications [5].

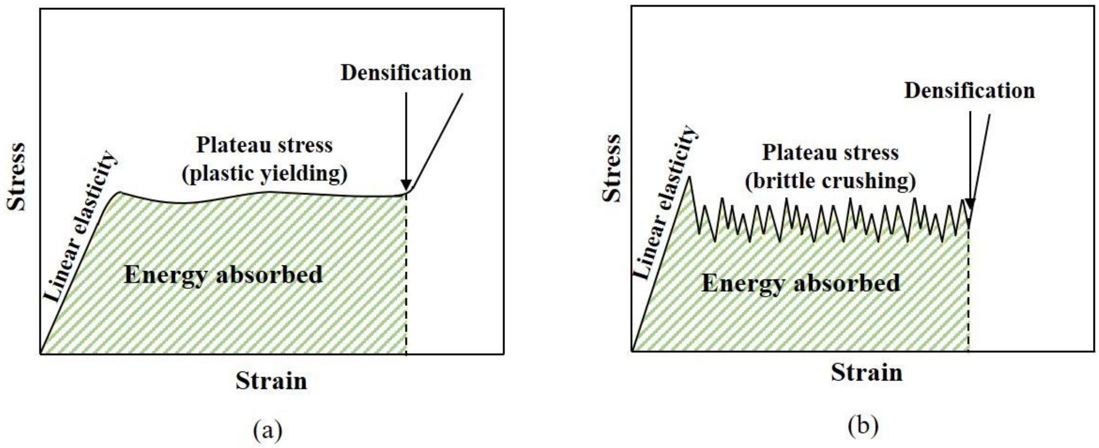

Figure 1.2. Stress-strain curves for (a) an elastic-plastic foam, and (b) an elastic-brittle foam during compression [1].

A large number of cellular metamaterials are currently used for impulsive loading applications in sports, automotive and defense [6]. Foams are the common energy-absorbing materials currently in use. Still, the defects and unreliable performances of the foams due to their stochastic nature lead to overdesign because of a high factor of safety considerations [6]. Lattice structures are gaining enormous attention because of their hierarchical orientation, high strength-to-weight ratio, and high energy absorption ability. With the rapid development of additive manufacturing, the fabrication of lattice structures became easy, which was earlier complicated by conventional manufacturing processes. It is known that the mechanical properties of the lattice structures depend on the topology of its unit cell, the material from which they are made, and the relative density. This prompted the researchers to develop novel lattice structures or modify the existing ones to achieve better mechanical properties. Lattice structures with a plethora of unit cell geometries were designed and fabricated by additive manufacturing to study their mechanical properties. Figure 1.3 shows some lattice structures with their unit cells. Most of the commonly studied lattice structures, i.e., body centered cubic (BCC), octet, etc., deform like common materials where they expand laterally when compressed by axial load [7–11]. However, it was possible to change the deformation behaviour of the lattice structures such that they contract laterally when compressed by axial load, thus showing negative Poisson’s ratio behaviour. The behaviour of a positive Poisson’s ratio (PPR), a negative Poisson’s ratio (NPR) and a zero Poisson’s ratio (ZPR) structure before and after a tensile load is applied is shown in Figure 1.4.

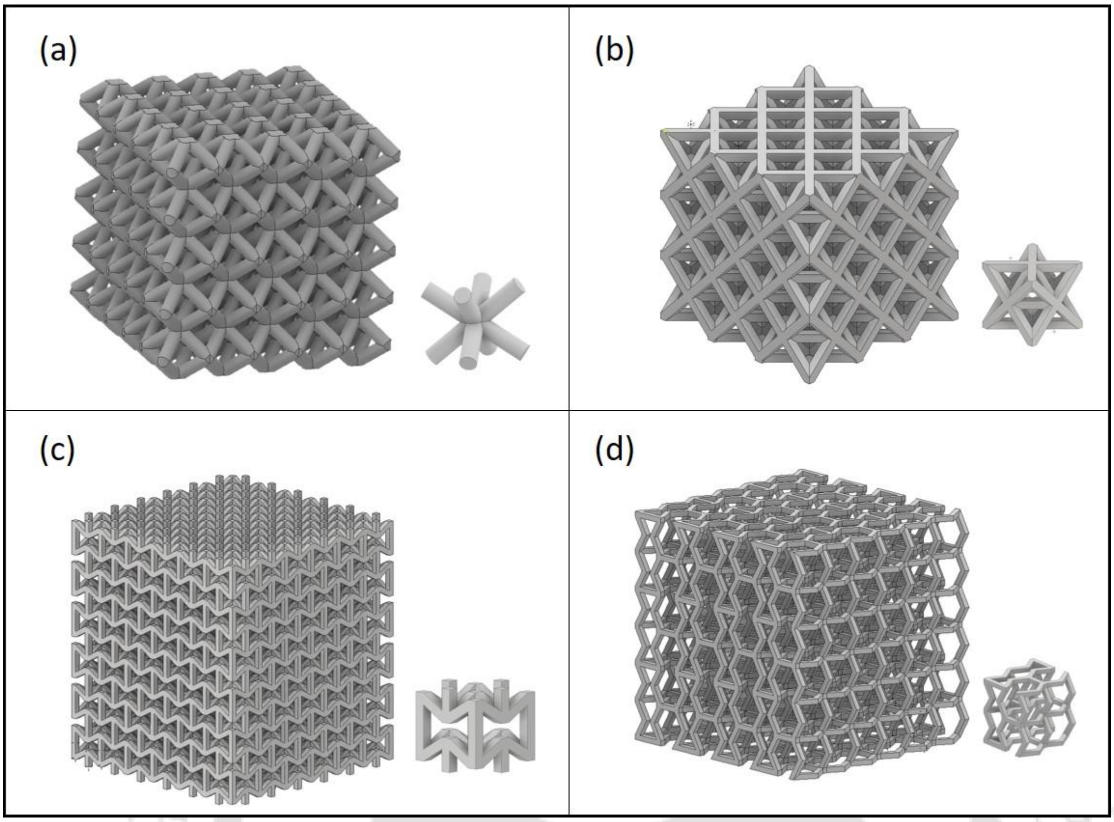

Figure 1.3. Different types of lattice structures with their unit cells, (a) body centered cubic (BCC), (b) octet, (c) 3D-reentrant and (d) 3D-reversed semi-reentrant.

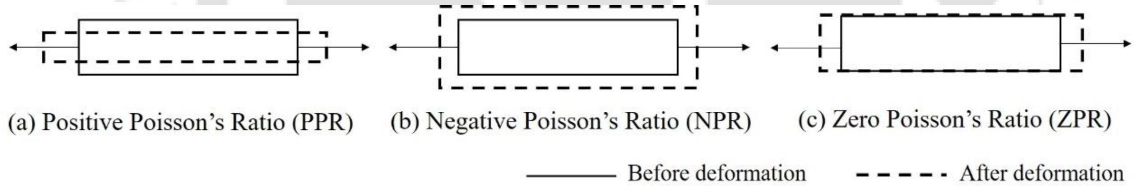

Figure 1.4. The behaviour of (a) positive Poisson's ratio (PPR), (b) negative Poisson's ratio (NPR) and (c) zero Poisson's ratio (ZPR) structures before and after deformation.

1.2 Negative Poisson's ratio or auxetic lattice structures

Poisson's ratio (υ) is defined as the negative ratio of lateral strain to axial strain [12]. It is given as

$$\upsilon = -\frac{lateral\ strain}{axial\ strain} \quad 1.2$$

Figure 1.4 shows the deformation behaviour of structures with different Poisson's ratios. The Poisson's ratio generally ranges from 0.25 to 0.33 for most materials. Only a few materials in nature exhibit negative Poisson's ratio, e.g., α-cristobalite, pyrolytic graphite, living cat skin, cow teat skin, etc. [13]. Lakes, in the year 1987, reported a foam structure with a negative Poisson's ratio [14]. Evans introduced the term 'auxetic' in 1991 for materials that exhibit a negative Poisson's ratio [15]. The word 'auxetic' originates from the Greek word 'auxetikos', which means 'that tend to increase' [16]. Some examples of auxetic lattice structures are shown in Figure 1.5. It can be seen that the structures expand laterally when a tensile load is applied, thus exhibiting a negative Poisson's ratio.

Researchers' interest in auxetic lattices has increased in the last two decades. The auxetic lattice structures have attracted attention because, compared to conventional materials, these structures can improve mechanical properties like shear resistance, indentation resistance, fatigue crack propagation, synclastic behaviour and fracture toughness [13]. The auxetic materials are classified into three groups based on their deformation mechanisms [17]:

- Reentrant type
- Chiral type
- Rotating unit type

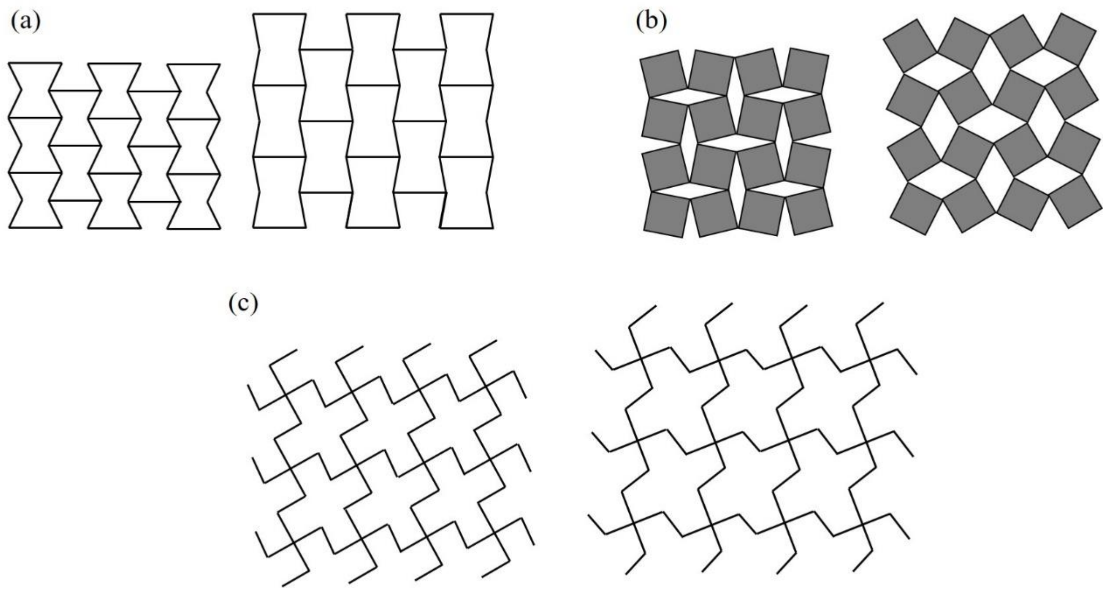

Figure 1.5. Auxetic lattice structures before and after deformation, (a) reentrant, (b) rotating squares and (c) missing ribs [18].

The auxetic structures were first developed as 2D structures, and 3D auxetic structures were developed to achieve a volumetric auxetic effect. In terms of energy absorption efficiency, auxetic structures are found to be superior to non-auxetic structures [19].

1.3 Zero Poisson's ratio lattice structures

Unlike the positive Poisson's ratio and negative Poisson's ratio structures, the zero Poisson's ratio (ZPR) structures do not undergo lateral deformation when stretched or compressed longitudinally, as shown in Figure 1.4(c). Natural cork is a well-known material with a zero Poisson ratio [20]. Mechanical metamaterials with zero Poisson's ratio have shown promising prospects in aircraft wing morphing, tissue engineering, bio-medical stents, and tubular sandwich structures [21–24]. The 2D semi-reentrant (SRE) lattice, one type of ZPR structure, was derived from the hexagonal honeycomb structure by Grima et al. [24]. The 2D reversed semi-reentrant (RSRE), 2D AuxHex, Silicomb, etc., are other lattice structures exhibiting zero Poisson's ratio [23,25–27]. Figure 1.6 shows different lattice structures exhibiting zero Poisson's ratio.

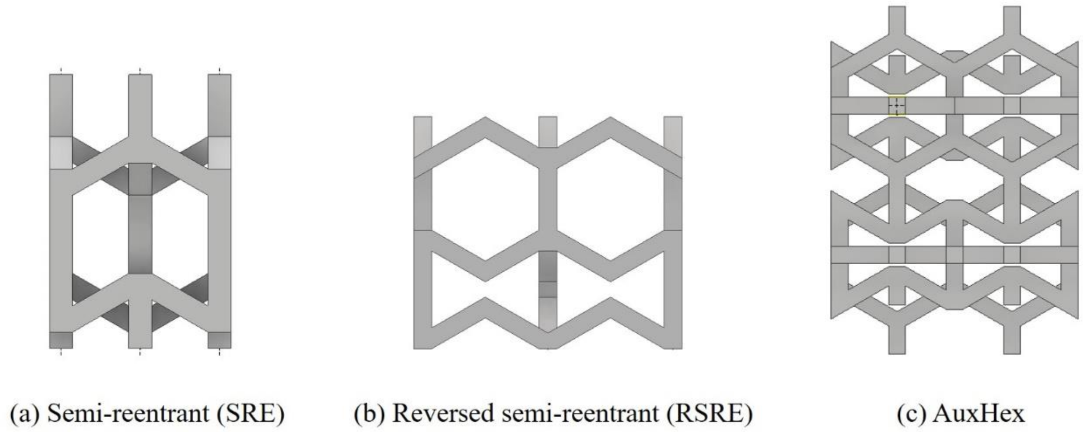

Figure 1.6. Zero Poisson's ratio (ZPR) lattice structures, (a) Semi-reentrant, (b) Reversed semi-reentrant and (c) Aux-Hex.

The main barrier to the applications of lattice structures is the fabrication of small and complex unit cells by conventional manufacturing methods. However, the recent development of modern manufacturing techniques like additive manufacturing has opened a new door to fabricate lattice structures on the macro, micro, and even nano scales.

1.4 Additive manufacturing

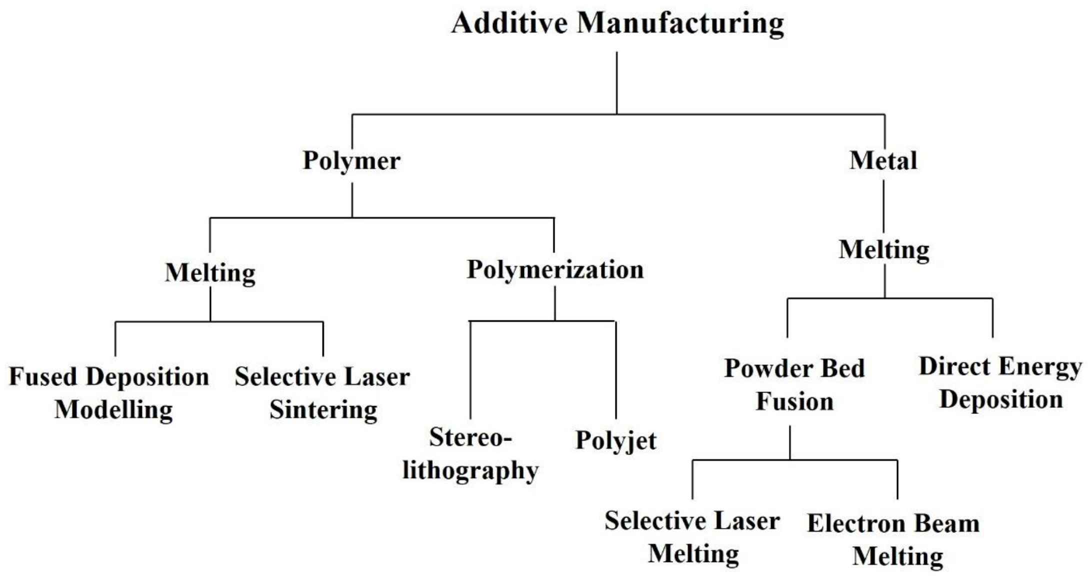

Figure 1.7. Common additive manufacturing processes for the fabrication of polymeric and metallic components.

Additive manufacturing or 3D-printing is a technique by which components can be fabricated by adding materials layer upon layer. Additive manufacturing technology has high manufacturability, and it can be used to print 3D objects directly from the CAD model without dedicated tooling [2]. By additive manufacturing, different materials like metals, polymers and composites can be fabricated [28]. Figure 1.7 shows the classification of some additive manufacturing techniques used to fabricate metallic and polymeric components. Metals can be fabricated by two main laser-based 3D-printing techniques, Powder Bed Fusion (PBF) and Direct Energy Deposition (DED) [2]. Out of the two, the lattice structures are fabricated by PBF techniques. DED cannot be used to manufacture lattice structures because the fabricated components have very rough surface quality [2]. Stainless steel (SS316), titanium alloy (Ti6Al4V), and aluminum alloy (AlSi10Mg) are the common metallic materials used to fabricate lattice structures [4].

There are different techniques of polymer fabrication, like Stereolithography (SLA), Fused Deposition Modelling (FDM), Selective Laser Sintering (SLS), etc. [29]. FDM is the most used 3D-printing technique for fabricating polymeric lattices [2]. The recently developed technique of polymer printing process by Hewlett-Packard (HP), known as Multi Jet Fusion (MJF), can fabricate components with better features than the FDM [30]. The most commonly used polymers for 3D-printing are acrylonitrile butadiene styrene (ABS), polyamide 12 (PA12), polylactide (PLA), thermoplastic polyurethane (TPU), polycarbonate (PC) etc. [29].

The advantages of additive manufacturing processes are:

- It is capable of fabricating products having complex geometry with high precision.
- The amount of materials required is less compared to traditional methods of manufacturing.
- Design flexibility and mass customization can be achieved by additive manufacturing.

The disadvantages of additive manufacturing processes are:

- The structures produced are generally anisotropic in nature.
- Large-scale production by additive manufacturing is not preferred because of excessive time consumption.

1.5 Research motivation

The increasing need for cellular structures has encouraged the design of innovative cellular structures with enhanced mechanical properties to meet engineering demands. The advent of additive manufacturing has made it easier to fabricate lattice structures with complicated shapes. While much of the research on lattice structures has focused on those with positive Poisson's ratio, the lattice structures with negative and zero Poisson's ratio have also been explored in the last few years. These negative and zero Poisson’s ratio structures possess exceptional properties that make them highly attractive for engineering fields like automobile, aerospace and biomedical industries. As the demand for these lattice structures continues to grow across various industries, it is crucial to improve their mechanical properties continuously. This can be achieved by creative design ideas, novel techniques of manufacturing and novel materials. Improving the design of existing cellular structures is important to ensure that these structures with enhanced mechanical properties meet the evolving engineering demands and contribute to the advancements in science and technology.

Unlike the numerous studies on positive Poisson's ratio lattices, only a few studies have worked on improving the mechanical properties of the lattice structures with negative or zero Poisson's ratio. Although different techniques were explored, e.g., using variable strut thickness of the unit cell, using dual-phase lattices, tactical modification of unit cell topology, graded-density lattices, polymer-filled lattices, etc., to enhance mechanical properties of lattice structures, these techniques have been rarely used for negative or zero Poisson's ratio lattices. To the best of the author's knowledge, no study had been published on negative or zero Poisson's ratio lattices having multiple unit cell topologies, i.e., dual-phase lattice or variable strut thickness. However, a few studies on improving the mechanical properties of negative and zero Poisson's ratio lattices through tactical modification of unit cell topologies are available in the published literature. Therefore, there is an imminent need to apply different techniques to enhance the mechanical properties of the negative or zero Poisson's ratio lattice structures. In addition, most of the lattice structures are studied under quasi-static loading conditions though many applications require investigation of lattice structures under high-strain rate loading.

1.6 Aim of the thesis

This thesis aims to develop negative and zero Poisson's ratio lattice structures with enhanced mechanical properties. The objectives involve several key aspects, including the improvement of mechanical properties of the negative Poisson's ratio lattice by replacing uniform cross-section struts with tapered struts. This work also propose composite material-inspired multilattice structures to improve the mechanical properties of negative Poisson's ratio lattices by incorporating high-strength lattice reinforcements. The study also aims to design zero Poisson's ratio lattices through a combination of negative and positive Poisson's ratio lattice unit cells by following the conventional composite rule of mixture. Furthermore, the mechanical performance of zero Poisson's ratio tubular lattices are enhanced by tactical modification of its unit cell. Ultimately, this research work aims to conduct a comprehensive comparative analysis of the mechanical properties of the newly proposed lattice structures with existing well-known lattices in the field.

1.7 Outline of the thesis

- Chapter 2 reviews the literature on different types of auxetic and zero Poisson's ratio (ZPR) metamaterials, along with their properties and applications. The different techniques to improve the mechanical properties of the existing lattice structures are also discussed.
- Chapter 3 discusses the methodologies implemented to study the mechanical response of the auxetic and ZPR lattice structures. The techniques employed to fabricate the lattice structures, along with the details of experimental tests and numerical simulations are reported.
- Chapter 4 discusses the design of tapered 3D-reentrant structures and the results obtained from the compression of these structures at quasi-static and high-strain rate loading.
- Chapter 5 reports a new method to design auxetic structures with enhanced mechanical properties by employing the composite rule of mixture. The deformation behaviour of these structures was studied by numerical simulations and they are corroborated with experiments.
- Chapter 6 demonstrates that the composite rule of mixture can be adopted to design ZPR lattice structures. The mechanical properties of the proposed ZPR lattice structures were compared with the commonly studied ZPR lattices.
- Chapter 7 reports a strut-reinforced semi-reentrant honeycomb (SR-SRH) lattice, which can exhibit zero Poisson's ratio up to a large strain. The compression properties of these structures were investigated by numerical simulations and experiments.
- Chapter 8 discusses the design of two optimized SR-SRH tubular lattice structures that can be used for applications requiring high-energy absorption or high-strength. Design of experiments (DoE) is employed to study the influence of input geometric parameters on the output mechanical properties.
- Chapter 9 outlines the major conclusions drawn from this thesis work and the scope for future work.

CHAPTER 2. LITERATURE REVIEW

This chapter reviews different lattice structures and techniques to enhance their mechanical properties. Section 2.2 discusses the classification of the commonly studied auxetic structures. The unique properties of the auxetic structures, along with their potential applications across different industries, are presented in Sections 2.3 and 2.4. Section 2.5, 2.6 and 2.7 discusses the different types of ZPR lattice structures, their properties and applications, respectively. Lastly, Section 2.8 is dedicated to the different techniques adopted to improve the mechanical performance of the lattice structures.

2.1 Lattice structures

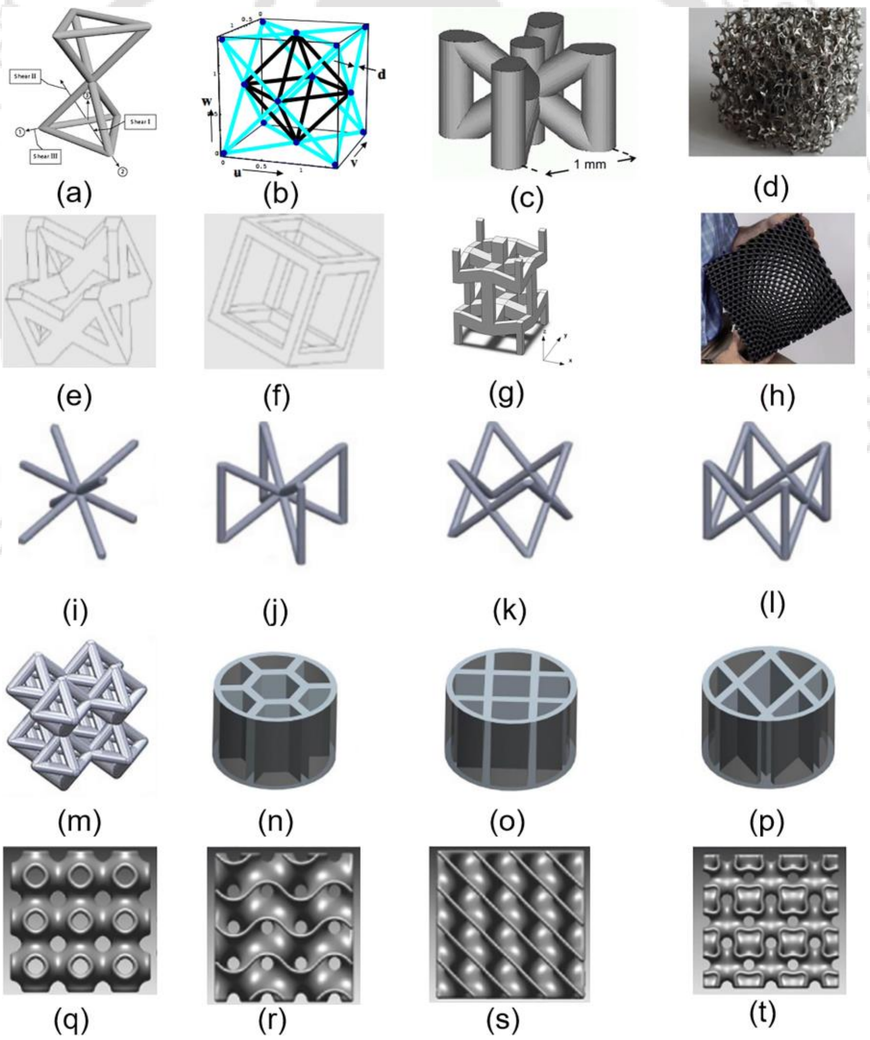

Figure 2.1. Different types of unit cells of lattice structures (Reproduced with permission from [2]).

The lattice structures are made up of interconnected network of struts or plates in a definite pattern. The unit cell topology of the lattice structures may be varied to achieve different mechanical properties. Numerous studies have been conducted on lattice structures with unique properties. Figure 2.1 shows unit cells of different lattice structures. The body centered cubic (BCC) lattice exhibits high energy absorbing ability. On the other hand, the octet lattice can exhibit high strength and stiffness during compression [31]. The hexagonal honeycomb is one of the commonly studied structures whose topology can be changed such that the structure can exhibit negative or zero Poisson's ratio during deformation [32]. The lattice structures exhibiting negative Poisson's ratio are called auxetic structures. The classification of commonly studied auxetic structures with their properties and applications are discussed in the next sections.

2.2 Types of auxetic structures

2.2.1 Reentrant structures

The reentrant structure was originally proposed by Gibson et al. [33], which is a derivative of the conventional hexagonal honeycomb structure. The unit cell of the reentrant auxetic structure is shown in Figure 2.2. In case a tensile load is applied, the oblique struts of the reentrant structures are subjected to bending and stretching simultaneously, which results in the expansion of the unit cells and an increase in the volume of the structure. This results in an increase in the dimension of the cell, and Poisson's ratio becomes negative [34]. Smith et al. analyzed the geometry of the 2D-reentrant structure, and the Poisson's ratio (υ_{12}) and the elastic modulus (E_1) along the loading direction are given as [35]:

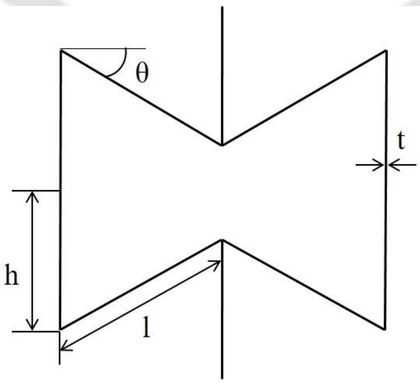

Figure 2.2. The unit cell of the 3D-reentrant lattice.

$$\upsilon_{12} = \frac{\sin\theta\,(\frac{h}{l}+\sin\theta)}{\cos^2\theta} \qquad 2.1$$

$$E_1 = E_s b\,(\frac{t}{l})^3\,\frac{(\frac{h}{l}+\sin\theta)}{b\cos^3\theta} \qquad 2.2$$

where, h is half of the length of the horizontal strut, l is the length of inclined struts, θ is the angle, b is the thickness of the strut along the plane of paper and E_s is the Young's modulus of the base material. Many studies have shown the mechanical behaviour of 2D-reentrant structures [36–39].

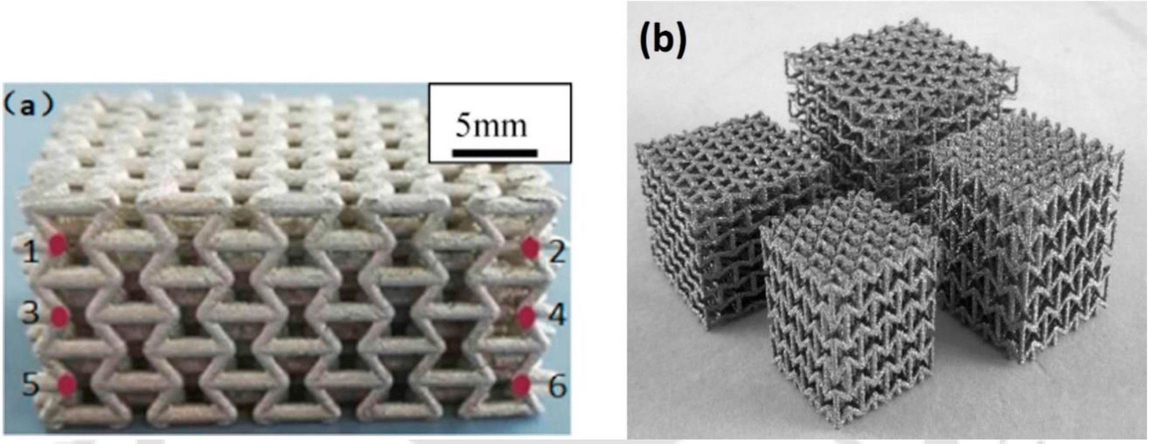

Figure 2.3. Lattices structures made of 3D-reentrant unit cells (Reproduced with permission from [40,41]).

The analytical studies of the 3D-reentrant structure were conducted by Yang et al. [41,42]. They derived the relations between the unit cell geometric parameters with the Poisson's ratio, elastic modulus and compressive strength. They also validated the models with experimental results, which agreed with the analytic results. Xue et al. [40] fabricated Al-based auxetic structures and studied their mechanical characteristics and failure behaviour by varying various parameters (reentrant angle, strut length, strut diameter) of the auxetic structure. The 3D-reentrant structure was deformed by the bending of the reentrant struts, and this bending was throughout the whole layer without any localization. They found that the compressive strength, as well as Poisson's ratio, strongly depends on the strut diameter, strut length, and reentrant angle. Also, the more negative the value of Poisson's ratio, the larger the compressive strength. The 3D-reentrant lattice structures are shown in Figure 2.3. Geng et al. [43] developed theoretical models to predict the mechanical properties (stiffness, Poisson's ratio, strength) of 3D-reentrant structures manufactured by Selective Laser Melting using AlSi10Mg alloy. They studied the geometrical errors and defects in the fabrication of the reentrant structures. The decrease in laser scanning speed and increase in laser power leads to an increase in surface roughness of the bottom part of the horizontal struts. They concluded that the properties of the reentrant structures depend not only on the topology but also on the geometric as well as surface defects. The excessive melting and severe powder adhesion affect the strength of the nodes of the strut. The ultimate tensile strength and strain at break decreases because of the presence of geometric defects. The study by Novak et al. focused on the effect of high-strain rate on the auxetic structures, and they evaluated the critical velocity by experimental and computational analysis [44]. They used Ti6Al4V alloy to print the auxetic structures by selective electron beam melting. The high strain rate tests were conducted by a one-stage gas gun with a velocity of up to 200 m/s. They observed that the influence of strain rate was very high due to changes in the deformation mode. The deformation mode changed from quasi-static to shock when the velocity was increased beyond a critical value. Logakannan et al. performed dynamic tests by Instron VHS machine at a speed of 5 m/s on the 3D-reentrant structures [45]. They found that the buckling of struts was the dominant deformation mechanism in both quasi-static and high-strain rate tests. The initial peak stresses were significantly higher in dynamic tests than in quasi-static tests.

2.2.2 Chiral lattice structures

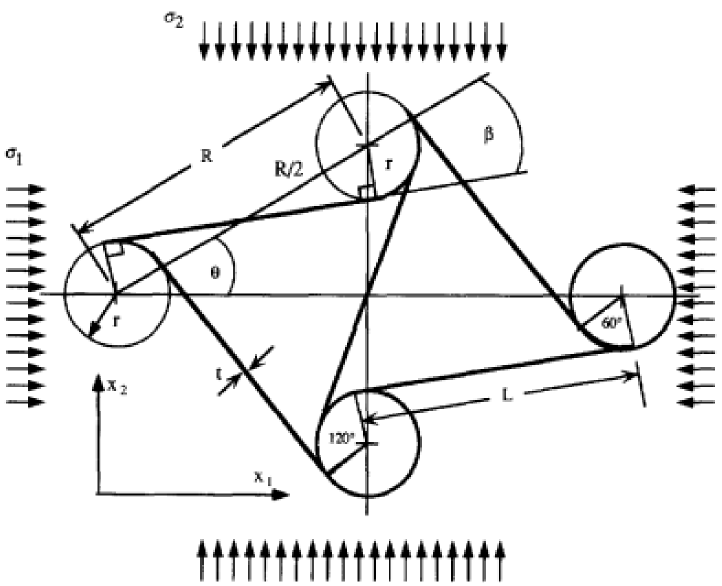

Figure 2.4. The geometry of the chiral unit cell (Reproduced with permission from [46]).

A chiral structure consists of a central ring in which the ligaments are attached tangentially that are not superimposable in its mirror image. The auxetic behaviour of these structures is due to the rotation of the rigid rings that causes winding and unwinding of the ligaments attached to the rings. The chiral network is generated by connecting the chiral unit-cells. Chiral lattice structures can exhibit a Poisson's ratio of -1 [17]. The geometry of the chiral unit cell analyzed by Prall and Lakes [46] is shown in Figure 2.4. Young's modulus for loading in different directions is equal due to the tangential constraint of ligaments on the rings. The Young's modulus (E) is given as [46]:

$$E = E_s\sqrt{3}\frac{t^3}{L^3}\frac{L^2}{r^2} \qquad 2.3$$

where, E_s is the Young's modulus of the base material, and t, L and r are geometrical parameters shown in Figure 2.4.

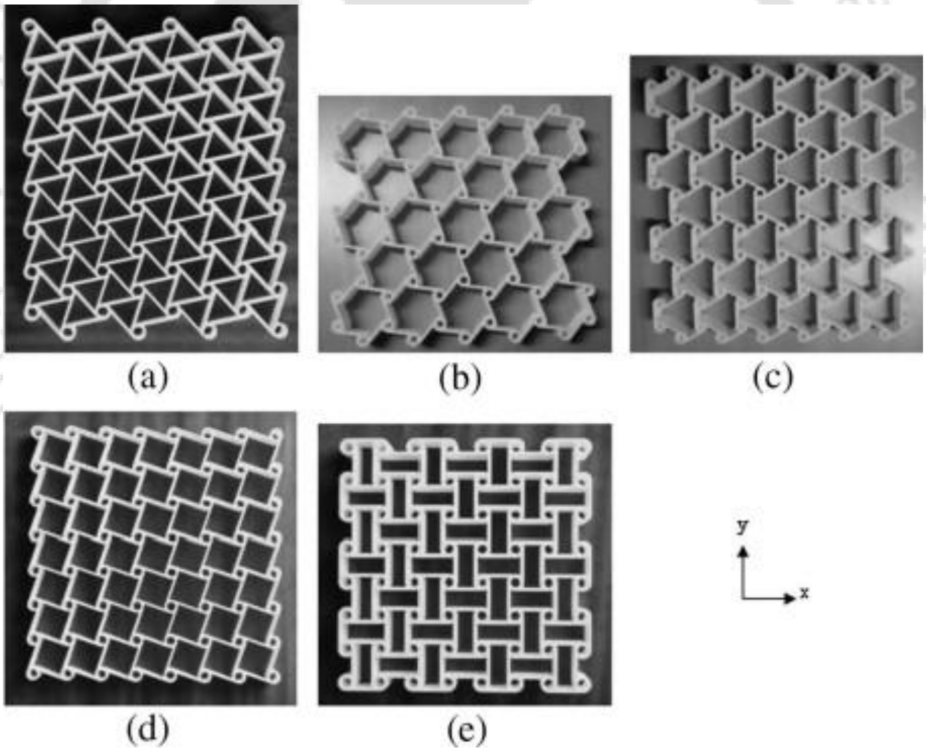

Figure 2.5. Types of chiral structures: (a) hexachiral (b) trichiral (c) anti-trichiral (d) tetrachiral and (e) anti-tetrachiral (Reproduced with permission from [47]).

The rings are attached on the opposite sides of the ligaments for the chiral structures, while for the anti-chiral structures, the rings are attached on the same sides of the ligaments (Figure 2.5). The constraints on rotational symmetry need to be followed to create periodic chiral structures [16]. The names of the chiral structures are derived from the number of ligaments attached to a ring and the connection of the ligaments on the sides of the rings. In Figure 2.5(a), six ligaments are attached to the ring and the rings are attached on the opposite sides of the ligaments, hence, named hexachiral structure.

Wu et al. [48] proposed two types of 3D-chiral structures, chiral-chiral-antichiral and chiral-antichiral-antichiral, and fabricated them by Selective Laser Sintering using nylon. The 3D-chiral structures are shown in Figure 2.6. They studied the deformation behaviour of the structures in which elastic bending deformation of the struts and rotation of the nodes were dominant. The chiral struts showed full-wave deformation mode, while the anti-chiral struts showed half-wave deformation mode. Such structures can be used in vibration attenuation, biomechanical devices and morphing structures.

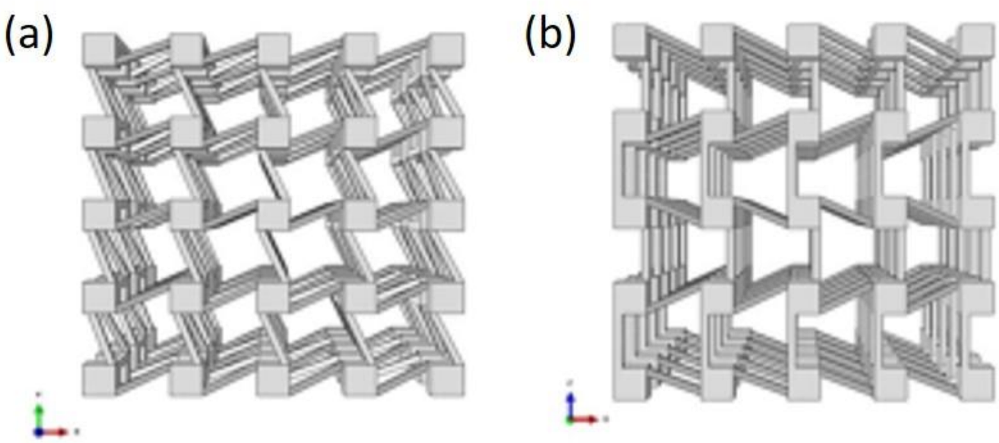

Figure 2.6. 3D-chiral auxetic lattices [48].

2.2.3 Rotating polygonal structures

The auxetic behaviour of the rotating polygons is obtained from the rotation of the rigid polygons connected through hinges. Rotating squares, rotating rectangles, rotating triangles, etc., are examples of rotating polygonal structures [17]. A rotating square model proposed by Grima et al. [49] is shown in Figure 2.7. A Poisson's ratio value of −1 can be achieved in these structures. For unit thickness, Young's modulus can be obtained as [49]:

$$E_1 = E_2 = k_h \frac{8}{l^2(1-sin\theta)} \quad 2.4$$

$$k_h = \begin{pmatrix} S_{11} & S_{12} & 0 \\ S_{21} & S_{22} & 0 \\ 0 & 0 & 0 \end{pmatrix} = \frac{1}{E}\begin{pmatrix} 1 & 1 & 0 \\ 1 & 1 & 0 \\ 0 & 0 & 0 \end{pmatrix} \quad 2.5$$

where, k_h is the stiffness constant of the hinges, l is the length of the sides of the square, and θ is the angle between the squares, as shown in Figure 2.7. Rotating unit models were fabricated by cutting slit perforations in sheets. Figures 2.8(a) and (b) show the undeformed and deformed shapes of the structures made of rotating rectangles and triangles, respectively. The auxetic behaviour can be clearly observed during the deformation of these structures.

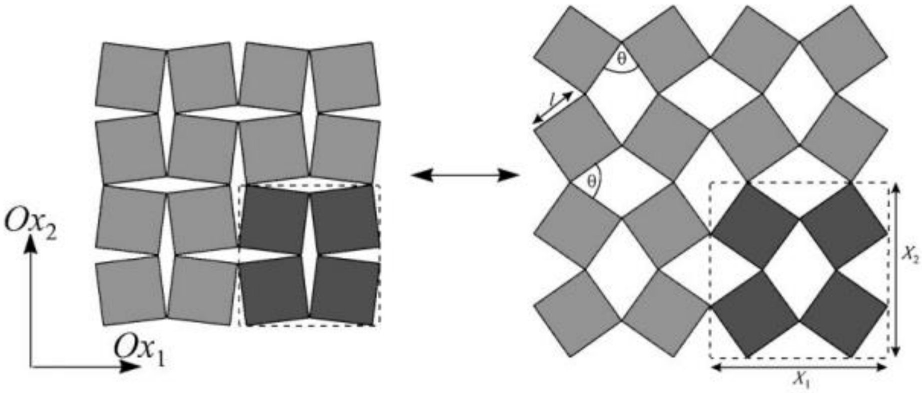

Figure 2.7. Deformation of rotating square structures (Reproduced with permission from [49]).

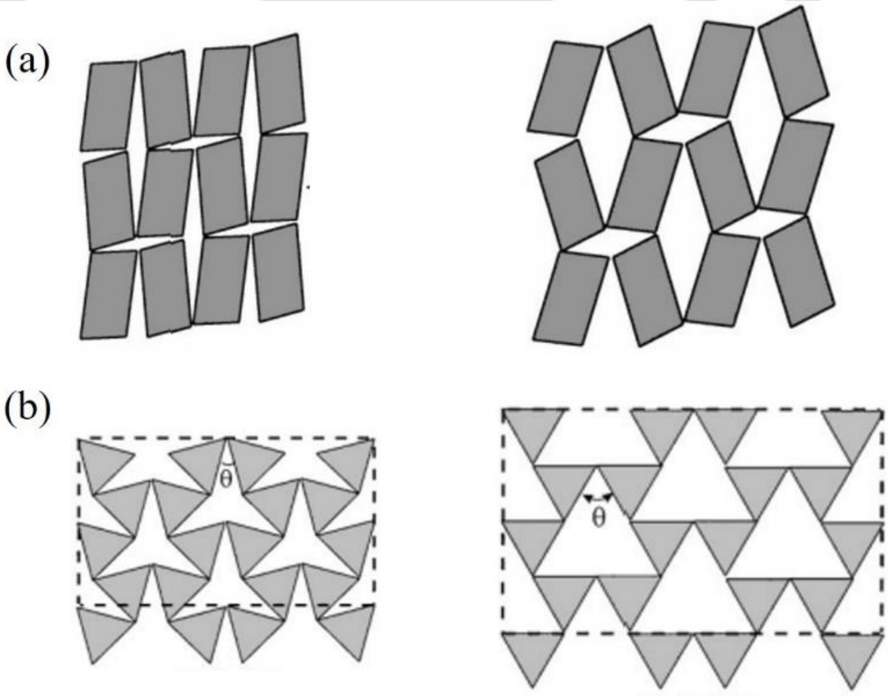

Figure 2.8. Deformation of (a) rotating rectangles and (b) rotating triangles auxetic structures (Reproduced with permission from [49]).

2.3 Properties of auxetic structures

Apart from the high strength-to-weight ratio and high energy absorption ability, the auxetic structures possess some peculiar properties not found in non-auxetic structures. These properties are described below:

2.3.1 Indentation resistance

When a conventional material is indented, the material present in the vicinity of the indenter will move perpendicular to the applied load, as shown in Figure 2.9(a). However, when an auxetic material is indented, it will laterally contract [Figure 2.9(b)]. The material flows into the impact vicinity and thus, the area becomes dense. This results in higher hardness of auxetic materials [50]. According to the classical theory of elasticity, the indentation resistance is related to the material hardness (H), and it is given as [19]:

$$H \,\alpha\, \left(\frac{E}{1-\upsilon^2}\right)^{\gamma} \quad 2.6$$

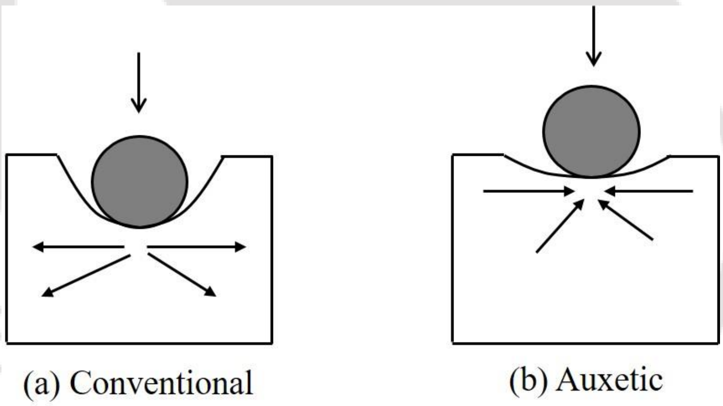

Figure 2.9. Indentation behaviour of (a) conventional and (b) auxetic materials [19].

where, E is the Young's modulus of the base material, υ is the Poisson's ratio and γ is assumed to be 1 or 2/3 in the scenario of uniform pressure distribution or Hertzian indentation. It can be observed from Equation 2.6 that when the value of υ is −1, the hardness tends to be infinity.

2.3.2 Shear resistance

The auxetic structures have more shear resistance than conventional materials. According to the classical theory of elasticity, for a 3D isotropic material, the elastic behaviour can be predicted by two of the four elastic constants, i.e. Young's modulus, bulk modulus, shear modulus, and Poisson's ratio. The relationship between the shear modulus and the Poisson's ratio is given as [51]:

$$G = \frac{E}{2(1+\upsilon)} \tag{2.7}$$

It can be observed from Equation 2.7 that the value of shear modulus increases as Poisson's ratio decreases.

2.3.3 Fracture toughness

The materials that exhibit a negative Poisson's ratio are reported to have better fracture toughness than conventional materials [14]. The auxetic materials also have lower crack propagation. Donoghue et al. reported that a higher amount of energy is required for a crack to propagate in auxetic laminate [52]. Yang et al. reported that the fracture toughness of auxetic materials is two times that of conventional materials [53].

2.3.4 Synclastic behaviour

During out-of-plane loading, a conventional material deforms to form a saddle shape, whereas an auxetic material deforms to form a dome shape. This behaviour is called synclasticity and is shown in Figure 2.10. This property has applications in the medical and sports industries [19,51]. It is possible to achieve synclastic behaviour in auxetic materials without any manufacturing methods [19].

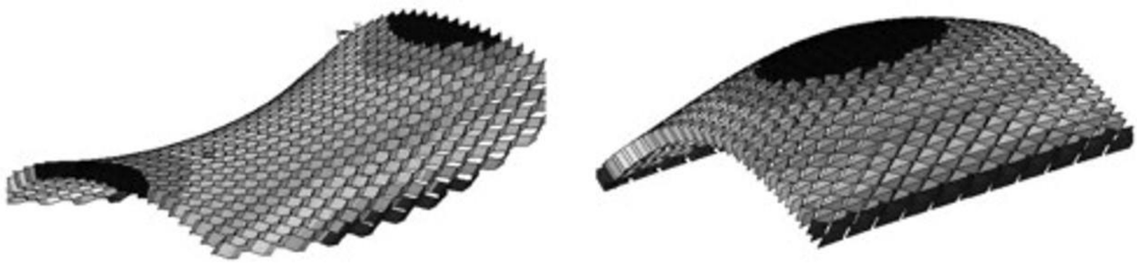

(a) Hexagonal (saddle shape) (b) Auxetic (dome shape)

Figure 2.10. Out-of-plane bending of (a) hexagonal structure and (b) auxetic structure (Reproduced with permission from [54]).

2.3.5 Variable permeability

Most of the auxetic materials possess porous microstructure and the size of these pores can be varied during compression and tensile deformation. The auxetic materials can be used as filters using this behaviour [55,56]. Due to their unique pore opening characteristics, the auxetic materials can be used in the range of macro-scale to nano-scale filtration processes. Figure 2.11 shows the variable permeability of auxetic structures.

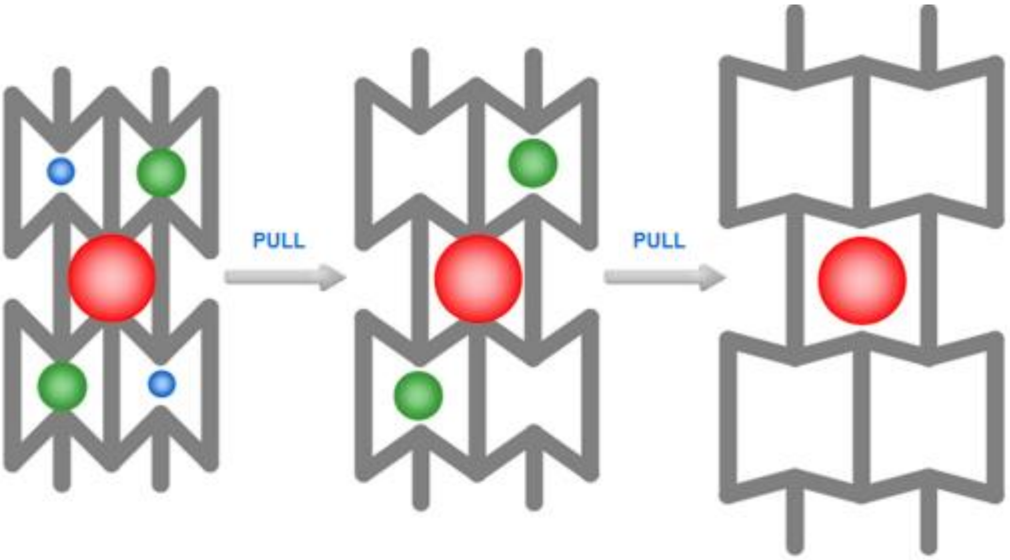

Figure 2.11. Auxetic structures used as filters (Reproduced with permission from [19]).

2.4 Applications of auxetic structures

2.4.1 Energy absorbing devices in military, automobile and sports applications

Figure 2.12. Applications of auxetic structures to improve the impact resistance of armored vehicles (Reproduced with permission from [57]).

Studying the dynamic behaviour of auxetic materials is crucial if they are to be used for applications like impact protection, energy absorption, etc. Many researchers have studied the quasi-static compression properties of auxetic structures. However, studies on dynamic behaviour and strain rate sensitivity of auxetic structures of both polymers and metals are very rare. The properties in dynamics are generally different from that of quasi-static behaviour [58].

Imbalzano et al. [57] conducted a numerical study on the dynamic and energy absorption characteristics of auxetic structures. The effect of Poisson's ratio on the impact resistance was conducted by varying geometrical parameters. From the study, they concluded that auxetic structures with lower values of Poisson's ratio performed better. The auxetic sandwich panel absorbed very high energy of projectile impact at a velocity of 200 m/s, and the back face displacements were also reduced due to localized densification and plastic deformation. They further concluded that the auxetic sandwich panels have promising protective applications. Figure 2.12 shows a composite auxetic material with potential application in blast resistance. Military personnel, vehicles, and temporary reinforced shelters often face threats such as abrasion, sharp edges, ballistic projectiles and blasts. The protective clothing used in defense requires a range of high-performance garments, including thermal undergarments, combat jackets, and body armor. The challenge lies in enhancing the resilience of bulletproof vests and helmets against impacts and shrapnel. One approach is to incorporate auxetic materials into the textile structures, which can effectively distribute the force from different directions and absorb energy. This compensates for the impact when vests or helmets experience a strike from a specific direction. By utilizing auxetic structures, when a bullet hits, it mitigates the intense kinetic energy generated during the impact [51,59].

(a) (b)

Figure 2.13. Sports shoe with (a) auxetic skin and (b) auxetic sole (Reproduced with permission from [19]).

Yang et al. [60] conducted finite element studies on reentrant, arrowhead and honeycomb structures. They used three different polymers, i.e., polylactic acid and two types of thermoplastic polyurethane, to fabricate the auxetic structures. They concluded that pads could be designed for protection as the impact force can be taken away to other areas by specifically laying auxetic structures in different areas. The bottom layer experiences very less force as the force is distributed to transverse areas by the auxetic structures. Thus, auxetic materials can be used in helmets, armor, body protection pads and other energy absorbing applications. Finite element simulations are conducted by Sanami et al. for a new type of auxetic honeycomb for its potential applications in helmets, gloves and pads related to sports [61]. Their work showed that more energy is required to intent an auxetic foam using a ball indenter than conventional foam to a depth of 10 mm. When auxetic structures are used in helmets, the rotational acceleration can be reduced due to their ability to change the shear modulus through Poisson's ratio. This helps reduce the severity of the direct impact of auxetic materials compared to conventional foams [62]. D30 (helmet manufacturer) used unique auxetic geometry to design and develop the Trust Stealth Helmet Pad System, which they claimed to provide extreme comfort and high-performance protection exceeding the required level, and it also maintains consistence performance on second impact. Figure 2.13 shows auxetic materials used as shoe skin and shoe soles. In automobiles, light-weight tubular metamaterials can be used as energy absorbers to improve crashworthiness [63,64].

2.4.2 Medical applications

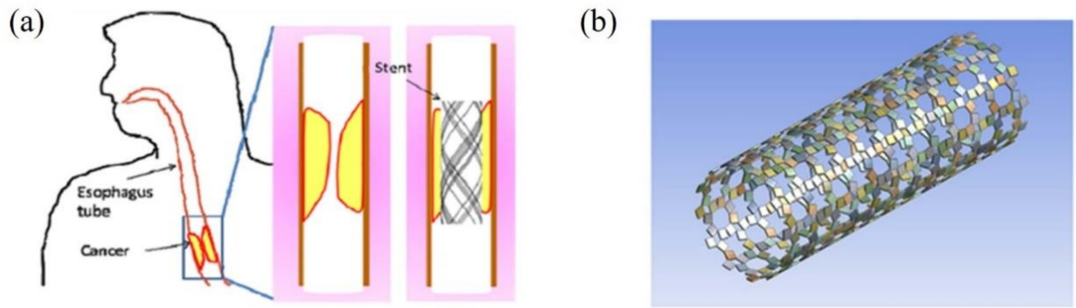

Figure 2.14. Stent used to open oesophageal constriction, and (b) auxetic oesophagus stent. (Reproduced with permission from [65]).

Coronary artery disease and oesophageal cancer are the common cause of death globally. In recent research, the application of auxetic metamaterials has been put forth as a novel approach to the design of mechanically adjustable stents [66]. These innovative materials have been successfully incorporated into the fabrication of various stent types, including angioplasty stents [67–70] and oesophageal stents [71–73]. Figure 2.14 shows a stent implemented in the oesophagus.

Kolken et al. [74] developed hybrid meta-biomaterials combining auxetic and conventional components (Figure 2.15). These innovative meta-implant designs were observed to exert compressive forces on both sides of their contact lines with the adjacent bone. As a result, the likelihood of failure at the bone-implant interface was reduced, lowering stress shielding and improving bone ingrowth.

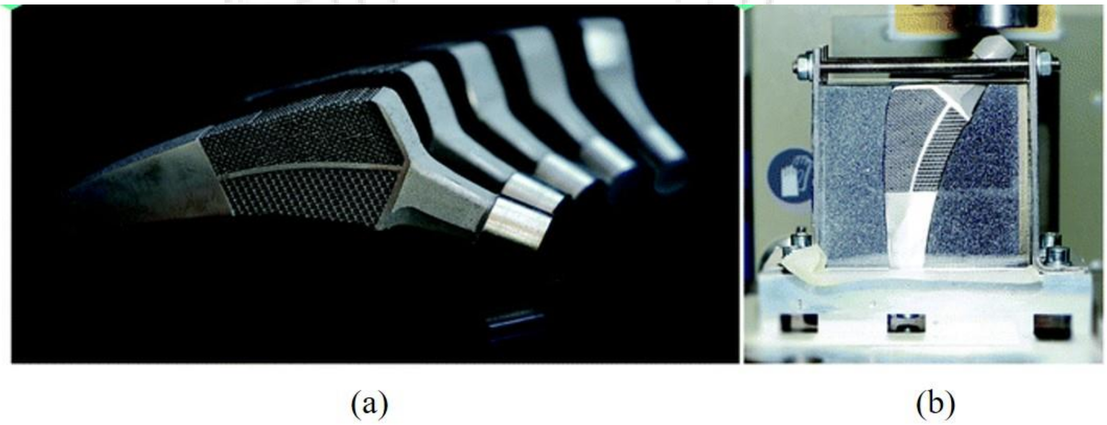

Figure 2.15. (a) Additively manufactured hip implant, and (b) test setup of implant surrounded by bone-mimicking materials [74].

A summary of applications of auxetic structures in different applications is shown in Table 2.1 [13].

2.5 Types of ZPR lattice structures

2.5.1 Semi-reentrant (SRE) structures

A single unit cell of the semi-reentrant (SRE) honeycomb structure, proposed by Grima et al. [24], consists of features of two different unit cells: the conventional honeycomb structure that exhibits positive Poisson's ratio and the reentrant honeycomb structure that exhibits negative Poisson's ratio. The unit cells of the hexagonal honeycomb, reentrant and semi-reentrant structures are shown in Figure 2.16. The mechanical behaviour of the 2D-SRE lattices was mostly studied [75,76]. The Young’s modulus (E) of the SRE structure, when loaded perpendicular to struts with length ‘h’ can be calculated as [24]

$$E = \left(\frac{t}{l}\right)^3 \left(\frac{l}{h}\right) \frac{E_s cos\theta}{sin^2\theta} \quad 2.8$$

Table 2.1. Applications of auxetic structures (Reproduced with permission from [13]).

Field	Applications
Aerospace	Vanes for gas turbine engine, thermal protection, aircraft nose-cones, wing panel, sounds and vibration absorber, rivet
Automotive	Bumper, cushion, thermal protection, sounds and vibration absorber parts that need shear resistant, fastener
Biomedical	Bandage, wound pressure pad, dental floss, artificial blood vessel (the wall thickness increases when a pulse of blood flows through it), artificial skin, drug release unit, ligament anchors. Surgical implants (similar to that of bone characteristics)
Composite	Fiber reinforcement (because it reduce the cracking between fiber and matrix)
Military	Helmet, bullet proof vest, knee pad, glove, protective gear (better impact property)
Sensors/Actuators	Hydrophone, piezoelectric devices, various sensors (the low bulk modulus makes them more sensitive to hydrostatic pressure)
Textile	Fibers, functional fabric, color-change straps or fabrics, threads

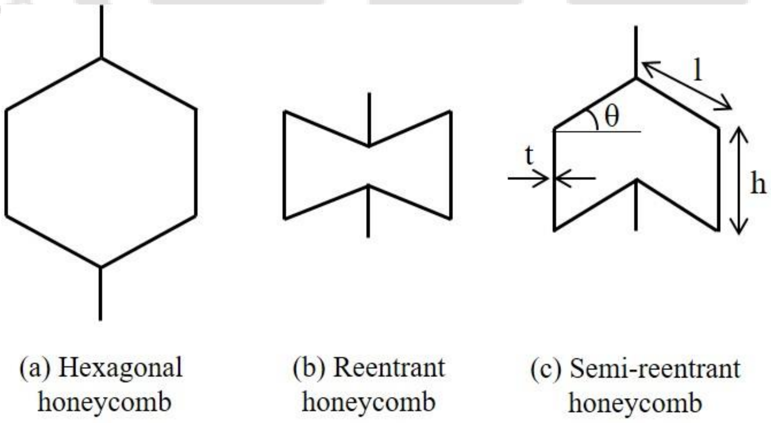

Figure 2.16. Unit cells of (a) hexagonal honeycomb, (b) reentrant honeycomb and (c) semi-reentrant honeycomb structures [24].

where, t is the thickness of the struts, l is the length of inclined struts, h is the length of vertical struts, θ is the angle of the inclined struts with the horizontal axis and E_s is the Young's modulus of the base material. The SRE structures have also been designed as 3D lattice and tubular lattice structures by Wang et al. [77] and Wang et al. [78], as shown in Figure 2.17. The tubular lattice metamaterials can be helpful in different engineering fields like the medical and automobile industries [65].

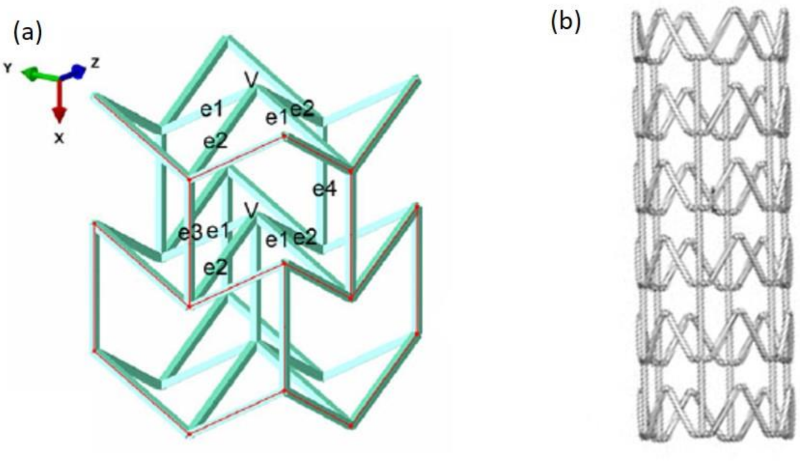

Figure 2.17. (a) The unit cell of 3D SRE structure, and (b) tubular SRE structure (Reproduced with permission from [77,78])

2.5.2 Aux-Hex and Silicomb structures

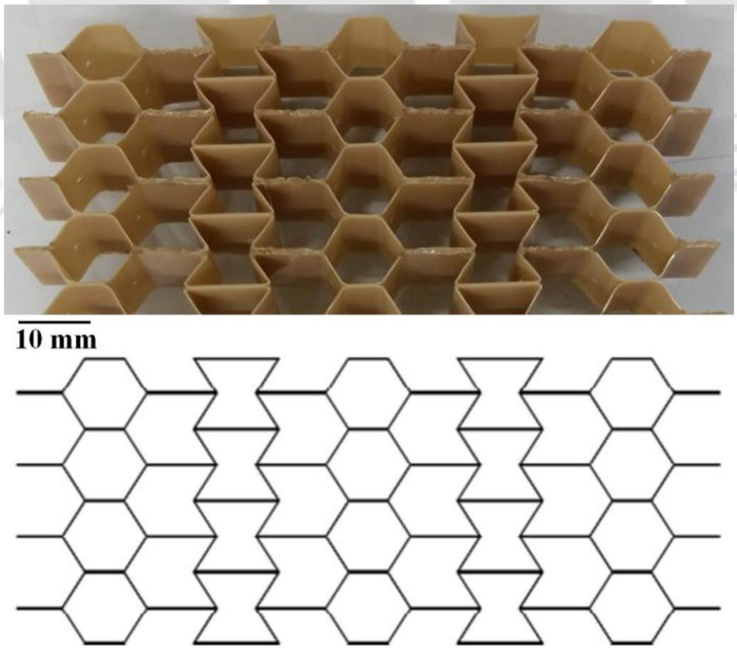

Figure 2.18. The fabricated 2D-Aux-Hex lattice structure (Reproduced with permission from [25]).

The Aux-Hex hybrid structure consists of three different types of unit cells: the hexagonal honeycomb, the reentrant honeycomb, and the semi-reentrant honeycomb [25]. The unit cells and lattice structures of the Aux-Hex structure are shown in Figure 2.18. If the number of unit cells of the three base structures is the same, the overall structure exhibits zero Poisson's ratio. The hinge distance in the lateral direction remains unchanged for the semi-reentrant unit cell. At the same time, the negative Poisson's ratio behaviour of the reentrant structure is compensated by the positive Poisson's ratio of the hexagonal honeycomb structure. The Aux-Hex structures were also designed as tubular lattices by Liu et al. and 3D lattices by Guo et al. [26,79].

A curved Silicomb structure using the Kirigami technique was designed by Chen et al. [80]. Figure 2.19 shows the unit cell and fabricated structure of the Silicomb lattice. The unit cell representation consists of two walls (L and H) with a thickness of t, a depth of b, and two internal angles (φ and θ). The curved Silicomb configuration can be designed as core structures that can achieve minimal density and maximum stiffness coefficients. Virk et al. studied the mechanical response and energy dissipation of Silicomb kirigami structures [27]. An accordion-like 3D lattice structure that exhibits zero Poisson’s ratio was designed by Chen et al. [81].

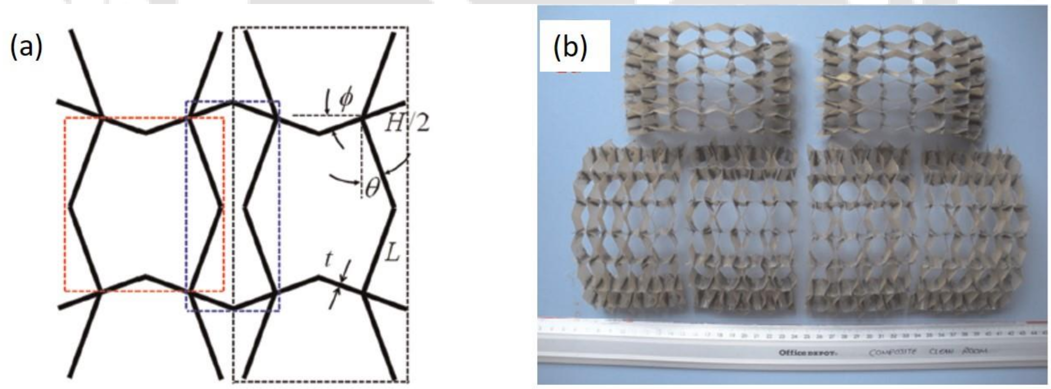

Figure 2.19. The unit cell of Silicomb structure and (b) the final fabricated curved Silicomb structures [80].

2.5.3 Bio-inspired ZPR lattices

Some bio-inspired lattice structures were designed in recent years that can exhibit zero Poisson’s ratio. Hamzehei et al. introduced a 2D-reentrant-based zero Poisson's ratio metamaterial based on the 2D image of a DNA molecule [82]. Figure 2.20(a) shows the DNA-inspired design of the ZPR structure. The DNA-inspired structures have better energy absorbing ability than the conventional ZPR structures. Zadeh et al. [83,84] proposed a novel Fish cell cellular metamaterial exhibiting zero Poisson's ratio in both the orthogonal in-plane directions. They showed the ZPR behaviour of the Fish cell structures by numerical simulations and validated them by experiments. These Fish cell structures can be used in wing morphing applications. The unit cell of the Fish cell lattice is shown in Figure 2.20(b). The fish-cell-based zero Poisson's ratio cylindrical tube was designed by Qin et al. [85], and the linear buckling and the vibration behaviour of the metamaterial were investigated using numerical and experimental analyses.

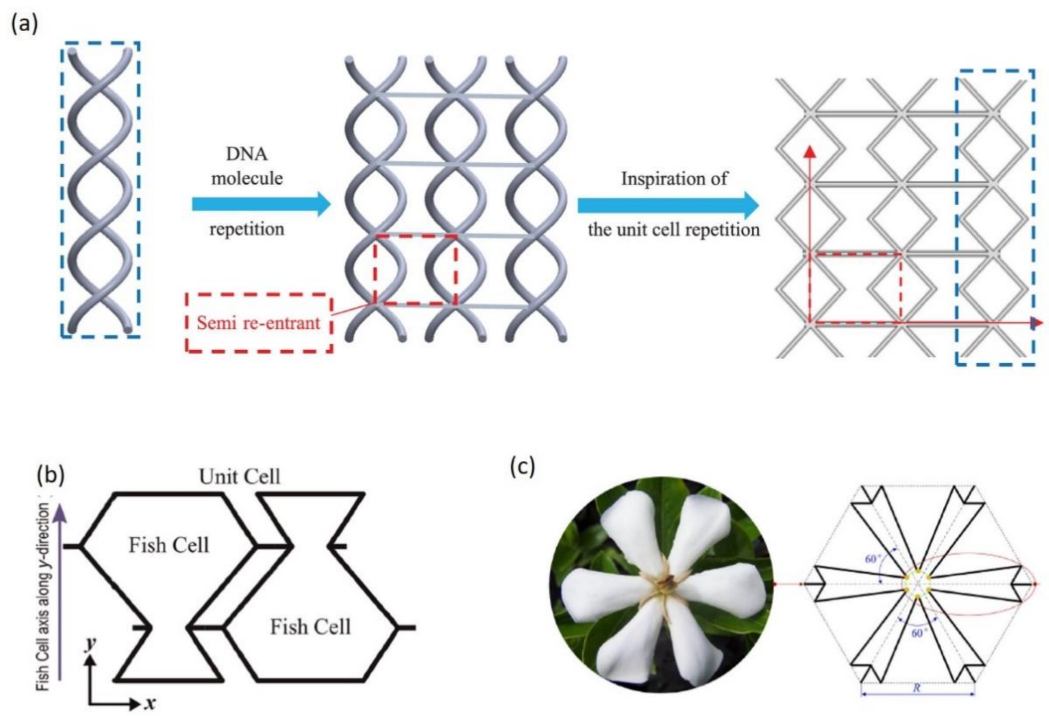

Figure 2.20 (a). DNA-inspired ZPR lattice, (b) Fish-cell unit cell, and (c) Gardenia-inspired ZPR lattice unit cell (Reproduced with permission from [82,83,86]).

A novel gardenia-inspired ZPR lattice structure was proposed by Feng et al. [86]. Figure 2.20(c) shows the unit cell of the gardenia-inspired ZPR lattice. Numerical, theoretical and experimental analyses were conducted to understand its mechanical behaviour. The mechanical properties of cellular metamaterials inspired by cuttlebone were studied by Mao et al. [87]. The cuttlebone structure, composed of lamellar septa, demonstrates greater strength and energy-absorption capacity compared to octet truss lattice, as well as traditional polymer and metal foams. Moreover, the cuttlebone-inspired structures exhibited zero Poisson's ratio during compression.

2.6 Properties of ZPR lattice structures

Cylindrical shaped surfaces

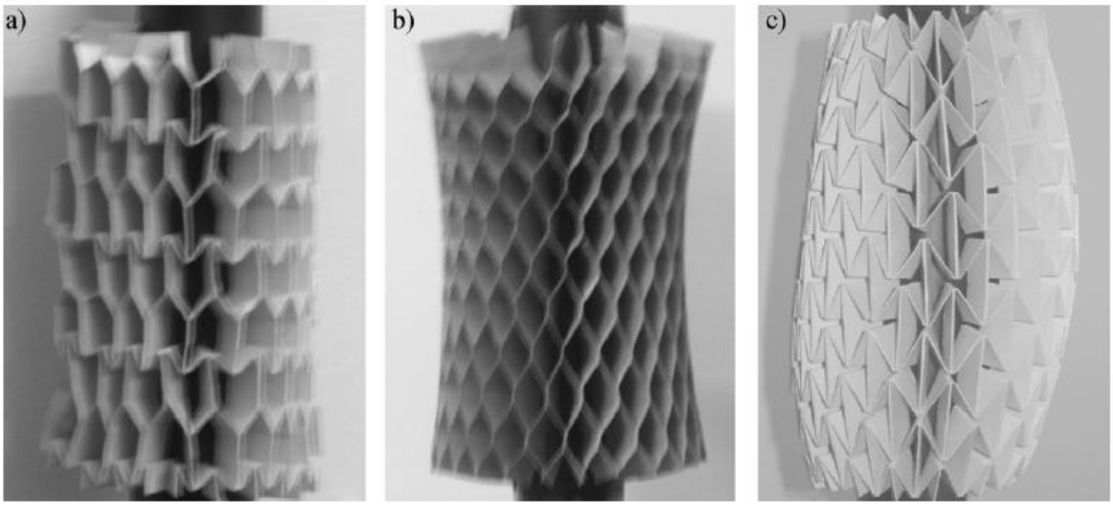

Figure 2.21. Tubular structures obtained from (a) semi-reentrant (b) conventional and (c) reentrant honeycombs (Reproduced with permission from [24]).

Apart from the applications where ZPR structures can be used where lateral deformation is undesired, the ZPR structures can be easily transformed into tubular structures [24]. Conventional honeycombs and auxetic honeycombs are not suitable for transforming into cylindrical structures because they naturally form saddle and dome shapes, respectively. Figure 2.21 shows the behaviour of conventional, reentrant and semi-reentrant structures in cylindrical shapes. This happens because when a conventional honeycomb is bent downwards in one direction, its upper surface is stretched, causing the upper surface to contract and curve upwards, forming a saddle shape. On the other hand, in auxetic honeycombs, downward bending or extension in one direction leads to expansion in the lateral direction, causing the honeycomb to bend downward in that direction and form a dome shape. However, semi-reentrant honeycombs are not affected in the lateral direction when bent, allowing them to form a cylindrical surface. This feature can benefit ZPR structures to be used as honeycomb cores in sandwich composites that must be transformed into tubular structures. [75].

2.7 Applications of ZPR lattice structures

2.7.1 Wing-morphing

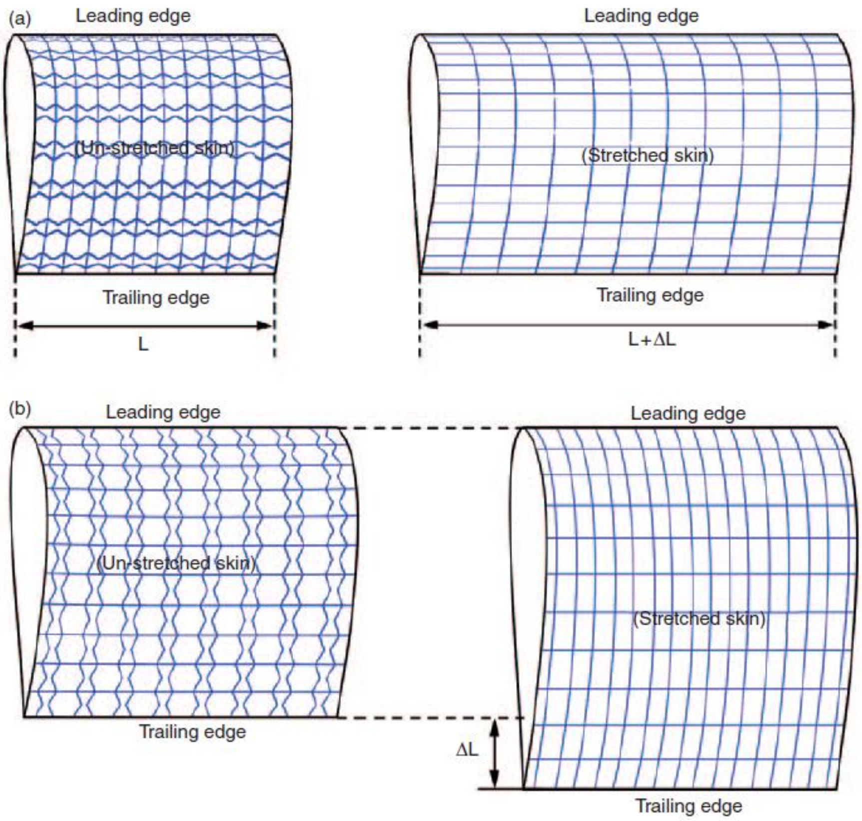

Figure 2.22. Use of accordion-type ZPR structures in one-dimensional wing morphing (Reproduced with permission from [21]).

Aircraft wing morphing is a technique in which the aircraft can change the shape of the wings to adapt to the desired flight conditions. This technique can reduce fuel consumption by minimizing the drag force associated with the flight modes [88]. Olympio and Gandhi studied the effect of using accordion and hybrid ZPR honeycomb for one-dimensional morphing applications [21]. The use of ZPR skins in one-dimensional wing morphing is shown in Figure 2.22. Their analysis showed that ZPR structures could benefit 1D-morphing applications compared to conventional structures. Huang et al. designed a novel ZPR structure made of tessellations of hexagons and thin plates that demonstrate exceptional bending compliance at large strains, making them highly suitable for designing composite structures used in airframe morphing applications [89]. Novel ZPR lattice structures for multiple in-plane morphing were also designed and the mechanical properties were studied by numerical simulations and experiments [90–92].

2.7.2 Bio-medical applications

The ZPR structures are promising in tissue engineering, in which a scaffold having a zero Poisson's ratio is beneficial to emulate the behaviour of the native tissue and to transmit forces to the host tissue site during wound healing. The ZPR scaffolding is advantageous in engineering ligaments, cartilage, and brain tissues, which exhibit nearly zero Poisson's ratio [22,93].

Lattice metamaterials in the form of tubular structures have recently gained wide attention from researchers. Generally, the 2D-planar lattice in the form of a sheet is rolled up to build a tubular structure. Negative or zero Poisson’s ratio tubular lattice can benefit angioplasty, oesophageal and cardio-vascular stent applications [66,78,94]. Wang et al. designed and fabricated a semi-reentrant honeycomb-based zero Poisson’s ratio cardiovascular stent using a novel screw-extrusion-based 3D-printing technique and determined the mechanical properties of the fabricated stents [78]. The ZPR stent developed was able to tackle the problem of longitudinal foreshortening that was observed in other non-ZPR tubular stents.

2.7.3 Pressure tubes

The ZPR structures can be used as cylindrical shells of underwater equipment or submersible structures. These ZPR structures find applications as a pressure-resistant protective cover for marine structures. They are intended to prevent circumferential extrusion stress that may occur when they experience radial forced compression from underwater distributed pressure [95]. Li et al. focused on examining the sound insulation and pressure-resistant properties of cylindrical sandwich metastructures made up of both homogeneous and graded SRE ZPR unit cells [96]. The designed meta-structures exhibit excellent vibroacoustic attenuation properties within specific frequency ranges associated with pre-strained band gaps. Additionally, they can safely withstand hydrostatic pressure equivalent to a depth of 1000 meters, all while maintaining low weight-bulk ratios.

2.8 Different techniques to improve the mechanical properties of lattice structures

In this section, we have discussed the different techniques to improve the mechanical properties of the existing lattice structures. However, these techniques were commonly used for the positive Poisson's ratio lattice structures, and only a few studies have implemented these techniques to improve the mechanical properties of the negative Poisson's ratio (NPR) and zero Poisson's ratio (ZPR) lattice structures. Looking at the potential of NPR and ZPR lattice structures in different applications, these techniques must be applied to improve the mechanical of the NPR and ZPR structures.

2.8.1 Variation of strut thickness of the unit cells

Improving the mechanical properties of the lattice structures by varying the cross-section of the struts in the unit-cells of the lattice structures is possible. A few investigations on positive Poisson's ratio lattices showed that using struts with variable cross-sections instead of uniform cross-sections can improve the mechanical properties of lattice structures [97,98]. Dejean et al. reported that slightly tapered (minimum to maximum strut diameter ratio of 0.8) struts could yield the highest compressive stress for octet lattice structures [97]. Cao et al. worked on a modified rhombic dodecahedron lattice structure, designed by varying the cross-section of the struts, and performed high strain rate tests by split Hopkinson pressure bar (SHPB) [98]. They introduced a shape parameter factor ‘α’, which was the ratio of the difference between maximum and minimum strut thickness to the maximum strut thickness. They found that with the increase in α, the compressive strength of the lattice increased first and then decreased. Figure 2.23 shows a rhombic dodecahedron lattice with uniform and tapered struts. Qi et al. designed octet and truncated octahedron lattices with uniform and tapered struts and reported that the tapered struts could reduce the elastic anisotropy and increase the elastic modulus of the lattices [99]. It can be found from the above studies that the use of tapered struts instead of uniform struts improved the mechanical properties of the lattice struts. However, the amount of improvement was different for different lattice structures.

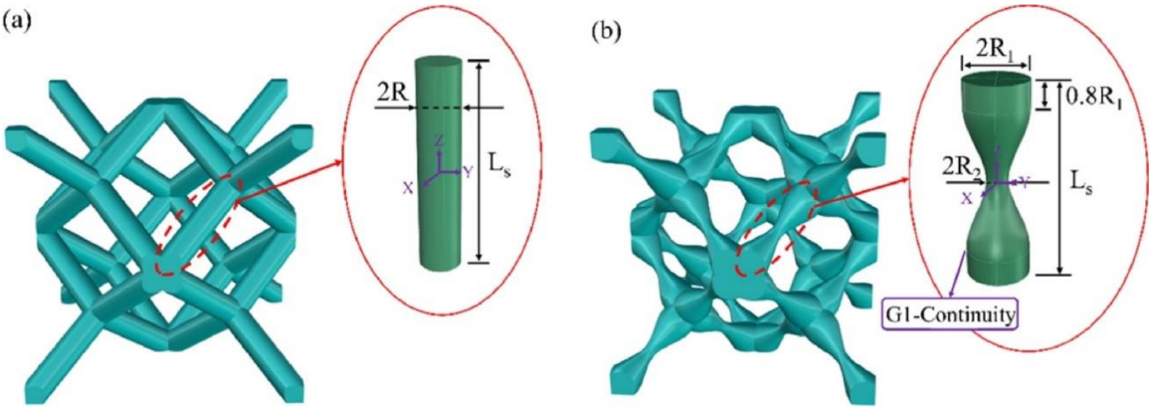

Figure 2.23. Rhombic dodecahedron lattice unit cell with (a) uniform struts and (b) tapered struts (Reproduced with permission from [98]).

2.8.2 Hybrid lattice unit cells

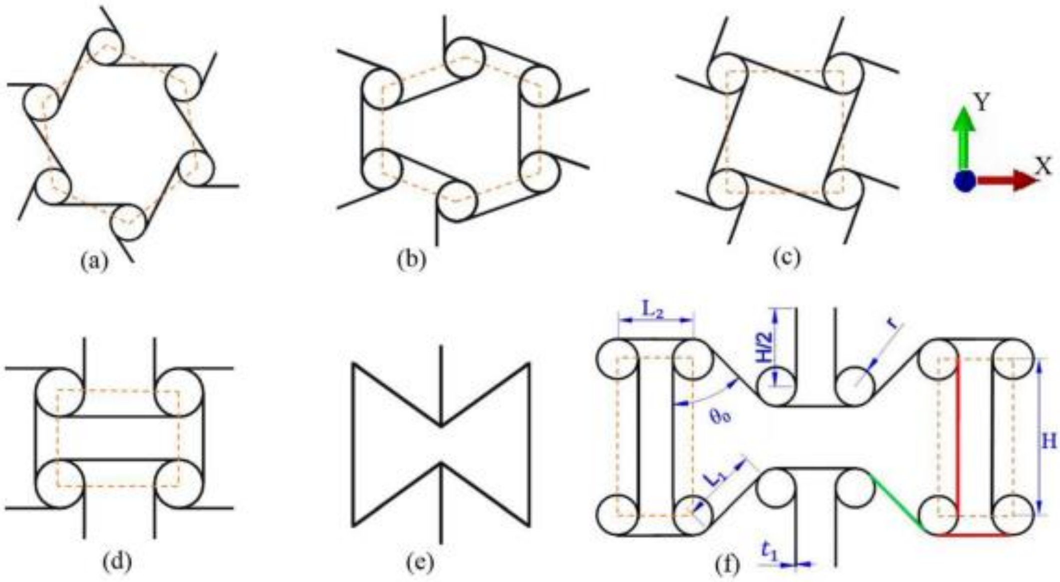

Figure 2.24. Unit cell of (a) trichiral honeycomb, (b) anti-trichiral honeycomb, (c) tetrachiral honeycomb, (d) anti-tetrachiral honeycomb, (e) reentrant and (f) hybrid reentrant chiral auxetic (RCA) structure (ligament for trichiral is shown in green and ligament for anti-trichiral is shown in red (Reproduced with permission from [100]).

Lattice structures fabricated previously were generally made of a single type of unit cell arranged in a single orientation. In hybrid lattice structures, the unit cells of two different lattices were combined to design a single unit cell. The hybrid unit cell comprised the features of both the parent unit cells, resulting in improved mechanical properties. Alomarah et al. designed a hybrid auxetic structure named Reentrant Chiral Auxetic (RCA) structure which was a combination of reentrant, chiral and antichiral auxetic structures [100]. The hybrid unit cell designed by Alomorah et al. is shown in Figure 2.24.

Alomorah et al. also studied the compression behaviour of the hybrid RCA lattices in quasi-static and dynamic loading conditions [101,102]. They found that the newly designed RCA structure had improved compressive stress and specific energy absorption than the original reentrant, chiral and antichiral structures [103]. White et al. designed interpenetrating lattices, where two or more lattices intertwine within the same volume without any direct connection [104]. This innovative approach granted the ability to construct interpenetrating structures that control energy transfer through surface interactions. Consequently, even with a single print material, it was possible to achieve multifunctional or composite-like responses. The interpenetrating lattices have exceptional mechanical properties, including enhanced toughness, negative stiffness behaviour, and electromechanical coupling.

2.8.3 Multi-lattice structures

Another method of strengthening lattices is by designing a lattice architecture with different sub-domains made of different lattices. Among such studies, Pham et al. mimicked the strengthening mechanisms of crystalline materials, i.e., grain boundary strengthening and precipitate strengthening, in lattice structures, to change the collapse mechanism of the lattice and hence improve the mechanical properties [105]. Grain boundary strengthening was mimicked by arranging a single type of lattice in multiple orientations, and precipitate strengthening was mimicked by multiple unit cell geometries. Figure 2.25 shows a multi-phase lattice in which high-strength lattices in the form of meta-precipitates are incorporated into the matrix of the low-strength lattices. The inclusion of meta-precipitates improved the mechanical properties of the lattice structures. Inspired by precipitation strengthening, Lu et al. fabricated a lattice having improved mechanical properties using Fused Deposition Modeling (FDM) in which both the meta-precipitates and the matrix were made of the same type of lattice but smaller unit cells were used as meta-precipitates as compared to that of the surrounding matrix [106]. Xiao et al. also designed a lattice with hard octet unit cells in a soft matrix of body centered cubic (BCC) lattice to enhance the mechanical properties [31]. Xiao et al. also used octet lattice as reinforcements and placed them along the diagonal planes in the BCC lattice matrix to form OCT-BCC lattice in which they were able to change the deformation behaviour of the original BCC lattice structure and thus improve the mechanical properties [107]. A zero Poisson's ratio hybrid lattice can be designed by combining a positive Poisson's ratio

(PPR) and a negative Poisson's ratio (NPR) lattice. The AuxHex lattice can exhibit zero Poisson’s ratio that was designed by combining a hexagonal honeycomb (PPR) and a reentrant auxetic (NPR) structure [25]. Chen et al. proposed a novel strategy based on topology optimization using equal volume fractions of positive and negative Poisson’s ratio (0.3 and −0.3) structures to achieve zero Poisson’s [108].

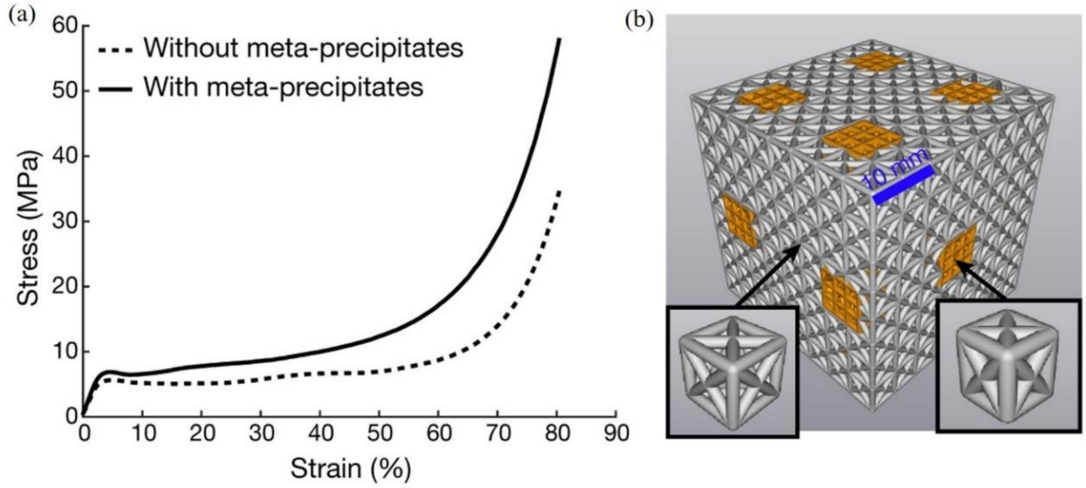

Figure 2.25. Stress-strain plots of lattices without and with meta-precipitates and (b) lattice structure with meta-precipitates (Reproduced with permission from [105]).

2.8.4 Graded density lattice structures

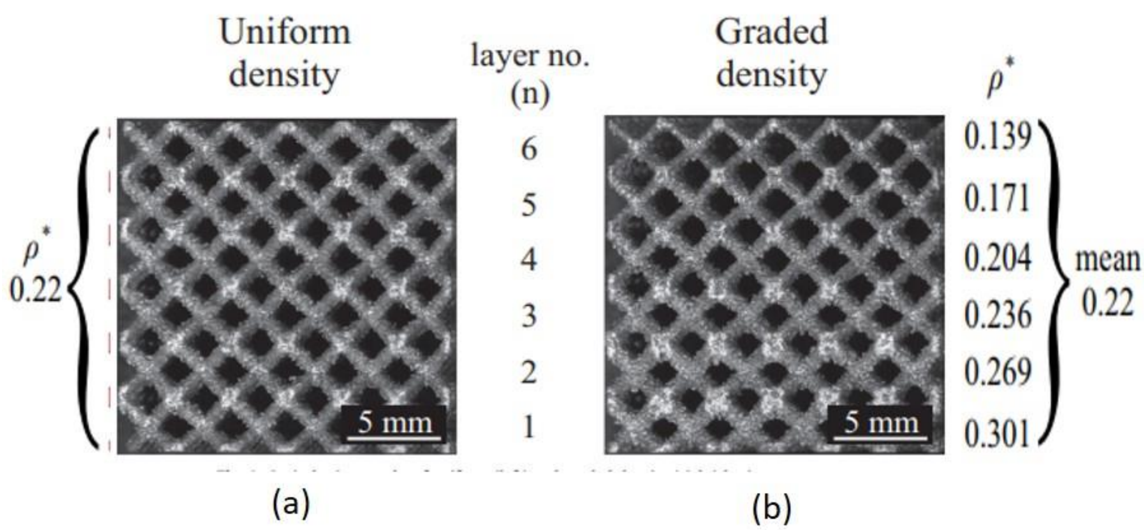

Figure 2.26. Lattice structures with (a) uniform density and (b) graded density (Reproduced with permission from [109]).

The graded density lattice structures are designed so that each horizontal layer of lattice perpendicular to the loading direction has a different relative density. Generally, the relative density of the graded density lattice is less at the top and gradually increases towards the bottom. Maskery et al. studied the crushing behaviour of graded density body centered cubic (BCC) lattice by quasi-static compression [109]. The comparison of the design of the graded density structure with the uniform density structure is shown in Figure 2.26. The graded density BCC structures collapsed layer by layer, starting from the region of lower density to higher density. The gradual strengthening and the ability to absorb an increasing amount of energy until densification makes graded structures highly appealing for advanced applications. Xiao et al. designed uni-directional and bi-directional graded density 2D reentrant structures by selective laser melting using AlSi10Mg and observed change in the deformation behaviour of the graded density structures compared to the uniform non-graded structure, which led to the improved mechanical properties of the graded reentrant structures [110]. Novak et al. studied the compression and shear failure of graded density chiral auxetic structures [111]. Their study concluded that graded auxetic structures were less stiff and underwent gradual failure, whereas uniform structures were stiffer but experienced abrupt failure at lower strains.

2.8.5 Polymer-filled lattice structures

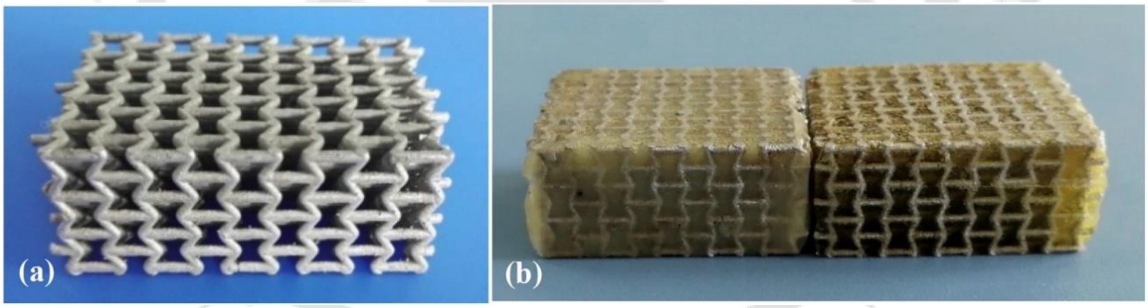

Figure 2.27. (a) Original reentrant auxetic lattice and (b) polymer-filled reentrant auxetic lattice (Reproduced with permission from [112]).

Lattice structures fabricated by additive manufacturing (AM) and filled with polymers lead to superior behaviour with exceptional mechanical properties. Pasquale et al. designed BCC and BCCZ lattice structures and filled them with polymers based on three different mixtures of polyol, isocyanate and extender with variable compositions [113]. The polymer-filled lattice demonstrated an enhanced ability to absorb elastoplastic energy, up to 75% higher than the combined energy absorption of each constituent material. Fila et al. designed and fabricated different auxetic structures by 3D printing and then filled the auxetic structures with strain-rate sensitive polymers like polyurethane and gelatin and conducted high strain-rate tests [114]. They reported 5-10% higher specific energy absorption in the case of polymer-filled auxetic structures when compared with structures without filling. A lattice structure made of aluminum and reinforced with polymer fillers was successfully fabricated using pressure infiltration technology, and the compressive mechanical properties of these resulting auxetic composites were studied by Xue et al. [112]. The results indicate that these lattices possessed superior elastic modulus, compressive strength, and energy absorption capacity compared to the original aluminum-based auxetic lattice structures. This improvement can be attributed to the enhanced interaction between the struts and the polymer filler, which was aroused from the unique deformation characteristics of the auxetic lattice structures. Figure 2.27 shows the original lattice and the corresponding polymer-filled lattices. A hybrid metamaterial consisting of an auxetic cellular structure combined with a silicon filler was produced by Novak et al. and those were subjected to both quasi-static and dynamic compressive loading conditions [115]. The results showed that the polymer-filled specimens exhibited higher plateau stress levels but lower densification strain than the base specimens with a chiral auxetic structure. Additionally, the polymer-filled specimens demonstrated significantly greater energy absorption capacity.

2.9 Summary

The classification of different types of auxetic and ZPR lattice structures were studied in this chapter. The auxetic structures possess unique properties, such as higher indentation resistance, shear resistance, fracture toughness, etc. that are not found in non-auxetic structures. The auxetic structures can be used for energy absorbing applications in the military, automobile and sports industries. The ZPR structures also find potential in wing-morphing and bio-medical applications. Furthermore, the various techniques to improve the mechanical properties of the lattices, like variation of strut thickness, graded-density lattices, polymer-filled lattices, etc., were also discussed.

2.10 Research gaps and objectives of the thesis

Research Gaps

Looking at the potential applications of NPR and ZPR lattice structures, there is an urgent need to explore techniques to design NPR and ZPR lattice structures with enhanced mechanical properties. The research gaps obtained from the extensive literature review are:

- The different techniques to improve the mechanical properties of the lattices, such as, variable strut thickness of the unit cell, dual-phase lattices, tactical modification of unit cell topology, graded-density lattices, and polymer-filled lattices, are mostly studied for positive Poisson's ratio lattices.
- No known studies are available on multiple unit cell topologies i.e. dual-phase lattice, and variable strut thickness for negative or zero Poisson's ratio lattices.
- Only a few studies are available on improving the mechanical properties of negative and zero Poisson's ratio lattices through tactical changes of the already well-known unit cell topology.
- Most of the studies focus on studying the mechanical behaviour of the lattices at quasi-static loading, while many real-world applications require analysis under high-strain rate loading.

Objectives of the thesis:

This work aims to design additively manufactured negative and zero Poisson's ratio lattice structures with enhanced mechanical properties. The following objectives have been identified to achieve the aim of this thesis work:

- To enhance the mechanical properties of the negative Poisson's ratio lattice by replacing the uniform struts with tapered struts.
- To improve the mechanical properties of negative Poisson's ratio lattice structures using high-strength lattice reinforcements.
- To design zero Poisson's ratio lattices by combining both negative Poisson's ratio lattice unit-cell and positive Poisson's ratio lattice unit-cell and using the composite rule of mixture.
- To improve the mechanical properties of the zero Poisson's ratio tubular lattice by tactically modifying the already-known unit cells.
- Compare the mechanical properties of the proposed lattices with the well-known lattice structures exhibiting similar Poisson's ratio behaviour.
-

CHAPTER 3. MATERIALS AND METHODS

This chapter discusses the different research methodologies employed to study the mechanical properties of the lattice structures. Section 3.1 discusses the design of the lattice structures. The fabrication techniques of the lattice structures by metallic and polymer materials, along with the parent material properties, are discussed in Sections 3.2 and 3.3, respectively. Section 3.4 describes the details of the finite element simulations to investigate the deformation mechanism and mechanical properties of the lattice structures. The subsequent sections discuss the mechanical testing of the lattices by quasi-static compression and high-strain rate analysis by split Hopkinson pressure bar (SHPB).

3.1 Design of lattice structures

Novel strategies to design lattices that can have enhanced mechanical properties than the existing ones are studied in this thesis. The design of the lattice structure plays the most crucial role in controlling the mechanical properties. The mechanical response of the lattice structure depends on the unit cell topology and relative density. The lattice structures were designed using computer-aided design (CAD) software, Autodesk Inventor 2018. The design of the lattices was done taking into account the minimum printability by the additive manufacturing machine. With a modest additive manufacturing machine, it is possible to fabricate lattices with a minimum strut thickness of 0.7 mm. The details on the design of the various lattice structures are included in the corresponding chapters. The CAD models for the additively manufactured product were generated in standard tessellation language (.stl) format. The .stl format of the design deals with the layer-by-layer topography of the model. These .stl files were transferred into the additive manufacturing machine to fabricate the lattices.

3.2 Fabrication of metallic lattice structures

Selective Laser Melting (SLM), a Powder Bed Fusion (PBF) process, was used to fabricate the metallic lattice structures. The 3D-reentrant metallic lattice structures were fabricated using the EOS M290 SLM machine at Innovae3D Pvt. Ltd. This technique uses a laser beam to fully melt the metal powder, which is applied as very thin layers on a platform [116]. The laser beam is focused on the desired area by a series of mirrors. The crosssectional area of the component is built layer by layer by melting and re-solidifying the metal powder and leveling the metal powder layer using a re-coater (Figure 3.1). The powder particles can be selectively melted wherever desired by redirecting and focusing the laser beam by computer-generated patterns [28]. The packing and size distribution of powder are the crucial factors that determine the efficacy of this technique. Fine resolution and very good printing quality make this process suitable for printing complex structures. Different metal powders like stainless steel, Nickel super-alloys, Ti-alloy, and Al-alloy can fabricate parts by the SLM process [6].

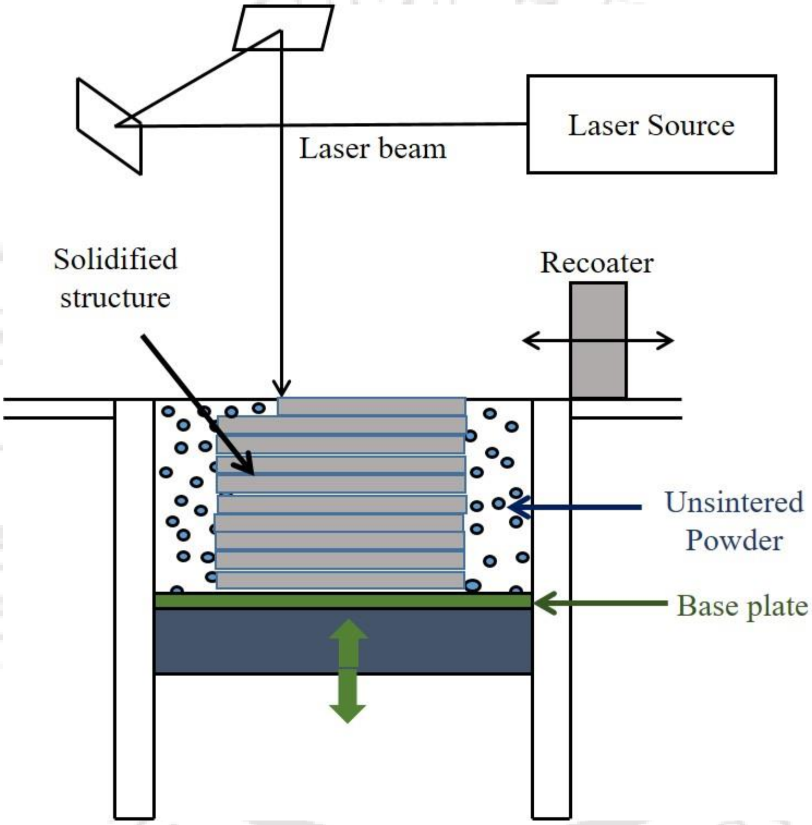

Figure 3.1. Selective Laser Melting (SLM) 3D-printing process [6].

The main advantage of Powder Bed Fusion is that the powder bed itself is used as a support structure which solves the problem of removing the supporting material. The major drawbacks are that it is a slow and costly process. SLM is a similar technique when compared to Selective Laser Sintering (SLS), Direct Metal Laser Sintering (DMLS) and Direct Metal Laser Melting (DMLM). Different companies use different terminologies as a trademark for their products.

The process parameters affect the quality of the manufactured part in additive manufacturing. Therefore, it is crucial to select optimal parameters to achieve the desired mechanical performance [117–119]. For fabricating the 3D-reentrant lattice structures, the laser power was set at 360W, and the layer thickness was 30 μm. The chosen scan strategy involved a stripe pattern with a scan speed of 1300 mm/s and a hatch spacing of 0.18 mm. Once the building process was completed, the fabricated part was separated from the built bed using electro-discharge machining (EDM).

3.2.1 Selection of metallic material

The generally used metallic materials for Selective Laser Melting are 316L stainless steel, Ti-alloy (Ti-6Al-4V) and Ni-based superalloys (In 718) [28]. 316L stainless steel is a type of low-carbon steel that is corrosion-resistant and has high strength. 3D-printed 316L stainless steel offers good ductility and high thermal properties. Ti-alloys have good corrosion resistance, high strength-to-weight ratio and stiffness making them useful in biomedical, aerospace and automobile industries [120]. SLM of Ni-based superalloys have been studied because of their applications at high temperatures, such as aircraft engines and gas turbine blades. These alloys have excellent strength as well as wear and corrosion resistant at high temperatures [121].

Besides these, AlSi10Mg is a new addition to the materials used in SLM. Al-alloys are light in weight, have good mechanical properties and are corrosion-resistant. AlSi10Mg is the lightest material to be used for additive manufacturing of metals. It was found that besides processing parameters, powder content and morphology also influence the quality of the SLM product. Smaller and spherical types of powder led to the production of components with higher relative density compared to larger and irregularly shaped powder [121].

The material of choice for the fabrication of the 3D-reentrant lattice structures was AlSi10Mg. Among the commonly used metallic materials in additive manufacturing, AlSi10Mg is one of the lightest options, making it ideal for applications requiring lightweight structures [109,122,123]. The AlSi10Mg feedstock powder used in the fabrication process had a spherical morphology, with an average diameter of 40 μm. The size distribution of the powder followed a Gaussian distribution, with D10 = 15 μm, D50 = 40 μm, and D90 = 55 μm, indicating the range of particle sizes present in the powder.

Table 3.1 provides the chemical composition of the feedstock powder. AlSi10Mg powder is near-eutectic, with a balanced aluminum (Al) and silicon (Si) ratio. This composition is advantageous as it lowers the melting temperature of aluminum, allowing for concurrent solidification of all phases involved in the process [124,125].

Table 3.1. Composition of AlSi10Mg powder.

Si	Fe	Cu	Mn	Mg	Zn	Ni	Pb	Sn	Ti	Al
9-11	0.55	0.05	0.45	0.2-0.45	0.1	0.05	0.05	0.05	0.15	Balance

3.2.2 Properties of parent material

Figure 3.2. ASTM E8 AlSi10Mg tensile specimens fabricated by Selective Laser Melting.

The properties of the parent material were evaluated by uniaxial tensile testing of AlSi10Mg tensile specimens. Three sub-size E8 specimens were designed and fabricated in the same batch with the lattice structures (Figure 3.2). The designed tensile specimen had a gauge length of 25 mm, width of 6 mm and thickness of 3 mm. The tensile tests were conducted in a Shimadzu AGX-100 universal testing machine with a 100kN load cell. The stress-strain plots of the three samples are shown in Figure 3.3. The average values of Young’s modulus, 0.2% offset yield strength, ultimate tensile strength and strain at break of the three samples are mentioned in Table 3.2.

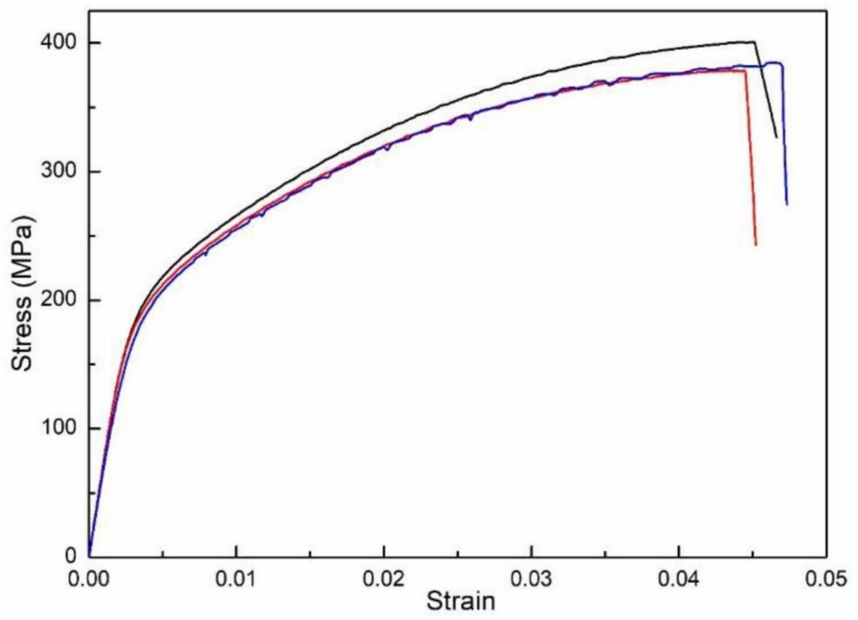

Figure 3.3. Stress-strain plots obtained from tensile tests of ASTM E8 samples.

Table 3.2. Mechanical properties of AlSi10Mg fabricated by additive manufacturing

Young's Modulus (GPa)	Yield strength (MPa)	Ultimate strength (MPa)	Strain at break
67.35	197.04	388.05	0.046

3.3 Fabrication of polymeric lattice structures

A 3D printing technology called Multi Jet Fusion (MJF) has been developed by HP recently, which can be used to fabricate lattice structures with Polyamide 12 (PA12). This new type of printer can achieve high dimensional accuracy, functionality and accuracy than the currently available 3D printing technologies. Another advantage of this technique is that it can produce components with isotropic mechanical properties, independent of the direction in which printing is done [30].

The building technique begins by applying a thin layer of powder on the platform. Then a fusing agent is applied in a continuous pass to the powder layer, where the powders are meant to fuse (Figure 3.4). Smooth surfaces and fine details are obtained by applying a detailing agent to the contours of the component to be produced. The detailing agent prevents the fusion of the powder particles at the contours to improve resolution. The polymer is heated by infrared lamps placed over the powder bed. The fusing agent absorbs infrared energy and converts it to thermal energy, which sinters and then binds the powder materials. Thus, a layer is formed by the fused components. This process is repeated and the component is fused layer by layer as the build plate moves down, forming the 3D component. Compared to other PBF techniques, MJF is faster which uses planar infrared radiation rather than point-wise fusion [126].

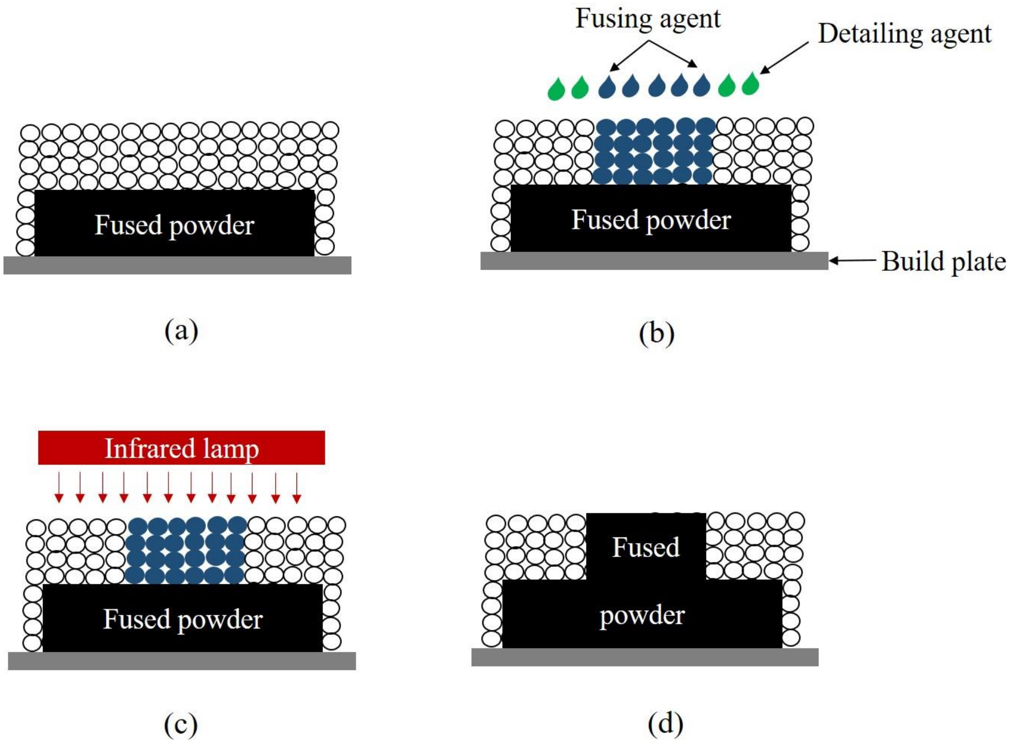

Figure 3.4. Multi Jet Fusion 3D printing process [30].

3.3.1 Polymeric material selection

Polyamide 12 (PA12) is the material used for fabricating the lattice structures by Multi Jet Fusion. PA12 is one of the most widely used materials in additive manufacturing [127]. It is a thermoplastic polymer that belongs to the nylon family and has good toughness and energy-absorbing capabilities [30]. The melting temperature of PA12 is higher than its crystallization temperature. Thus during 3D printing, the crystallization process is delayed, and therefore it reduces the residual stress accumulation and distortion. Certain additives like silicon carbide, carbon nanotubes, and glass beads, when used with polyamide 12, improve the mechanical properties of the printed components [126]. The PA12 powder used in Multi Jet Fusion has very fine grains resulting in parts with lower porosity than those produced by laser sintering processes. Figure 3.5 shows some lattice specimens fabricated from AlSi10Mg and polyamide 12.

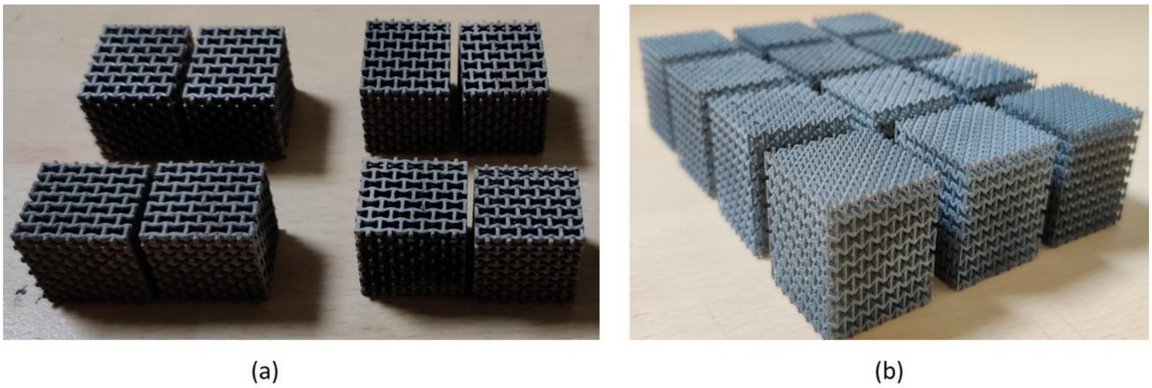

Figure 3.5. Some lattice specimens fabricated from (a) AlSi10Mg and (b) Polyamide 12.

3.3.2 Properties of parent material

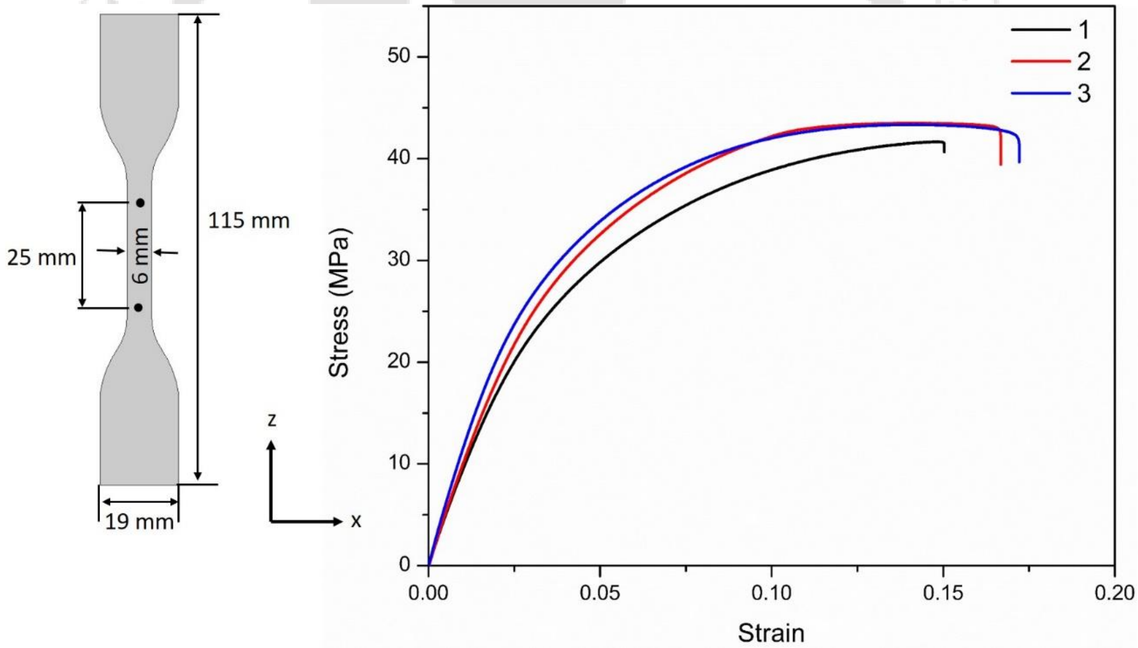

Figure 3.6(a) CAD model of D638 tensile specimen and (b) stress-strain plots of PA12 made D638 specimens.

To investigate the mechanical properties of the parent material, i.e., polyamide 12 (PA12), used to fabricate the lattice structures, uniaxial tensile tests were conducted using Shimadzu AGS-X 100kN Universal Testing Machine (UTM). Figure 3.6(a) shows the tensile specimen made as per ASTM D638 standard, and Figure 3.6(b) shows the stress-strain curves of the three specimens. The elastic modulus, yield strength, ultimate tensile strength, and elongation at break obtained from the three repeated experiments are mentioned in Table 3.3. For the polymer lattice structures fabricated in different batches, tensile specimens were also fabricated along the lattice structures in each batch. The mechanical properties obtained from tensile tests of D638 specimens in each batch were nearly identical, as reported in Table 3.3. O'Connor et al. and Cai et al. reported that the strength of the samples fabricated by the MJF technique is independent of the three building directions, but the elongation at break of the samples printed in the z-direction was lower than the other two built directions [126,128]. However, Sillani et al. reported the highest value of tensile strength in the z-direction with nearly similar values of elongation at break in all three building directions [129]. All the samples were printed along the z-direction in this work.

Table 3.3. Mechanical properties of 3D-printed PA12 samples.

Elastic modulus (GPa)	Yield strength (MPa)	Ultimate tensile strength (MPa)	Elongation at break (%)
1.057 ± 0.180	21.69 ± 1.84	42.73 ± 1.07	16.20 ± 1.18

3.4 Finite element simulations

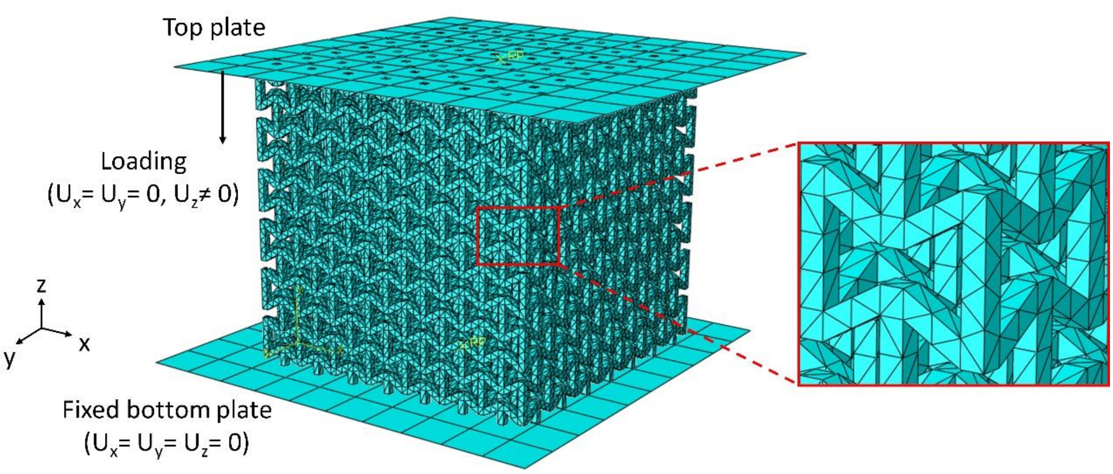

Figure 3.7. Finite element model showing the lattice specimen under compression.

Abaqus/Explicit was used for the finite element simulation of the lattice structures because the crushing of the lattice to very large strain involves three types of non-linearity (mentioned below) which cannot be simulated by implicit solver [30]:

- The material non-linearity in which the local stress in the lattice exceeds the linear elastic limit of the parent material and it involves plastic deformation.
- The geometrical non-linearity due to the large deformation of the lattice structure.
- The contact non-linearity due to the interaction of the struts during crushing.

The size of the lattice samples used for simulation was the same as in the experiments. Figure 3.7 shows the meshed 3D-reentrant auxetic lattice structure with the boundary conditions. The bottom plate was modeled with all degrees of freedom constrained, and the top plate was allowed to move in the negative z-direction to compress the sample. The top plate was allowed to move at a deformation speed such that the kinetic energy was negligible compared to the internal energy during the whole duration of the numerical simulation. Figure 3.8(a) shows the plot of energy vs. time for deformation speed of 500 mm/sec for the 3D-reentrant structure shown in Chapter 6. The kinetic energy is negligible compared to the internal energy (<1%), which suggests the simulation can mimic quasi-static conditions at a velocity of around 500 mm/sec. This ensured that the effect of inertia was eliminated and the numerical simulation achieved quasi-static compression. This analysis was performed for all the studies in this thesis and appropriate deformation speed was considered. 'Frictionless' general contact algorithm (explicit) in the tangential direction was used to avoid the penetration of the two plates with the lattice and for the self-contact of the lattice structure during compression. Solid 10-node modified quadratic tetrahedron (C3D10M) elements were used to mesh the lattice structures, and 4-node 3D bilinear rigid quadrilateral (R3D4) elements were used to mesh the top and bottom plates. The mess convergence study [Figure 3.8(b)] performed for the 3D-reentrant lattice in Chapter 6 showed a very small difference in the stress-strain curve up to the densification strain obtained using a mess size of 1 mm and 1.5 mm. However, the number of elements of the 3D-reentrant lattice increased from 118,442 to 245,874 when the mess size was changed from 1.5 mm to 1 mm. The computation time increased drastically with the decrease in mess size, and hence, the mess size used was 1.5 mm in that study. Mess convergence studies were performed for other studies, and appropriate mess sizes were considered to obtain significant accuracy in results while keeping an affordable computation time. Isotropic hardening was employed with elasto-plastic mechanical properties from the experimental stress–strain plots obtained from tensile tests of parent materials. The compressive stress was calculated based on the reaction force developed in the bottom plate during compression, and the compressive strain was obtained from the displacement of the top plate.

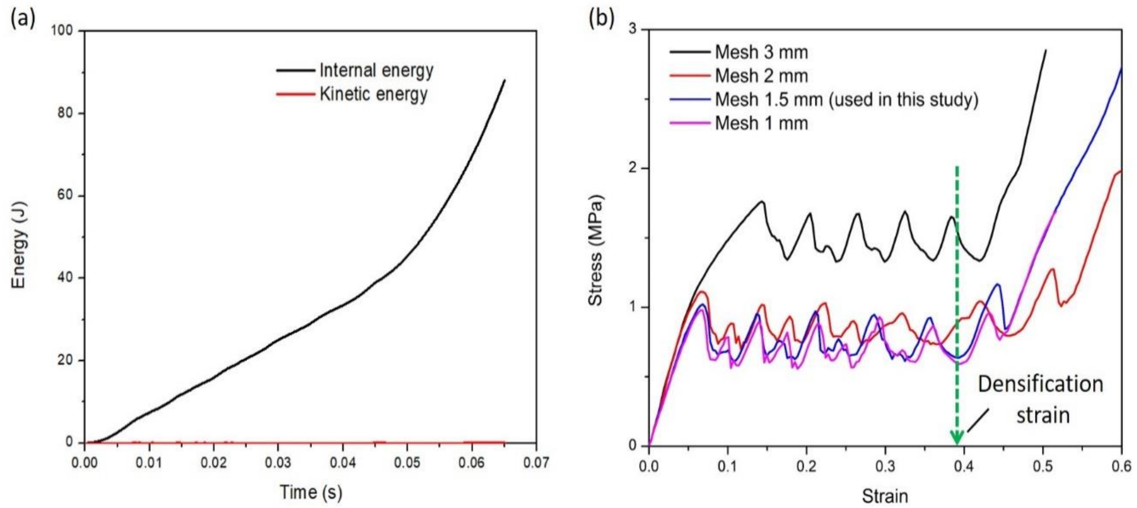

Figure 3.8 (a) Energy vs. time plot, and (b) mess-sensitivity obtained from numerical simulations.

3.5 Quasi-static mechanical test

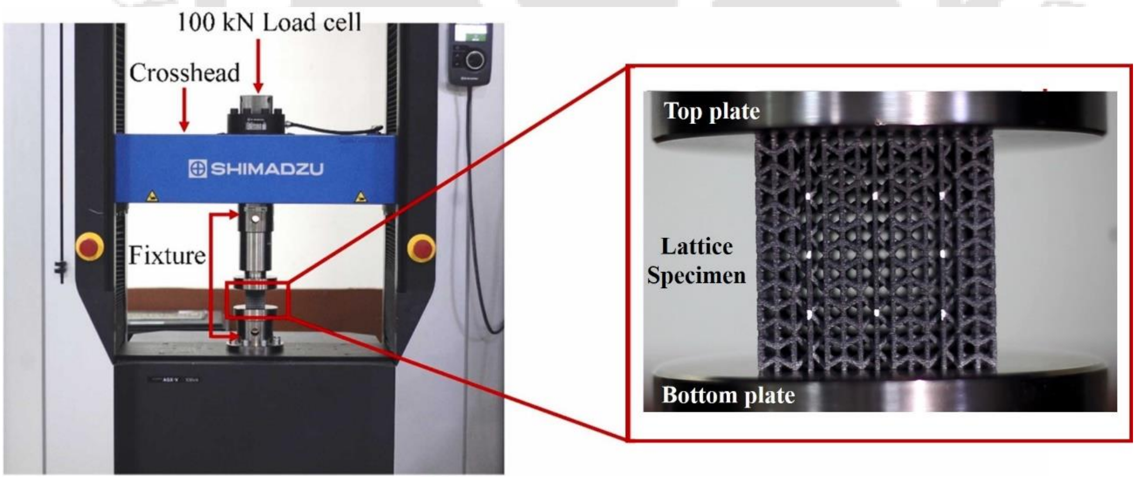

Figure 3.9. Experimental setup for quasi-static compression of lattice structures.

The quasi-static uniaxial compressive mechanical tests of the fabricated lattice structures were conducted on Shimadzu AGS-X 100kN Universal Testing Machine (UTM). The lattice samples were compressed at a particular velocity such that a quasi-static strain rate of 10^{-3} s^{-1} is achieved. The deformation of the lattice structures was captured by Canon

EOS 500D digital camera. Two repeated compression tests were conducted for a specific lattice structure. The quasi-static compressions were conducted until the densification of the samples was observed and the stress-strain plots were obtained. Figure 3.9 shows the quasi-static compression test setup.

3.6 Calculation of Poisson's ratio

The Poisson's ratios were calculated from numerical simulations and experiments for all the lattice structures. For the numerical simulations, Poisson's ratios were obtained by calculating the change in the positions of the nodes during compression. White marks were drawn on the fabricated lattices to calculate the Poisson's ratios from the experiments, as shown in Figure 3.9(a). As the quasi-static compression of the lattice samples occurred, the white dots were displaced from their original positions [Figure 3.9(b)], which was recorded by the digital camera. Images were obtained at different strains and compared to calculate the change in the lateral and longitudinal displacement of the white dots using MATLAB software. The Poisson's ratio (ν) was calculated using the following equation,

$$\nu = -\frac{(l_1' - l_1)/l_1}{(l_2' - l_2)/l_2} \qquad 3.1$$

where, the dimensions l_1 and l_1' are the average lateral distances between the white dots before and after compression, respectively, and l_2 and l_2' are the average axial distance between the white dots before and after compression, respectively, shown in Figure 3.10. The Poisson's ratio was calculated until the first localized buckling of the lattice structures.

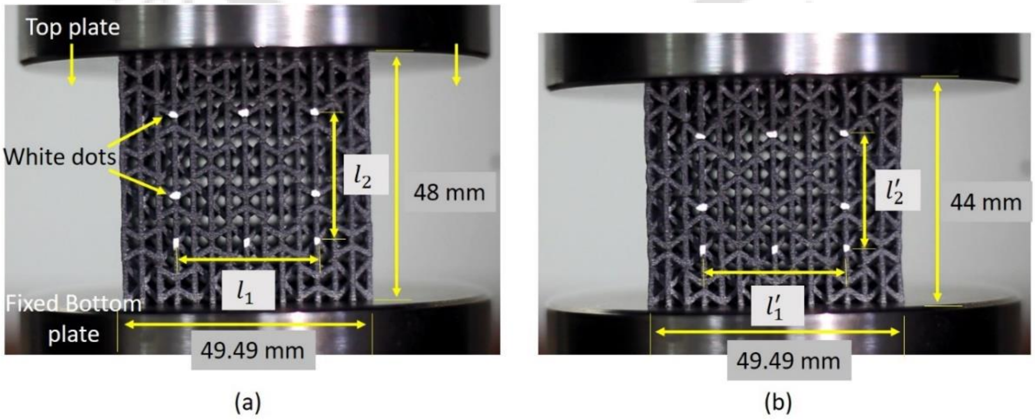

Figure 3.10. The lattice sample with white dots, (a) before compression and (b) after compression.

3.7 Split Hopkinson pressure bar (SHPB) test

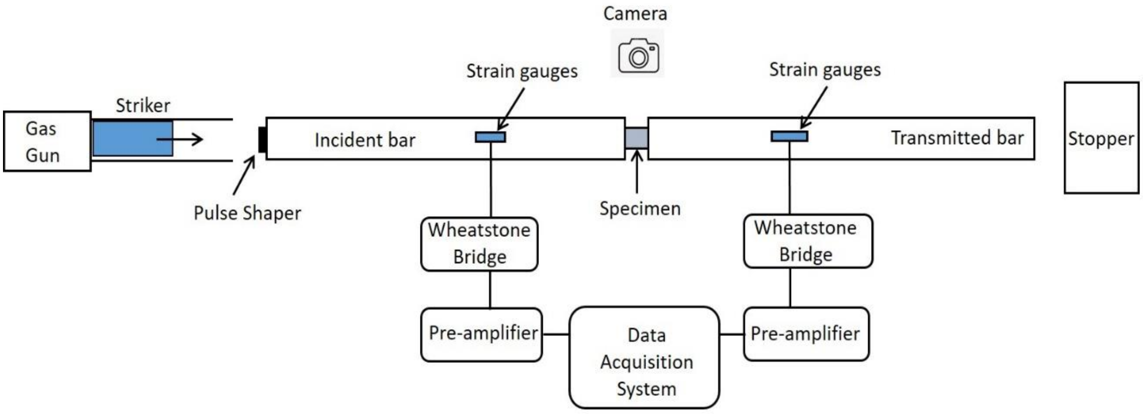

Figure 3.11. Schematic of split Hopkinson pressure bar (SHPB) setup.

The dynamic behaviour of the auxetic structures was investigated by the split Hopkinson Pressure bar (SHPB) test, which can be used to study material behaviour at a high strain rate of up to 10^4 s^{-1}. The schematic of a SHPB test is shown in Figure 3.11. The SHPB test setup consists of a striker, an incident bar and a transmitted bar. The test sample was sandwiched between the incident and the transmitted bar. The striker, incident and transmitted bars were made of maraging steel with a 20 mm diameter. The length of the striker was 350 mm and the length of the incident bar was 1530 mm, whereas the transmitted bar was 1350 mm. A pair of strain gauges were placed diametrically opposite to the center of both the incident and transmitted bars. The strain gauges were connected to the data acquisition system via the signal-amplifying circuit. A copper pulse shaper of 0.3 mm thickness was attached on one end of the incident bar where the striker hit the incident bar. A high-speed camera, Photron FASTCAM SA1.1, with 100000 frames per second, was placed in front of the specimen to capture the deformation behaviour. The SHPB test setup with some of the components is shown in Figure 3.12. When the striker was fired by the compressed air, it hit the incident bar and the incident pulse travelled through the incident bar. The incident pulse reached the junction of the incident bar and the specimen, and due to an impedance mismatch, part of it was reflected to the incident bar (reflected pulse). The other part travelled through the specimen and reached the transmitted bar (transmitted pulse). The incident, reflected and transmitted pulses were recorded by the strain gauges and acquired by the data acquisition system through the amplifying circuit. From one-dimensional elastic wave theory, the following formulas were used to calculate the strain rate ($\dot{\varepsilon(t)}$), engineering strain ($\varepsilon(t)$) and engineering stress ($\sigma_s(t)$) [130]:

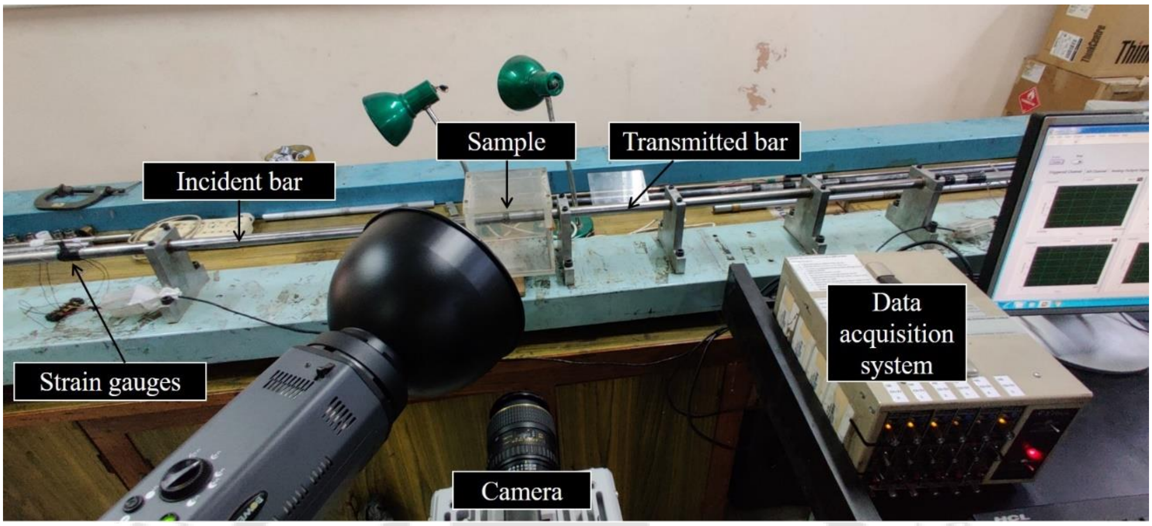

Figure 3.12. SHPB test setup showing different components.

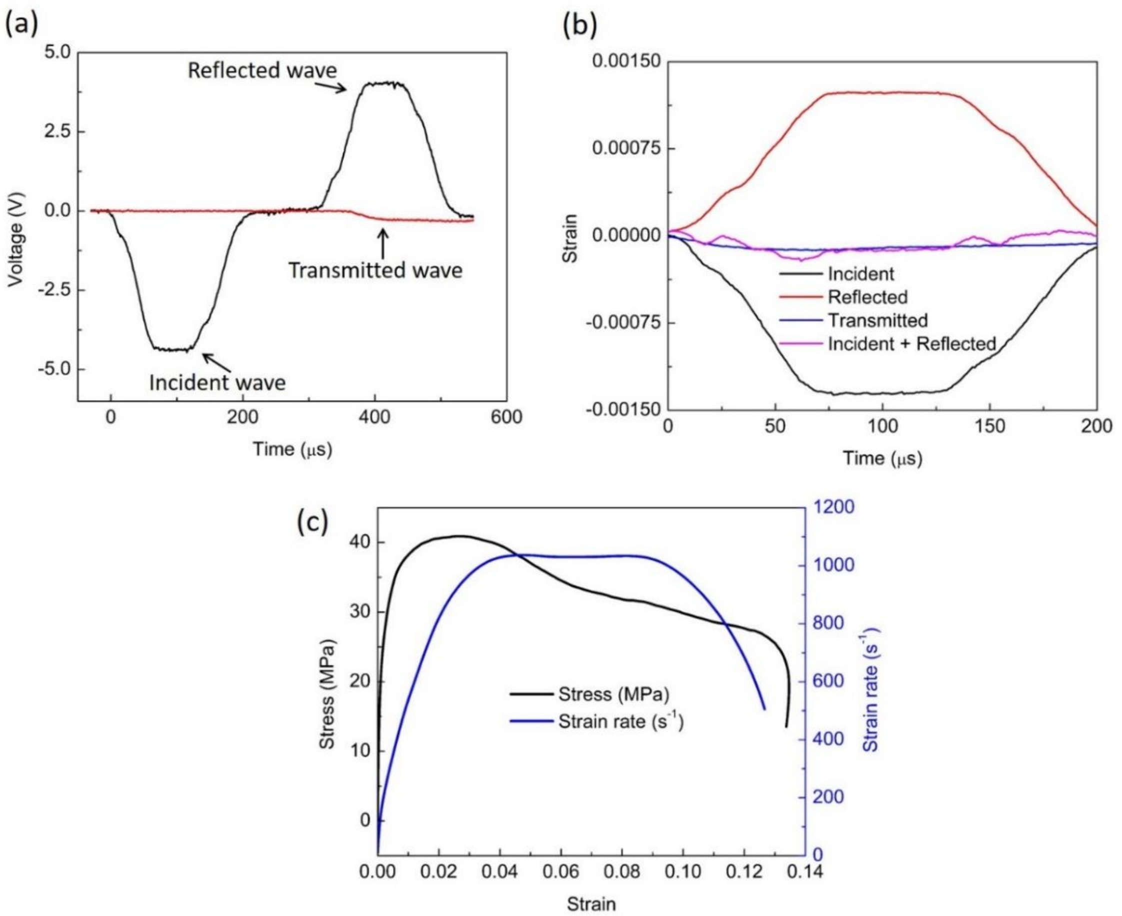

Figure 3.13(a) Signals obtained from SHPB test of AlSi10Mg lattice samples, (b) superimposed waveforms during SHPB test, and (c) engineering stress and strain rate vs. strain for AlSi10Mg lattice.

$$\dot{\varepsilon(t)} = -\frac{2C_0}{L}\varepsilon_r(t) \qquad 3.2$$

$$\varepsilon(t) = -\frac{2C_0}{L}\int_0^t \varepsilon_r(t)dt \qquad 3.3$$

$$\sigma_s(t) = E\,\frac{A_0}{A}\,\varepsilon_t(t) \qquad 3.4$$

where, C_0 is the wave speed, which is calculated as $C_0 = \sqrt{\frac{E}{\rho}}$, where E is Young's modulus of the bar material and ρ is the density of the bar material, L is the length of the specimen, ε_r is reflected strain, ε_t is the transmitted strain, A_0 is the area of cross-section of the bar, and A is the area of cross-section of the sample. The incident, reflected and transmitted waveforms obtained during the SHPB test of an AlSi10Mg auxetic lattice is shown in Figure 3.13(a). Figure 3.13(b) shows the calculated signals of incident, reflected and transmitted waveforms which are superimposed for comparison. It can be observed from Figure 3.13(b) that the forces at both the incident bar and the transmitted bar are in dynamic equilibrium, and the homogenization hypothesis is satisfied. Figure 3.13(c) shows that the strain rate at 1000 s^{-1} is nearly constant during dynamic compression, proving the experiments were reliable. Two repeated experiments for each sample were performed to ensure repeatability.

3.8 Summary

This chapter presented the different techniques of 3D printing employed to fabricate the lattice structures. The metallic lattices were fabricated by powder bed fusion-based Selective Laser Melting with AlSi10Mg as the parent material, while HP Multi Jet Fusion fabricated the polymer lattices with polyamide 12 as the parent material. Tensile coupons were fabricated according to ASTM standards to study the properties of the parent materials. Abaqus/Explicit was used to study the mechanical response of the lattice structures by finite element simulations. The details on the selection of meshed elements, the loading velocity, the calculation of output responses, etc., from the simulations, were discussed. Universal Testing Machine was used to experimentally investigate the quasi-static response of the lattice structures. A split Hopkinson pressure bar was used to investigate the dynamic response of the lattice structures.

CHAPTER 4. QUASI-STATIC AND DYNAMIC BEHAVIOUR OF VARYING CROSS-SECTION METALLIC 3D-REENTRANT LATTICE

The lattice structures consisting of struts with varying cross-section have enhanced mechanical performance than the lattice structures with struts of uniform cross-sections. However, the amount of improvement varies for different lattices. This technique to enhance the mechanical properties of the auxetic lattices has not been reported earlier. This chapter presents the design of novel 3D-reentrant auxetic lattices with struts of varying cross-section. The design and fabrication of the 3D-reentrant lattices with varying cross-section or tapered struts is described in Section 4.1. Section 4.2 demonstrates the behaviour of the tapered-strut lattices at quasi-static loading. The tapered-strut lattices are compressed along two directions, and the mechanical properties are compared with the original 3D-reentrant lattice. Section 4.3 investigates the behaviour of these lattices at high strain rate. The influence of tapered struts on mechanical properties like compressive strength, elastic modulus and Poisson's ratio at both quasi-static and high-strain rates are studied.

4.1 Design and fabrication of metallic 3D-reentrant auxetic lattices

4.1.1 Design of 3D-reentrant auxetic lattices

The 3D-reentrant auxetic structures exhibit a negative Poisson's ratio during deformation. Figure 4.1(a) shows the geometric parameters of the 3D-reentrant structure, where ‘h’ is the length of the vertical strut, ‘l’ is the length of the oblique or reentrant strut, ‘θ’ is the reentrant angle and ‘t’ is the thickness of the struts. Figure 4.1(b) shows the 3D view of the unit cell of the 3D-reentrant structure. Two different unit cell geometries of the 3D-reentrant structure were designed in this study by changing the unit cell parameters. The lattices with different unit cell parameters are mentioned in Table 4.1. The geometric parameters were varied such that the overall relative density of both structures remains the same. The length of strut ‘l’ was kept constant as 2 mm for all the designs, and to maintain the h/l ratio, the length of strut ‘h’ was only varied. For Design 1, ‘h’ was 4 mm and ‘l’ was 2 mm to achieve an h/l ratio of 2, and for Design 2, ‘h’ was 3 mm and ‘l’ was 2 mm to achieve an h/l ratio of 1.5.

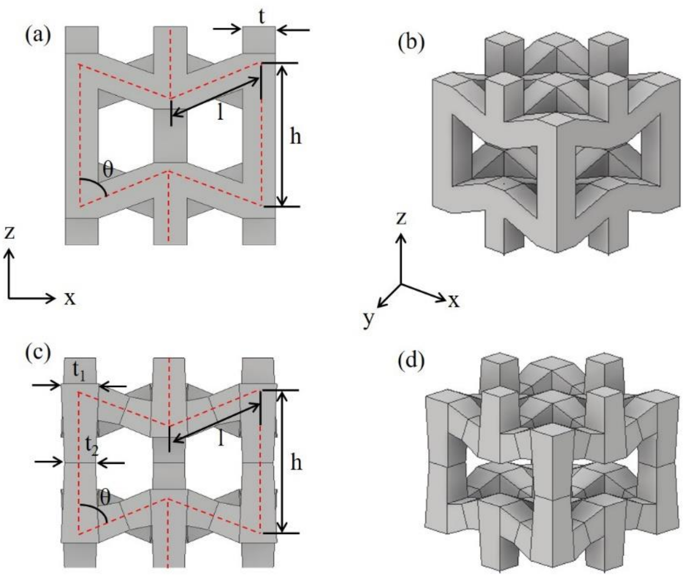

Figure 4.1. (a) Unit cell parameters of a uniform strut 3D-reentrant structure, (b) 3D view of uniform strut 3D-reentrant structure, (c) Unit cell parameters of a tapered strut 3D-reentrant structure and (d) 3D view of tapered strut 3D-reentrant structure.

Table 4.1. Unit cell parameters of 3D-reentrant structure.

Design	**h/l**	**θ**	**Relative density (%)**
Design 1 (D1)	2	60°	27.2
Design 2 (D2)	1.5	70°	27.1

The main objective of this study is to design novel tapered 3D-reentrant auxetic structures and compare their mechanical properties with uniform or regular strut 3D-reentrant structures. Tapered struts were designed by varying the strut thickness of all the struts in the unit cell. The unit cell parameters of the tapered reentrant structure are shown in Figure 4.1(c). Figure 4.1(d) shows the 3D view of the tapered reentrant unit cell. For both design configurations mentioned in Table 4.1, the 3D-reentrant structures with tapered struts were designed to have the same unit cell size and relative density as the corresponding uniform strut 3D-reentrant. Table 4.2 shows the geometric parameters of all the tapered strut 3D-reentrant auxetic structures for both the designs, i.e., Design 1 (D1) and Design 2 (D2). The unit cell was repeated in three mutually perpendicular directions (x, y, and z) to generate the lattice structures.

4.1.2 Fabrication of 3D-reentrant auxetic lattices

All the six lattices mentioned in Table 4.2 were fabricated by laser powder bed fusion-based technology by EOS M290, manufactured by EOS GmbH, Germany, with AlSi10Mg as the parent material. The lattice structures were fabricated along the x-direction as shown in Figure 4.2. No support structures were used during the fabrication process.

The relative densities of the as-designed and as-fabricated samples are shown in Table 4.2. It can be seen that the relative densities of the as-fabricated samples were slightly lower than those of the as-designed samples. During the manufacturing of the components in the laser powder-based fusion process, the difference in cooling rates at the surface and the subsurface of the components led to shrinkage during fabrication [131]. This shrinkage in the manufactured components caused the change in the designed and the actual relative densities. The change in relative densities between the as-designed and as-fabricated samples was in the range of 0.73% - 2.95%. Figure 4.2 shows the size of the lattice structures used for quasi-static and dynamic tests.

Table 4.2. Geometric parameters of the regular and tapered 3D-reentrant structures.

No.	**Design**	**h/l**	**θ**	**t_1 (mm)**	**t_2 (mm)**	**$\alpha = t_2/t_1$**	**Designed relative density (%)**	**Actual relative density (%)**
1	D1-regular (reg)	2	60°	0.7	0.7	1	27.2	26.7
2	D1-tapered 1 (tap 1)			0.825	0.65	0.78	27.4	26.8
3	D1-tapered 2 (tap 2)			0.9	0.6	0.66	27.4	26.7
4	D2-regular (reg)	1.5	70°	0.7	0.7	1	27.1	26.9
5	D2-tapered 1 (tap 1)			0.8	0.65	0.81	27.2	26.4
6	D2-tapered 2 (tap 2)			0.875	0.6	0.68	27.4	26.8

4.2 Quasi-static deformation behaviour

The mechanical properties of the lattice structures were studied by loading them along the x and z-directions (Figure 4.2). Figure 4.3 shows the stress-strain plots of all the lattice structures obtained from the quasi-static experiments. For clarity, only one stress-strain curve was shown from two experiments for each configuration.

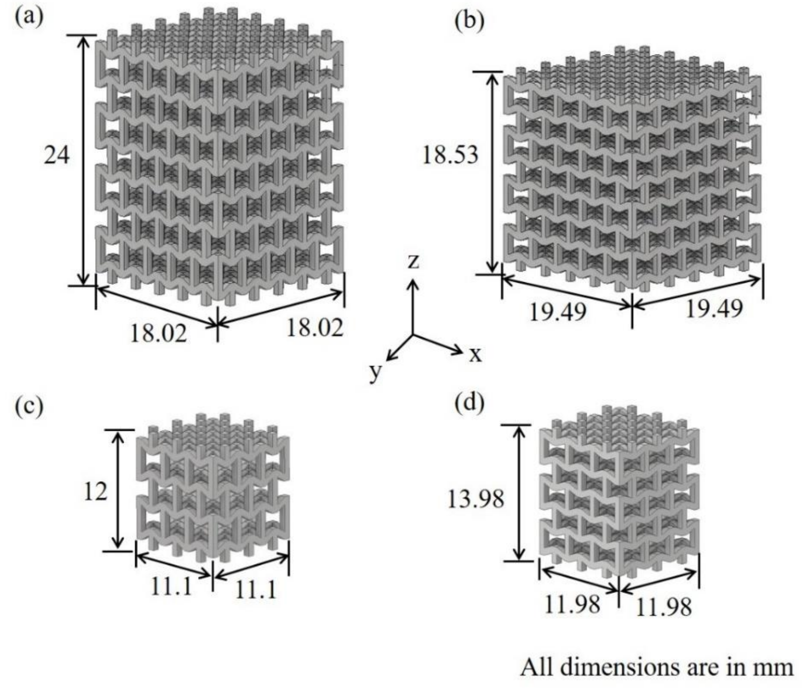

Figure 4.2. Quasi-static test specimen for the lattices, (a) Design 1-regular (D1-reg), (b) Design 2-regular (D2-reg), and SHPB test specimen for (c) D1-reg and (d) D2-reg.

4.2.1 Deformation behaviour of Design 1 auxetic lattices

4.2.1.1 Loaded along z-direction:

The stress-strain behaviour of Design 1-regular and tapered lattice structures loaded along the z-direction is shown in Figure 4.3(a). Figure 4.4(a) shows the images from the video frames of the deformation of regular strut 3D-reentrant auxetic structure with an H/L ratio of 2 and θ = 60˚. In the elastic region, it can be seen that the stress was directly proportional to strain, and the whole structure deformed uniformly. Peak compressive stress of 18.2 MPa was observed at a strain of 0.036 [Figure 4.3(a)], after which buckling of the vertical struts at the topmost layer was observed [red dotted lines in Figure 4.4(a)]. When all the vertical struts of the top layer buckled, the whole top layer collapsed and the stress dropped to 29.37% of the original peak stress. Yang et al. [42] reported this type of deformation behaviour for a large h/l ratio of the reentrant lattice. The stress increased when the remaining layers started resisting the applied load. The stress dropped again after the collapse of the vertical struts of the second layer. The stress kept on oscillating as the buckling of the vertical struts occurred layer after layer. Figure 4.4(a) also shows the deformation behaviour obtained from the numerical simulation for the Design 1-regular structure. It was also observed in the numerical simulation that the deformation occurred layer-by-layer by buckling of vertical struts. However, the sequence-wise collapse in the structure was different than that obtained from the experiment.

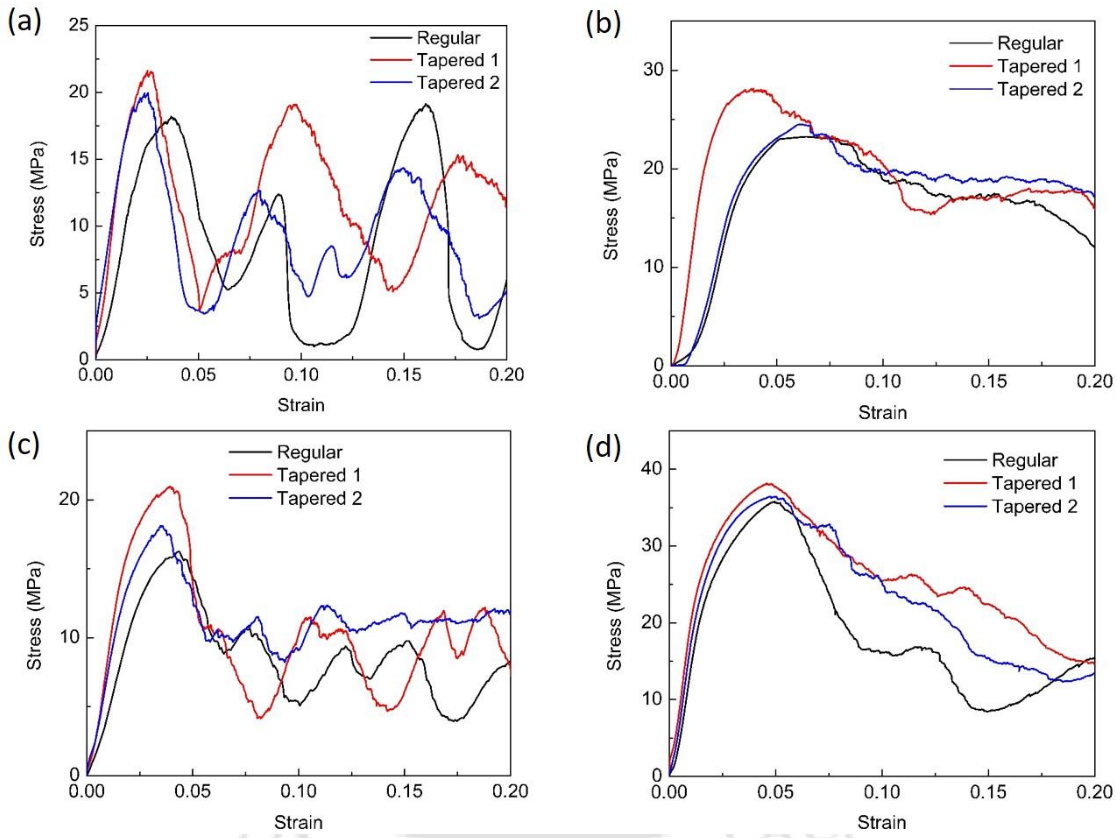

Figure 4.3. Stress-strain plots obtained from quasi-static compression of Design 1 structures loaded along (a) z-direction, (b) x-direction, and Design 2 structures loaded along (c) z-direction, (d) x-direction.

The stress-strain plot of Design 1-tapered 1 (D1-tap 1) structure is shown in Figure 4.3(a), which reveals the initial maximum compression stress of the tapered 1 3D-reentrant auxetic structures to be more than the regular strut 3D-reentrant structure when loaded along the z-direction. The deformation behaviour of the D1-tap 1 structure when loaded in the z-direction is shown in Figure 4.4(b). The deformation mechanism was the same as that of the regular strut lattice structure for the tapered 1 and tapered 2 structures, where localized buckling of the vertical struts occurred [only D1-tap 1 is shown in Figure 4.4(b)]. The vertical struts in the top layer buckled first, followed by the buckling of the vertical struts in the bottom layer. The sequence of yielding of the vertical struts in a particular layer was dominated by the defects generated during the 3D printing of the structures. The layer with more defects, called the critical layer, collapsed first compared to layers with fewer defects. Figure 4.4(b) also shows the deformation behaviour obtained from the numerical simulation for the Design 1-tapered 1 structure.

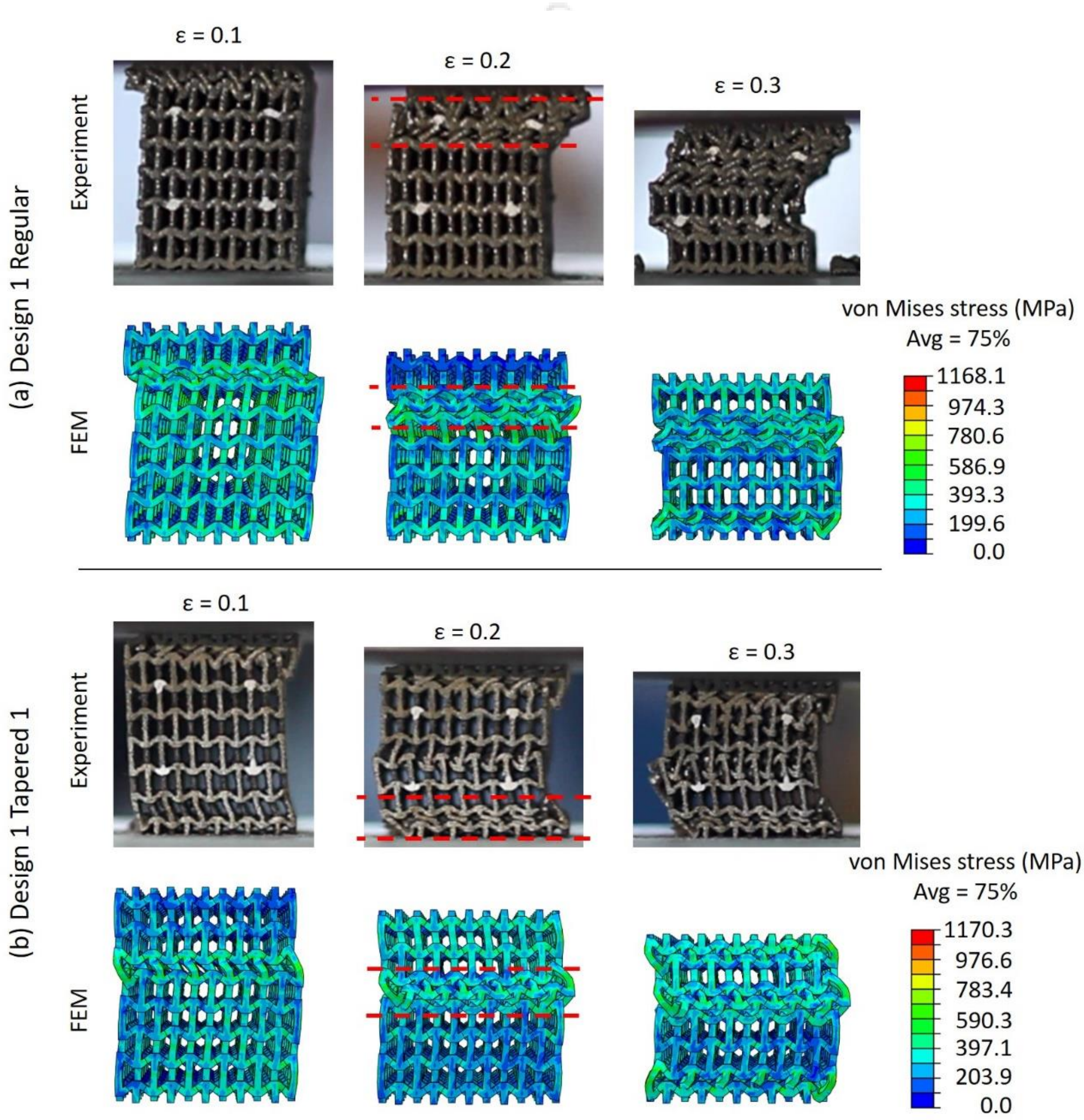

Figure 4.4. Deformation behaviour obtained from experiments and FEM for Design 1 (a) regular and (b) tapered 1 structure, loaded along the z-direction.

4.2.1.2 Loaded along x-direction

When the D1-reg 3D-reentrant structure was loaded in the x-direction, the structure deforms elastically, and a peak stress of 23.2 MPa is observed in the stress-strain plot in Figure 4.3(b). The deformation behaviour of the D1-reg structure obtained from experiments and numerical simulations is shown in Figure 4.5(a). After the elastic deformation, the structure collapsed by bending and folding of the reentrant struts. As the compression load was increased, diagonal shear band formation was observed [shown as the red line in Figure 4.5(a)]. The stress dropped continuously with an increase in strain after the failure by shear occurred [Figure 4.3(b)]. The shear band formation was also observed in the numerical simulation in Figure 4.5(a).

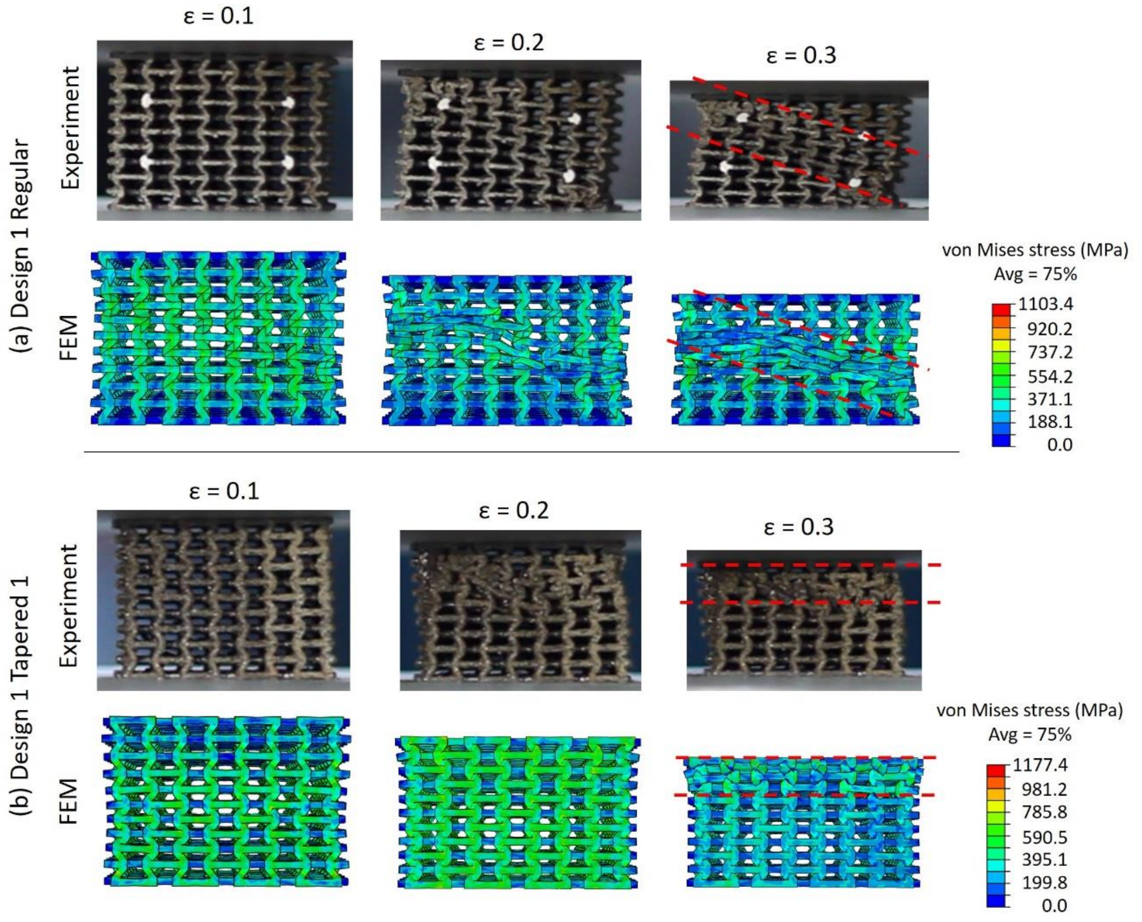

Figure 4.5. Deformation behaviour obtained from experiments and FEM for Design 1 (a) regular and (b) tapered 1 structures, loaded along the x-direction.

When the D1-tap 1 structure was loaded along the x-direction, there was a change in the deformation behaviour when compared to the D1-reg 3D-reentrant structure. The formation of a shear band was not observed for the tapered design. Instead, crushing in the topmost layer occurred, which was followed by crushing of the layer underneath [Figure 4.5(b)]. Thus, the whole structure was crushed with the increase in load, and the compressive stress also increased for the D1-tap 1 structure as compared to the D1-reg structure [Figure 4.3(b)]. A similar deformation behaviour was observed in the numerical simulation of the D1-tap 1 structure loaded along the x-direction [Figure 4.5(b)].

4.2.2 Deformation behaviour of Design 2 auxetic lattices

4.2.2.1 Loaded along z-direction

The stress-strain plots of all the Design 2 3D-reentrant lattice structures loaded along the z-direction are shown in Figure 4.3(c). The Design 2 (D2) regular and tapered strut lattice structures loaded along the z-direction deformed in a similar manner as that of the lattice structures of Design 1 loaded along the z-direction. Buckling of vertical struts was the dominant deformation mechanism for the Design 2 lattice structures. However, it was observed from the stress-strain plots (Figure 4.3) that the fluctuations in the stress-strain curves were less severe for the D2 lattice structures, which was because the length of the vertical struts for the Design 2 lattices were 3 mm compared to the length of the vertical strut for Design 1 lattices, which were 4 mm. Due to longer length of the vertical struts, the Design 1 lattices exhibited larger buckling, which led to large oscillations in the stress-strain plots. The D2 tapered 1 structure had the highest compressive strength compared to the D2 regular and the D2 tapered 2 lattice structures.

4.2.2.2 Loaded along x-direction

The stress-strain plots of all the Design 2 lattices loaded along the x-direction are shown in Figure 4.3(d). The lattice structures of Design 2 deformed in a similar manner as Design 1 loaded along the x-direction. Shear failure was observed for the uniform strut structure, but the tapered 1 lattice failed by layer-wise crushing. D2-tapered 1 lattice had slightly higher compressive strength than the D2-tapered 2 and the D2-regular lattice structures.

4.2.3 Stress-strain plots and stress distribution obtained from finite element simulations

The finite element simulations were able to accurately predict the deformation behaviour of the auxetic lattices, as shown in Figures 4.4 and 4.5. The stress-strain plots obtained from the finite element simulations for the tapered-1 lattices of Design 1 and Design 2, loaded along z and x-directions, are shown in Figure 4.6. These are also compared with the stress-strain plots obtained from experiments. Ductile damage modelling was employed to perform the numerical simulations. The details of the finite element simulations are discussed in Section 3.4. Upto the elastic limit, the stress-strain curves obtained from numerical simulations were almost identical to those obtained from experiments, after which some deviations were observed in the stress-strain plots in the plastic region. It was observed that the compressive strength and elastic modulus obtained from numerical simulations were slightly higher than the experiments. This difference was due to the various defects generated during the 3D printing of the lattice structures, which decreased the mechanical properties in the experiments.

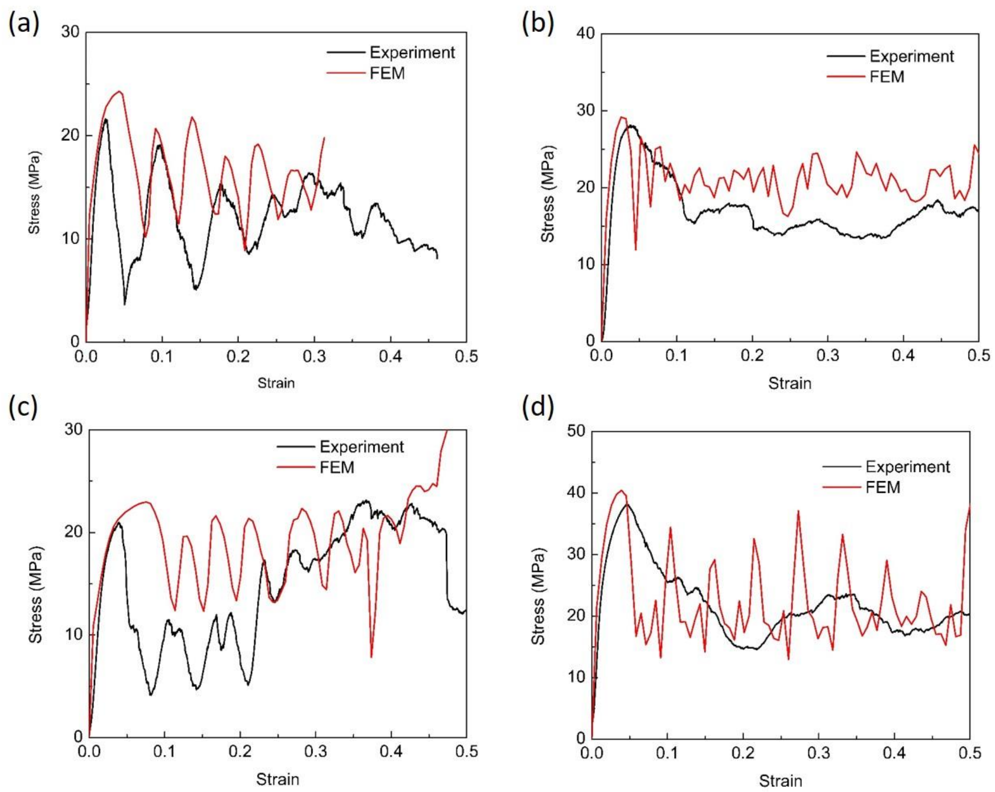

Figure 4.6. Stress-strain plots obtained from experiments and FEM for Design 1-tapered 1 lattice structures loaded along (a) z-direction, (b) x-direction, respectively, and Design 2-tapered 1 lattices loaded along (c) z-direction and (d) x-direction, respectively.

Stress concentration sites were observed at the reentrant/oblique struts of the uniform strut 3D-reentrant structures during deformation [Figure 4.7(a)]. When the ratio of taper was 0.8 (tap 1 design), the stress in the lattice structure was uniformly distributed, and the stress concentration disappeared [Figure 4.7(b)]. With an increase in the degree of taper (tap 2), it was observed that the stress concentration reappeared in the oblique struts [Figure 4.7(c)]. Thus, the stress-concentration sites in the 3D-reentrant structures can be eliminated with a slight degree of taper. It was also observed in the previous section that the tapered 1 design had the highest compressive strength and elastic modulus when loaded either along the z-direction or the x-direction. The increase in mechanical properties in the tapered 1 structures was because of uniform stress distribution and lack of stress concentration sites. Thus, it can be beneficial to design 3D-reentrant auxetic lattices with a slight taper to improve the mechanical properties.

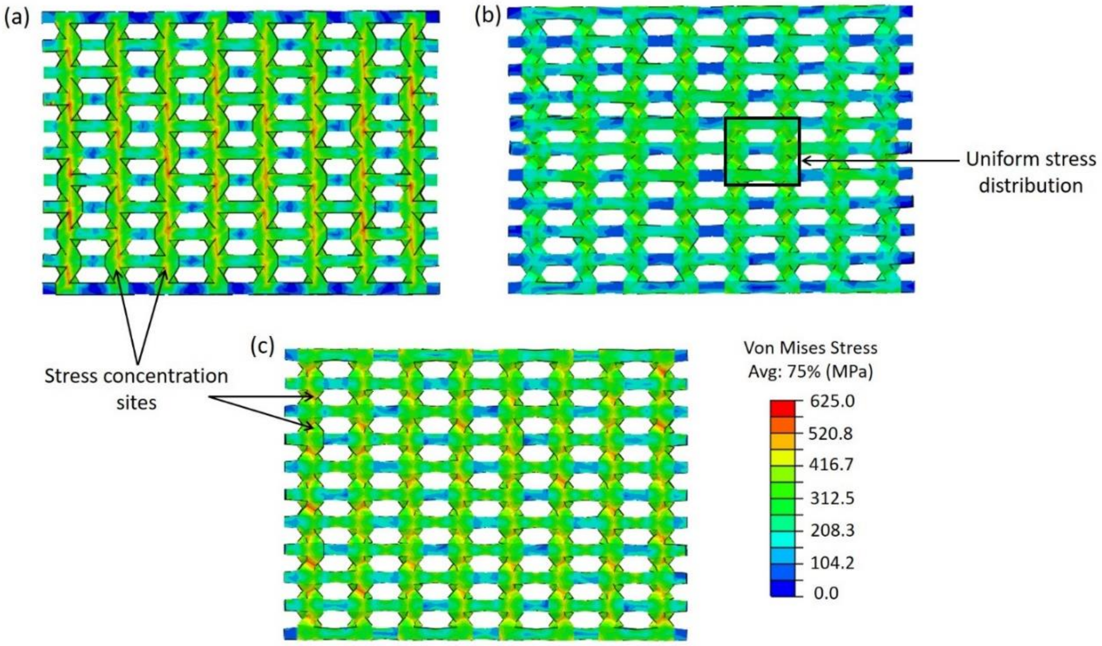

Figure 4.7. Stress distribution observed at a strain of 5% for Design 1 (a) regular, (b) tap 1, and (c) tap 2 lattices, respectively, loaded along x-direction.

4.2.4 Mechanical properties of lattice structures

The quasi-static mechanical properties of the 3D-reentrant auxetic lattice structures can be obtained from the stress-strain plots shown in Figure 4.3. The compressive strength was calculated as the first peak value of stress in the stress-strain plots. The elastic modulus was calculated as the compressive stress divided by the compressive strain within the elastic limit. The compressive stress and elastic modulus for all the lattice structures were calculated from the experimental stress-strain plots and are listed in Table 4.3. It can be seen from Table 4.3 that when the samples were loaded in the z-direction, the compressive strength and elastic modulus of Design 1 lattices were greater than the compressive strength and elastic modulus of Design 2 lattices, but when they were loaded along the x-direction, the results reversed. This observation was also reported by Yang et al. [41], where, when the 3D-reentrant lattices were loaded along the z-direction, an increase in the h/l ratio and a decrease in the angle led to an increase in the compression strength and elastic modulus. In contrast, when the 3D-reentrant lattices were loaded along the x-direction, an increase in the h/l ratio and a decrease in the angle led to a decrease in the compression strength and elastic modulus. In this study, the Design 1 lattices have an h/l ratio of 2 and θ of 60° and Design 2 lattices have an h/l ratio of 1.5 and θ of 70°. Thus, when loaded along the z-direction, the Design 1 lattices had the highest compressive strength and elastic modulus, but when loaded along the x-direction, the Design 2 lattices had the highest compressive strength and elastic modulus.

Table 4.3. Compressive strength and elastic moduli of all the 3D-reentrant auxetic lattice structures obtained from quasi-static tests.

Properties	**Design 1**						**Design 2**					
	z-direction			**x-direction**			**z-direction**			**x-direction**		
	Reg	Tap 1	Tap 2	Reg	Tap 1	Tap 2	Reg	Tap 1	Tap 2	Reg	Tap 1	Tap 2
Compressive strength (MPa)	18.2	21.5	19.8	23.2	28.0	24.5	16.2	20.9	18.0	35.6	38.1	36.4
Elastic modulus (GPa)	0.67	1.26	1.16	0.91	1.43	0.90	0.51	0.90	0.76	1.41	1.96	1.69

It was also observed from Table 4.3 that using tapered struts instead of uniform struts improved the mechanical properties of the lattice structures. The tapered 1 design has higher values of compressive strength and elastic modulus than the regular lattices, irrespective of the loading directions. However, with the increase in the degree of taper (tap 2), the mechanical properties decreased due to the formation of stress concentration sites which was discussed in the previous section. The D2-tap 1 lattice loaded along the x-direction has the highest value of compressive strength of 38.1 MPa, and the highest value of elastic modulus of 1.96 GPa. Thus, it is beneficial to design 3D-reentrant structures with up to a certain degree of taper to obtain a high strength-to-weight ratio and high modulus-to-weight ratio.

4.3 Dynamic deformation behaviour

4.3.1 Dynamic stress-strain plots and mechanical properties

The dynamic tests on the 3D-reentrant auxetic lattices were conducted using the split Hopkinson pressure bar (SHPB) at a strain rate of 1000 s^{-1}. More details on the test setup are discussed in Section 3.7. The stress-strain plots obtained from the dynamic tests for all the uniform and tapered strut 3D-reentrant lattices loaded along the two different directions are shown in Figure 4.8. The compressive strengths of the 3D-reentrant lattices obtained from the dynamic tests were slightly higher than those obtained from quasi-static tests. The comparison between the compression strengths of the 3D-reentrant lattices obtained from the quasi-static and the high-strain rate tests are shown in Figure 4.9. The AlSi10Mg lattice structures showed little strain rate sensitivity in all the lattice specimens except in D2-tap 2 structure, where the compressive strength obtained from the quasi-static test was more than the compressive strength obtained from the high-strain rate test. It was observed that the compressive strength of the 3D-reentrant structures in the high-strain rate tests followed a nearly similar trend in most cases as the quasi-static tests, in which the tapered 1 3D-reentrant structures had the highest compressive strength than those of the regular strut 3D-reentrant lattices.

4.3.2 Deformation behaviour of Design 1 lattice structures

The deformation behaviour of the Design 1 3D-reentrant structures with uniform and tapered struts loaded along the z-direction is shown in Figure 4.10(a). It was observed that the regular strut lattice structure was deformed by uniform compression during the initial deformation, and the deformation became localized as the compression progressed. Dynamic crushing was observed in the layer near the incident bar during the high-strain rate test, which caused the struts in that layer to fracture. Instead of plastic buckling observed in the quasi-static compression [Figure 4.4(a)], the lattice structure failed by dynamic crushing at a high-strain rate test. The struts did not get enough time to fail by buckling in the dynamic test. The tapered 3D-reentrant structures also deformed by the same deformation mechanism as the uniform strut 3D-reentrant structure [Figure 4.10(a)] when loaded along the z-direction.

When the Design 1 3D-reentrant lattice structures were loaded along the x-direction, bending of the oblique struts occurred during the initial deformation, after which localized crushing of the lattice structures was observed, as shown in Figure 4.10(b). The fracture of the struts occurred during the dynamic crushing of all the lattices.

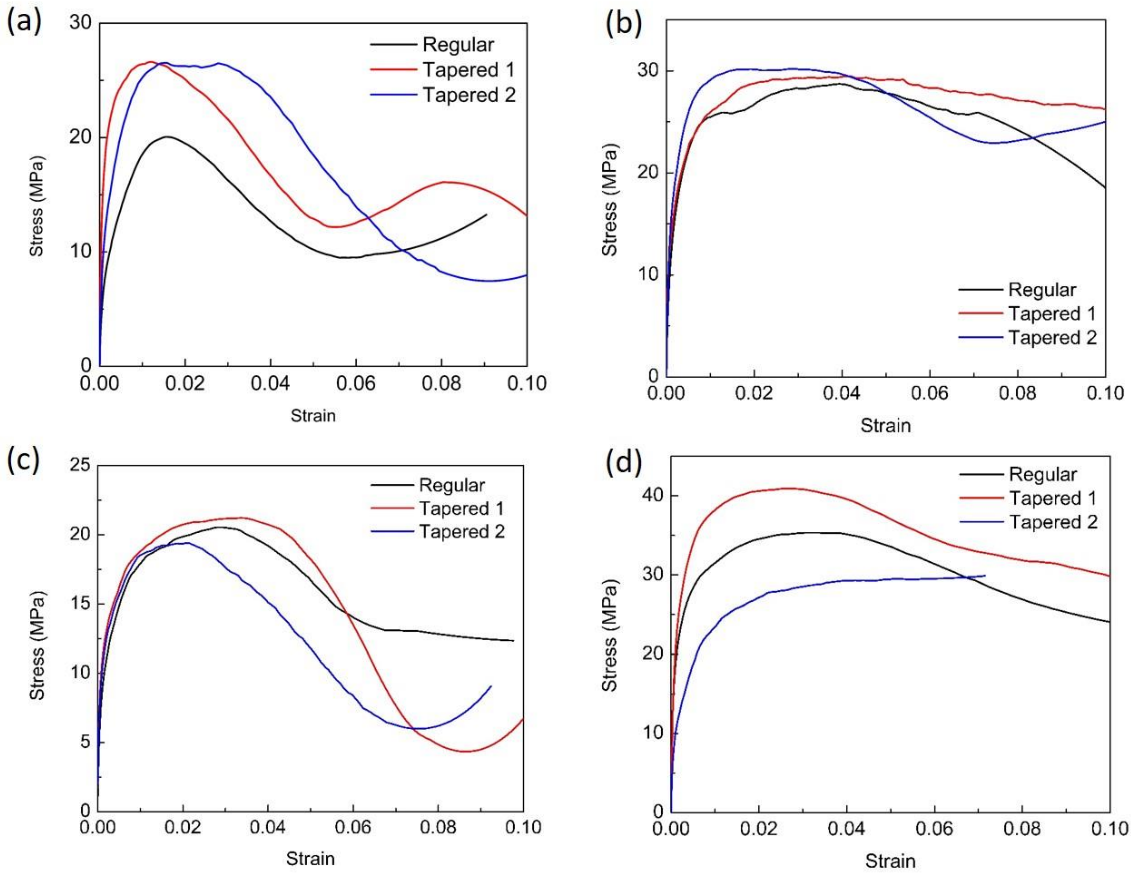

Figure 4.8. Dynamic stress-strain plots for Design 1 lattices loaded along (a) z-direction, (b) x-direction, respectively, and Design 2 lattices loaded along (a) z-direction, (b) x-direction, respectively.

4.3.3 Deformation behaviour of Design 2 lattice structures

The deformation behaviour of the Design 2 3D-reentrant lattices with uniform and tapered struts loaded along the z-direction is shown in Figure 4.11(a). The Design 2 3D-reentrant lattices were also deformed by dynamic crushing like the Design 1 lattices during the high-strain rate tests. Uniform compression was observed during the initial strain, and with increased strain, the lattice structures deformed locally by crushing the entire layer.

When the Design 2 3D-reentrant lattices were loaded along the x-direction [Figure 4.11(b)], the lattice structures first deformed elastically by bending of the inclined struts.

A diagonal shear plane was observed in Figure 4.11(b) during the deformation of the regular strut lattice. The fracture of the struts was observed along the diagonal shear plane. This type of diagonal shear plane was also observed during the deformation of the D2-tapered 1 lattice structure [Figure 4.11(b)]. The D2-tapered 2 lattice structure deformed by localized collapse.

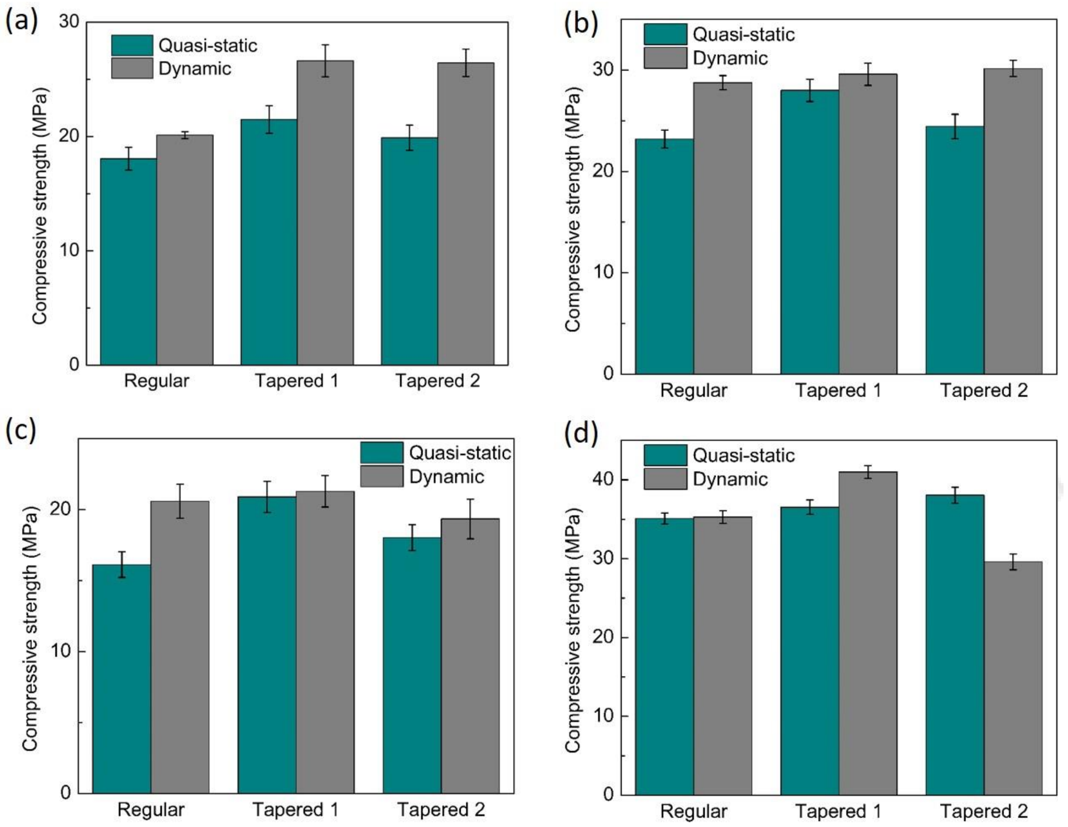

Figure 4.9. Comparison of compressive strengths obtained from quasi-static and dynamic tests for Design 1 lattices loaded along (a) z-direction, (b) x-direction, respectively, and Design 2 lattices loaded along (c) z-direction and (d) x-direction, respectively.

4.4 Auxetic behaviour

The Poisson's ratio vs. strain curves obtained from numerical simulations of quasi-static tests for all the uniform struts and tapered struts 3D-reentrant structures of both Design 1 and Design 2 lattices are shown in Figure 4.12. It can be observed that the effect of Poisson's ratio was more when the structures were loaded along the x-direction. For regular strut 3D-reentrant structures of Design 1, the negative value of Poisson's ratio had reached a minimum value of −0.58 when loaded along the x-direction, compared to −0.17 when loaded along the z-direction. For the regular strut 3D-reentrant structure of Design

2, the negative value of Poisson's ratio has reached a minimum value of −0.72 when loaded in the x-direction, compared to −0.18 when loaded in the z-direction (Figure 4.12). The average values of Poisson's ratio obtained from the quasi-static compression tests are mentioned in Table 4.4, which are also compared with the numerical simulations. It can be interpreted that the effect of negative Poisson's ratio was highest for the regular or uniform strut 3D-reentrant structure. The Poisson's ratio decreased with the increase in the degree of taper of the struts. This was due to decreased effective length of oblique struts in the tapered 3D-reentrant structures (Figure 4.13). The effect of negative Poisson's ratio in the 3D-reentrant structures was due to the bending of the oblique struts. With the decrease in the length of the oblique struts, the actual length subjected to bending was reduced, and it could not undergo much deformation and thus, the auxetic effect decreased.

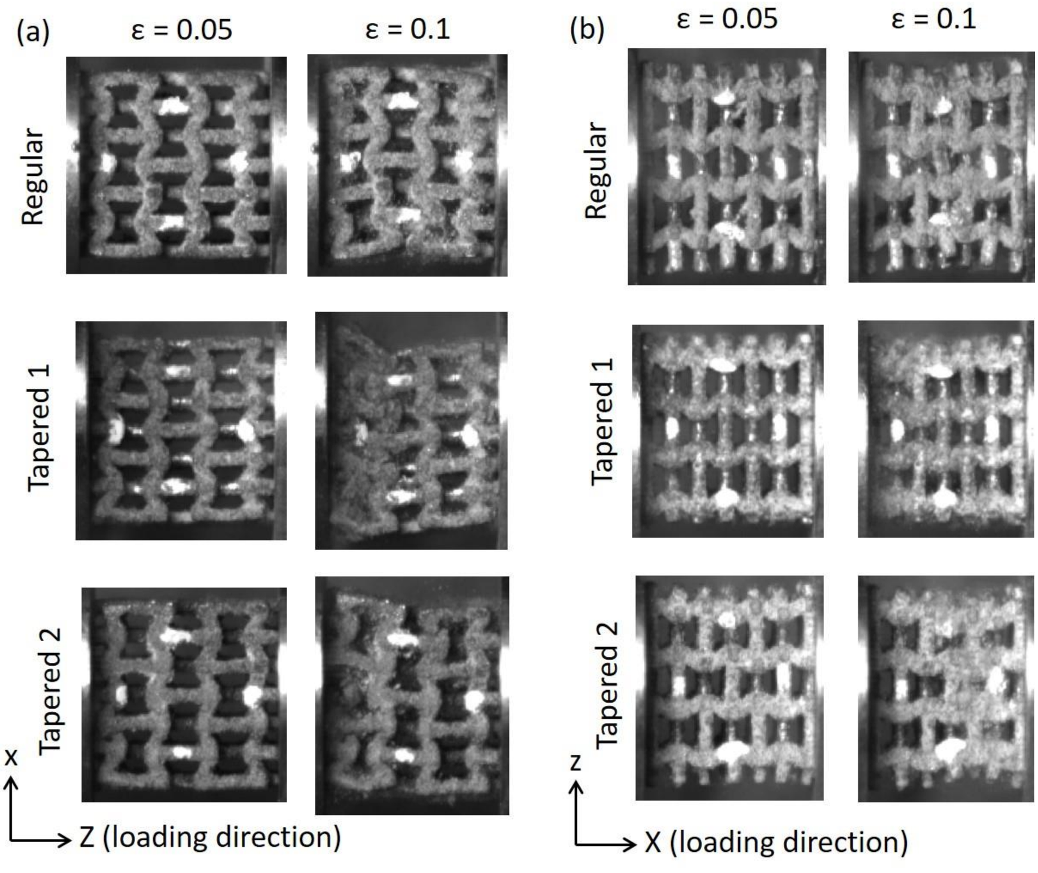

Figure 4.10. Dynamic deformation of Design 1 3D-reentrant lattices loaded along (a) z-direction and (b) x-direction, respectively.

The Poisson's ratio values obtained from Design 1 and Design 2 3D-reentrant lattices loaded along the z-direction were nearly identical (Table 4.4). It was because when the samples were loaded along the z-direction, the buckling of the vertical struts mainly dominated the deformation, and the bending of the oblique struts was not much dominant. However, when the samples were loaded along the x-directions, the deformation was dominated by the bending of the oblique struts. Since the effective length of the oblique struts of Design 2 structures was more than those of Design 1 (Figure 4.13), the Design 2 structures exhibited a more auxetic effect when loaded along the x-direction.

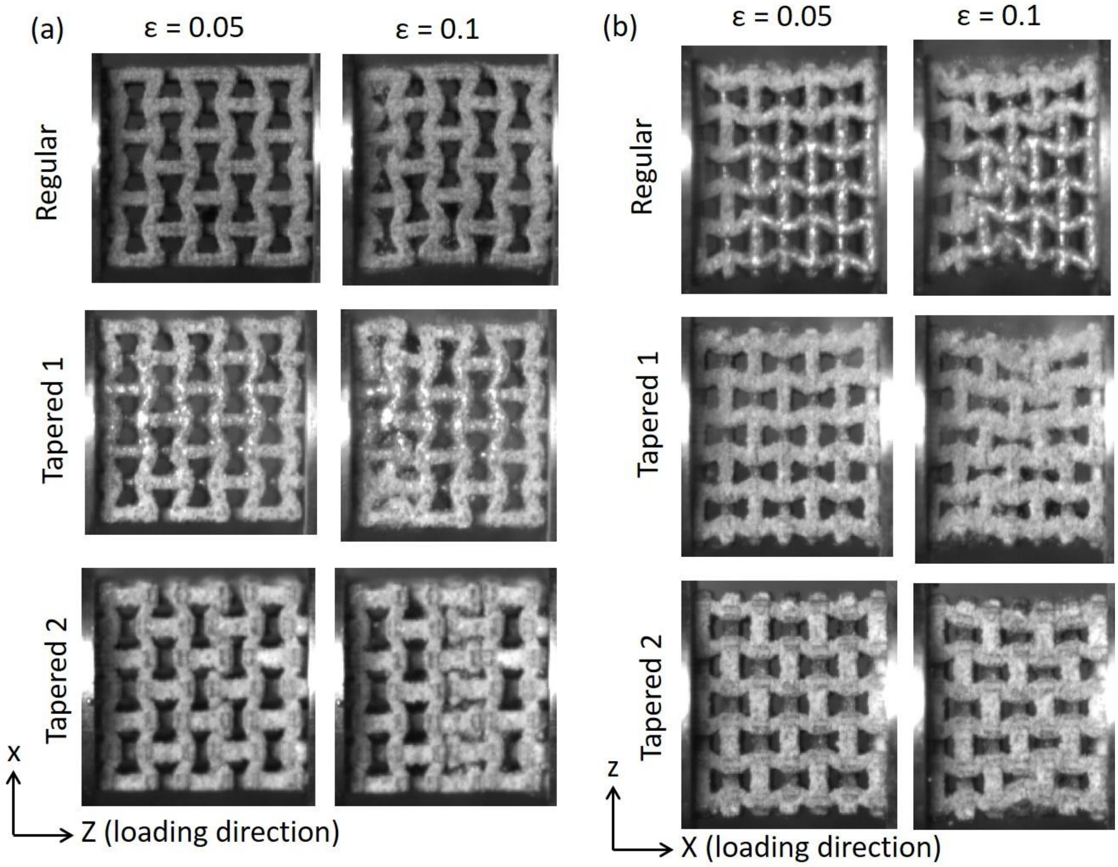

Figure 4.11. Dynamic deformation of Design 2 3D-reentrant lattices loaded along (a) z-direction and (b) x-direction, respectively.

The Poisson’s ratios of the 3D-reentrant auxetic lattice structures obtained from SHPB tests are shown in Table 4.5. It can be observed that the Poisson's ratio values showed a similar trend in dynamic loading conditions as that of the quasi-static results in which the regular strut 3D-reentrant lattice had a more negative value of Poisson's ratio than the tapered strut lattices. However, Poisson's ratio values obtained from the dynamic tests were less than those obtained from quasi-static results. This can be because of the size effect, where the size of the lattices used for the high-strain rate tests was smaller than those used for quasi-static tests. Yang et al. also reported a similar behaviour in which the Poisson's ratio values were sensitive to the number of unit cells in the lattice samples [41]. The decrease in the Poisson's ratio in the dynamic tests was more than those obtained from the quasi-static tests when the samples were loaded along the x-direction. Logakannan et al. used the same size of the samples in both the quasi-static and dynamic tests. They reported that the Poisson's ratio values of the auxetic structures obtained from the dynamic tests were less than those obtained from the quasi-static tests [45]. They said it could be because the struts had less time to deform during the dynamic tests than the quasi-static tests, resulting in a lower auxetic effect. The Poisson's ratios were also calculated for the dynamic tests until the localized deformation was observed.

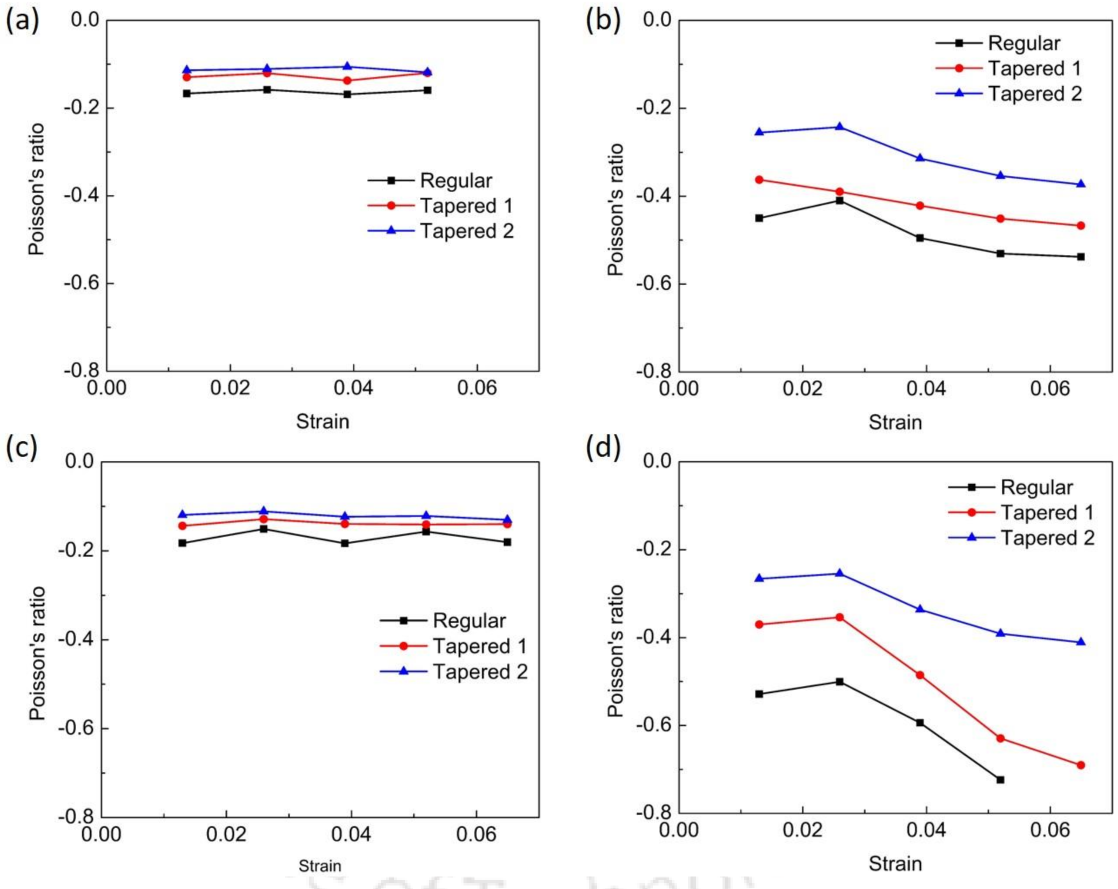

Figure 4.12. Poisson’s ratio vs. strain plots for Design 1 lattices loaded along (a) z-direction and (b) x-direction, respectively, and Design 2 lattices loaded along (c) z-direction (d) x-direction, respectively.

Table 4.4. Poisson's ratio of 3D-reentrant structures obtained from quasi-static tests and finite element simulations.

	Design 1						Design 2					
	z-direction			x-direction			z-direction			x-direction		
	Reg	Tap 1	Tap 2	Reg	Tap 1	Tap 2	Reg	Tap 1	Tap 2	Reg	Tap 1	Tap 2
Expt	−0.15 ± 0.05	−0.13 ± 0.02	−0.10 ± 0.04	−0.46 ± 0.07	−0.40 ± 0.06	−0.32 ± 0.6	−0.17 ± 0.08	−0.15 ± 0.03	−0.13 ± 0.05	−0.55 ± 0.05	−0.48 ± 0.08	−0.37 ± 0.07
FEM	−0.16	−0.13	−0.11	−0.48	−0.42	−0.31	−0.17	−0.14	−0.12	−0.59	−0.51	−0.33

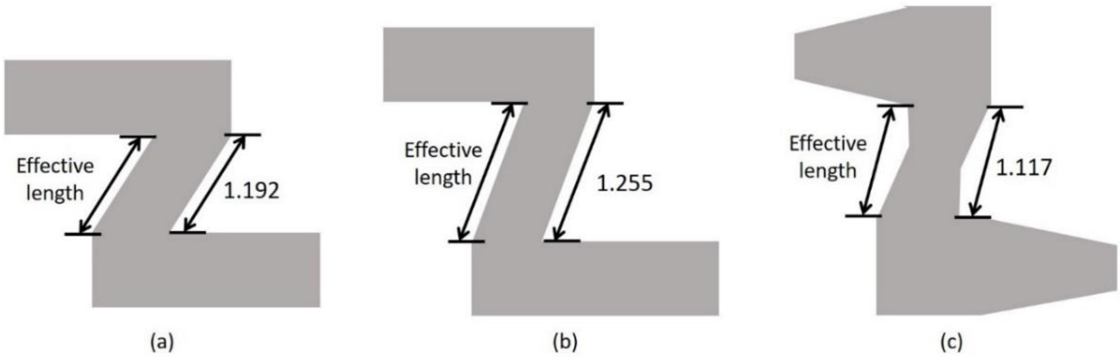

Figure 4.13. Effective length of oblique struts for (a) Design 1-regular lattice, (b) Design 2 regular lattice, and (c) Design 2 tapered 1 lattice.

Table 4.5. Poisson's ratio of 3D-reentrant auxetic lattices obtained from SHPB tests.

Design 1						Design 2					
z-direction			x-direction			z-direction			x-direction		
Reg	Tap 1	Tap 2	Reg	Tap 1	Tap 2	Reg	Tap 1	Tap 2	Reg	Tap 1	Tap 2
−0.14 ± 0.01	−0.13 ± 0.03	−0.08 ± 0.02	−0.25 ± 0.03	−0.22 ± 0.02	−0.20 ± 0.1	−0.15 ± 0.02	−0.15 ± 0.03	−0.13 ± 0.04	−0.32 ± 0.02	−0.27 ± 0.03	−0.19 ± 0.01

4.5 Summary

The quasi-static and dynamic mechanical properties of the tapered 3D-reentrant lattices that exhibited negative Poisson's ratio were investigated in this work. The lattice structures were fabricated by laser powder-based fusion (PBF) based additive manufacturing technique with AlSi10Mg as the printing material. Uniaxial compression of the AlSi10Mg-based lightweight lattice structures were conducted along two different loading directions. The split Hopkinson pressure bar (SHPB) was used to study the dynamic compression behaviour of the lattice structures at a strain rate of 1000 s^{-1}. The major findings of this study were that the 3D-reentrant lattice with a certain variation in the cross-section of the strut showed improved mechanical properties than the uniform strut 3D-reentrant lattice in both quasi-static and dynamic loading conditions. The compressive strength of the tapered 3D-reentrant lattices increased by 7-28% than the uniform-strut 3D-reentrant lattice structures. Numerical simulations were also conducted to study the deformation evolution of the lattice structures. The Poisson's ratio values of −0.15 to −0.55 was obtained for the uniform strut 3D-reentrant lattice structures, and it decreased with the increase in the degree of taper of the struts in both quasi-static and dynamic loading. Thus, altering the strut cross-section from uniform to a certain degree of taper for the 3D-reentrant lattice led to improved mechanical properties with a slight compromise in the auxetic behaviour.

CHAPTER 5. COMPOSITE-INSPIRED AUXETIC MULTILATTICE STRUCTURES WITH IMPROVED STRENGTH AND ENERGY ABSORPTION

In this chapter, a novel technique to improve the mechanical properties of the auxetic lattices by using high-strength lattices reinforcements is demonstrated. This technique to improve the mechanical properties of the auxetic lattices has not been studied before. This study showed that the Young's modulus and the Poisson's ratio of these multilattices can also be predicted by the conventional composite-rule of mixture. Section 5.1 presents the design and fabrication of the composite-inspired lattice structures. Section 5.2 discusses the deformation mechanisms and stress-strain response of the lattice structures. The mechanical properties of the composite inspired lattices are discussed in Section 5.3. Section 5.4 demonstrates that the elastic modulus and Poisson's ratio of these lattices can be predicted by the composite rule of mixture. Lastly, Section 5.5 studies the effects of increase in volume fraction of the reinforcement lattices on the mechanical properties of the composite-inspired lattices.

5.1 Design and fabrication of lattice structures

5.1.1 Design of composite-inspired multilattice structures

In this study, two different types of lattices were combined to fabricate a composite-materials-inspired lattice structure with improved mechanical properties. The 3D-reentrant lattice was used as the base structure in this investigation. The 2D and 3D views of a 3D-reentrant unit cell along with different unit cell parameters are shown in Figure 5.1(a) and (b), respectively. The relative density of the 3D-reentrant unit cell (ρ_r) can be expressed as [40,43]

$$\rho_r = \frac{4t_1^2h+16t_1^2l}{(2Lsin\theta)^2\times2(H-Lcos\theta)} \tag{5.1}$$

where, H is the length of vertical strut, L is the length of inclined strut, θ is the reentrant angle and t_1 is the thickness of the strut, $h = H + \frac{t_1(1-cos\theta)}{sin\theta}$; and $l = L - \frac{t_1}{sin\theta}$.

With an increase in the H/L ratio and decrease in θ, the 3D-reentrant lattice exhibits higher Young's modulus and compressive strength when loaded in the z-direction (Section 4.2.4).. However, the H/L ratio and θ used in this study are fixed, and taken as 2 and 45˚, respectively. The elastic modulus of the 3D-reentrant unit cell (E_r) is given as [41,42]:

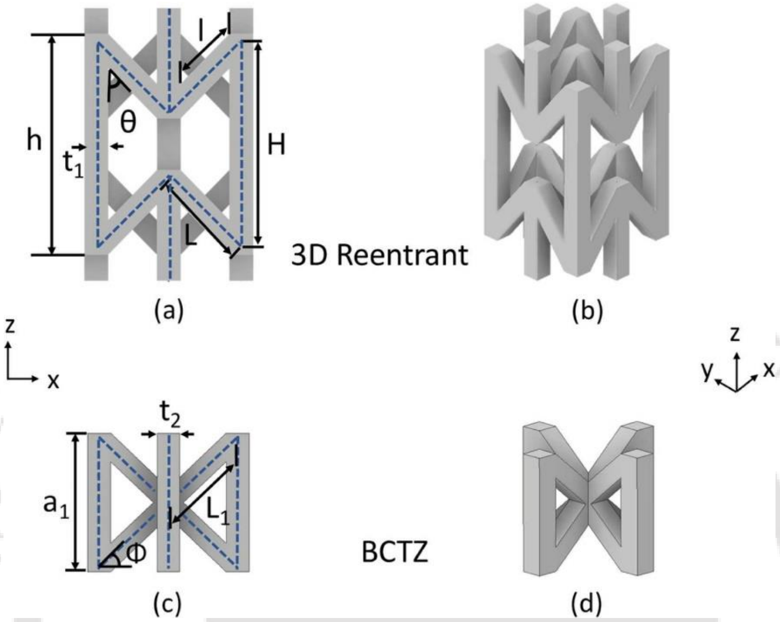

Figure 5.1. (a) 2D view and (b) 3D view of a 3D-reentrant unit cell showing the unit cell parameters, (c) 2D view and (d) 3D view of a BCTZ unit cell showing the unit cell parameters.

$$E_r = \frac{\alpha - cos\theta}{\left(\frac{2\alpha L^2 sin^2\theta}{E_m t_1^2}\right) + \left(\frac{L^4}{2E_m t_1^4} + \frac{3L^2}{5G_m t_1^2}\right) sin^4\theta} \qquad 5.2$$

where, α is the ratio of the length of vertical strut to the length of inclined strut (H/L), E_m and G_m are the elastic modulus and shear modulus of the parent material.

The reinforcement lattice was chosen as body centred tetragonal with vertical struts (BCTZ), which is a modified form of BCCZ unit cells. The 2D and 3D views of a BCTZ unit cell along with different unit cell parameters are shown in Figure 5.1(c) and (d), respectively. The relative density of the BCTZ unit cell (ρ_b) can be determined as

$$\rho_b = \frac{t_2^2 a_1 + 8 t_2^2 L_2}{a_1 \times a_2^2} \qquad 5.3$$

where a_1 is the height of the BCTZ unit cell, a_2 is the length as well as the breadth of the unit cell, t_2 is the strut thickness, and $L_2 = L_1 - \frac{t_2}{cos\Phi}$ in which L_1 is the length of the inclined strut.

The BCC or BCCZ unit cell can be generated from the z-direction struts of the 3D-reentrant lattice. Since the shape of the 3D-reentrant unit cell is not cubic, the BCTZ unit cell was considered instead of the BCCZ unit cell to maintain compatibility between the matrix and reinforcement lattices. The theoretical elastic modulus of the BCCZ unit cell has been developed by Li et al. [132]. The expression for elastic modulus of BCTZ unit cell (E_b) can be derived as:

$$E_b = \frac{t_2^2 E_m sin\Phi}{a_2^2}\left(\frac{1}{sin\Phi} + 4\, sin^2\Phi + \frac{t_2^2 cos^2\Phi}{L_1^2}\right) \quad 5.4$$

where, Φ is the angle of inclination. The quasi-static compression stress-strain plots of the 3D-reentrant lattice and the BCTZ lattice of the same relative density are shown in Figure 5.2(a) and (b), respectively. The average compressive strengths of the 3D-reentrant and the BCTZ lattices having same relative density obtained from experimental results in Figure 5.2(a) and (b) are 0.75 MPa and 4.26 MPa respectively, and the average elastic moduli of the 3D-reentrant and the BCTZ structures obtained from experimental results in Figure 5.2(a) and (b) are 32.25 MPa and 109.71 MPa respectively. The BCTZ lattice outperformed the 3D-reentrant lattice in terms of compressive strength and elastic modulus. Hence, the BCTZ lattices are appropriate to be used as reinforcements in the matrix of 3D-reentrant lattice to improve its stiffness, strength, and energy absorption ability without compromising the negative Poisson’s ratio characteristic. Figure 5.3(a) and (b) show the 2D and 3D views, respectively, of combined unit cells of the BCTZ and the 3D-reentrant lattices. The BCTZ lattice reinforcements were distributed in different patterns to design different multilattice composite structures.

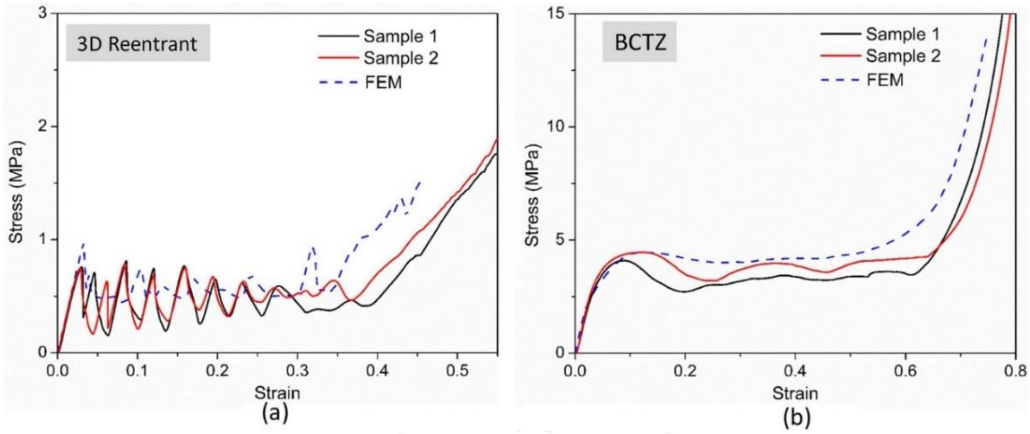

Figure 5.2. Compressive stress-strain plots of (a) 3D-reentrant, (b) BCTZ lattices.

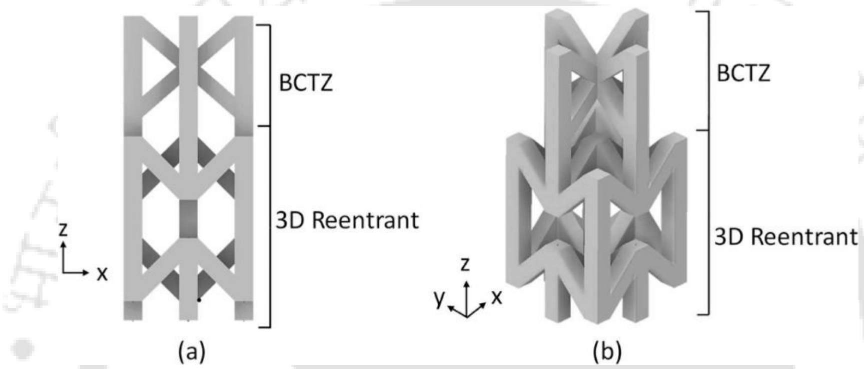

Figure 5.3. (a) 2D view and (b) 3D view of a part of multilattice structure showing combined BCTZ and 3D-reentrant unit cells structure.

There are three different designs of multilattice composite-inspired structures considered in this study. These three multilattice structures and both the parent lattices, i.e. 3D-reentrant and BCTZ, have the same overall dimensions and relative densities. The cross-section of the struts for all the lattice structures is square in shape. The design parameters of the multilattice structures are mentioned in Table 5.1. Figure 5.4(a) shows the 3D view of the Continuous Fibre Reinforced Multilattice (CFRM) structure, and Figure 5.4(b) shows the layerwise design on the x-z plane of all the multilattice composite structures.

Table 5.1. Design parameters of the multilattice structures.

Reentrant unit cell				BCTZ unit cell				No. of unit cells in (x × y × z)	Size (mm^3) (x × y × z)
H (mm)	L (mm)	θ (°)	t_1 (mm)	a_1 (mm)	a_2 (mm)	Φ (°)	t_2 (mm)		
6	3	45	0.71	3.9	4.242	41.04	0.71	7 × 7 × 5	30.4 × 30.4 × 38.8

The three designs of multilattice structures have 10% volume fractions of BCTZ reinforcements in the matrix of 3D-reentrant lattice. The spatial distribution of the precipitates was done in such a way that they are distributed symmetrically throughout the matrix. The three multilattice composite- inspired designs are:

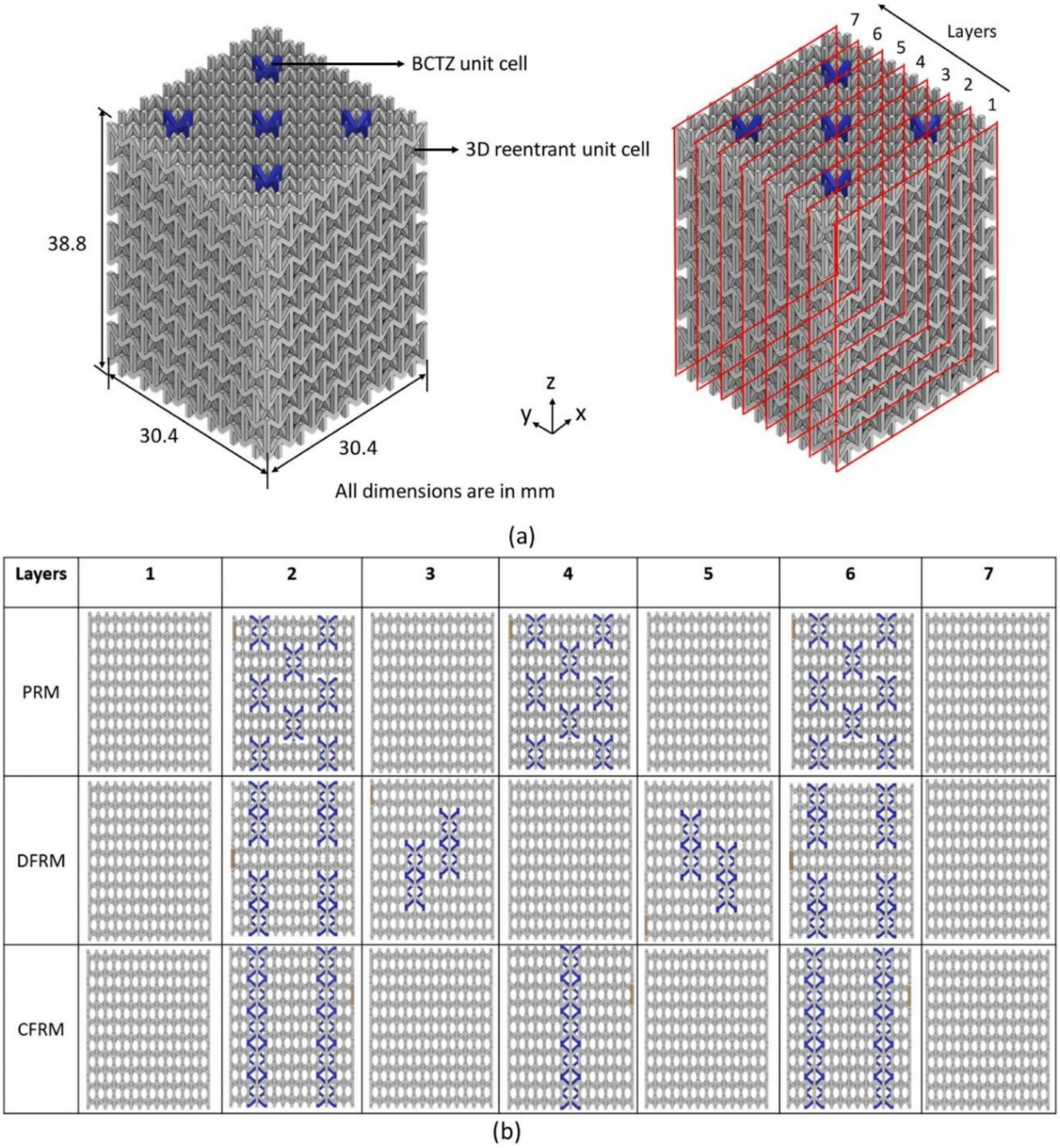

Figure 5.4. (a) 3D view of a CFRM composite structure and (b) layerwise 2D view on the x-z plane of different multilattice composite structures.

- **Particle Reinforced Multilattice (PRM) composite structure**: The BCTZ lattice reinforcements are incorporated as particle-like structures and distributed symmetrically in the matrix of 3D-reentrant lattice. Each particle-like reinforcement, which consists of two BCTZ unit cells, has a size same as that of a unit cell of the 3D-reentrant lattice.

- **Discontinuous Fibre Multi-lattices (DFRM) composite structure**: The BCTZ lattice reinforcements are distributed symmetrically as short fibre-like structures in the matrix of the 3D-reentrant lattice. The short fibre-like reinforcements, which are oriented parallel to the loading direction, have a length equal to the length of two unit cells of the 3D-reentrant lattice in the loading direction.
- **Continuous Fibre Multi-lattices (CFRM) composite structure**: The fibre-like BCTZ lattice reinforcements are distributed symmetrically along the loading direction in the matrix of 3D-reentrant lattice. These fibre-like reinforcements have a length same as that of the entire multilattice structure in the loading direction.

Table 5.2. Dimensions and relative densities of printed lattice structures.

Sample	Sample dimension			Mass (g)	Measured relative density (%)	Designed relative density (%)
	x (mm)	y (mm)	z (mm)			
3D-reentrant	30.6	30.6	38.9	6.68	19.9	21.6
PRM	30.7	30.6	39.1	6.54	19.3	
DFRM	30.7	30.5	39.0	6.67	19.8	
CFRM	30.5	30.6	39.0	6.59	19.6	
BCTZ	30.7	30.6	38.8	6.62	19.7	

5.1.2 Fabrication of lattice structures

The HP Multi Jet Fusion was used to fabricate the lattice samples in this study. Polyamide 12 (PA12) is the material used for fabricating lattice structures by Multi Jet Fusion. The volume and mass of the fabricated samples were measured to determine the relative density. Table 5.2 shows the average dimensions, masses, and relative densities of three samples for each of the five lattice structures. The change in relative density of the fabricated samples compared to that of the computer-aided design is due to the internal porosities and the surface defects generated during the Multi Jet Fusion process. Cai et al. reported internal porosities of 5.07% in the final product made of PA12 printed by MJF technique, while Xu et al. (2019) found 7% porosity in MJF-printed PA12 parts [128,133]. Hence, the porosities generated in the lattice structures studied in this work are close to the values mentioned in the above literature.

5.2 Deformation mechanism and stress-strain response

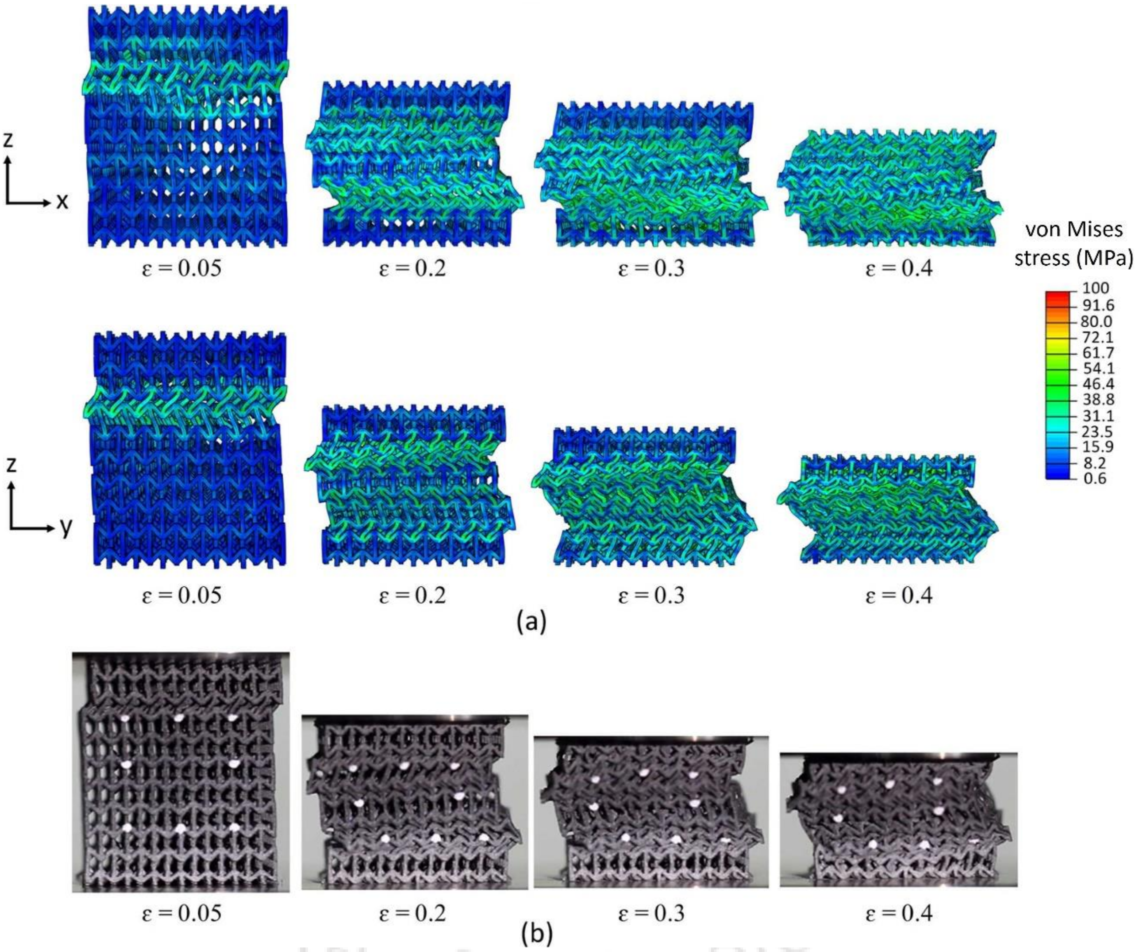

Figure 5.5. Deformation mechanism of 3D-reentrant lattice structure at different nominal strains (ε), (a) on x-z and y-z planes predicted by the finite element simulation, and (b) observed in the experiment.

The mechanical behaviour of the lattice structure can be understood by studying the stress-strain response and the sequence of deformation patterns. Figure 5.5 shows the quasi-static deformation behaviour of the 3D-reentrant lattice structure at different strains for both numerical simulation and experiment. The localized layerwise buckling of vertical struts was the dominant deformation mechanism of the 3D-reentrant lattice structure in the numerical simulations. The deformation patterns on the x-z and the y-z planes are the same, as shown in Figure 5.5(a). Moreover, the same deformation mechanism of localized layerwise buckling was observed in the experiment as well [Figure 5.5(b)]. This type of deformation mechanism was also observed for the 3D-reentrant lattice in the previous chapter. Due to finite lateral size, i.e., a finite number of unit cells along the lateral direction of the lattice structure, the vertical struts undergo bending moment. Initially, the outer faces of the vertical struts at the lateral edges of the lattice structure were subjected to bending moment that was not balanced by the internal struts. The bending moment experienced by the vertical struts at the lateral edges further increased with the increase of deformation as the compression progressed. This led to localized buckling of one of the horizontal layers of unit cells and resulted in the collapse of the entire layer. Thus, the buckling of the vertical struts took place in a layer-by-layer manner resulting in fluctuation of stress level in the stress-strain curve, as shown in Figure 5.7(a).

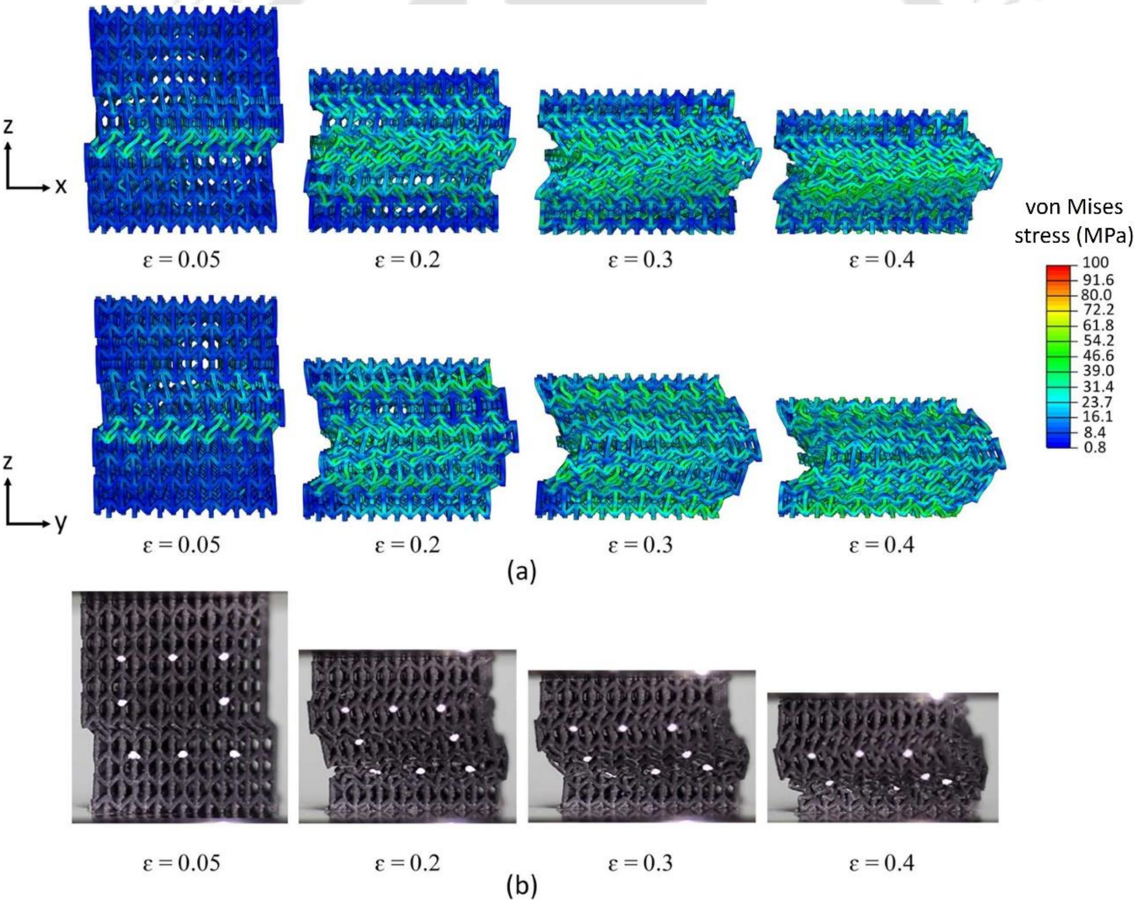

Figure 5.6. Deformation mechanism of CFRM structure at different nominal strains (ε), (a) on x-z and y-z planes predicted by the finite element simulation, and (b) observed in the experiment.

After the initial peak stress of 0.75 MPa at a nominal strain of 0.028 (Sample 2), the first collapse of the vertical struts in the second horizontal layer of unit cells from the top was observed [Figure 5.5(b)], which resulted in the first stress drop in the experimental stress-strain curve [Figure 5.7(a)]. The remaining layers carried the load with an increase in deformation, and the stress increased again. Then the vertical struts in the fourth horizontal layer of unit cells from the top collapsed, and the stress dropped again, thus resulting in fluctuation of stress level. After all the layers had collapsed one after the other, the whole structure densified. During densification, all the struts of the lattice structure jam together, and the pore space within the entire structure squeezes out. The densification strain was calculated as 0.37 from the energy efficiency vs. strain plot (Section 5.3.2).

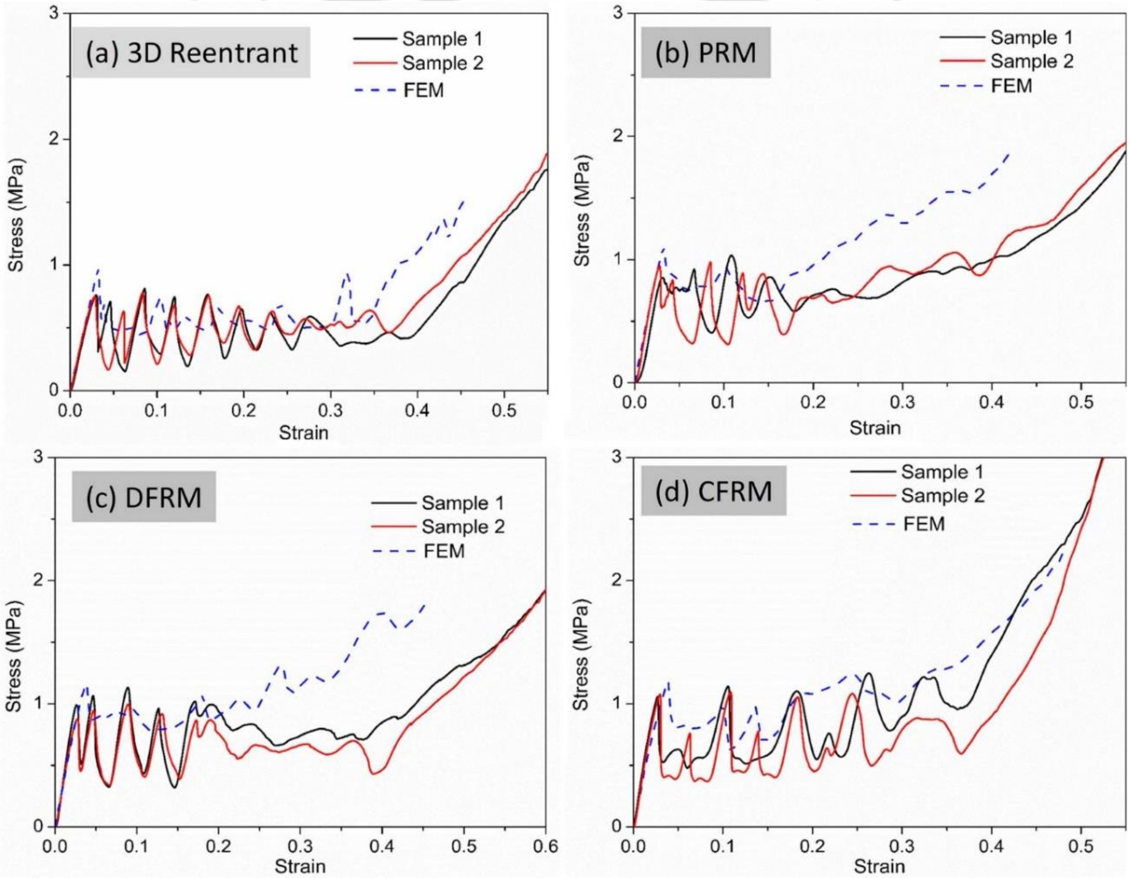

Figure 5.7. Compressive stress-strain plots of (a) 3D-reentrant lattice, (b) PRM, (c) DFRM and (d) CFRM structures.

The comparison of the stress-strain plots of the numerical simulations and experiments shows that the compressive strength is higher in the numerical simulation than that of the experiments [Figure 5.7(a)]. This is due to the internal porosity and surface defects such as strut waviness generated during the fabrication of the structures by HP Multi Jet Fusion. A considerable difference in the samples' designed and measured relative densities due to these defects was observed and has already been reported in Table 5.2. However, the densification strains were approximately the same in both the numerical simulation and the experiments.

Like the deformation mechanism of the 3D-reentrant lattice structure, buckling of vertical struts was the dominant deformation mechanism for the three different multilattice composite structures. Since the volume fraction of the BCTZ lattice reinforcement was only 10%, the overall deformation mechanism of the multilattice composite structures was dominated by the deformation mechanism of the matrix phase, i.e. the 3D-reentrant lattice. Figure 5.6 shows the deformation mechanism of the continuous fibre reinforced multilattice (CFRM) structure. The deformation pattern, i.e., the buckling of vertical struts of the 3D-reentrant unit cells, is similar in both the finite element simulation and the experiment but the sequence of the collapse of the layers was not identical. The high-strength BCTZ reinforcements resisted the compressive force during elastic deformation, and thus the compressive strength and elastic modulus of the multilattice structure increased. As the strain increased, the buckling of the vertical struts of the 3D-reentrant lattice took place. With further deformation, the layer-wise collapse of the 3D-reentrant structures in different layers were observed. The DFRM and PRM multilattice structures also collapsed layer by layer in a similar fashion by buckling of vertical struts of the 3D-reentrant structure, and thus, fluctuations in the stress-strain response were observed. Figure 5.7(b), (c), and (d) show the stress-strain plots of the three different multilattice composite structures. The stress-strain plots for only two out of the three samples of each multilattice composite structure are shown for clarity. The stress-strain plots of the multilattice composite structures obtained from numerical simulations were found to have higher values of compressive strength than the experimental results. The mechanical properties of the different lattice structures are discussed in detail in Section 5.3.

5.3 Mechanical properties of lattice structures

5.3.1 Compressive strength and elastic modulus

The compressive strength of a lattice structure was considered the first peak value of stress after the elastic deformation in the compressive stress-strain plot. Table 5.3 shows the average values of the compressive strengths and elastic moduli of three samples for each of the four lattice structures. The three multilattice composite structures have higher compressive strengths and higher elastic moduli than those of the 3D-reentrant lattice structure. It can be observed that the compressive strengths of the multilattice composite structures are 21.3-40.0% higher for experimental results and 13.0-21.6% higher for numerical simulation when compared with 3D-reentrant lattice structures. The higher value of the compressive strength of the multilattice composite structures than that of the base 3D-reentrant lattice was because of the presence of BCTZ lattice as the reinforcements in the matrix of 3D-reentrant lattice. The higher strength and stiffness of the BCTZ lattice compared to those of the 3D-reentrant lattice contributed to the increase in compressive strength. Figure 5.8 shows the deformation pattern obtained from numerical simulation on a cross-section parallel to the x-z plane of the PRM structure. The rectangles with red outlines show the BCTZ lattice reinforcements. The region enclosed by yellow lines depicts the buckled layer of unit cells at a nominal strain of 0.045. It can be seen that the out-of-plane buckling of the vertical struts of the PRM structure took place in the whole layer enclosed by the yellow lines except the BCTZ reinforcement present in that layer. Thus, the particle-like BCTZ lattice reinforcements resisted the localized buckling, contributing to the increase in the strength of the multilattice composite structure.

Table 5.3. Average compressive strengths and elastic moduli of different lattice structures.

Mechanical properties	3D-reentrant		PRM		DFRM		CFRM	
	Expt	FEM	Expt	FEM	Expt	FEM	Expt	FEM
Average compressive strength (MPa)	0.75	0.97	0.91	1.10	0.94	1.15	1.05	1.18
Average elastic modulus (MPa)	32.25	30.52	38.19	36.66	39.25	37.03	40.10	36.79

The CFRM structure exhibited the highest value of compressive strength for both the experimental and numerical results. The CFRM structure showed a significant increase of 40.0% compressive strength compared to the pure 3D-reentrant lattice. Similarly, compared to the pure 3D-reentrant lattice structure, the elastic moduli of the CFRM structure show 18.0-24.3% and 20.0-21.3% improvements for experimental and numerical results, respectively. The increase in strength to elastic modulus ratio was 13.0% for the CFRM structure compared to the pure 3D-reentrant lattice structure. Thus, such a multilattice composite structure can be useful in the biomedical application for potential fully-porous heavy-load-bearing orthopaedic bone implants in which high strength to stiffness ratio is desired to reduce the stress-shielding effect.

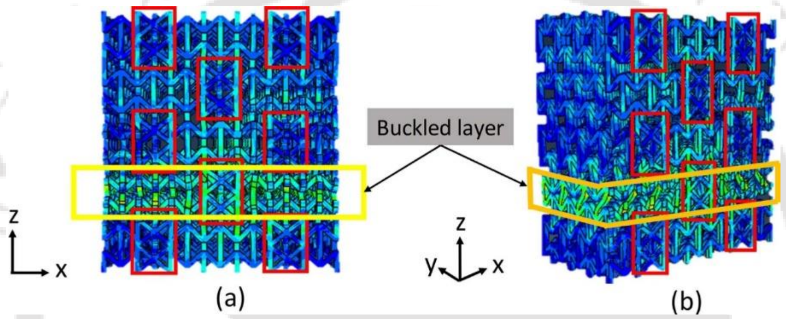

Figure 5.8. Buckling of a layer of unit cells and deformation of BCTZ lattice reinforcements at a nominal strain of 0.045 shown on a cross-section of PRM structure, (a) 2D view and (b) 3D view showing out-of-plane buckling.

5.3.2 Energy absorption ability

The area under stress (σ) - strain (ε) plot estimates the deformation energy absorbed per unit volume (E) of the lattice structure. It is defined as [30]

$$E = \int_0^{\varepsilon_d} \sigma(\varepsilon)\, d\varepsilon \qquad 5.5$$

The energy absorption is calculated until the densification strain (ε_d) is reached. For a cellular structure, very little energy is absorbed during the elastic deformation. Most of the energy for a cellular structure is absorbed in the plateau region of the stress-strain curve. For better energy absorption, the plateau stress should be of high magnitude spreading over a wide range of strain. The plateau regime starts after the yield strain and continues until the onset of densification. The densification strain is the value of strain after which the stress increases drastically with an increase in strain. After this point, the cellular structure starts transmitting a high magnitude of stress, making it incapable of further use in energy-absorbing applications. The densification strain can be calculated from the energy efficiency vs. strain plot. The energy efficiency is given by [134]

$$\eta = \frac{\int_0^{\varepsilon_0} \sigma(\varepsilon) d\varepsilon}{\sigma(\varepsilon_0)} \quad 5.6$$

where, η is the energy efficiency, ε and $\sigma(\varepsilon)$ are the strain and stress, and ε_0 and $\sigma(\varepsilon_0)$ are the nominal strain and the corresponding nominal stress at a particular instant.

The energy efficiency is maximum at densification strain (ε_d), and it can be mathematically expressed as

$$\left.\frac{d\,\eta(\varepsilon)}{d\varepsilon}\right|_{\varepsilon=\varepsilon_d} = 0 \quad 5.7$$

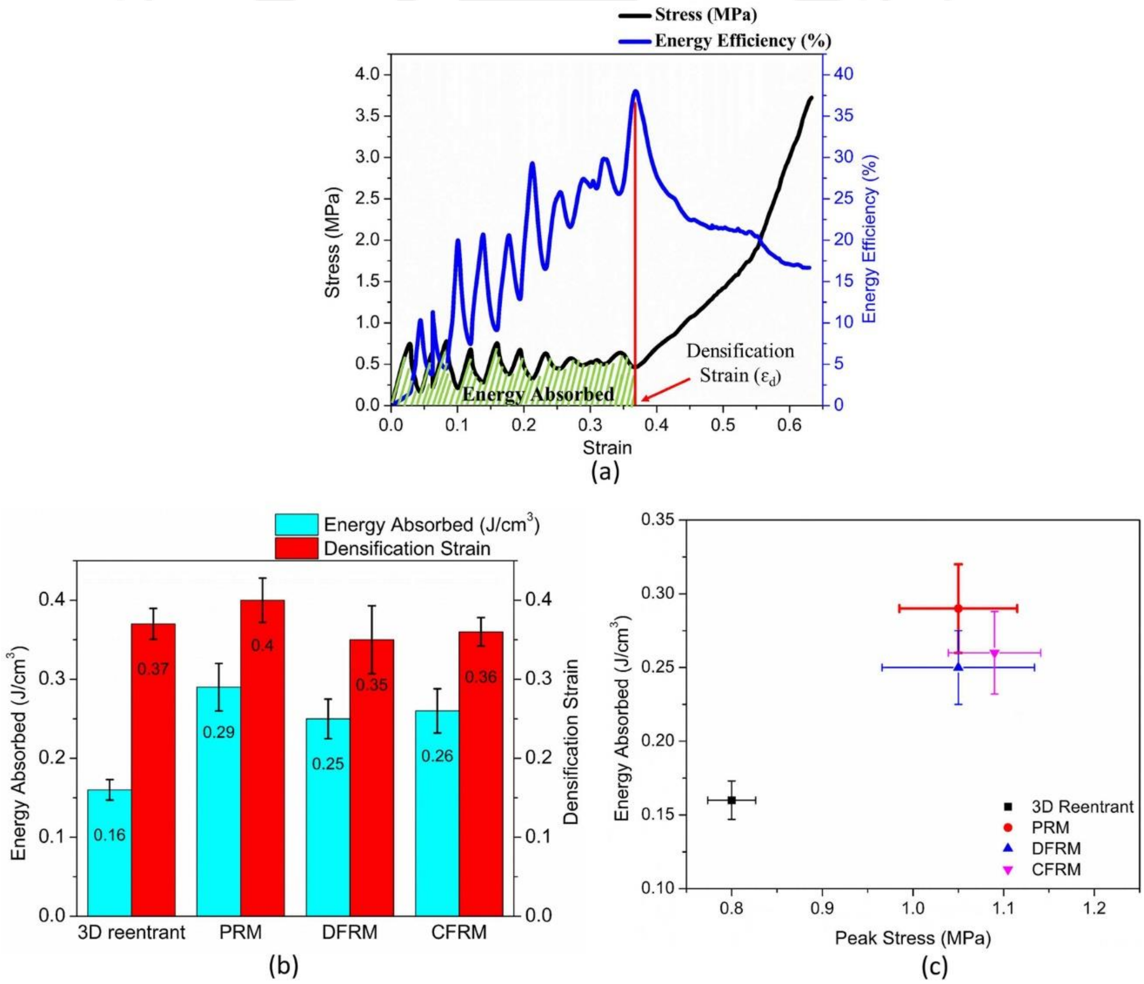

Figure 5.9. (a) Stress and energy efficiency vs. strain plots to find the densification strain of 3D-reentrant lattice structure, (b) energy absorbed per unit volume and densification strain of different lattice structures, and (c) the energy absorbed per unit volume vs. peak stress of different lattice structures.

Figure 5.9(a) shows the energy efficiency vs. strain plot of a 3D-reentrant lattice structure. The area under the stress-strain plot until the densification strain is the energy absorbed by the lattice structure during compression.

The energy absorbed per unit volume and the densification strain for all four structures are calculated and shown in Figure 5.9(b). The PRM structure showed the highest value of energy absorption, followed by the CFRM and DFRM structures, respectively. The energy absorption per unit volume increased by 56.2-81.2% due to the presence of the BCTZ lattice reinforcement in the three multilattice structures. The high strength of the BCTZ lattice reinforcements led to the elevated stress levels, thus increasing the area under the stress-strain plot.

For a structure to be used for energy absorbing applications, it should absorb energy without transmitting higher stress across the structure than the maximum limit specified for a particular application [30,135]. Thus, a lattice structure that can absorb high energy without transmitting high stress is ideal for energy-absorbing applications. Figure 5.9(c) shows the energy absorbed per unit volume (E) vs. peak stress transmitted (σ_p) for different lattice structures. The PRM structure exhibited the highest energy absorption ability among the three multilattice composite structures, whereas the peak stress attained by the PRM structure is lower than that of the CFRM structure. The high energy absorption of the PRM structure was due to the high densification strain [Figure 5.9(b)] and a slight post-yield hardening effect observed after a nominal strain of around 0.2 [Figure 5.7(b)]. The densification strain of the PRM structure was found to be the highest among all the four lattice structures, including the pure 3D-reentrant lattice. The peak stress and energy absorption ability of the PRM structure were 21.3% and 81.3% higher than those of the pure 3D-reentrant lattice [Figure 5.9(c)]. The ratio of energy absorption to peak stress for the PRM structure is 0.28 compared to 0.24 for both the CFRM and the DFRM structures and 0.20 for the pure 3D-reentrant lattice. Thus, the PRM structure was found to be the better suited for high-energy absorbing applications.

5.3.3 Poisson's ratio

This study aims to improve the strength and energy absorption ability of 3D-reentrant lattice while maintaining its negative Poisson's ratio characteristic. Figure 5.10 shows a plot between Poisson's ratios vs. strain for the different lattice structures obtained from numerical simulations. The BCTZ lattice exhibited a Poisson's ratio of 0.28. Among all the structures, the 3D-reentrant lattice structure has the highest negative value of Poisson's ratio, showing a higher auxetic effect than the three multilattice structures. The auxetic behaviour of the 3D-reentrant lattice is due to the inward movement of the reentrant struts and the bending of the vertical struts during compression. The Poisson's ratio was calculated during the elastic deformation until the onset of the first buckling of vertical struts, after which the deformation of the lattice structures became localised, and the Poisson's ratio calculation became invalid.

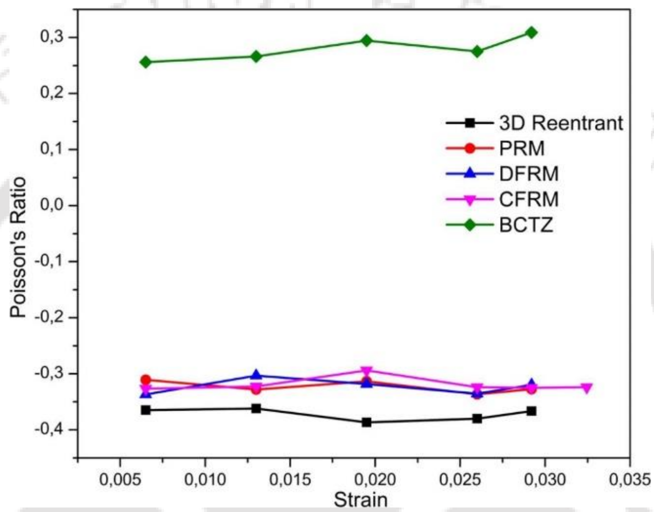

Figure 5.10. Poisson's ratio vs. strain plots of different lattice structures obtained from numerical simulations.

The multilattice composite structures showed auxetic behaviour, but the degree of auxeticity was less than that of the pure 3D-reentrant lattice structure. The weakening of the auxetic effect of the multilattice composite structures compared to the pure 3D-reentrant lattice structure was due to the presence of the BCTZ unit cells that reduced the lateral contraction of the multilattice composite structures during compression. Table 5.4 shows the comparison of the values of Poisson's ratios of the 3D-reentrant lattice structure and the three multilattice composite structures obtained from the experiments with those of the numerical simulations. The experimental values of Poisson's ratio were calculated as the average ratio of the lateral strain to the longitudinal strain at equal intervals during the elastic deformation taken from three repeated experiments. The Poisson's ratio values obtained from experiments and numerical simulations are found to be in good agreement.

Table 5.4. Poisson's ratio of the different lattice structures.

	3D-reentrant	PRM	DFRM	CFRM
Numerical simulation	−0.39	−0.32	−0.32	−0.32
Experiment	−0.37	−0.32	−0.32	−0.32

5.4 Prediction of elastic modulus and Poisson's ratio using composite rule of mixture

The volume fraction of the reinforcements significantly influences the deformation behaviour and the mechanical properties of the multilattice composite structures. To understand the effect of reinforcements on the mechanical properties, the PRM and the CFRM structures with a 25% volume fraction of BCTZ lattice as reinforcements were fabricated in addition to the previously mentioned multilattice composite structures with a 10% volume fraction of reinforcements. This study finds a quantitative approximation of the elastic modulus and Poisson's ratio of the multilattice composite structures from the Young moduli and Poisson's ratios of the constituent lattices. Xiao et al. used the rule of mixture used for composite materials to predict the elastic modulus of a multi-cell hybrid lattice consisting of BCC and octet lattice structures [31]. The rule of mixture for composite material predicts the elastic modulus of the composite material bounded by the upper and the lower limit. The upper bound and the lower bound of elastic moduli of the composite are expressed as [136]:

$$E_c(u) = V_m E_m + V_r E_r \tag{5.8}$$

$$E_c(l) = \frac{E_m\, E_r}{V_m E_r + V_r E_m} \tag{5.9}$$

where, $E_c(u)$ and $E_c(l)$ are the upper bound and the lower bound of elastic moduli of the composite material, V_m and V_r are the volume fractions of the matrix and the reinforcements, respectively, and E_m and E_r are the elastic moduli of the matrix and reinforcements, respectively. In this study, the multilattice structures were designed by mimicking fibre reinforced and particle reinforced composite materials. Hence, it is explored whether the rule of mixture used for composite materials can be employed to predict the elastic modulus of multilattice structure. Figure 5.11(a) shows that the elastic moduli of the multilattice composite structures fall within the upper bound, and the lower bound curves of elastic moduli plotted using the rule of mixture used for composite materials (Equations 5.8 and 5.9). Thus, the rule of mixture for composite materials can be employed to predict the elastic modulus of a multilattice composite structure. The CFRM composite structure has a higher elastic modulus value than the other types of multilattice composite structures for both 10% and 25% volume fractions of BCTZ lattice reinforcements. The elastic modulus of the CFRM and the PRM structures with 25% BCTZ lattice reinforcements are 51.2 MPa and 46.2 MPa, respectively. Since BCTZ lattice reinforcements are present in the form of long continuous fibres in the CFRM structure extending throughout the length of the entire structure in the loading direction, the strain experienced by the fibre-like BCTZ lattice reinforcements and the 3D-reentrant lattice matrix are the same. Hence, like uniaxial continuous fibre reinforced composite materials, the elastic moduli of the CFRM structures match with the upper bound curve of the rule of mixture following the isostrain condition [136]. The other two multilattice structures, PRM and DFRM, do not follow isostrain conditions due to the discontinuity of reinforcements in the loading direction, and hence their elastic moduli lie within the upper bound and the lower bound limits.

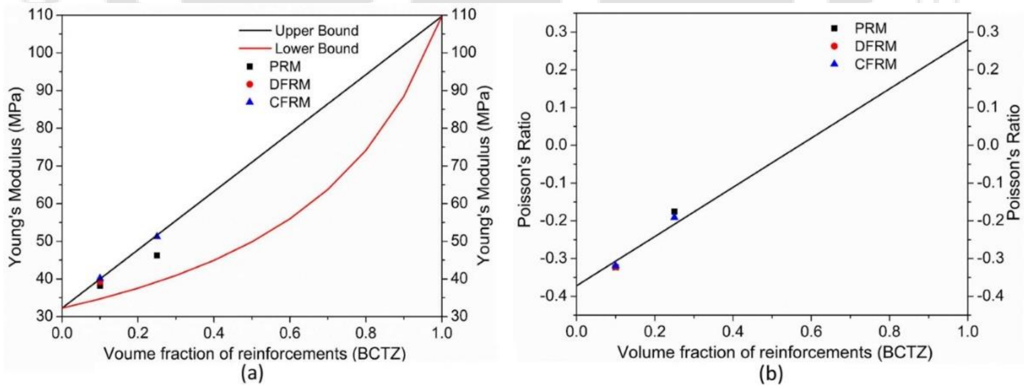

Figure 5.11. Rule of mixture for composite materials used to predict (a) elastic moduli and (b) Poisson's ratios of multilattice structures.

These auxetic lattice structures are composite structures consisting of BCTZ lattice reinforcements having a positive Poisson's ratio in a matrix of 3D-reentrant lattice having a negative Poisson's ratio. This study found that the Poisson's ratio of a multilattice composite structure can also be predicted by the composite rule of mixture, similar to the prediction of elastic modulus of the structure. The Poisson's ratio υ_c of composite material is expressed as

$$\upsilon_c = \upsilon_m V_m + \upsilon_f V_f \quad 5.10$$

where, υ_m and υ_f are the volume fractions of matrix and reinforcements of the composite materials, respectively. Since the BCTZ lattice has a positive Poisson's ratio and the 3D-reentrant lattice has a negative Poisson's ratio, the increase in volume fraction of BCTZ lattice reinforcements decreases the auxetic effect of the multilattice composite structure as discussed in Section 5.3.3. The Poisson's ratios of the multilattice composite structures for different volume fractions of reinforcements are in good agreement with the predictions made by the rule of mixture used for composite materials, as shown in Figure 5.11(b). The values of Poisson's ratio for the PRM and the CFRM structures with a 25% volume fraction of BCTZ lattice reinforcements were found to be −0.17 and −0.19, respectively. The Poisson's ratio values for the three different multilattice composites with a 10% volume fraction of BCTZ lattice reinforcements were already mentioned in Table 5.4. To the authors' knowledge, no previous literature has reported the prediction of Poisson's ratio for lattice structures using the rule of mixture. This study demonstrates that replacing a pure auxetic lattice with a multilattice composite structure can be used as a technique to tailor the Poison's ratio of the metamaterial for a specific application.

5.5 Effects of increase in volume fraction of reinforcements

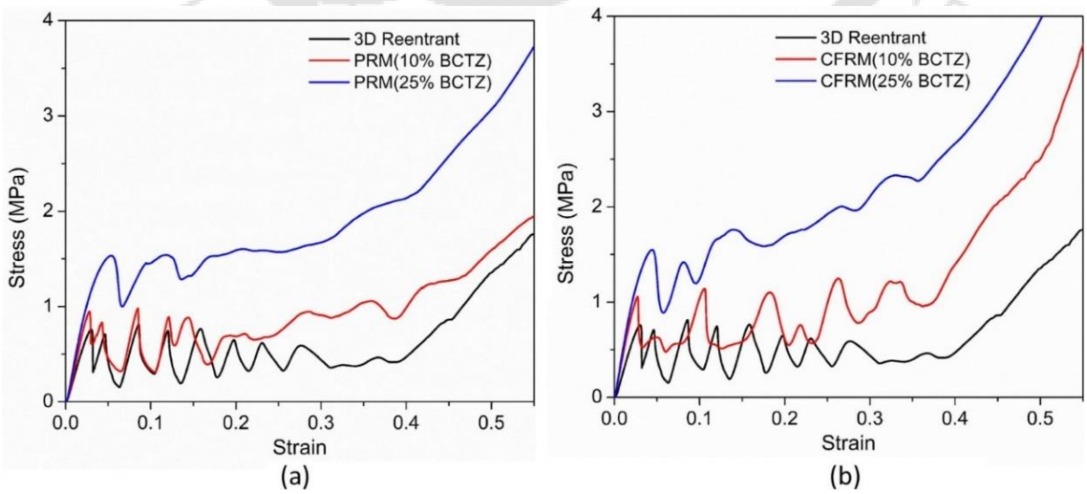

Figure 5.12. Experimental compressive stress-strain plots of (a) PRM structures and (b) CFRM structures with different volume fractions of BCTZ lattice reinforcements compared with the pure 3D-reentrant lattice structure.

The results discussed in Section 5.3 contain mechanical properties of multilattice composite structures with only a 10% volume fraction of BCTZ lattice reinforcements. The effects of the increase in volume fraction of the reinforcements on the stress-strain response of the multilattice composites are discussed in this section. Figure 5.12 shows the compressive stress-strain plots of the PRM and the CFRM composite structures with 10% and 25% volume fractions of BCTZ lattice reinforcements compared with the pure 3D-reentrant lattice structure. It can be interpreted that the stress-strain behaviour of the PRM and the CFRM structures with 10% reinforcements is dominated by the deformation behaviour of the matrix made of 3D-reentrant lattice. The stress-strain plots show fluctuation in the stress values due to layerwise buckling of the vertical struts of the multilattice structure, as discussed in Section 5.2. As the volume fraction of reinforcements increased from 10% to 25% in both the PRM and the CFRM structures, the number of peaks observed in the stress-strain plot decreased. The PRM and the CFRM structures with 25% reinforcements exhibited higher strain hardening compared to the PRM and the CFRM structures with 10% reinforcements. The CFRM structure with 25% reinforcements exhibited significant strain hardening after a nominal strain of around 0.18 as opposed to the PRM structure with 25% reinforcements before densification. The post-yield strain hardening behaviour, which occurs due to the high volume fraction of high strength BCTZ reinforcements, was consistent with the results obtained by Pham et al. [105]. In case of multi-phase materials, the hard phase provides the load bearing capability due to its high strength and the low strength matrix undergoes plastic deformation. The presence of hard phase restricts the deformation of the structure and leads to post-yield hardening [31]. Since the reinforcements in the CFRM structure are present as long fibres throughout the entire length along the loading direction, the reinforcements restricted the deformation of the 3D-reentrant matrix significantly, and thus, the CFRM structure exhibited higher post-yield hardening compared to the PRM structure. However, the difference in post-yield hardening of the two multilattice structures with low volume fraction, i.e. 10%, of reinforcement was not significant. The densification strain calculated using energy efficiency vs. strain plots using Equation 5.6 and 5.7 showed that the PRM structure with 25% reinforcements exhibited higher densification strain of 0.4 compared to 0.37 of the CFRM structure with 25% reinforcements. The energy absorption ability calculated from the experimental results of the PRM structure was 0.57 J/cm^3 compared to 0.56 J/cm^3 of the CFRM structure. The energy absorbed until densification by the two multilattice structures were nearly equal as the CFRM structure exhibited higher post-yield hardening but lower densification strain and the PRM structure exhibited lower post-yield hardening but higher densification strain. The densification strain and the energy absorption of the multilattice structures with 10% reinforcements have already been shown in Figure 5.9(b). Interestingly, the densification strains for both the PRM and the CFRM structures did not vary much with an increase in volume fraction of reinforcements from 10% to 25%. However, the energy absorption abilities of the two multilattice structures with 25% reinforcements increased to approximately two times the values obtained for the respective multilattice structures with 10% reinforcements. Although both of these multilattice composite structures with 25% volume fractions were able to absorb almost the same amount of energy, the CFRM structure showed a significant increase in stress level due to high post yield hardening, which is not desirable for high energy absorbing applications. Among the multilattice composite structures with 10% reinforcements, the PRM structure was found to be the best suited for high energy absorbing applications, as discussed in Section 5.3.2. For such applications, even with 25% reinforcements, the PRM structure can perform better than the CFRM structure as the stress level attained by the CFRM structure is increased due to the high strain hardening effect.

5.6 Summary

In this chapter, novel dual-phase lattice structures, named as ‘multilattice’ structures, were designed and fabricated by mimicking particle and fiber reinforced composite materials. The 3D-reentrant auxetic lattice, that exhibits negative Poisson’s ratio, was used as the matrix and body centered-tetragonal lattice with vertical struts (BCTZ), having high stiffness and high strength, was used as reinforcements. The mechanical response and deformation mechanics of the multilattice structures were investigated by numerical simulations and quasi-static compression tests. Due to the presence of BCTZ reinforcements, the multilattice structures exhibited superior strength and stiffness than the parent 3D-reentrant lattice without compromising the negative Poisson’s ratio behaviour. Moreover, the influence of volume fraction and type of the reinforcements on the mechanical properties of the multilattice structures were also studied. The multilattice structures exhibited higher densification strain and post yield hardening that led to higher energy absorption than the parent auxetic lattice. Elastic moduli and Poisson’s ratios of the multilattice structures were in good agreement with the predictions obtained from the conventional rule of mixture used for composite materials. This study suggested that the strength, stiffness, energy absorption and Poisson's ratio of multilattice structures can be tailored as per the requirement of load bearing applications and energy absorbing applications. The continuous fiber-reinforced multilattice (CFRM) can be useful for high strength structures while the particle-reinforced multilattice (PRM) is more appropriate for high energy-absorbing structures.

CHAPTER 6. A NOVEL STRATEGY TO DESIGN LATTICE STRUCTURES WITH ZERO POISSON'S RATIO

This chapter demonstrates that the composite-rule of mixture can be employed to design zero Poisson's ratio (ZPR) lattice structures with enhanced mechanical performance. This novel strategy can be useful to tailor the mechanical properties of the ZPR lattice structures. Section 6.1 presents the design and fabrication of the proposed composite-inspired ZPR lattices. The mode of deformation and stress-strain response of the proposed structures are discussed in Section 6.2. The zero Poisson's ratio behaviour of the proposed structures are demonstrated in details in Section 6.3. Section 6.4 investigates the mechanical properties of the ZPR lattices obtained from finite element simulations and experiments. Finally, mechanical properties of the proposed ZPR structures are compared with the commonly studied hexagonal honeycomb-based ZPR lattices in Section 6.5.

6.1 Design and Fabrication of ZPR multilattice structures

6.1.1 Proposed ZPR lattice structures

The composite-materials inspired ZPR structures are a combination of two different types of lattices with different mechanical properties. The first type of lattice used was the 3D-reentrant lattice with geometric parameters- vertical strut length (h), reentrant strut length (l) and reentrant angle (θ) shown in Figure 6.1(a). The second type of lattice is the body-centered tetragonal with vertical struts along z-direction (BCTZ) shown in Figure 6.1(b). The BCTZ lattice exhibits a higher modulus than the commonly studied body-centered cubic (BCC) lattice because of the inclusion of the vertical struts and the increase in the aspect ratio [137]. The isometric view of the 3D-reentrant and the BCTZ unit cells are shown in Figure 6.1(c) and (d). The lattice structures, i.e. the 3D-reentrant and BCTZ, used in this chapter are same as those used in Chapter 5, although a change in the size of the unit cells are considered in this chapter.

The key strategy in designing the composite lattice was to combine the 3D-reentrant and the BCTZ lattices such that the overall structure would exhibit zero Poisson's ratio with improved mechanical properties. For designing the composite-material inspired structure, the 3D-reentrant and the BCTZ unit cells were made to have the same size. The 3D-reentrant unit cell was first modeled, and then a compatible BCTZ unit cell was developed. Hence, the unit cell shape of the reinforcement lattice was made slightly longer than the conventional body-centered cubic unit cell. The values of θ, h and l were considered such that the 3D-reentrant unit cell had nearly equal dimensions along all the three mutually orthogonal directions- x, y and z.

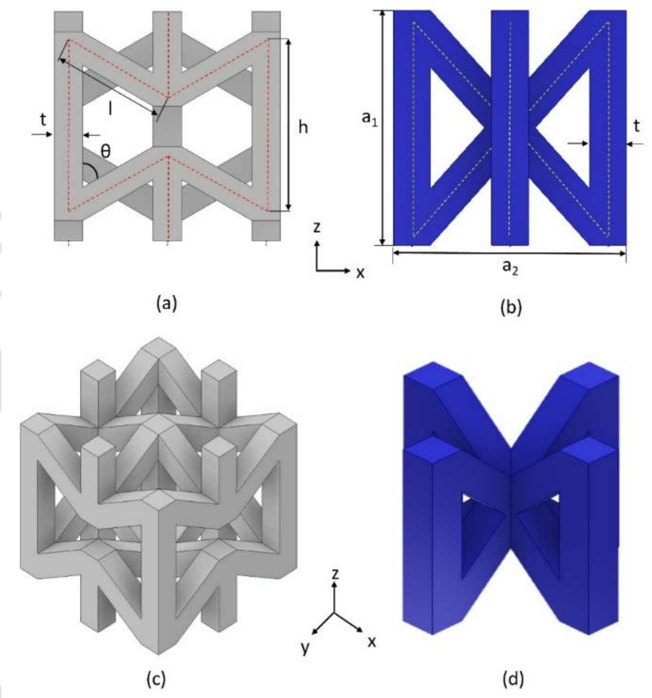

Figure 6.1. 2D view of unit cells with unit cell parameters of (a) 3D-reentrant and (b) BCTZ lattices, and 3D view of unit cells of (c) 3D-reentrant and (d) BCTZ lattices.

Both 3D-reentrant and BCTZ lattices were designed to have the same size, the same number of unit cells and the same relative density, and numerical simulations of quasi-static compression behaviour of these lattices were performed using Abaqus/Explicit to calculate their Poisson's ratios. The Poisson's ratios were calculated in the elastic range until the localized buckling was observed. The BCTZ and the 3D-reentrant lattices exhibited Poisson's ratios of 0.32 and −0.24, respectively.

For designing the composite ZPR structures, having BCTZ and 3D-reentrant lattices in the form of reinforcement and matrix, respectively, composite rule of mixture was used to predict the volume fraction of reinforcements required for achieving zero Poisson's ratio. The rule of mixture for the Poisson's ratio of the composite structure (ν_c) is given by [136]:

$$\nu_c = \nu_m V_m + \nu_r V_r \qquad 6.1$$

where, ν_m and ν_r are the Poisson's ratio of the matrix and the reinforcements, respectively, and V_m, V_r are the volume fractions of the matrix and the reinforcements, respectively. When the reinforcements in the form of BCTZ lattices has a volume fraction of 42.8%, the Poisson's ratio of the composite lattice structure becomes zero, which is presented graphically in Figure 6.2.

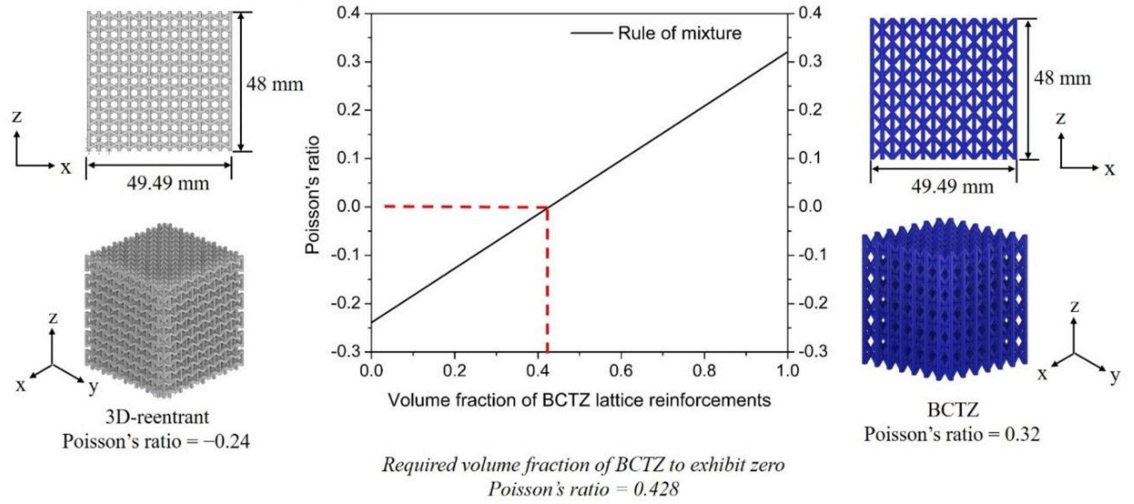

Figure 6.2. Evaluation of the BCTZ reinforcement volume fraction required to attain zero Poisson's ratio of the composite lattice using the composite rule of mixture.

Two composite-inspired lattice structures were designed having a reinforcement volume fraction of 42.8%, namely fiber-reinforced ZPR (F-ZPR) lattice structure and particle reinforced ZPR (P-ZPR) lattice structure, mimicking the fiber-reinforced and the particle-reinforced composite materials. Figure 6.3 illustrates two adjacent 3D-reentrant and BCTZ unit cells along with their junction. The unit cell parameters of the composite-materials inspired ZPR structures are listed in Table 6.1. Figure 6.4(a) and (b) show the F-ZPR and P-ZPR composite structures, respectively. Figure 6.4(c) shows the distribution of the BCTZ and the 3D-reentrant unit cells in different layers of the P-ZPR and F-ZPR lattice structures. The seven layers shown in Figure 6.4(c) were stacked along the y-direction to generate the 3D composite-inspired lattice structure. The composite lattice structures had the same relative density, the same overall structure size and the same number of unit cells as the original 3D-reentrant and the original BCTZ lattice structures. In the P-ZPR lattice structure, the BCTZ unit cells were symmetrically distributed as particle-like reinforcements in the 3D-reentrant lattice. Similarly, for the F-ZPR lattice structure, the

BCTZ unit cells were laid symmetrically as fiber-like reinforcements extended along the direction of loading throughout the entire length of the lattice.

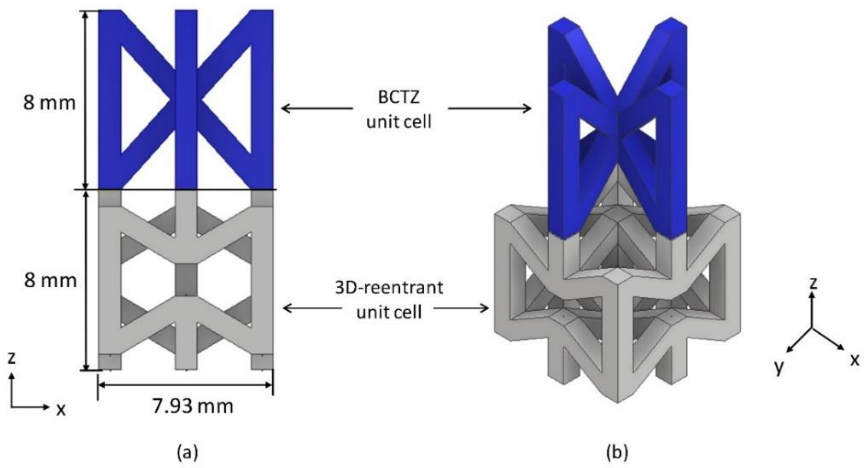

Figure 6.3. Two adjacent unit cells of 3D-reentrant and BCTZ lattices shown as (a) front view and (b) isometric view.

Table 6.1. Parameters of composite-inspired ZPR lattice structures.

Unit cell						**Relative density (%)**	**Size of the lattice (mm^3)**	**No of unit cells (x × y × z)**
H (mm)	L (mm)	t (mm)	Θ	a_1 (mm)	a_2 (mm)			
6	4	1	60°	8	7.92	19.8	49.49 × 49.49 × 48	7 × 7 × 6

Table 6.2. Relative densities and masses of samples fabricated by HP Multi Jet Fusion technique.

Sample	**Designed relative density (%)**	**Measured relative density (%)**	**Mass (g)**
3D-reentrant	19.70 ± 0.15	18.14 ± 0.13	20.33 ± 0.49
BCTZ			21.04 ± 0.19
P-ZPR			21.40 ± 0.07
F-ZPR			20.93 ± 0.31
SRE			20.20 ± 0.24

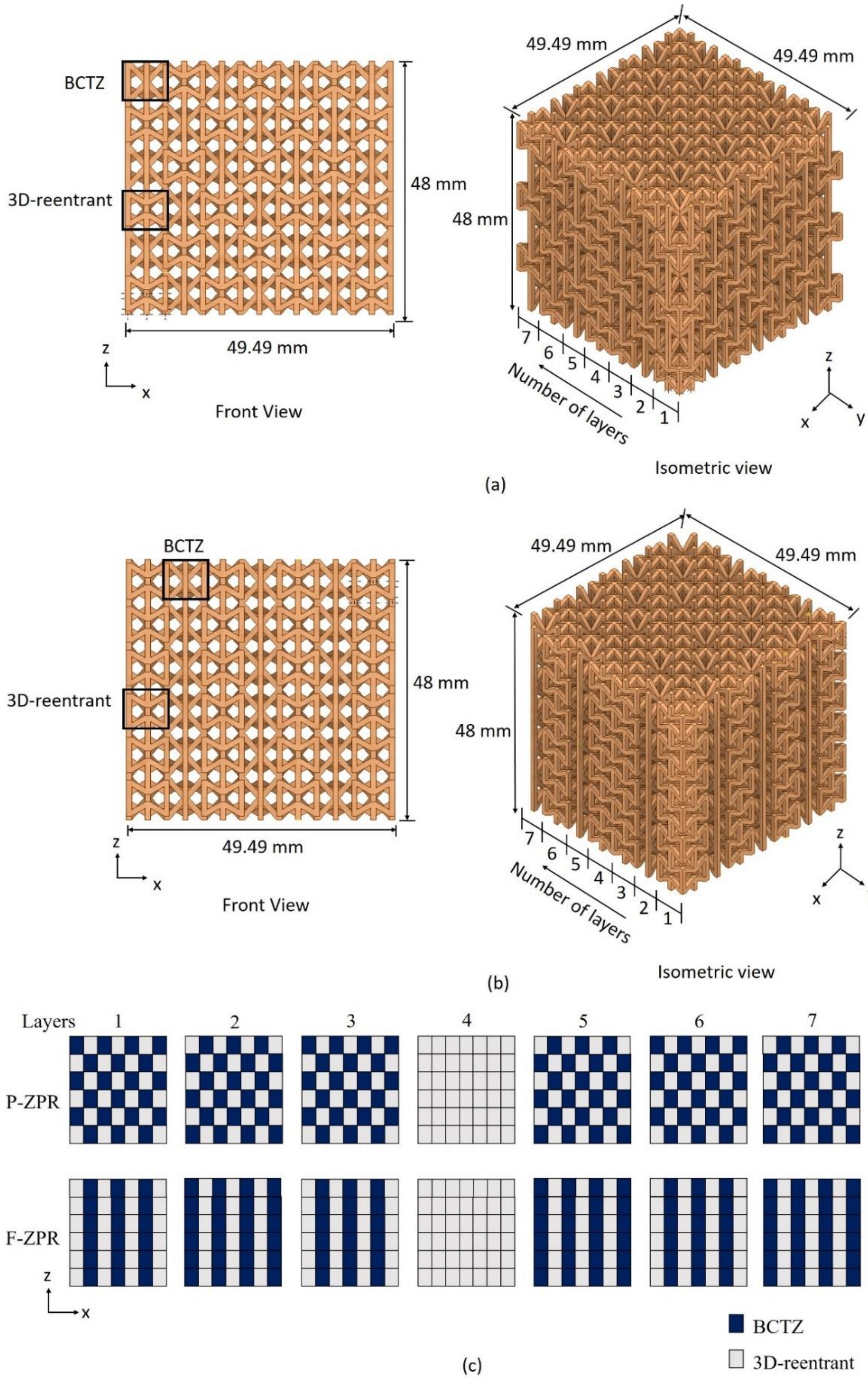

Figure 6.4. Front view and isometric view of (a) P-ZPR composite lattice structure and (b) F-ZPR composite lattice structure, and (c) layerwise arrangements of the BCTZ and the 3D-reentrant unit cells in the P-ZPR and the F-ZPR lattices on the x-z plane.

HP Multi Jet Fusion technique was used to fabricate all the lattice structures with polyamide 12 (PA12) as printing material. Two samples were printed for each design. ASTM D638 tensile specimens were fabricated in the same batch as the lattice structures to determine the material parameters of the parent material for using in the numerical simulations. The obtained materials properties of the parent materials are discussed in Section 3.3.2. The relative densities, as well as the masses of the fabricated lattices, are mentioned in Table 6.2.

6.1.2 Previously-studied ZPR lattice structures

The mechanical properties of the proposed ZPR composite lattices designed in this work were compared with the already existing ZPR lattice designs [24–26,77,79,93,138]. Researchers have investigated several lattice unit cells that exhibit zero Poisson's ratio, as mentioned in Section 2.5. However, all these lattice structures have one type of unit cell throughout the entire lattice. In addition, most of the previously-studied lattice structures have two-dimensional lattice configurations. In this work, only those existing lattices that are derivative of hexagonal honeycomb, like the reentrant lattice, and have three-dimensional lattice geometry were chosen to compare with the proposed ZPR composite lattice structures. The three 3D-ZPR lattice structures chosen for the comparison are the semi reentrant (SRE), the reverse semi reentrant (RSRE) and the Auxhex structures. The three ZPR unit cells can be made to have the same unit cell parameters (h, l and θ) as the 3D-reentrant unit cell used as the matrix in the P-ZPR and the F-ZPR lattices. The strut thicknesses of the previously-studied ZPR lattices were varied to maintain the same relative density as the proposed P-ZPR and F-ZPR structures. The unit cells and the lattice structure of SRE, RSRE and AuxHex are shown in Figure 6.5. The SRE lattice was fabricated along with the P-ZPR, F-ZPR, 3D-reentrant and BCTZ lattices, and a mechanical test was performed to corroborate the numerical simulation results. The mechanical properties of RSRE and AuxHex lattices were studied using only numerical simulations.

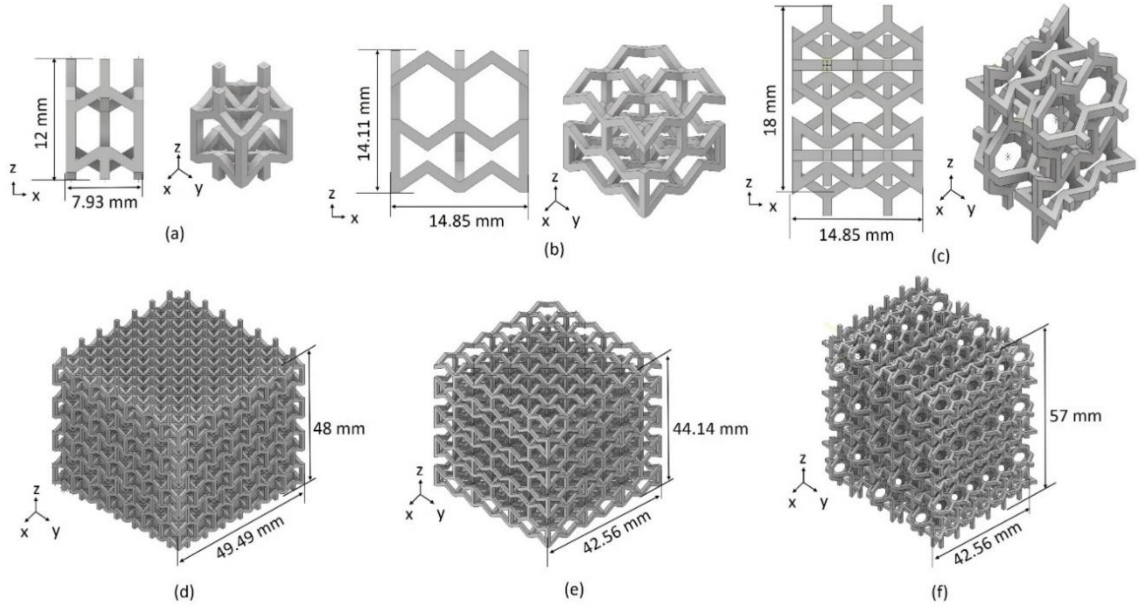

Figure 6.5. Unit cells of 3D ZPR structures: (a) semi reentrant (b) reverse semi reentrant (c) Auxhex lattices and (d), (e), (f) the lattice structures corresponding to the unit cells shown in (a), (b), (c), respectively.

6.2 Stress-strain response and mode of deformation

6.2.1 Parent lattices

The compressive mechanical behaviour of the parent lattice structures was investigated by studying their deformation behaviour and stress-strain response. Figure 6.6 show the mode of deformation of the 3D-reentrant parent lattice as well as the BCTZ parent lattice structures, respectively, obtained from the compression tests. Figure 6.7(a) shows the compressive stress-strain response derived from numerical and experimental investigations for the 3D-reentrant structure. As the compression occurred, the 3D-reentrant structure first deformed elastically, and maximum compressive stress with a value 0.91 MPa was attained at a strain of 0.052 for sample 1. After the peak compressive stress, localized buckling of the topmost layer occurred, and a sudden drop in the stress was observed in the compressive stress-strain plot [Figure 6.7(a)]. After that, the unbuckled layers started to bear the load, and the stress increased again with the increase in strain. Thereafter, the stress reached a maximum value, and then the stress dropped again due to the buckling of the second layer from the top. Thus, with each localized buckling of different layers one after the other (Figure 6.6), the stress-strain curve was oscillating, and the number of oscillations obtained in the compressive stress-strain curve corresponds to the number of layers buckled. Finally, at a strain of 0.384, the whole structure densified, and the compressive stress monotonically increased with an increase in strain. The deformation pattern and the stress-strain plot of the BCTZ structure are shown in Figure 6.6. The peak compressive stress attained for sample 1 was 4.17 MPa. After the peak compressive stress, the buckling of the vertical struts, i.e. the struts along the z-direction, occurred throughout the structure, due to which a stress-drop was observed at a strain of 0.084 in Figure 6.7(b). At a strain of 0.2, the BCTZ structure deformed severely in the bottom portion of the specimen (Figure 6.6). The densification of the BCTZ lattice structure occurred at a strain of 0.67.

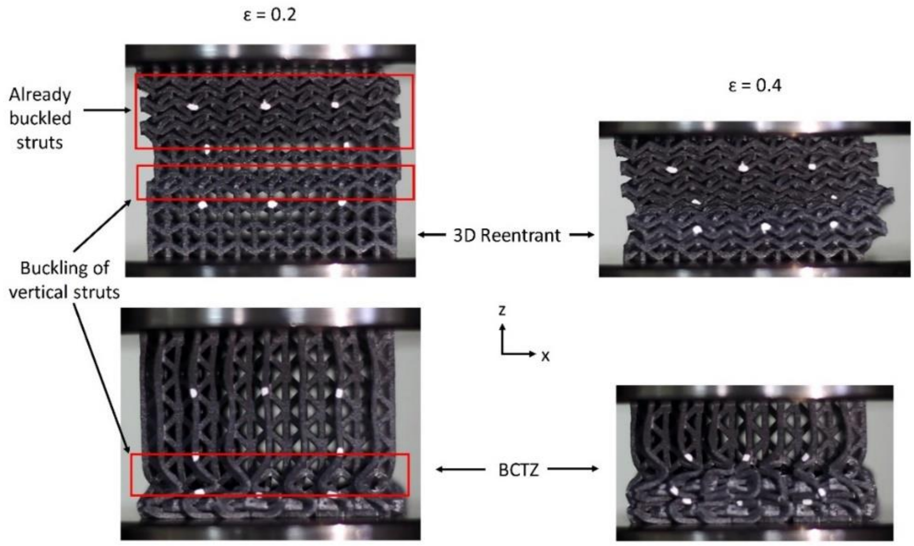

Figure 6.6. Deformation behaviour of the 3D-reentrant, and the BCTZ parent lattices during the compression test.

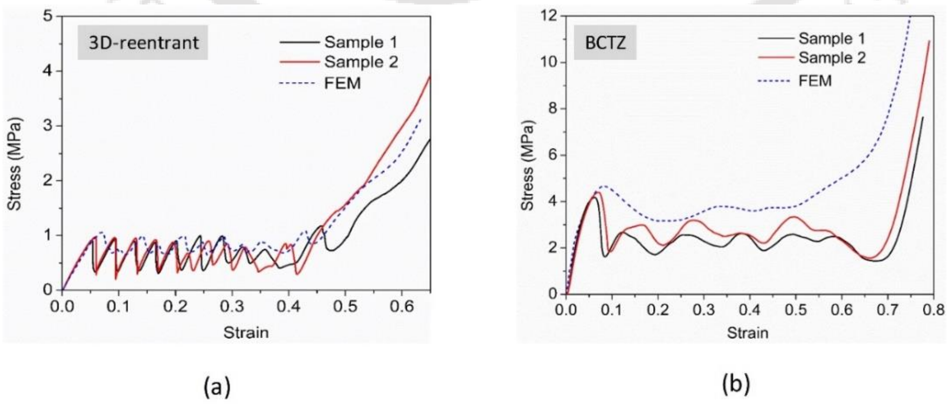

Figure 6.7. Engineering stress-strain curves obtained from numerical simulations and mechanical compression tests for (a) the 3D-reentrant and (b) the BCTZ parent lattice structures.

6.2.2 ZPR composite lattices

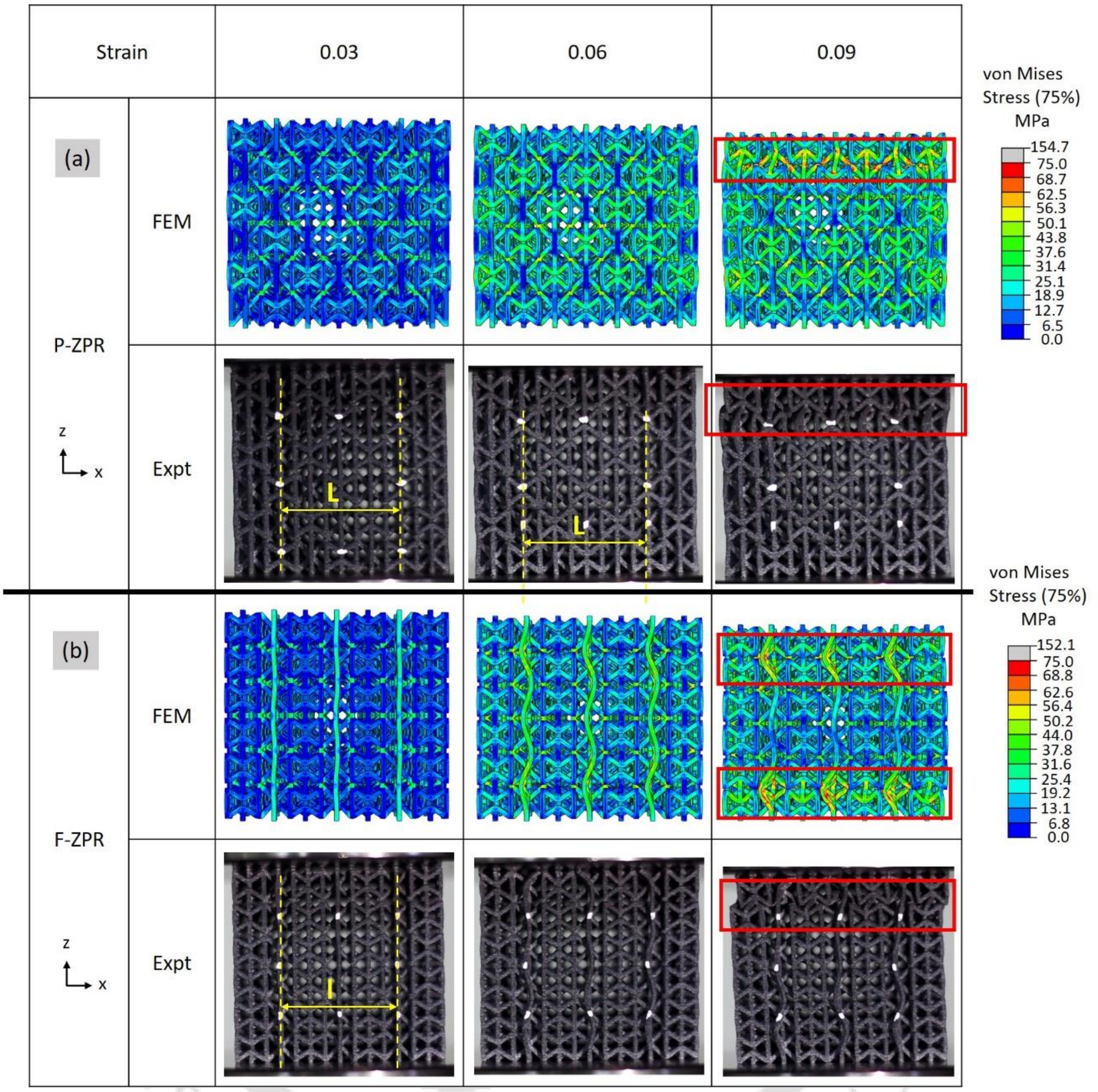

Figure 6.8. Deformation behaviour observed in numerical simulations and experiments at different strains for (a) the P-ZPR structure and (b) the F-ZPR structure.

The deformation behaviour observed in numerical simulations and experimental investigations for the P-ZPR and the F-ZPR structures until the strain of 0.09 are shown in Figure 6.8(a) and (b), respectively. Figure 6.9(a) and (b) shows the numerical and experimental stress-strain response of the ZPR structures. Both ZPR structures exhibited linear behaviour during the initial part of deformation, as shown in Figure 6.9(a) and (b). With the increase in compressive strain, the P-ZPR structure attained a peak value of stress of 1.67 MPa at a strain of 0.061 in mechanical test and 1.98MPa at a nominal strain of 0.078 in numerical simulation [Figure 6.9(a)]. After the peak stress is reached, the localized buckling of the struts that are parallel to the z-direction in the P-ZPR structure occurred, which is highlighted at a strain of 0.09 for both numerical and experimental results in Figure 6.8(a). The BCTZ unit cells were uniformly distributed in the 3D-reentrant lattice matrix; as a result, a uniform von Mises stress distribution was observed at a nominal strain of 0.06 in the entire P-ZPR structure [Figure 6.8(a)]. The vertical struts of the BCTZ unit cells were subjected to low stresses initially, while the vertical struts of 3D-reentrant lattices started bending as observed at a strain of 0.06 for the P-ZPR structure in Figure 6.8(a). As the compression progressed, the inclined struts of the top and the bottom halves of 3D-reentrant unit cells started to come in contact with each other, and then severe localized deformation was observed in the P-ZPR structure, which is highlighted at a strain of 0.09 in Figure 6.8(a).

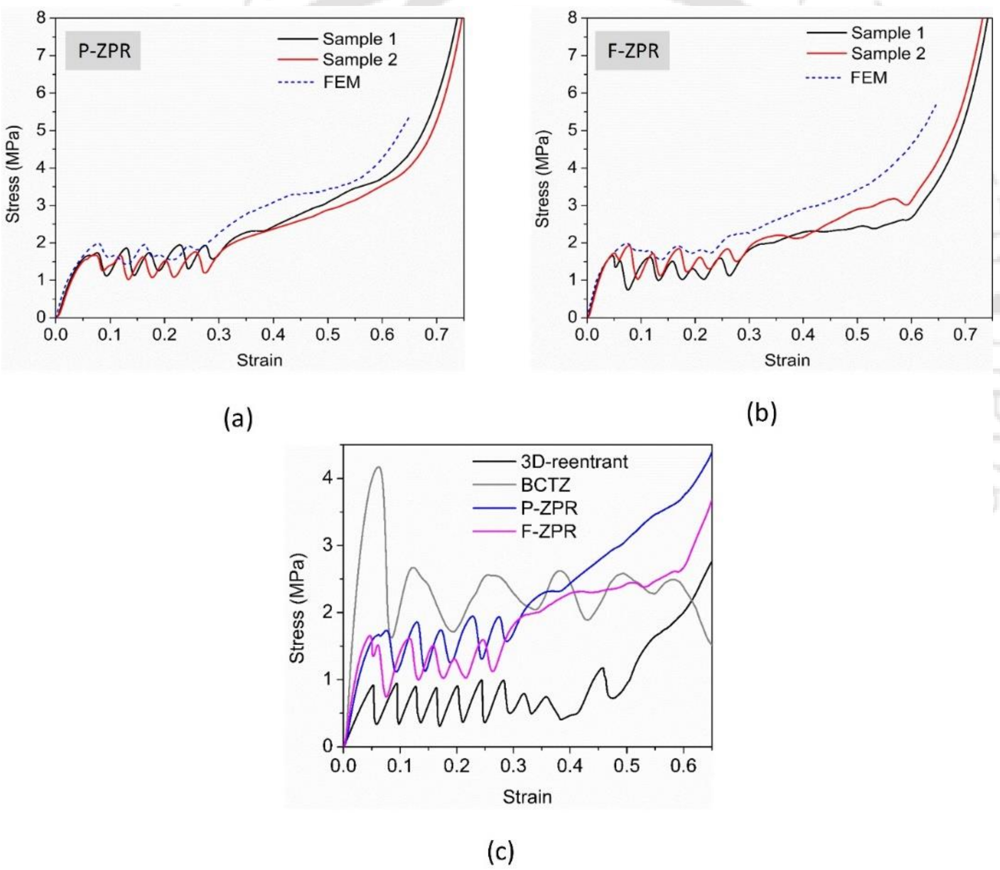

Figure 6.9. Engineering stress-stress plots obtained from numerical simulations and experiments for (a) P-ZPR structure and (b) F-ZPR structure and (c) comparison of stress-strain curves obtained from sample 1 of 3D-reentrant, BCTZ, P-ZPR and F-ZPR lattice structures.

In contrast, in the F-ZPR structure, the BCTZ structures were laid as long fiber-like substructures throughout the sample along the loading direction. Early buckling of the struts parallel to the z-direction in the BCTZ unit cells of the F-ZPR structure can be seen at a strain of 0.06 in Figure 6.8(b). As the deformation progressed, the localized plastic buckling occurred at a particular horizontal layer of unit cells [seen at strain 0.09 in Figure 6.8(b)], and eventually, the entire F-ZPR structure collapsed layer by layer. Figure 6.9(c) shows the comparison of stress-strain curves obtained from sample 1 of 3D-reentrant, BCTZ, P-ZPR and F-ZPR lattice structures.

To understand the difference between the deformation mechanisms of the parent and the composite lattices, a few unit cells of the deformed structures obtained from finite element simulations are presented at two different nominal strains of 0.06 and 0.09 in Figure 6.10. For the 3D-reentrant lattice, the vertical struts were subjected to axial compression, and the oblique struts were subjected to a combined effect of bending and stretching. No visible bulging of the 3D-reentrant unit cells occurred at a strain of 0.06 [Figure 6.10(a)], and the layerwise collapse of the lattice was observed from a strain of 0.09 [Figure 6.10(b)]. The joints act as plastic hinge for the localized buckling of the vertical struts. The buckling of vertical struts of the BCTZ lattice was visible at a strain of 0.06, and as the compression progressed, the buckling became more severe at a strain of 0.09 [Figure 6.10(c) and (d)]. In contrast to the parent 3D-reentrant lattice, the 3D-reentrant unit cells of the P-ZPR and the F-ZPR composite lattices experienced bulging due to extensive bending of the vertical struts [Figure 6.10(e) and (g)]. The bulging in the 3D-reentrant unit cells of the F-ZPR structure was less severe than that of the P-ZPR structure due to significant buckling of the vertical struts of the fiber-like BCTZ reinforcements in the F-ZPR structure [Figure 6.10(e) and (g)]. For the P-ZPR structure, the localized buckling of the vertical struts at the junction of the 3D-reentrant and the BCTZ unit cells occurred at large strain [Figure 6.10(f)], and subsequently, the entire layer collapsed. For the F-ZPR structure, along with the buckling of the vertical struts of the BCTZ unit cells, the vertical struts at the junction of two consecutive 3D-reentrant unit cells also buckled, which led to the collapse of the entire layer [Figure 6.10(h)].

After the first peak compressive stress was attained, similar to the deformation of the parent 3D-reentrant structure, the P-ZPR and the F-ZPR structures were deformed by the layerwise localized collapse of the struts that are parallel to z-direction (Figure 6.8). However, the number of stress-drops, each of which was associated with the collapse of a single layer of unit cells, of both the ZPR structures was reduced compared to the parent 3D-reentrant auxetic structure. It was because, after a nominal strain of ~0.3, the P-ZPR and F-ZPR lattice structures exhibited significant strain hardening behaviour due to the BCTZ lattices as reinforcements [Figure 6.9(c)]. The deformation behaviour changed from layerwise collapse to a more uniform collapse at a large strain. The compressive strength, elastic modulus and energy absorbed during the deformation of the composite-materials inspired ZPR lattice structures, which were obtained from the stress-strain plots, are reported in Section 6.4.

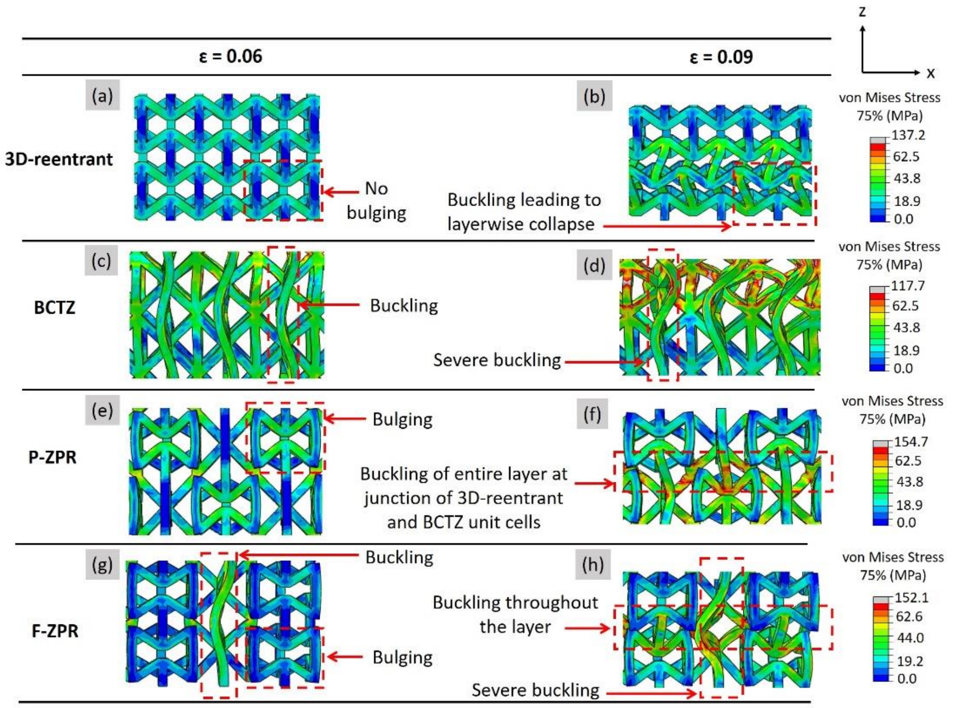

Figure 6.10. Deformation mechanisms of 3D-reentrant lattice at (a) 6% strain and (b) 9% strain, BCTZ lattice at (c) 6% strain and (d) 9% strain, P-ZPR composite lattice at (e) 6% strain and (f) 9% strain, and F-ZPR lattice at (g) 6% strain and (h) 9% strain.

6.3 Zero Poisson’s ratio behaviour

Both the P-ZPR and the F-ZPR structures exhibited near-zero Poisson's ratio during the initial part of deformation as shown in Figure 6.11(a). During the compression of the 3D-reentrant unit cell, the inclined struts moved inward, and the vertical struts underwent bending to exhibit lateral contraction. However, because of the existence of the BCTZ lattice as reinforcements, which expand laterally when compressed, the negative Poisson’s ratio of the 3D-reentrant was neutralized, and the overall deformation of the composite lattice structure resulted in zero Poisson’s ratio. The P-ZPR structure exhibited near-zero Poisson's ratio up to a strain of 0.072 before the first localized buckling. In the F-ZPR structures, the Poisson’s ratio was calculated until the onset of the buckling of the struts parallel to the z-direction, i.e., up to a strain 0.033. Figure 6.11(b) shows the Poisson's ratio predicted by the composite rule of mixture of the parent lattices with those evaluated from numerical and experimental investigations of the proposed ZPR structures. The Poisson's ratios of the ZPR structures matched well with the composite rule of mixture. A detailed analysis of the ZPR behaviour of the composite-inspired structures is performed in the next sub-sections.

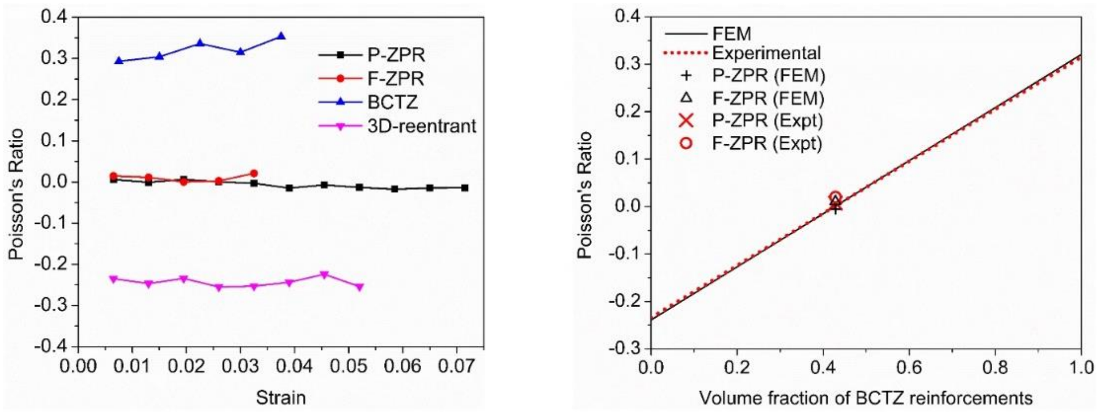

(a) (b)

Figure 6.11. (a) Poisson's ratios calculated from numerical investigations of different lattice structures, and (b) composite rule of mixture for Poisson's ratios obtained from numerical and experimental investigations.

6.3.1 F-ZPR lattice structure

The fiber reinforced ZPR structure consists of columns of BCTZ unit cells in the matrix of the 3D-reentrant unit cells as shown in Figure 6.12(a). Figure 6.12(b) shows the variation of Poisson's ratios of the individual unit cells of the 3D-reentrant and the BCTZ structure with strain. The average values of the Poisson's ratios of the individual unit cells were nearly same as that of the entire parent lattice structures [Figure 6.11(a)]. The average Poisson's ratios of BCTZ unit cell and BCTZ lattice are 0.325 and 0.32, respectively. Similarly, the average Poisson's ratios of 3D-reentrant unit cell and 3D-reentrant lattice are −0.22 and −0.24, respectively. In the F-ZPR structure, the lateral expansion of the column of BCTZ unit cells during compression was accommodated by the lateral contraction of the columns of 3D-reenetrant unit cell on either side (Figure 6.12(a)). The expansion and contraction of the constituent lattices led to zero Poisson's ratio of the overall composite lattice (Figure 6.11(a)).

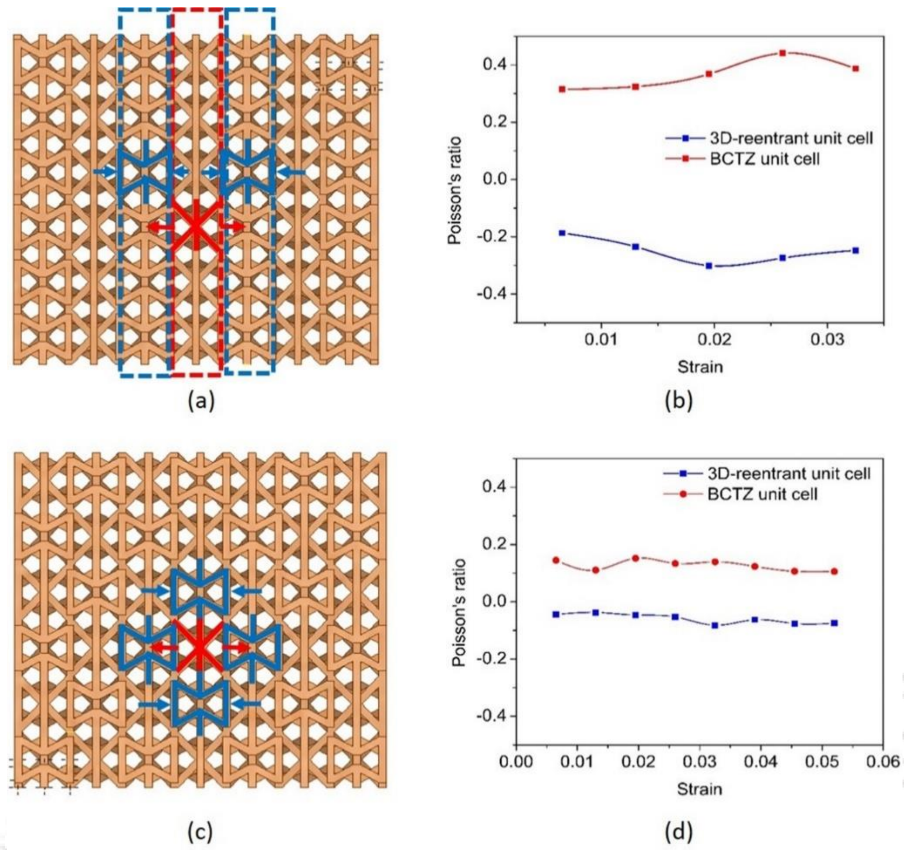

Figure 6.12. F-ZPR structure showing (a) contraction of columns of 3D-reentrant unit cells and expansion of a column of BCTZ unit cells, (b) variation of Poisson's ratios with strain for individual unit cells of 3D-reentrant and BCTZ; and P-ZPR structure showing (c) contraction of 3D-reentrant unit cell and expansion of BCTZ unit cell, (d) variation of Poisson's ratios with strain for individual unit cells of 3D-reentrant and BCTZ.

6.3.2 P-ZPR lattice structure

In the P-ZPR structure, the BCTZ unit cells are distributed as particles in the 3D-reentrant lattice structure. The lateral contraction of the 3D-reentrant unit cells at the top and bottom of the BCTZ unit cell constrained the lateral expansion of the BCTZ unit cell [Figure 6.12(c)], thereby reducing the Poisson's ratio of BCTZ unit cell to 0.11 [Figure 6.12(d)]. Similarly, the BCTZ unit cells at the top and bottom of the 3D-reentrant unit cell restricted the lateral contraction of the 3D-reentrant unit cell, which reduced the local auxetic effect of 3D-reentrant unit cell with a Poisson's ratio value of −0.08 [Figure 6.12(d)].

In contrast, the 3D-rentrant unit cells on either side in the same horizontal layer did not constrain the lateral expansion of the BCTZ unit cell and vice versa. In fact, the lateral contraction of the neighboring 3D-reentrat unit cells in the same horizontal layer accommodated the lateral expansion of the BCTZ unit cell. However, the zero value of

Poisson's ratio of the overall structure was ensured by maintaining an appropriate volume fraction of the BCTZ unit cells [Figure 6.11(a) and Figure 6.2].

6.4 Mechanical properties of the ZPR lattices

6.4.1 Compressive strength

The mechanical properties of the composite-materials inspired ZPR lattice structures were evaluated from the stress-strain plots presented in Section 6.2. The first peak value of stress evaluated from the compressive stress-strain curve is called as the compressive strength of the lattice in this study. The compressive strengths of the P-ZPR and the F-ZPR structures are mentioned in Table 6.3. The compressive strengths of the P-ZPR and the F-ZPR structures were in between the compressive strengths of the parent lattices. The average values of the compressive strength obtained from the experimental results of the 3D-reentrant lattice were 0.94 MPa and the BCTZ lattice was 4.28 MPa.

The compressive strength and the elastic modulus obtained from the numerical simulations are higher than the experimental results, as seen in Table 6.3. During the manufacturing of the lattice structures using the HP Multi Jet Fusion technique, some defects like porosities and strut waviness were generated [128,133]. These defects also resulted in a decrease in the relative densities of the fabricated samples than the actual relative densities of the designed samples, as mentioned in Table 6.2. The cumulative effects of these defects led to the decrease in the compressive strengths as well as elastic moduli of the fabricated lattice structures in experiments compared to the numerical simulations.

Table 6.3. Mechanical properties evaluated from numerical and experimental results of the proposed ZPR composite lattice structures.

Mechanical properties	**P-ZPR**		**F-ZPR**	
	FEM	**Experiment**	**FEM**	**Experiment**
Compressive strength (MPa)	1.97	1.67 ± 0.01	1.98	1.69 ± 0.04
Elastic modulus (MPa)	47.01	42.98 ± 0.93	55.45	51.14 ± 0.34
Energy absorption ability (J/cm^3)	1.36	1.32 ± 0.02	1.27	1.12 ± 0.07

6.4.2 Elastic modulus and its prediction using the composite rule of mixture

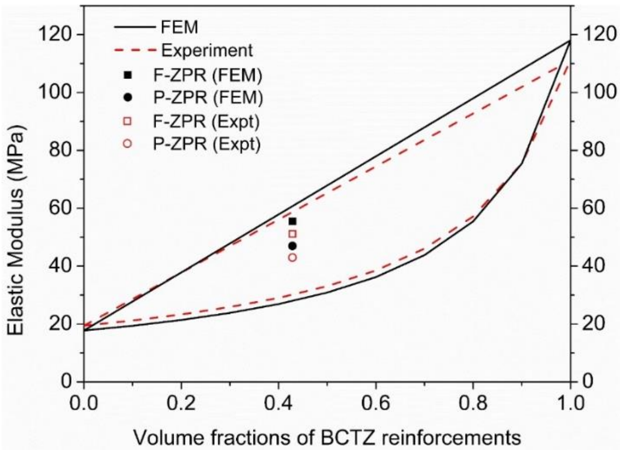

Figure 6.13. Prediction of the elastic moduli of the ZPR lattice structures using the composite rule of mixture.

The average values of the elastic modulus for the 3D-reentrant as well as the BCTZ structure evaluated from experiments were 19.45 MPa and 111.14 MPa, respectively. Table 6.3 shows the values of elastic moduli evaluated from the numerical and experimental results of the P-ZPR and F-ZPR structures. The composite rule of mixture was used to predict the elastic moduli of the ZPR structures. The upper bound elastic modulus (E_{cu}) and the lower bound elastic modulus (E_{cl}) of the composite rule of mixture are given by [136]:

$$E_{cu} = V_m E_m + V_r E_r \tag{6.2}$$

$$\frac{1}{E_{cl}} = \frac{V_m}{E_m} + \frac{V_r}{E_r} \tag{6.3}$$

where, V_m is the volume fraction of the matrix and V_r is the volume fraction of the reinforcements. Similarly, E_m and E_r are the elastic moduli of the matrix and reinforcements, respectively. Figure 6.13 shows the upper bound as well as the lower bound curve for the ZPR structures obtained from numerical as well as experimental results. The values of elastic moduli evaluated from the numerical simulations and the average values of the elastic moduli obtained from two repeated experiments of the F-ZPR and P-ZPR structures were in between the limits of the upper bound and the lower bound curves. The F-ZPR structure in which the BCTZ reinforcements were laid as long fibers throughout the composite structure has a higher value of elastic modulus than the P-ZPR structure where the BCTZ lattices were distributed in the form of particles. The elastic modulus of the F-ZPR structure was close to the upper bound curve. The upper bound curve is calculated considering the isostrain condition, in which the matrix and the fiber experience the same amount of strain, and the lower bound curve follows the isostress condition in which the matrix and reinforcements are distributed in the form of laminates stacked perpendicular to the loading direction [136]. In the case of the F-ZPR structure, the length of the fiber-like BCTZ reinforcements is the same as the lattice structure along the loading direction satisfying the isostrain condition. Hence, the stiff BCTZ reinforcements increased the elastic modulus of the entire structure to a value close to the upper bound curve. The elastic modulus of the P-ZPR structure is less than the F-ZPR structure but the value lies in between the upper bound and the lower bound curves (Figure 6.13). The decrease in elastic moduli in the experiments than the numerical simulations was due to the defects like porosities and strut waviness of the fabricated samples. Thus, the elastic moduli of both P-ZPR and F-ZPR structures lie within the area in between the upper bound and the lower bound curves of the composite rule of mixture.

6.4.3 Energy-absorption ability

The energy-absorption ability of a lattice structure can be calculated as the area under the stress-strain curve until the onset of densification. Mathematically, the energy absorption ability per unit volume (E) is defined as [30]:

$$E = \int_0^{\varepsilon_d} \sigma(\varepsilon)\, d\varepsilon \qquad 6.4$$

where, ε_d is the densification strain, ε is the strain and $\sigma(\varepsilon)$ is the stress. The energy efficiency versus strain plot is used to calculate the densification strain (ε_d). The energy efficiency (η) is mathematically defined as [134]:

$$\eta = \frac{\int_0^{\varepsilon_0} \sigma(\varepsilon) d\varepsilon}{\sigma(\varepsilon_0)} \qquad 6.5$$

where, $\sigma(\varepsilon_0)$ is the nominal stress and ε_0 is the nominal strain at that instant of time.

When the densification strain (ε_d) is reached, the energy efficiency becomes maximum, and it can be mathematically expressed as [134]:

$$\left.\frac{d\eta(\varepsilon)}{d\varepsilon}\right|_{\varepsilon=\varepsilon_d} = 0 \qquad 6.6$$

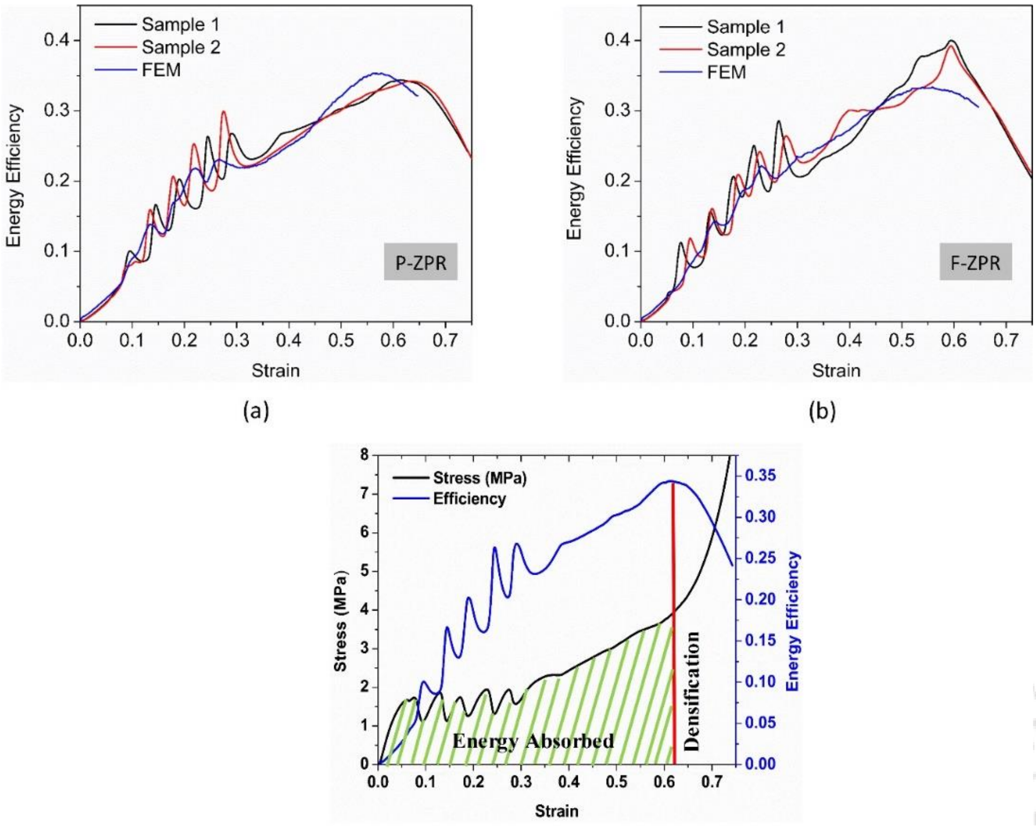

Figure 6.14. Densification strain calculated from energy efficiency vs. strain plot of (a) the P-ZPR and (b) the F-ZPR structure, and (c) the energy absorption per unit volume calculated as the area under the stress-strain curve until the densification strain of sample 1 of the P-ZPR structure.

After calculating the densification strain, the energy-absorbing abilities of the ZPR structures were calculated using Equation 6.4. The plots between the energy efficiency and the strain for the P-ZPR and the F-ZPR lattice structures are shown in Figure 6.14(a) and (b), respectively. Figure 6.14(c) shows the energy absorption per unit volume obtained from the stress-strain plot for sample 1 of the P-ZPR structure evaluated until the densification strain, which was determined from the energy efficiency versus strain curve. The energy-absorbing ability of the P-ZPR and the F-ZPR structures calculated from numerical simulations and experiments are mentioned in Table 6.3.

6.5 Comparison with previously-studied ZPR structures

The mechanical properties of the two proposed ZPR lattice structures were compared using numerical simulations with the three other ZPR structures found in previously published literature [Figure 6.5 of Section 6.1.2]. However, among the three ZPR structures investigated in previous studies, only the 3D semi-reentrant (SRE) lattice structure was fabricated for mechanical testing because the SRE structures exhibited superior mechanical properties than the other two previously studied ZPR structures. The deformation behaviour of the SRE structure during the quasi-static compression test is shown in Figure 6.15(a). Similar to the 3D-reentrant structure, the localized buckling of the struts parallel to the loading direction was the prominent deformation mode for the SRE lattice. Figure 6.15(b) shows the compressive stress-strain graphs of the SRE lattice obtained from numerical simulation and experiments. Figure 6.15(c) compares the stress-strain curves of sample 1 of P-ZPR, F-ZPR and SRE lattice structures. Since the SRE structure did not have any reinforcements, it did not undergo strain hardening like the P-ZPR and the F-ZPR lattice structures.

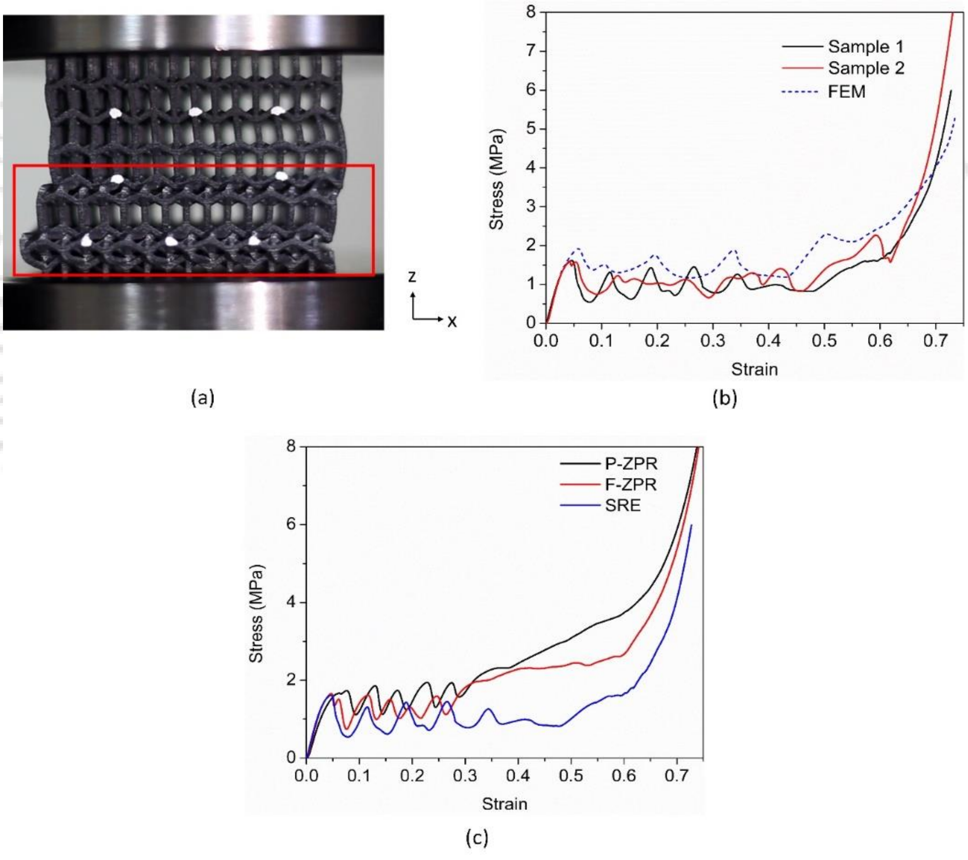

Figure 6.15. (a) Deformation behaviour of the SRE lattice showing localized buckling at a nominal strain of 0.2, (b) the stress-strain plot of SRE lattice structure, and (c) the comparison of stress-strain curves obtained from sample 1 of P-ZPR, F-ZPR and SRE structures.

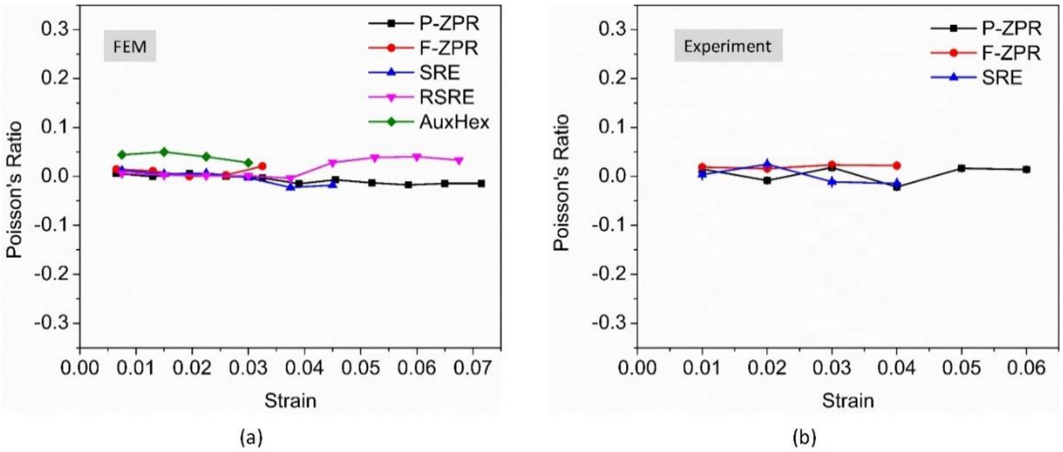

Figure 6.16. Poisson's ratio vs. strain for various ZPR lattices calculated from (a) numerical simulations, and (b) experiments.

The Poisson's ratio versus strain curves for various ZPR structures evaluated from the numerical simulations and experiments are shown in Figure 6.16(a) and (b), respectively. All the structures displayed near-zero Poisson's ratio up to a particular value of strain, after which the vertical struts buckled locally, and the structures no longer exhibited zero Poisson's ratio. Among all the ZPR structures, the P-ZPR and the RSRE structures displayed zero Poisson's ratio effect up to large strains, 0.072 and 0.068, respectively, shown in Figure 6.16(a). However, the RSRE structure exhibited very low values of mechanical properties compared to most other ZPR structures (Figure 6.17). Figure 6.17(a) shows that the compressive strength of the P-ZPR and F-ZPR structures are higher than the previously studied ZPR structures. In addition, the F-ZPR structure has the highest elastic modulus among all the ZPR structures considered in this study [Figure 6.17(b)]. Thus, for the same relative density, the composite-materials inspired ZPR structures can exhibit near-zero Poisson's ratio along with higher values of compressive strength as well as elastic modulus than the previously studied ZPR structures. Figure 6.17(c) shows the comparison of the energy absorption abilities of various ZPR structures. Although the P-ZPR structure exhibited a slightly lower elastic modulus than the SRE structure, the energy absorption ability of the P-ZPR structure was more than two times higher than the SRE structure. Thus, the significant energy absorption ability of the two ZPR composite lattice structures makes them an excellent choice for zero-Poisson's-ratio applications where the structure requires high crashworthiness.

The crushing behaviour of the different ZPR structures was also studied by evaluating the crush load efficiency (CLE), which is the ratio of mean crushing load (MCL) and global peak crushing force (GPCF). It can be expressed as [139]:

$$CLE = \frac{MCL}{GPCF} \tag{6.7}$$

where, $$MCL = \frac{\text{Total energy absorbed (E)}}{\text{Maximum crushing displacment}} \tag{6.8}$$

Initial peak crushing force (IPCF) is the first peak force during the crushing process, whereas global peak crushing force (GPCF) is the maximum force during the entire crushing process. Maximum crushing displacement corresponds to the displacement of the lattice up to densification strain. The IPCF in this study is the load corresponding to the compressive strength. The IPCF, GPCF, MCL and CLE were evaluated for the different ZPR structures and are shown in Table 6.4.

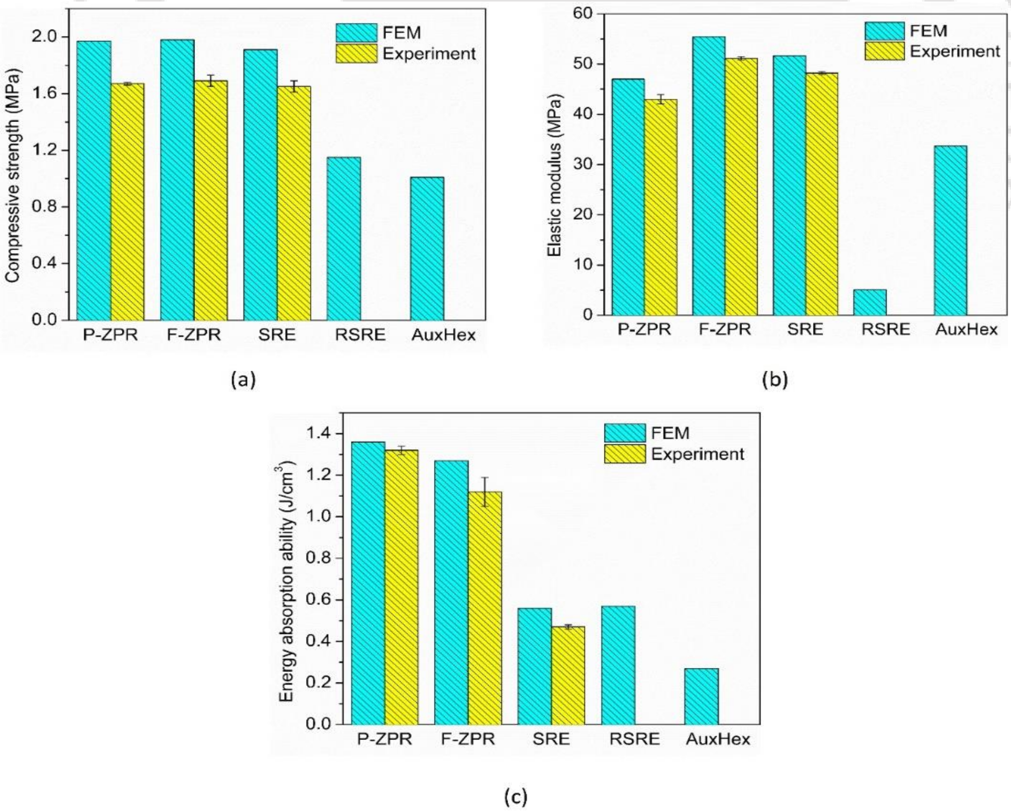

Figure 6.17. Comparisons of (a) compressive strengths, (b) elastic moduli and (c) energy absorption abilities of various ZPR structures.

Table 6.4. Comparison of parameters of sample crushing behaviour.

Design	IPCF (N)	GPCF (N)	MCL (N)	CLE
P-ZPR	4826.21	9623.32	5878.27	0.62
F-ZPR	4850.71	9746.18	5817.41	0.60
SRE	4679.22	5601.47	3399.79	0.59
RSRE	2083.83	2736.41	1880.58	0.68
AuxHex	2357.87	2357.87	1360.98	0.58

Farrokhabadi et al. mentioned that the structures having higher value of CLE are more efficient for energy absorbing applications [140]. However, a higher value of CLE does not ensure higher energy absorption ability. In this study, the RSRE lattice exhibited the highest value of CLE. On the contrary, for the same relative density, the RSRE lattice had significantly lower energy absorption ability, compressive strength and Young's modulus than that of the P-ZPR and the F-ZPR structures (Figure 6.17).

It is important to mention that all previous studies on ZPR structures are based on single type of unit cell configuration. It may be cumbersome to develop a new ZPR lattice structure with improved mechanical properties. However, in this study, instead of developing a new unit cell geometry, the proposed ZPR structures can be made using the existing unit cell geometries. The mechanical properties of the composite-material inspired ZPR structures developed in this work can be further improved by the following methods:

- Using a lattice as reinforcements that have higher strength as well as higher elastic modulus than the BCTZ lattice.
- Increasing the volume fraction of the reinforcement lattice.

The Poisson's ratio of the 3D-reentrant lattice can be changed by altering its unit cell parameters: vertical-strut length (h), reentrant-strut length (l) and reentrant angle (θ). The 3D-reentrant structure can be designed to exhibit a more negative value of Poisson's ratio so that a larger amount of high strength positive-Poisson's-ratio reinforcements are required for the overall structure to have zero Poisson's ratio.

6.6 Summary

In this work, lattice structures exhibiting zero Poisson's ratio were designed by mimicking composite materials in which a positive Poisson's ratio exhibiting lattice was incorporated as reinforcements in the matrix of a negative-Poisson's-ratio lattice structure. Numerical simulations were conducted to study the quasi-static mechanical behaviour of the proposed zero-Poisson's-ratio structures, and the results were corroborated with experiments. The elastic moduli as well as Poisson's ratios obtained from numerical and experimental results were within the limits of the conventional rule of mixture for composite materials. These composite-materials inspired lattices with zero Poisson's ratio resulted in superior mechanical properties than three commonly studied zero Poisson's ratio structures found in previously published literature. Thus, the proposed strategy of improving the mechanical properties of zero Poisson's ratio lattice structures using a reinforcement lattice can be more promising than the conventional method of tuning the unit cell geometry of a zero Poisson's ratio lattice.

CHAPTER 7. A HIGH ENERGY ABSORBING LATTICE EXHIBITING ZERO POISSON'S RATIO UP TO LARGE STRAIN

The zero Poisson's ratio lattice structures can be beneficial for tissue engineering, wing-morphing and crash-resistant applications. This chapter proposes a novel lattice structure that can exhibit high-energy absorption, along with zero Poisson's ratio till a high value of strain. The design and fabrication of the ZPR lattice structure is presented in Section 7.1. The deformation behaviour and the mechanical properties obtained from finite element simulations and experiments of the proposed ZPR lattice are discussed in Section 7.2. The comparison of the mechanical properties of the proposed ZPR lattice with the commonly studied ZPR lattice is demonstrated in Section 7.3.

7.1 Design and fabrication of the ZPR lattice

7.1.1 Design of SR-SRH lattice structure

Grima et al. designed the semi-reentrant honeycomb (SRH) structure inspired by the hexagonal honeycomb and the reentrant honeycomb structures.[24] The SRH structure was able to exhibit zero Poisson's ratio during deformation. The new lattice designed in this work is named as strut-reinforced semi-reentrant honeycomb (SR-SRH) structure. This structure consists of additional struts for improved stability during deformation such that the lattice structure can exhibit zero Poisson's ratio for larger strain. Also, the inclusion of the additional struts attributed to improved mechanical properties. The design and nomenclature of the unit cell of the SR-SRH structure are shown in Figure 7.1(a), in which '2h' is the length of the horizontal strut, 'l' is the length of the inclined/oblique strut, 'θ' is the angle between the inclined strut and the horizontal strut and 't' is the thickness of the strut. The unit cell of the SR-SRH is repeated in both x and z directions to design the SR-SRH lattice structure shown in Figure 7.1(b). Figure 7.1(c) shows the 3D view of the lattice structure with the lattice parameters: H is the height of the lattice, L is the length of the lattice, and T is the thickness of the lattice. The values of the unit cell parameters and the lattice parameters are mentioned in Table 7.1.

The relative density of the SR-SRH unit cell can be calculated as:

$$\rho_{SR-SRH} = \frac{t\,(h+l')}{h\;l\;sin\theta} \qquad 7.1$$

$$\text{where } l' = l - \frac{t}{\sin\theta} \qquad 7.2$$

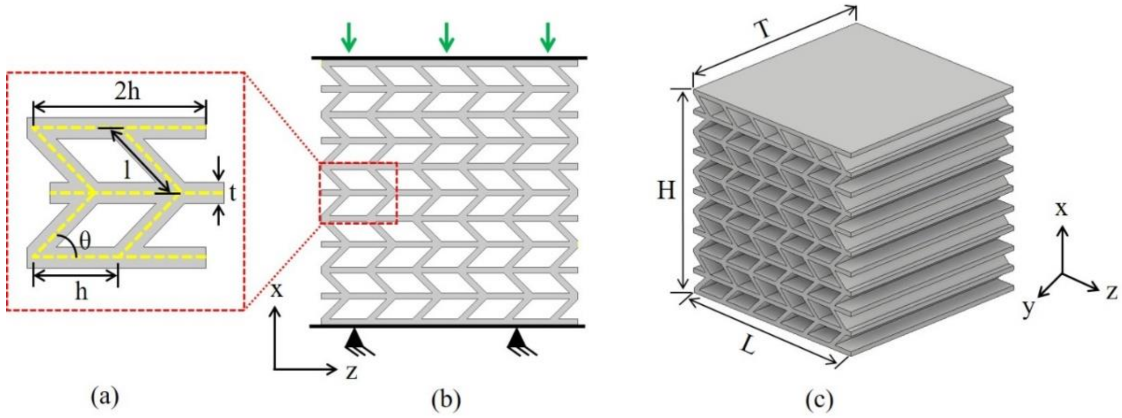

Figure 7.1. (a) Unit cell, (b) front view, and (c) 3D-view of the Strut-reinforced semi-reentrant honeycomb (SR-SRH) lattice structure.

Table 7.1. Design parameters of SR-SRH lattice structure.

Unit cell				**Lattice structure**		
h (mm)	**l (mm)**	**θ**	**t (mm)**	**H (mm)**	**L (mm)**	**T (mm)**
7.5	6	45°	1	43.43	43.45	45

7.1.2 Fabrication of lattice structures

The SR-SRH lattice structures were fabricated by HP Multi Jet Fusion (MJF) with polyamide 12 (PA12) as the printing material. Two samples were fabricated to check the repeatability of the experiments. The lattice structures were fabricated along the loading direction, i.e., the x- direction shown in Figure 7.1(c). The tensile specimens were fabricated in the same batch with the lattice structures and in the same direction to obtain the mechanical properties of the parent PA12 material.

7.2 Deformation behaviour and mechanical properties

The deformation behaviour of the SR-SRH lattice structure obtained from experiments and numerical simulation are shown in Figure 7.2(a) and (b), respectively. The numerical simulation was able to exactly predict the deformation mode of the SR-SRH lattice. Figure

7.2(b) shows a zoomed-in unit cell to understand the deformation behaviour. Due to the compressive load 'P' [Figure 7.2(b)], the oblique struts [struts with length 'l' in Figure 7.1(a)] will experience both bending and stretching. The net deflection (δ) obtained due to the force components is given as:

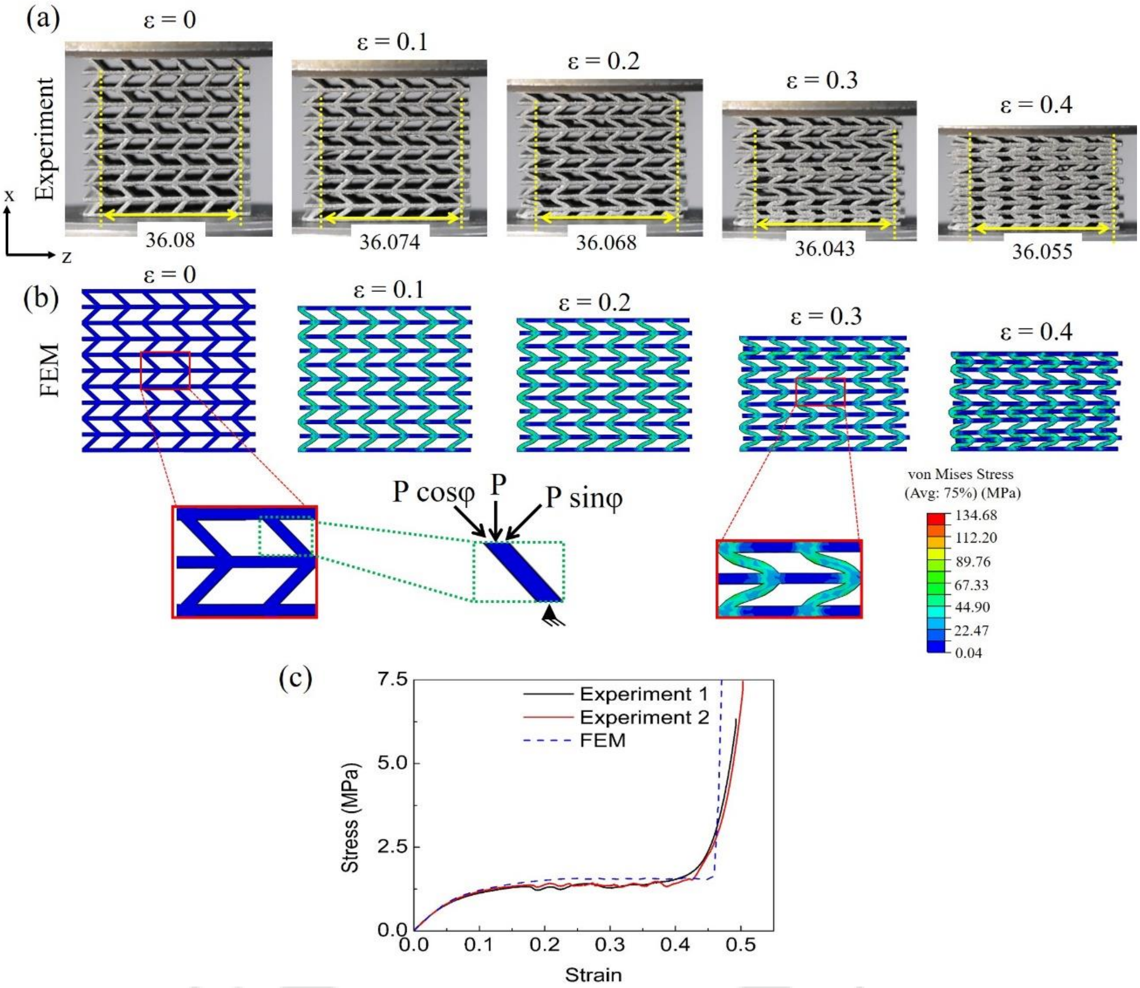

Figure 7.2. Deformation behaviour of SR-SRH lattice structure obtained from (a) experiment, (b) numerical simulation, and (c) compressive stress-strain plots of SR-SRH lattice from numerical simulation and experiments.

$$\delta = \delta sin\varphi + \delta cos\varphi \quad 7.3$$

where, $\varphi = 90° - \theta$

From standard beam theory, the deflection of one end of the beam with respect to the other is given by:

$$\delta sin\varphi = \frac{Pl^3 sin^2\varphi}{12E_s I} \quad 7.4$$

And deflection due to the stretching of the beam is given as

$$\delta cos\varphi = \frac{Pl\, cos\varphi}{AE_s} \quad 7.5$$

Where E_s is Young's modulus of the parent material, $I = \frac{t^4}{12}$, and $A = t^2$.

For the current lattice structure with design parameters mentioned in Table 7.1,

$$\frac{\delta sin\varphi}{\delta cos\varphi} = \frac{l^2\, sin^2\varphi}{t^2\, cos^2\varphi} = 36 \quad 7.6$$

Therefore, bending of the inclined struts is considered the dominant deformation mechanism. The horizontal struts [with length '2h' in Figure 7.1(a)] do not undergo any change in shape, which can be seen from the deformation images at various strains in Figure 7.2(a) and (b). However, the horizontal struts add stability to the structure during the deformation process, and the structure deforms by progressive collapse, maintaining the zero Poisson's ratio effect. The compressive stress-strain plot obtained from FEM and experiments matched well, as shown in Figure 7.2(c). The stress-strain plot consists of the elastic regime, followed by a stress plateau, where most of the energy is absorbed, after which the structure densified and the stress rises with respect to strain. The mechanical properties obtained from the stress-strain plots of the SR-SRH lattices from experiments and numerical simulation are mentioned in Table 7.2.

Table 7.2. Mechanical properties of SR-SRH lattice structure obtained from experiments and FEM.

Properties	**Peak compressive Strength (MPa)**	**Young's Modulus (MPa)**	**Energy absorption ability (kJ/m^3)**
Experiment	1.43 ± 0.03	15.8 ± 0.2	523 ± 19
FEM	1.55	16.67	616

7.3 Comparison of SR-SRH lattice with the original SRH lattice

A semi-reentrant honeycomb (SRH) lattice with unit cell parameters, as same as the SR-SRH lattice mentioned in Table 7.1, has been designed to compare the deformation mode and mechanical properties with the SR-SRH lattice designed in this work. The deformation mode of the SRH lattice structures has been shown in Figure 7.3(a). It is observed that the bending of inclined struts was the dominant deformation mechanism up to a strain of 0.2, after which the SRH lattice deformed by global buckling, which is observed at a strain of 0.3. The ZPR effect was lost after the global buckling occurred. The Poisson's ratio vs. strain plots for the SR-SRH and SRH lattices are shown in Figure 7.3(b). The Poisson’s ratio calculated from FEM and experiments matched well for the SR-SRH lattice. Both the ZPR lattices exhibited near-zero Poisson’s ratio behaviour during deformation. However, the SR-SRH lattice exhibited ZPR behaviour for a larger strain range, i.e., more than a strain of 0.4, compared to the SRH lattice structure that exhibited ZPR effect till a strain of only 0.24. The large ZPR strain range for the SR-SRH lattice was because of the extra struts that provided additional stability to the structure.

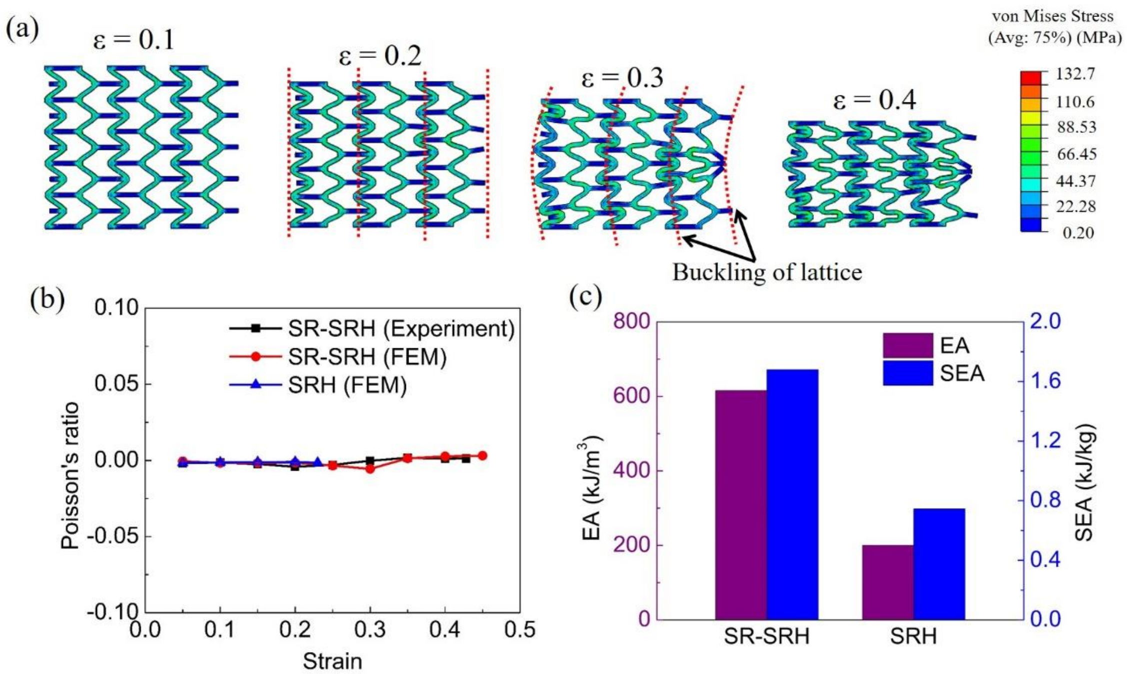

Figure 7.3. (a) Deformation behaviour of SRH lattice obtained from numerical simulations, (b) Poisson's ratio vs. strain plots of SR-SRH and SRH lattice structures, and (c) Energy absorption (EA) and Specific energy absorption (SEA) of SR-SRH and SRH lattice obtained from numerical simulations.

The energy absorption ability of these ZPR lattice structures was also calculated and shown in Figure 7.3(c). The energy absorption (EA) is calculated as the area under the stress-strain graph. Mathematically, it is given as

$$EA = \int_0^{\varepsilon_z} \sigma \, d\varepsilon \quad 7.7$$

where, ε_z is the zero-Poisson's-ratio strain limit, σ is the stress, and ε is strain. The energy absorption ability of the ZPR lattice structures was only calculated until the ZPR effect was observed. For the SR-SRH lattice, the ZPR effect was observed until the structure densified. The densification strain observed was 0.428 in the experiments and 0.45 in the numerical simulations. After the structure densified, the structural integrity was lost and could no longer exhibit the ZPR effect. For the SRH lattice, the ZPR effect was only observed till a strain of 0.24, after which global buckling of the structure occurred. The specific energy absorption (SEA) of both the ZPR lattices was also calculated as:

$$SEA = \frac{EA}{\rho} \quad 7.8$$

where, ρ is the density of the lattice structure. The SEA for the SR-SRH and SRH lattices are also shown in Figure 7.3(c). The energy absorption ability of the SR-SRH lattice was three times more than the SRH lattice, and the SEA was 2.25 times more for the SR-SRH than the SRH lattice.

7.4 Summary

This chapter proposed a hexagonal-honeycomb-based lattice with a zero Poisson's ratio, named strut reinforced semi-reentrant honeycomb (SR-SRH). The proposed lattice structure made of Polyamide 12 was fabricated by the HP Multi Jet Fusion technique. Finite element analysis was conducted to investigate the mechanical behaviour of the lattice, and the result was corroborated with experiments. The numerical simulations and experiments revealed that the bending of oblique struts was the dominant deformation mechanism. The SR-SRH lattice exhibited zero Poisson's ratio up to a uniaxial strain of 42.8% which was 1.75 times more than the semi-reentrant honeycomb (SRH) lattice. The SR-SRH lattice also exhibited superior specific energy absorption (SEA) ability than the SRH lattice. With the improved mechanical properties, these lattices can be used in aerospace, automobile and biomedical applications.

CHAPTER 8. A HIGH-PERFORMANCE DESIGN OF TUBULAR LATTICE STRUCTURE HAVING ZERO POISSON'S RATIO

This chapter proposes zero Poisson's ratio (ZPR) tubular lattice structures based on the strut-reinforced semi-reentrant honeycomb (SR-SRH) lattices designed in the previous chapter. The ZPR tubular lattices can be used in biomedical stents, pressure tubes and crash-resistant applications in automobiles. The design and fabrication of the tubular lattices are discussed in Section 8.1. Design of Experiments (DoE) with Analysis of Variance (ANOVA) is employed to study the effect of input geometric parameters on the mechanical response like compressive strength, elastic modulus and energy absorption ability. The results obtained from ANOVA are discussed in Section 8.2. The influence of input geometric parameters are discussed in Section 8.3. The comparison of the mechanical properties of the proposed tubular structure with the semi-reentrant honeycomb is done in Section 8.4. Lastly, optimized tubular lattice structures for different applications are designed and discussed in Section 8.5 and 8.6, respectively.

8.1 Design and fabrication of ZPR tubular lattices

This section describes the design of zero Poisson's ratio tubular lattice structures, finite element analyses, design of experiments and fabrication of the optimized structures.

8.1.1 Design of ZPR tubular lattice structure

The lattice structure designed in this work is called the strut reinforced-semi reentrant honeycomb (SR-SRH) as discussed in Section 7.1.1 [Figure 8.1(a)]. The unit cell parameters of the SR-SRH structures are shown in Figure 8.1(a), in which h, l, θ *and* t represent the length of the horizontal strut, the length of the oblique strut, the slant angle and the thickness of the struts, respectively.

In this work, two tubular lattice structures were designed using the commercial software Autodesk Inventor. In the first design, which is named SR-SRH-1, the SR-SRH unit cell shown in Figure 8.1(a) is repeated along the x and the z-directions to form the 2D-lattice structure, as shown in Figure 8.1(b). Here, m is the number of unit cells along the x-direction, and n is the number of unit cells along the z-direction.

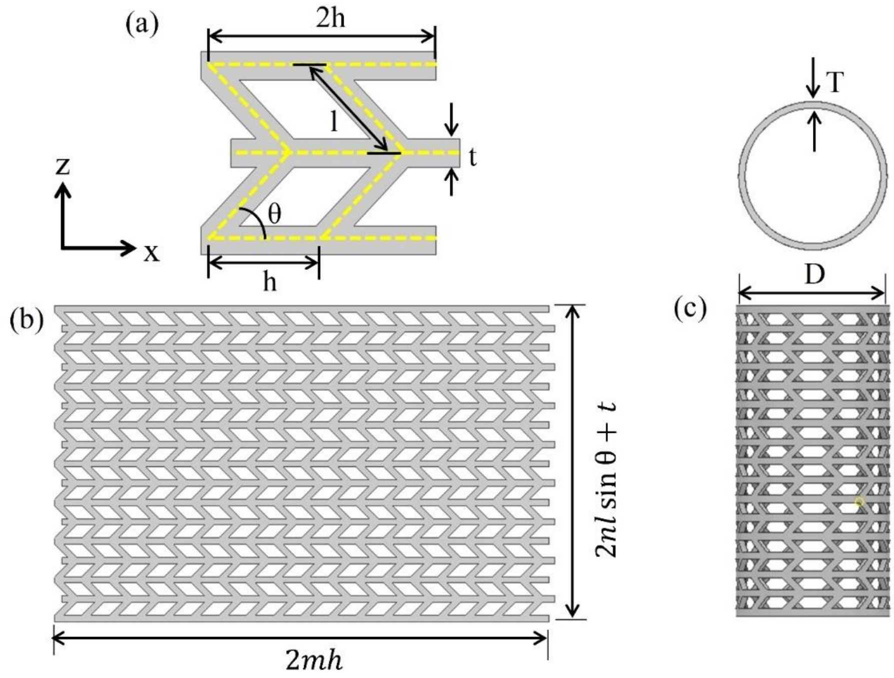

Figure 8.1. The structure SR-SRH-1 showing (a) the unit cell of the strut-reinforced semi-reentrant honeycomb, (b) the corresponding planar periodic lattice, and (c) the 3D-tubular lattice structure generated by folding the planar lattice shown in (b).

The dimensions of the lattice sheet shown in Figure 8.1(b) are given as:

$$M = 2mh \tag{8.1}$$

$$N = 2nl\ sin\theta + t \tag{8.2}$$

where, *M* is the length of the sheet along the x-direction, and *N* is the length of the sheet along the z-direction. The lattice sheet shown in Figure 8.1(b) is folded to form the tube, as shown in Figure 8.1(c). Hence, the perimeter of the tube is:

$$\pi D = M = 2mh \tag{8.3}$$

where, *D* is the diameter of the tube, and *T* represents the thickness of the tube.

The unit cell shown in Figure 8.1(a) is rotated 90° in the counter-clockwise direction to generate the second design named SR-SRH-2 [Figure 8.2(a)]. The unit cell is repeated in x and z-directions to form the 2D-lattice structure, as shown in Figure 8.2(b). Here, the lengths of the lattice sheet along the x-direction (*M*) and along the z-direction (*N*) are given as:

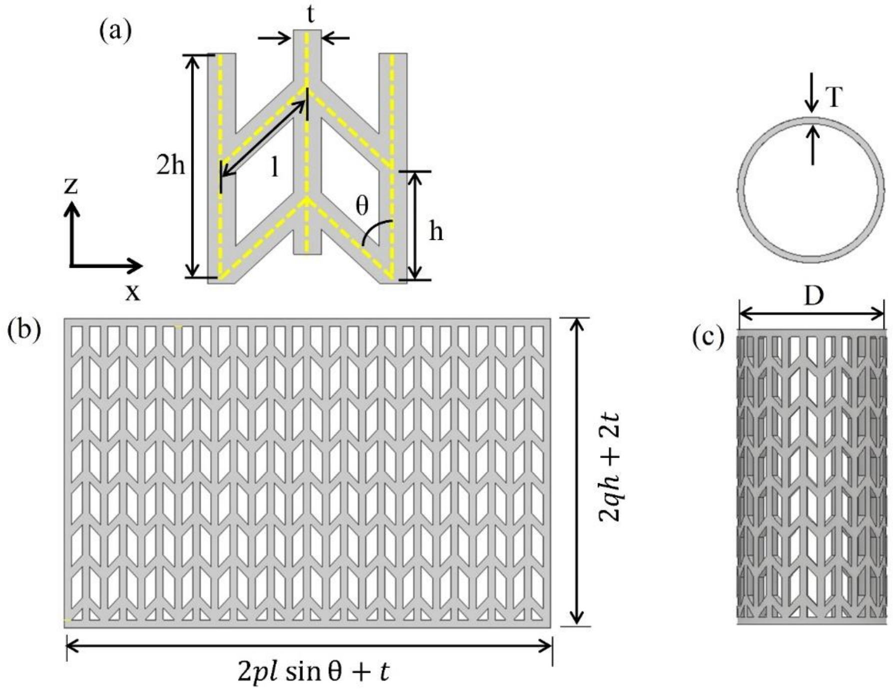

Figure 8.2. The structure SR-SRH-2 showing (a) the unit cell of the strut-reinforced semi-reentrant honeycomb, (b) the corresponding planar periodic lattice, and (c) the 3D-tubular lattice structure generated by folding the planar lattice shown in (b).

$$M = 2pl\ sin\theta + t \tag{8.4}$$

$$N = 2qh + 2t \tag{8.5}$$

where, p and q are the number of unit cells along the x-direction and the z-direction, respectively. Also, the perimeter of the tube [Figure 8.2(c)] generated from the sheet is

$$\pi D = M = 2pl\ sin\theta + t \tag{8.6}$$

8.1.2 Effect of unit cell geometric parameters on the mechanical properties using Design of Experiments

Design of Experiment (DoE) is a statistical approach for planning a minimum number of experiments or simulations to establish pragmatic relations between the input and response parameters [141]. The DoE and the Analysis of Variance (ANOVA) methods were used in this work to study the effects of the unit cell parameters (*h/l ratio* and *θ*) and tube thickness (T) on the mechanical properties of the ZPR tubular lattice structures. The Response Surface Method (RSM) with Face Centered Composite Design (FCCD) was employed to design the experiments. The RSM uses mathematical modeling using regression analysis to represent the best-fitted data in the 3D-surface plots from the interaction of the input parameters on the response parameters [141]. The response parameter (R) can be obtained in the form of a quadratic polynomial of input variables as:

$$R = a_o + \sum a_i x_i + \sum a_{ii} x_i^2 + \sum a_{ij} x_i x_j + b \quad 8.7$$

where, x_i, x_j are the input variables, b is the residue term, and a_o, a_i, a_{ii} and a_{ij} are the regression coefficients. This statistical modeling is processed to fit the experimental data and calculate the regression coefficients.

Table 8.1. Input parameters with different levels.

Input parameters	**Values**		
DoE levels	**−1**	**0**	**1**
h/l ratio	1	1.5	2
Angle (θ)°	22.5	45	67.5
Tube thickness / T (mm)	1	2	3

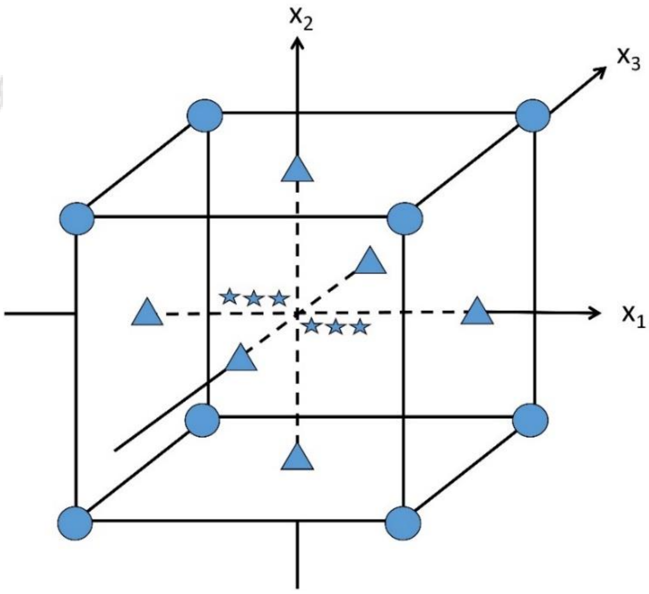

Figure 8.3. Face Centered Composite Design (FCCD) for 20 tests with six center points (stars), eight vertices (circles), and six face-center points (triangles).

In this work, the three input parameters were varied over three levels (−1, 0, 1), as shown in Table 8.1. The FCCD with 20 experiments was obtained in the form of a cube (Figure 8.3), in which there are six center points (stars), eight vertices (circles), and six face-center points (triangles), which resulted in a total of 20 experiments. The minimum values of the input parameters were considered based on the fabrication capability of the 3D-printing machine. All the tubular lattice structures were designed by maintaining the same relative density, which is calculated from Equation 7.1. The response parameters obtained from the numerical simulations were elastic modulus, compressive strength, ZPR strain limit before buckling and energy absorbed during deformation. The design of experiments matrix with the input parameters and the response parameters are shown in Table 8.2 for SR-SRH-1 and Table 8.3 for SR-SRH-2. The significance of the designed regression models was evaluated using Analysis of Variance (ANOVA).

Table 8.2. Design matrix of the input and response parameters for SR-SRH-1.

Sample No.	**Input parameters**			**Response parameters**			
	***h/l* ratio**	**Angle (*θ*)**	**Tube thickness / *T* (mm)**	**Elastic modulus (MPa)**	**Compressive strength (MPa)**	**ZPR strain limit (%)**	**Energy absorption (J/cm^3)**
1	1.5	45	2	44.01	2.85	15.87	0.335
2	2	22.5	1	14.77	0.98	12.22	0.083
3	1.5	45	2	44.01	2.85	15.87	0.335
4	1.5	45	1	56.47	2.59	6.48	0.220
5	2	67.5	1	133.69	2.96	2.29	0.050
6	1	67.5	3	115.01	5.07	9.80	0.387
7	1	22.5	3	4.60	0.77	34.00	0.176
8	1.5	45	2	44.01	2.85	15.87	0.335
9	1	22.5	1	7.65	0.97	21.11	0.131
10	1.5	45	2	44.01	2.85	15.87	0.335
11	1.5	45	3	34.79	2.54	21.40	0.409
12	1.5	67.5	2	119.83	4.75	6.64	0.236
13	1	67.5	1	148.34	4.2	3.11	0.096
14	1.5	22.5	2	7.61	0.87	21.80	0.131
15	2	22.5	3	6.41	0.64	16.80	0.076
16	1.5	45	2	44.01	2.85	15.87	0.335
17	2	45	2	45.04	2.47	14.42	0.224
18	1.5	45	2	44.01	2.85	15.87	0.335
19	2	67.5	3	104.53	3.98	9.72	0.304
20	1	45	2	40.89	2.82	17.71	0.380

Table 8.3. Design matrix of input variables and output responses for SR-SRH-2.

Sample No.	**Input parameters**			**Response parameters**			
	***h/l* ratio**	**Angle (*θ*)**	**Tube thickness / *T* (mm)**	**Elastic modulus (MPa)**	**Compressive strength (MPa)**	**ZPR strain limit (%)**	**Energy absorption (J/cm^3)**
1	2	45	2	521.27	7.86	1.65	0.076
2	2	22.5	3	523.15	8.30	1.47	0.114
3	1	67.5	3	309.84	7.75	3.16	0.160
4	1.5	67.5	2	364.83	7.80	1.80	0.081
5	1	22.5	1	366.06	3.30	0.89	0.021
6	1.5	45	1	394.69	4.09	0.89	0.025
7	1.5	45	2	381.18	7.65	1.79	0.076
8	1.5	45	2	381.18	7.65	1.79	0.076
9	1	22.5	3	321.25	6.11	1.80	0.067
10	1.5	45	2	381.18	7.65	1.79	0.076
11	1.5	45	2	381.18	7.65	1.79	0.076
12	1.5	45	2	381.18	7.65	1.79	0.076
13	2	67.5	1	513.66	3.60	0.75	0.020
14	1.5	22.5	2	415.76	6.01	1.39	0.055
15	1	45	2	323.17	6.80	2.09	0.088
16	2	67.5	3	463.80	8.74	2.09	0.112
17	1.5	45	2	381.18	7.65	1.79	0.076
18	1	67.5	1	330.92	5.62	1.64	0.069
19	1.5	45	3	360.92	8.19	2.25	0.115
20	2	22.5	1	540.60	4.00	0.75	0.019

8.1.3 Manufacturing of the ZPR tubular lattice structures

HP Multi Jet Fusion (MJF) 3D-printing technique was used to manufacture the tubular structures. Polyamide 12 (PA12) was used as the base material for fabricating the tubular structures. The tubular structures, which were optimized using the DoE technique for SR-SRH-1 and SR-SH-2, were manufactured, and quasi-static compression tests were performed to validate the numerical simulations.

8.2 ANOVA results

Analysis of Variance (ANOVA) was used to evaluate the significance of the models developed using Face Centered Composite Design (FCCD) based Response Surface Method (RSM) technique. The response parameters obtained from the finite element simulations were used to study the correlations with the input variables. Table 8.4 shows the ANOVA for SR-SRH-1. For the models to be significant, the F-value should be high, the probability value (p-value) should be less than 0.05 and the coefficient of determination (R^2) should be close to 1. Also, the difference between the adjusted R^2 and the predicted R^2 should be less than 0.2, indicating the model is not over-fit. Table 8.4 shows that all these conditions are satisfied, and the models are significant.

Table 8.4. Analysis of variance for SR-SRH-1.

Models	**F-value**	**p-value**	**R^2**	**predicted R^2**	**adjusted R^2**
Compressive strength	179.54	<0.0001	0.988	0.982	0.966
Elastic modulus	1085.54	<0.0001	0.998	0.997	0.992
Energy absorption ability	96.72	<0.0001	0.971	0.961	0.935
ZPR strain limit	53.45	<0.0001	0.934	0.917	0.841

For the SR-SRH-1, the correlations of the compressive strength, elastic modulus, and energy absorption ability with the input parameters, i.e., *h/l ratio,* θ and T, can be best fitted by the modified quadratic equations. In contrast, the ZPR strain limit can be best fitted by the modified two-factor integration.

The coefficients of the higher order terms, x_i^2 and $x_i x_j$ (Equation 8.7), higher than 0.05 (probability value/p-value), were eliminated from the equations using backward transformations. The correlations between the input and response variables obtained are as follows:

$$\text{Compressive strength} = 2.8 + 1.67\,(\theta) - 0.2829\,(h/l\ ratio) + 0.1329\,(T) - 0.2726\,(\theta \times h/l\ ratio) + 0.3001\,(\theta \times T) - 0.3281\,(T^2) \quad 8.8$$

$$\text{Elastic modulus} = 44.13 + 58.04\,(\theta) - 1.2\,(h/l\ ratio) - 9.56\,(T) - 4.26\,(\theta \times h/l\ ratio) - 6.38\,(\theta \times T) + 22.12\,(\theta^2) \quad 8.9$$

Energy absorption ability = 0.3243 + 0.0476 (θ) – 0.0433 (*h/l ratio*) + 0.0772 (T) + 0.0634 ($\theta \times T$) – 0.1573 (θ^2) 8.10

ZPR strain limit = 14.64 – 7.44 (θ) – 3.03 (*h/l ratio*) + 4.65 (T) + 3.15 ($\theta \times$ *h/l ratio*) 8.11

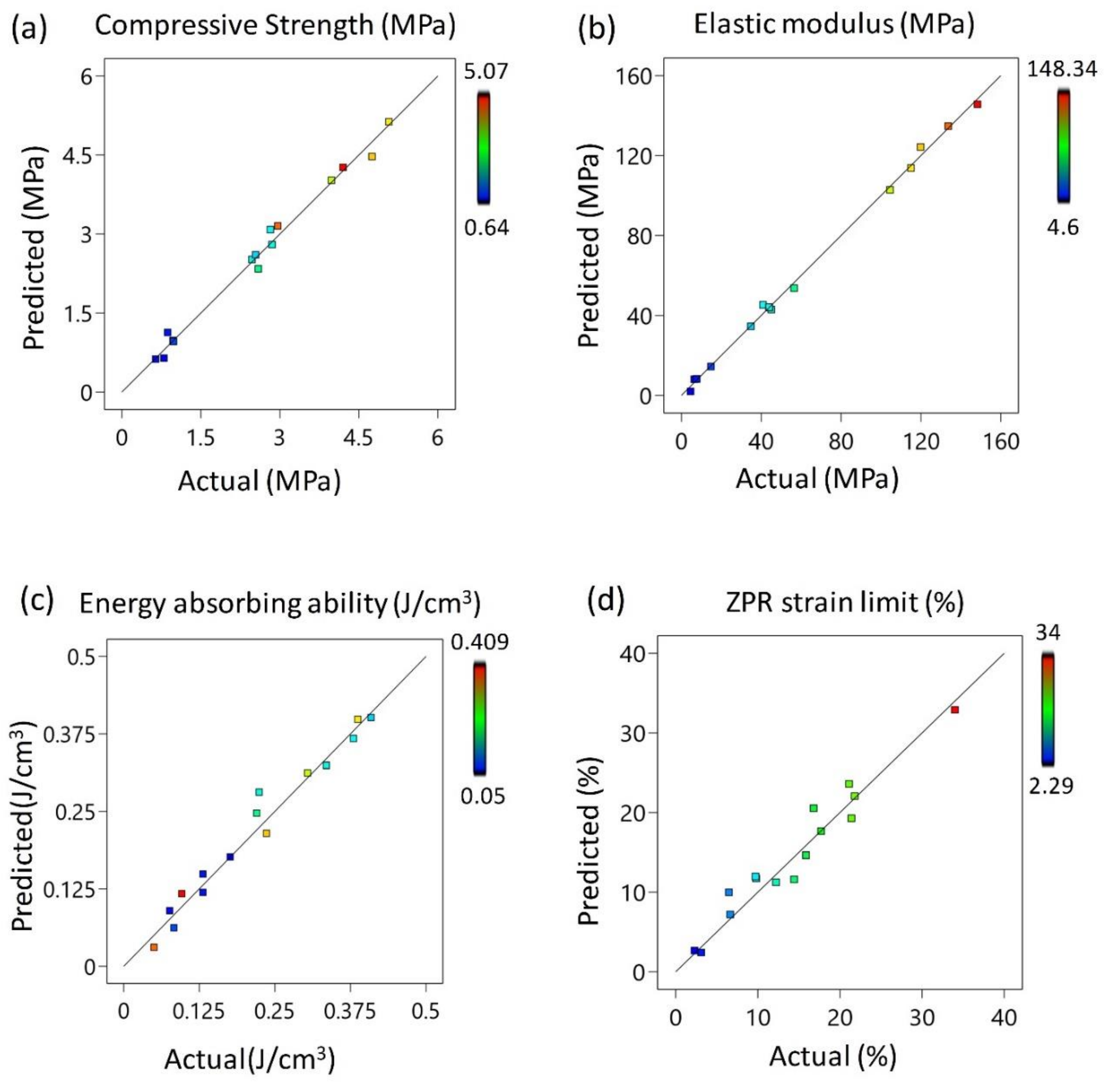

Figure 8.4. Comparison of (a) compressive strength, (b) elastic modulus, (c) energy absorption ability and (d) ZPR strain limit predicted by the models with the actual values obtained from the numerical simulations of SR-SRH-1.

The comparison between the prediction of the models (Equations 8.8-8.11) and the results obtained from the numerical simulations for all the response variables of SR-SRH-1 are shown in Figure 8.4. The predicted and actual values are in good agreement, which suggests that the results can be used for subsequent analyses. Similarly, for SR-SRH-2, Table 8.5 shows the ANOVA values for the significance of the models.

Table 8.5. Analysis of variance for SR-SRH-2.

Models	**F-value**	**P-value**	**R^2**	**Predicted R^2**	**Adjusted R^2**
Compressive strength	84.24	<0.0001	0.980	0.968	0.907
Elastic modulus	342.1	<0.0001	0.989	0.986	0.974
Energy absorption ability	75.51	<0.0001	0.964	0.951	0.842
ZPR strain limit	95.2	<0.0001	0.985	0.975	0.919

The predicted equations of the models for SR-SRH-2 are as follows:

$$\text{Compressive strength} = 7.52 + 0.579\,(\theta) + 0.292\,(h/l\ ratio) + 1.85\,(T) - 0.49\,(\theta \times h/l\ ratio) + 0.562\,(h/l\ ratio \times T) - 0.438\,(\theta^2) - 1.2\,(T^2) \quad (8.12)$$

$$\text{Elastic modulus} = 382.33 - 18.38\,(\theta) + 91.12\,(h/l\ ratio) - 16.7\,(T) + 39.04\,(h/l\ ratio)^2 \quad (8.13)$$

$$\text{Energy absorption ability} = 0.0739 + 0.0166\,(\theta) - 0.0063\,(h/l\ ratio) + 0.0416\,(T) - 0.0178\,(\theta \times h/l\ ratio) + 0.0061\,(h/l\ ratio \times T) \quad (8.14)$$

$$\text{ZPR strain limit} = 1.77 + 0.314\,(\theta) - 0.287\,(h/l\ ratio) + 0.585\,(T) - 0.1862\,(\theta \times h/l\ ratio) + 0.1538\,(\theta \times T) - 0.1536\,(\theta)^2 + 0.1214\,(h/l\ ratio)^2 - 0.1786\,(T)^2 \quad (8.15)$$

The comparison between the numerical simulation results and the predictions obtained from the models (Equation 8.12-8.15) for SR-SRH-2 is shown in Figure 8.5. Similar to SR-SRH-1, the predicted and actual values are in good agreement for SR-SRH-2.

8.3 Influence of the input variables on the mechanical properties

The response parameters, i.e., the mechanical properties corresponding to different input parameters for SR-SRH-1 and SR-SRH-2, are shown in Tables 8.2 and 8.3, respectively.

The effects of the input variables on the mechanical properties are discussed in detail in the following sections:

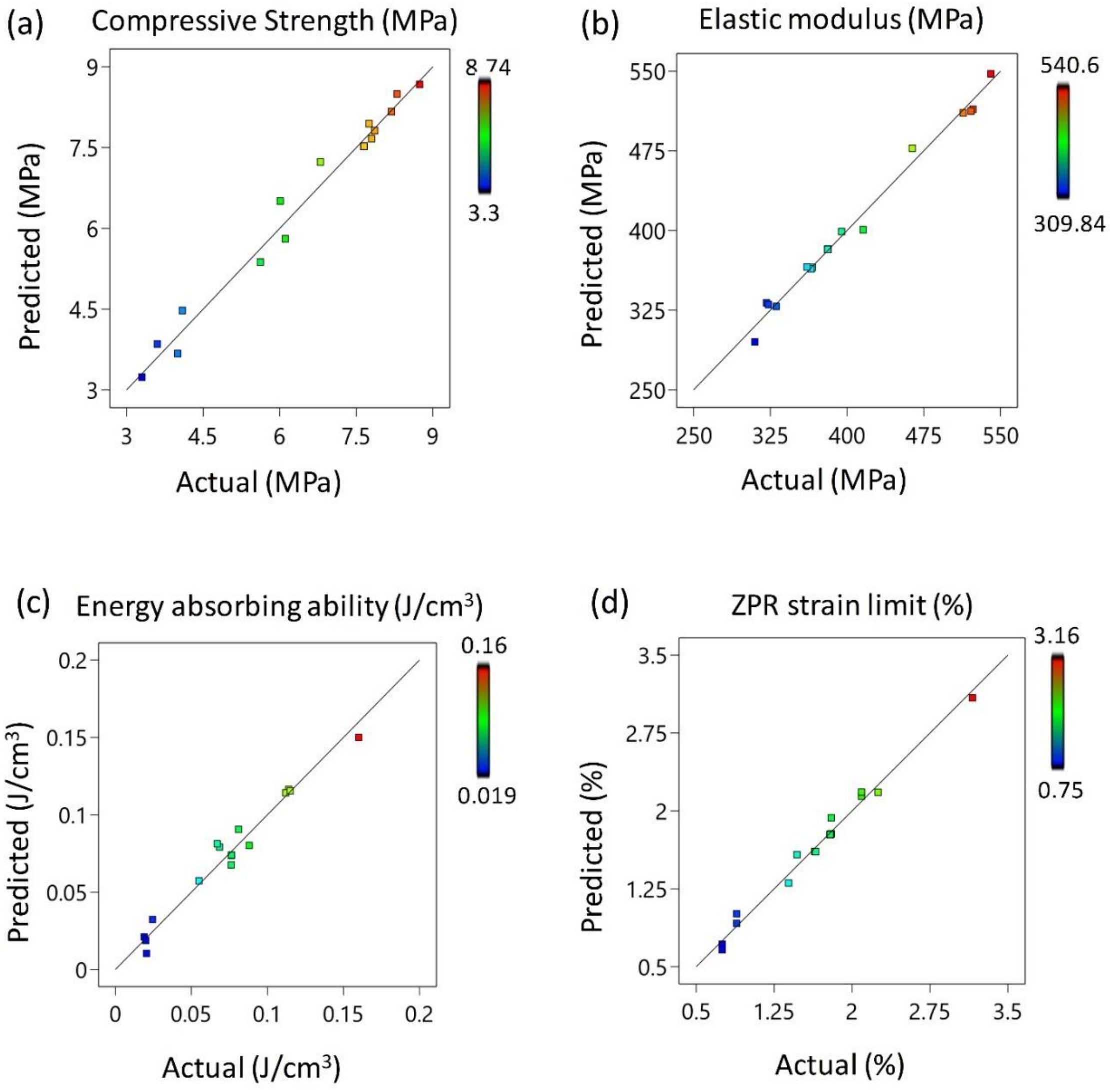

Figure 8.5. Comparison of (a) compressive strength, (b) elastic modulus, (c) energy absorption ability and (d) ZPR strain limit predicted by the models with the actual values obtained from the numerical simulations of SR-SRH-2.

8.3.1 Elastic modulus

The elastic modulus of the tubular structures was calculated as the ratio of compressive stress divided by the strain within the elastic limit. It was used to determine how the tubular structures would respond to the applied compressive stress. In the case of SR-SRH-1, the elastic modulus predominantly depends on the angle (θ) out of all the three input parameters, as shown in Figure 8.6. With an increase in the angle, the required force that causes the bending of the inclined struts increases significantly, thereby increasing the elastic modulus of the structure. In contrast, the *h/l ratio* has nearly no effect on the elastic modulus, and the elastic modulus decreases slightly with the increase in the tube thickness (*T*).

The SR-SRH-2 has significantly higher elastic moduli than that of SR-SRH-1, attributed to the vertical struts present along the entire length of the tubular structure in the loading direction. Due to the presence of vertical struts, the deformation of SR-SRH-2 tubular structures was dominated by stretching, unlike bending in the SR-SRH-1 tubular structures. The highest elastic modulus observed for SR-SRH-2 was 540.6 MPa compared to 148.34 MPa for SR-SRH-1. Figure 8.7 shows the interaction of elastic modulus with *h/l ratio*, θ and T for SR-SRH-2. Surface plots are not available for SR-SRH-2 because the higher order terms ($x_i x_j$) were eliminated in Equation 8.13 as they have a p-value less than 0.05. It can be observed from Figure 8.7 that the *h/l ratio* has a more dominating effect on the elastic modulus of SR-SRH-2 than the other two input parameters.

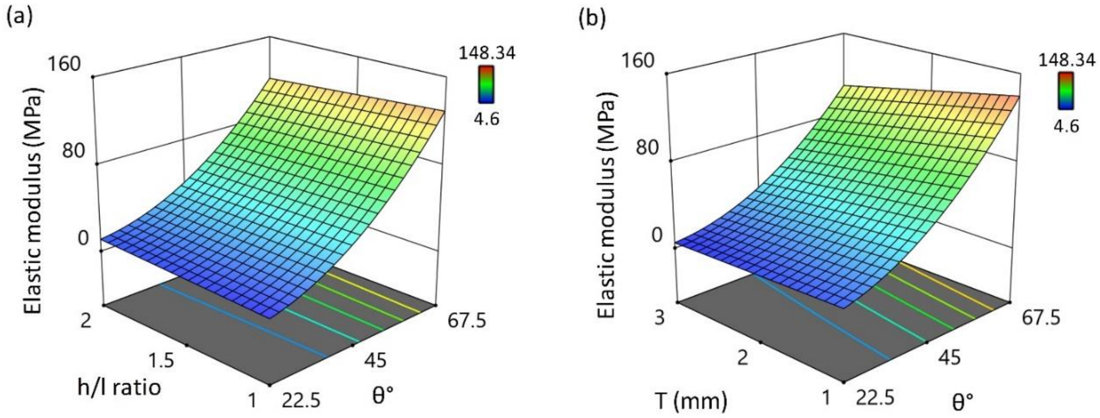

Figure 8.6. Effects of (a) *h/l ratio* and θ when tube thickness is 2 mm and (b) T and θ when *h/l ratio* is 1.5 on the elastic modulus of SR-SRH-1.

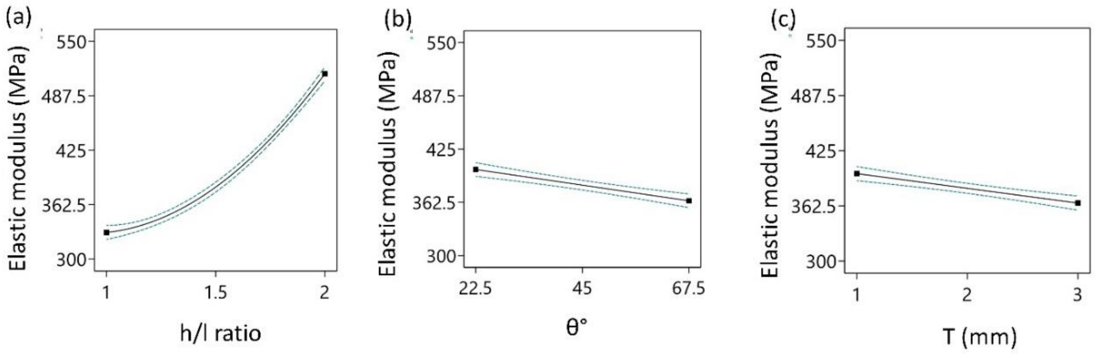

Figure 8.7. Interaction of elastic modulus with (a) *h/l ratio*, (b) θ and (c) T for SR-SRH-2.

8.3.2 Compressive strength

The compressive strength was used to measure the load-bearing capability of the tubular lattice structures. The compressive strength was measured as the peak value of stress obtained in the stress-strain plot before the densification or the buckling of the tubular lattice structure was observed. The influence of the input variables, i.e., the *h/l ratio*, θ and T, on the compressive strength of the SR-SRH-1 and SR-SRH-2 are shown in Figure 8.8 and 8.9, respectively. For the SR-SRH-1, θ has the dominant effect on the compressive strength than the other two input variables (Figure 8.8). In Figure 8.8(a), the compressive strength increases with a decrease in *the h/l ratio* at higher angles but does not vary much with the *h/l ratio* at lower angles. With the increase in θ, the compressive strength had a minimum value of 1.15 MPa at an angle of 22.5° and a maximum value of 4.37 MPa at an angle of 67.5°. Figure 8.8(b) shows that the compressive strength increases slightly and then decreases with an increase in T.

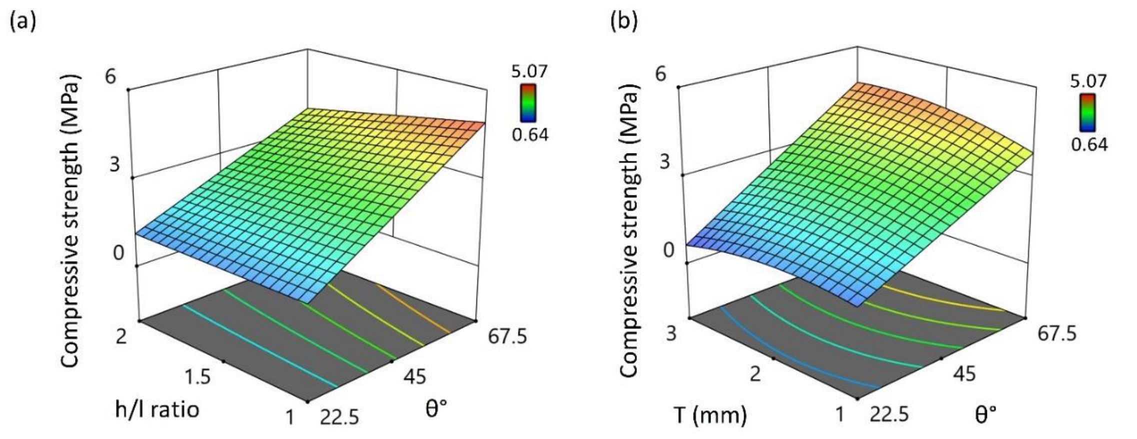

Figure 8.8. Effects of (a) *h/l ratio* and θ when T is 2 mm and (b) T and θ when *h/l ratio* is 1.5 on the compressive strength of SR-SRH-1.

For SR-SRH-2, the tube thickness (T) has the dominant influence on the compressive strength of the tubular lattice structure, as shown in Figure 8.9. The compressive strength had a minimum value of 4.41 MPa at T of 1 mm and a maximum of 8.33 MPa at T of 3 mm. The compressive strength increases with an increase in *the h/l ratio* at lower angles but remains almost constant with *the h/l ratio* at higher angles [Figure 8.9(a)]. The compressive strength increases significantly with an increase in T, which amplifies with an increase in *the h/l ratio* [Figure 8.9(b)]. The highest compressive strength observed was 8.74 MPa for an *h/l ratio* of 2, θ of 67.5° and T of 3 mm.

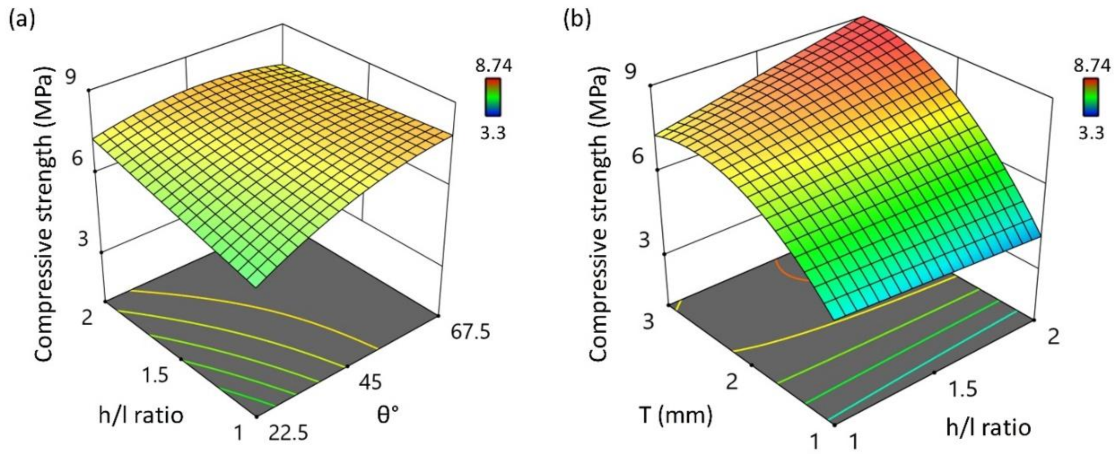

Figure 8.9. Effects of (a) *h/l ratio* and θ when T is 2mm and (b) T and *h/l ratio* when θ is 45° on the compressive strength of SR-SRH-2.

Table 8.2 and 8.3 showed that the SR-SRH-2 exhibited higher compressive strength than the SR-SRH-1 because the struts in the SR-SRH-2 acted as continuous columns along the entire tube length, i.e., parallel to the loading direction. And with an increase in the tube thickness (T), the thickness of the vertical struts also increases, which leads to an increase in compressive strength. Due to the increase in the T, the vertical strut can achieve higher loading bearing capacity because of the delay in buckling. The struts with less thickness buckled early and had lower compressive strength.

8.3.3 ZPR strain limit

During the compression of the tubular lattices, the ZPR strain limit was calculated until the ZPR effect ends, which generally results from either buckling of the tube or self-contact of the struts of the tube. Figure 8.10(a) shows the deformation behaviour of a tubular structure in which the ZPR effect was observed until the self-contact of the struts, and Figure 8.10(b) shows the stress-strain plot of the tubular structure. Similarly, Figure 8.11(a) and (b) show the deformation behaviour and the stress-strain curve, respectively, of another tubular structure in which the ZPR effect was observed until the buckling of the tube. The effects of geometrical input parameters on the ZPR strain limit for both SR-SRH-1 and SR-SRH-2 are shown in Figure 8.12. For the SR-SRH-1, the angle (θ) has the highest influence on the ZPR strain limit. The ZPR strain limit increased significantly with a decrease in angle θ [Figure 8.12(a)], though the effect was reduced for a higher *h/l ratio*. Similarly, the ZPR strain limit decreased with an increase in *the h/l ratio*, but the variation was almost negligible at higher angles [Figure 8.12(a)]. In addition, the ZPR strain limit also increased with an increase in the thickness of the tube (Table 8.2). In SR-SRH-1, with a decrease in angle *θ,* the oblique struts are more inclined to the horizontal axis, and hence, the deformation was dominated by bending of the oblique struts, which led to self-contact of the struts instead of buckling of the tube. This is the primary cause for the increase in the ZPR strain limit when the angle is less. With the increase in the *h/l ratio*, the number of unit cells along the x-direction (*i.e.*, *m* in Equation 8.1) decreased, which resulted in a decrease in the number of oblique struts, thereby decreasing the stability of the SR-SRH-1 structure, and hence, the ZPR limit reduced. The maximum ZPR strain limit was 34% for the SR-SRH-1 with *an h/l* ratio of 1, *T* of 3 mm and *θ* =22.5°.

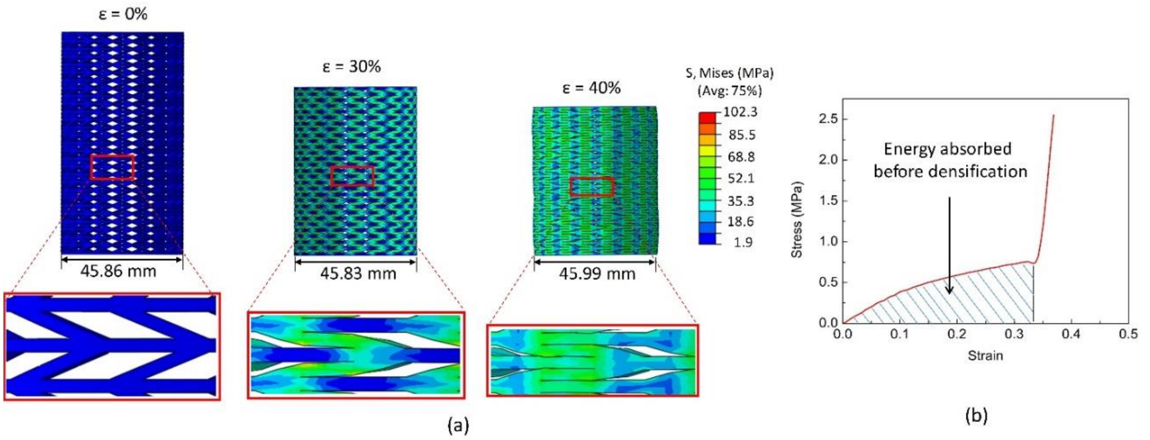

Figure 8.10. (a) Deformation behaviour showing ZPR effect until self-contact and (b) stress-strain plot of SR-SRH-1 with *h/l ratio* of 1, *T* of 3 mm and *θ* of 22.5°.

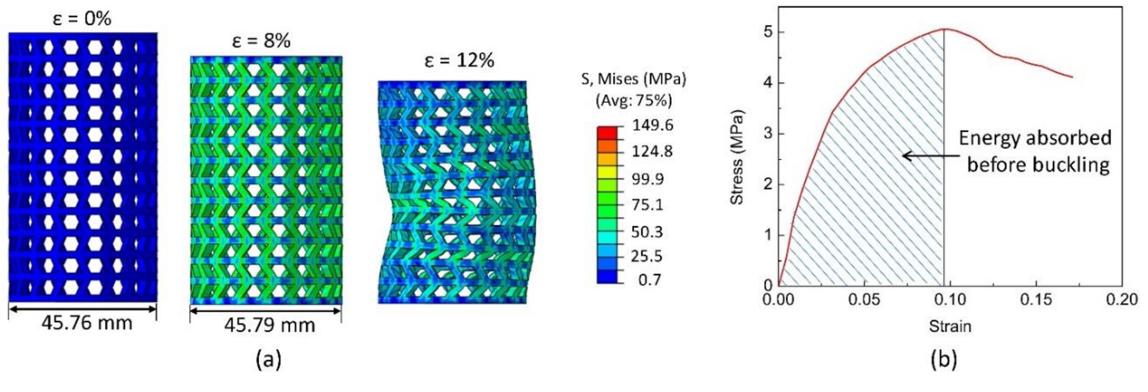

Figure 8.11. (a) Deformation behaviour showing ZPR effect until buckling and (b) stress-strain plot of SR-SRH-1 with *h/l ratio* = 1, *T* = 3 mm and *θ* = 67.5°.

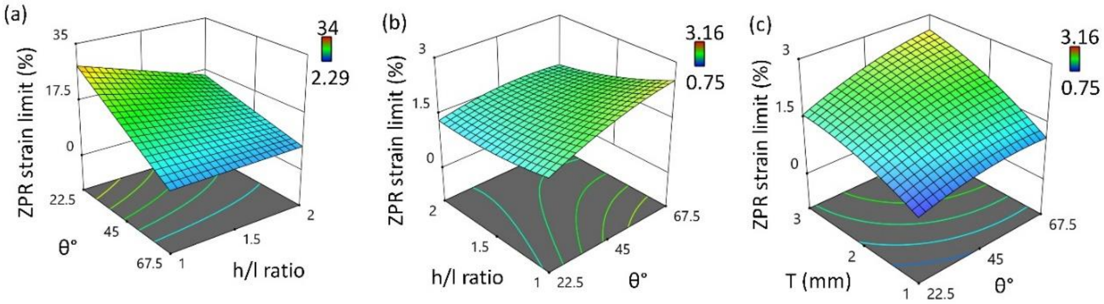

Figure 8.12. Effects of different geometrical parameters on ZPR strain limit: (a) effects of h/l ratio and θ of SR-SRH-1 with T of 2 mm, (b) effects of h/l ratio and angle of SR-SRH-2 with T of 2 mm, and (c) effects of T and θ of SR-SRH-2 with h/l ratio of 1.5.

For SR-SRH-2, the ZPR strain limit was significantly lower as compared to SR-SRH-1. The primary cause of this behaviour was the vertical struts acted as continuous columns and buckled at a very low strain. The tube thickness (T) was the dominant factor deciding the ZPR strain limit [Figure 8.12(b) and (c)]. The ZPR strain limit increased with an increase in angle θ [Figure 8.12(b) and (c)] though the effect was reduced for a higher h/l ratio. Similarly, the ZPR strain limit decreased with an increase in *the h/l ratio*, but the variation was almost negligible at lower angles [Figure 8.12(b)]. The highest ZPR strain limit was only 3.16 % for SR-SRH-2 with an *h/l ratio* of 1, T of 3 mm and θ =67.5°. The highest ZPR strain limit observed was 10.75 times higher in SR-SRH-1 than in SR-SRH-2.

8.3.4 Energy absorption ability

The energy absorption ability (EAA) of the tubular lattice is calculated as the area under the stress-strain curve and is expressed as

$$EAA = \int_0^{\varepsilon_d} \sigma \, d\varepsilon \qquad 8.16$$

where, ε_d is the ZPR strain limit, σ is the stress, and ε is the strain. The energy absorption ability of the ZPR tubular structures was calculated until the buckling of the tube or the self-contact of the struts. For the SR-SRH-1, the energy absorption ability increased first and then decreased with an increase in the angle θ [Figure 8.13(a)]. The peak value of the energy absorption ability was observed at an angle of ~45°. At higher angles, the energy absorption ability increased significantly with an increase in tube thickness though the effect was negligible at lower angles [Figure 8.13(a)]. The interactions of other parameters were not observed as the p-values of those terms were less than 0.05 and eliminated in Equation 8.10. For a tubular structure to be used for a zero-Poisson's-ratio application, the energy absorption ability of the structure can be considered up to the ZPR strain limit. Also, the structures having the higher ZPR strain limit exhibited lower compressive strength and vice versa. Figure 8.13(b) shows the stress-strain plots of three different tubular structures with the highest ZPR strain limit (H-ZSL), highest peak compressive strength (H-PCS) and highest energy absorption ability (H-EAA) for SR-SRH-1. Moreover, the mechanical properties obtained from the three stress-strain plots in Figure 8.13(b) are shown in Figure 8.13(c). The tubular lattice structure having the highest energy absorption ability exhibited intermediate values of ZPR strain limit of 21.4% and compressive strength of 2.54 MPa. Thus, the energy absorption ability up to the ZPR strain limit of the tubular lattice structure is a trade-off between the peak compressive strength and the ZPR strain limit.

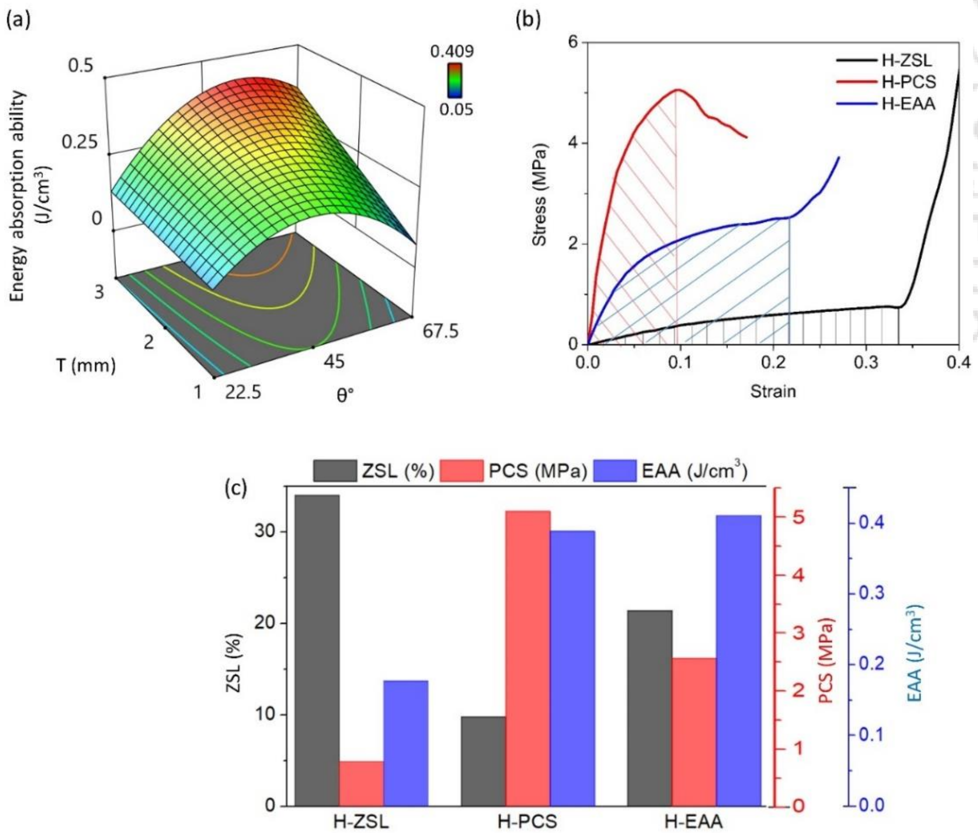

Figure 8.13. (a) Effects of tube thickness and angle on the energy absorption ability of SR-SRH-1with h/l ratio is 1.5, (b) stress-strain plots of three different SR-SRH-1 tubular structures with highest ZPR strain limit (H-ZSL), highest peak compressive strength (H-PCS) and highest energy absorption ability (H-EAA), and (c) bar diagram showing ZPR strain limit (ZSL), peak compressive strength (PCS) and energy absorption ability (EAA) of H-ZSL, H-PCS and H-EAA tubular structures.

For the SR-SRH-2, although the tubular lattices have higher peak compressive strength than the SR-SRH-1 tubular lattices but the SR-SRH-2 lattices have a significantly lower ZPR strain limit. Thus, the SR-SRH-2 lattices have lower energy absorption ability than the SR-SRH-1 lattices. The highest energy absorption ability of the SR-SRH-2 lattice structures was 0.115 J/cm^3, which is only 28 % of the highest energy absorption ability observed for SR-SRH-1.

8.4 Comparison of SR-SRH tubular lattices with semi-reentrant honeycomb (SRH) tubular structures

This section compares the proposed SR-SRH tubular structures were compared with the SRH tubular structures with the same relative density. Like the proposed tubular structures, SR-SRH-1 and SR-SRH-2, the unit cells of two SRH tubular structures, SRH-1 and SRH-2, were laid along two different directions, as shown in Figure 8.14(a) and (b). The variations of the mechanical responses of the SRH-1 and SRH-2 tubular structures, i.e. the design matrices, used for the design of experiments are mentioned in Tables 8.6 and 8.7, respectively.

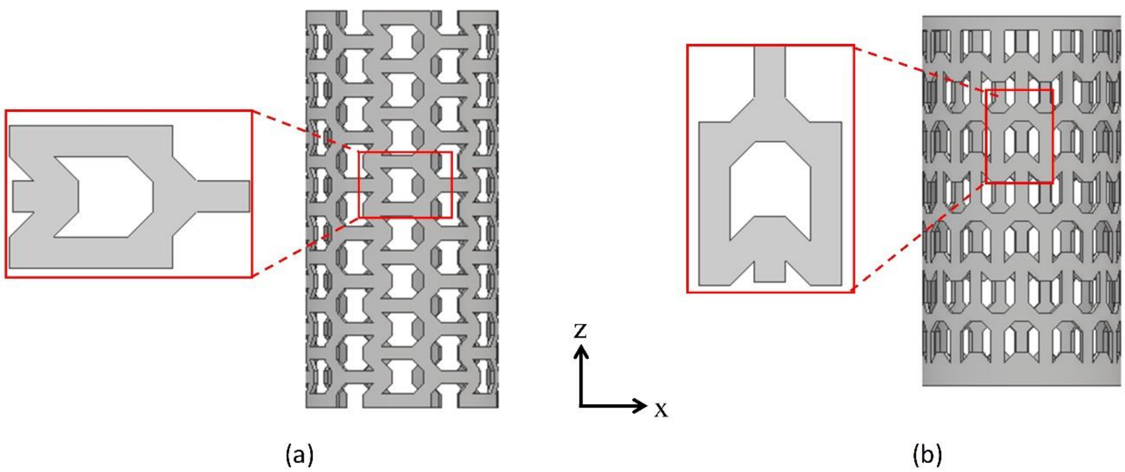

Figure 8.14. The unit cells and tubular lattice structures of (a) SRH-1 and (b) SRH-2, for an h/l ratio of 1.5, θ of 45° and T of 1 mm.

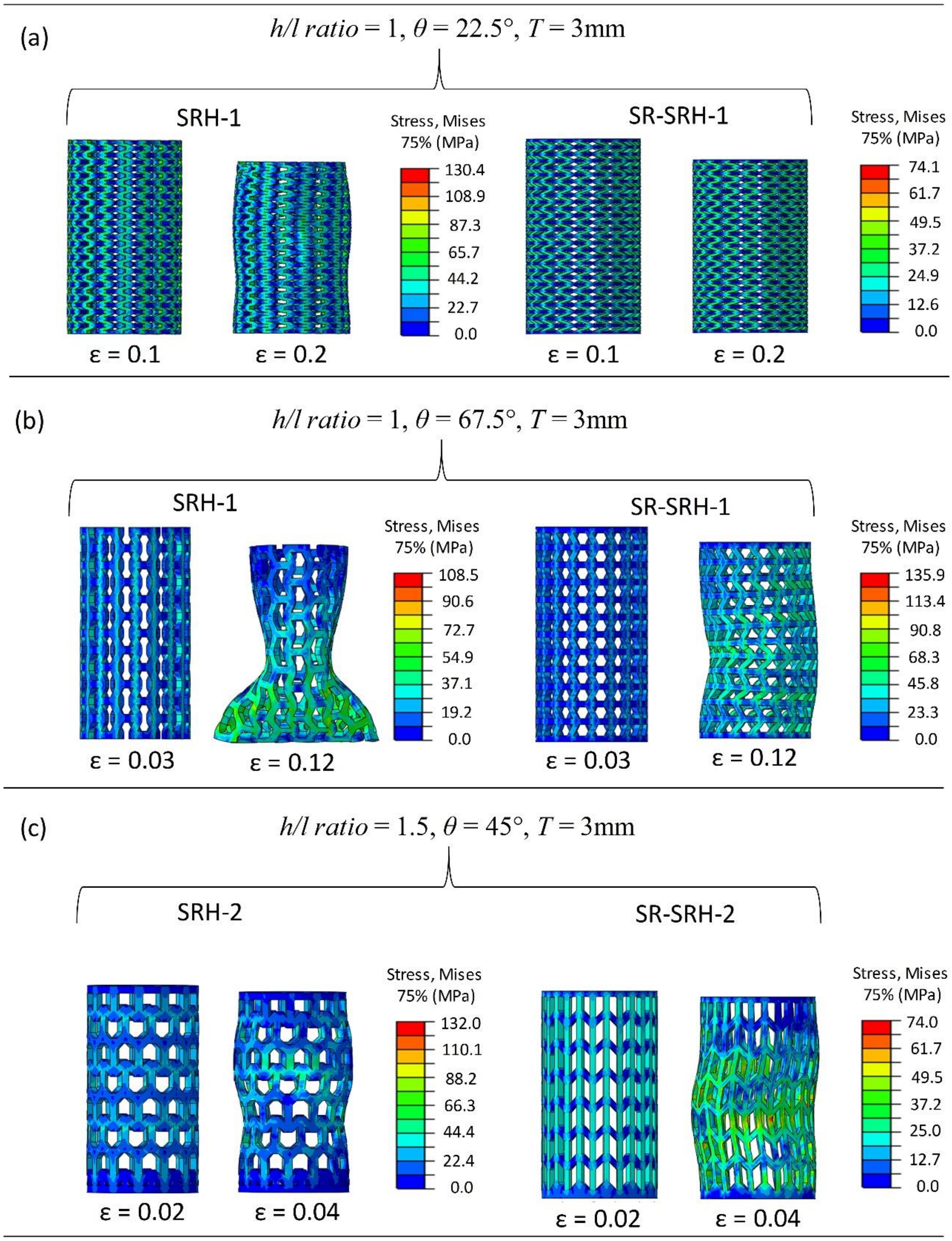

Figure 8.15. The difference in deformation behaviour of the proposed SR-SRH tubular structures with the original SRH structures: (a) SRH-1 and SR-SRH-1 for h/l ratio = 1, θ = 22.5° and T = 3mm (b) SRH-1 and SR-SRH-1 for h/l ratio = 1, θ = 67.5° and T = 3mm and (c) SRH-1 and SR-SRH-1 for h/l ratio = 1.5, θ = 45° and T = 3mm.

Table 8.6. Design matrix with input variables and output responses for SRH-1.

Sample No.	Input variables			Output responses			
	h/l ratio	Angle (°)	Tube thickness (mm)	Compressive strength (MPa)	Elastic modulus (MPa)	ZPR strain limit (%)	Energy absorption (J/cm^3)
1	1.5	45	2	5.52	148.84	4.4	0.178
2	1	67.5	3	6.97	249.64	4.05	0.21
3	1	22.5	3	2.35	21.91	15.74	0.22
4	1	22.5	1	1.75	37.97	5.36	0.0575
5	1.5	22.5	2	3.35	118.4	4.4	0.107
6	2	45	2	5.48	223.43	3.15	0.127
7	2	67.5	1	4	302.24	1.34	0.039
8	1.5	45	1	3.64	207.83	1.8	0.05
9	1.5	45	2	5.52	148.84	4.4	0.178
10	2	22.5	3	4.5	161.44	4.04	0.13
11	2	67.5	3	7.17	264.21	4.03	0.21
12	1.5	45	2	5.52	148.84	4.4	0.178
13	1	67.5	1	4.3	326.27	1.34	0.0388
14	1.5	45	2	5.52	148.84	4.4	0.178
15	1.5	45	2	5.52	148.84	4.4	0.178
16	2	22.5	1	3.3	187.53	1.75	0.044
17	1.5	45	2	5.52	148.84	4.4	0.178
18	1	45	2	4.52	138.08	5.38	0.169
19	1.5	67.5	2	6.43	296.55	2.7	0.127
20	1.5	45	3	5.72	173.65	5.85	0.231

8.4.1 Deformation mechanisms

The comparison of the deformation behaviour of SRH and the SR-SRH lattice structures is shown in Figure 8.15. As the angle θ significantly influenced the deformation behaviour of SRH and SR-SRH structures, the deformation behaviour of these structures is compared at both low and high angles in Figure 8.15(a) and (b), respectively. For the lower angle, θ=22.5°, with *h/l ratio*=1 and *T*=3mm, the buckling initiated at a strain of 15.7% after the initial uniform deformation for the SRH-1 structure, whereas SR-SRH-1 did not exhibit any buckling before starting of self-contact between struts at a strain of 34% [Figure 8.10(a)]. For higher angle, θ=67.5°, with *h/l ratio*=1 and *T*=3mm, both SRH-1 and SR-SRH-1 deformed by buckling after the initial uniform deformation, though the buckling of the SRH-1 tubular structure occurred much early at a strain of 4.05% compared to the buckling strain of 9.8% for the SR-SRH-1 tubular structure. As compared to SRH tubular structures for the same geometrical parameters, all SR-SRH-1 tubular lattices deformed by either self-contact or delayed buckling, due to which the proposed SR-SRH-1 structures achieved larger ZPR strain limit and higher energy absorption ability. In the case of SRH-2 and SR-SRH-2 tubular lattices [Figure 8.15(c)], both these structures were deformed by global bucking at very low strains (<0.035). These structures displayed much lower energy absorption abilities than the SR-SRH-1 tubular structure. However, due to the additional struts present along the loading direction, the SR-SRH-2 structure exhibited the highest compressive strength and elastic modulus among all the tubular lattice structures studied in this work.

Table 8.7. Design matrix with input variables and output responses for SRH-2.

No.	**Input variables**			**Output responses**			
	h/l ratio	**Angle (°)**	**Tube thickness (mm)**	**Compressive strength (MPa)**	**Elastic modulus (MPa)**	**ZPR strain limit (%)**	**Energy absorption (J/cm^3)**
1	1	45	2	4.16	133.26	3.62	0.092
2	2	67.5	3	6.88	227.23	3.63	0.157
3	1.5	45	2	5.01	226.02	2.33	0.087
4	1	67.5	1	3.01	91.356	3.77	0.067
5	2	22.5	1	3.49	346.02	0.91	0.0175
6	1	67.5	3	4.65	89.75	7.77	0.217
7	1.5	45	1	3.47	224.16	1.5	0.0311
8	1.5	45	2	5.01	226.02	2.33	0.087
9	1.5	67.5	2	6.81	207.23	3.63	0.124
10	1	22.5	1	2.77	201.58	1.51	0.027
11	1.5	45	2	5.01	226.02	2.33	0.087
12	1.5	45	2	5.01	226.02	2.33	0.087
13	1	22.5	3	3.63	190.75	2.07	0.042
14	2	45	2	6.11	290.13	2.11	0.0739
15	1.5	22.5	2	5.27	274.18	1.96	0.062
16	2	22.5	3	5.73	301.2	1.8	0.066
17	1.5	45	3	5.92	223.8	3.3	0.13
18	2	67.5	1	3.55	253.56	1.5	0.034
19	1.5	45	2	5.01	226.02	2.33	0.087
20	1.5	45	2	5.01	226.02	2.33	0.087

8.4.2 Energy absorption ability

The variation of the energy absorption ability with respect to the input variables of SRH-1 was similar to SR-SRH-1. In fact, both SR-SRH-1 and SRH-1 tubular structures exhibited the highest energy absorption ability for the same input parameters with an *h/l ratio* of 1.5, T of 3mm and θ of 45°. The SR-SRH-1 structure exhibited an energy absorption ability of 0.409 J/cm^3, 1.8 times that of the original SRH-1 structure. Compared to the SR-SRH-1 tubular structure, although the SRH-1 structures showed higher compressive strength due to thicker struts, they displayed a very low ZPR strain limit, which was the main cause for their lower energy absorption ability. The comparison of the highest values of the mechanical properties of these structures obtained from the design matrices (Table 8.2, 8.3, 8.6 and 8.7) is shown in Figure 8.16. The higher energy absorption ability of the SR-SRH-1 was due to the continuous struts throughout the tube circumference, which delayed the buckling of the structure during deformation, compared to the SRH-1 structure, which lacked strut continuity along the circumference.

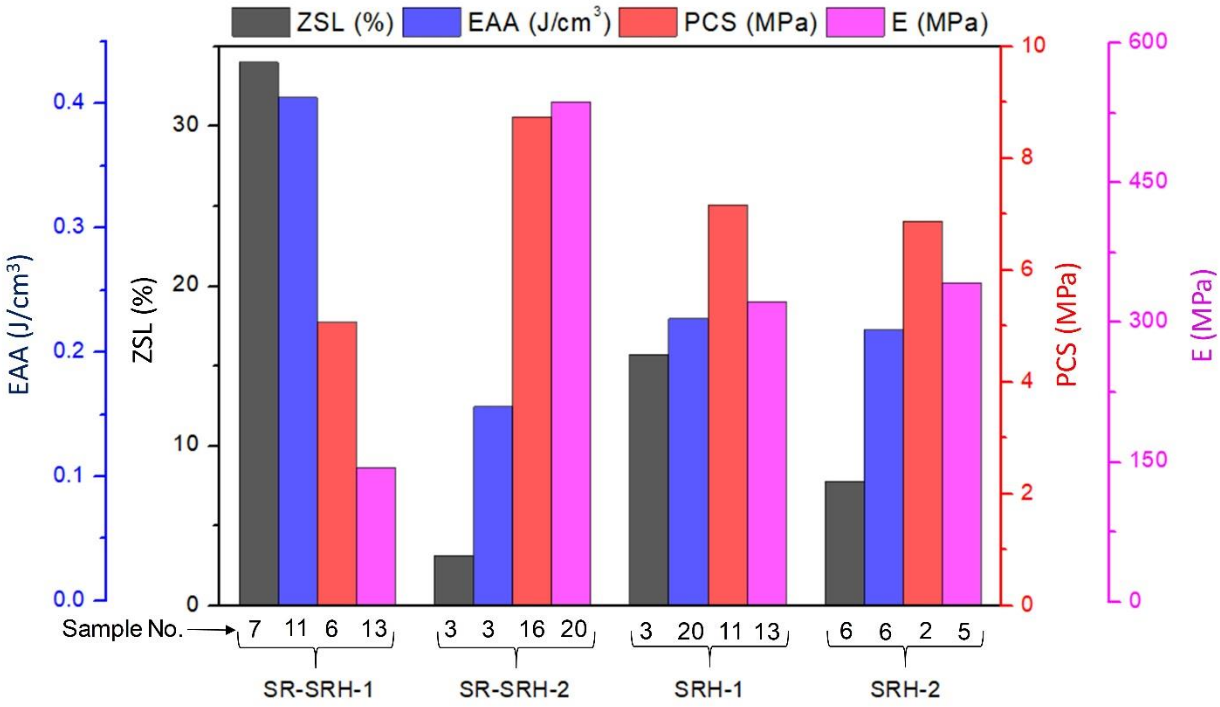

Figure 8.16. Comparison of the highest values of mechanical properties obtained from the design matrices (Table 2, 3, T1 and T2) of the proposed modified semi-reentrant honeycomb ZPR tubular structures, SR-SRH-1 and SR-SRH-2, with the original semi-reentrant honeycomb ZPR tubular structures, SRH-1 and SRH-2.

8.4.3 Compressive strength and elastic modulus

Both SR-SRH-2 and SRH-2 tubular structures exhibited the highest compressive strength for the same input parameters with an *h/l ratio* of 2, *T* of 3mm and θ of 67.5° (Table 8.3 and Table 8.7). The highest compressive strength of the SRH-2 was 6.88 MPa compared to 8.74 MPa of SR-SRH-2 (Figure 8.16). However, among the SRH structures, the SRH-1 tubular lattice with an *h/l ratio* of 2, θ of 67.5° and *T* of 3mm showed the highest compressive strength of 7.17 MPa (Figure 8.16). Nevertheless, it was still lower than the highest compressive strength observed for SR-SRH tubular lattice structures.

The highest elastic moduli of SRH-2 and SR-SRH-2 structures were 346.02 MPa and 540.6 MPa, respectively, both structures having the same input parameters of an *h/l ratio* of 2, T of 1mm and θ of 22.5° (Figure 8.16).

In summary, for nearly the same relative density and the same height and diameter of the ZPR tubular lattice structures, the SR-SRH-1 structure is appropriate for energy absorption applications, whereas the SR-SRH-2 structure can be used for high stiffness-high strength applications. Thus, a ZPR tube with superior mechanical properties can be achieved by changing the design configuration of the proposed ZPR tubular structure.

8.5 Optimized structure for highest ZPR strain limit and energy absorption ability

An optimized design of the SR-SRH-1 tubular lattice structures was determined to exhibit high energy absorption ability with a high ZPR strain limit. The goal is to develop a ZPR tubular lattice structure by maximizing the ZPR strain limit and the energy absorption ability keeping the input variables within the following limits.

$$1 \leq h/l\ ratio \leq 2 \quad 8.17$$

$$22.5° \leq \theta \leq 67.5° \quad 8.18$$

$$1mm \leq T \leq 3mm \quad 8.19$$

The optimized SR-SRH-1 tubular lattice structure made of PA12 was fabricated using HP Multi Jet Fusion 3D-printing technique. Two samples of the optimized structure were tested under compression to check the repeatability of the stress-strain behaviour and the deformation mechanism. The deformation behaviour of the optimized structure obtained from experiments and numerical simulations are shown in Figure 8.17(a) and (b), respectively. In the initial compression stage, up to a strain of ~20%, bending of inclined struts is the dominant local deformation mechanism, as shown in Figure 8.17(c). The mechanical properties suggested by DoE and those obtained from numerical simulation and experiments are listed in Table 8.8. The optimized structure started buckling slightly at a strain of ~25% in finite element simulation and ~21% in the experiment. The buckling phase, in which the ZPR effect was lost, ended at a strain of ~32% for both numerical simulation and experiment, and after that, the uniform deformation of the structure reappeared and continued beyond densification. The intermediate buckling phase helped delay the densification, which enhanced the energy absorption till densification.

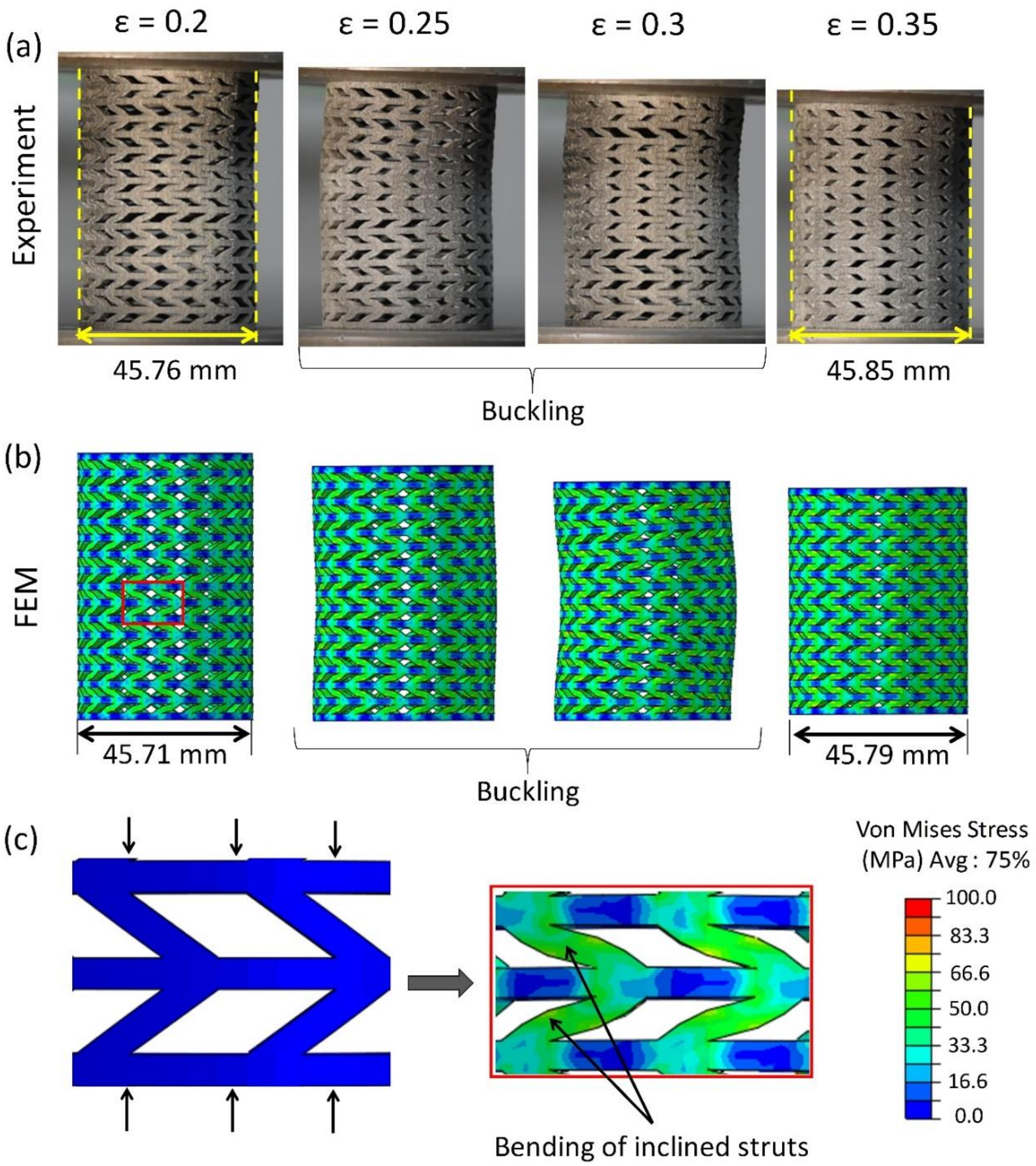

Figure 8.17. Deformation behaviour of optimized SR-SRH-1 tubular lattice obtained from (a) experiment and (b) finite element simulation, and (c) zoomed image showing the deformation of the tubular lattice by bending of inclined struts.

The Poisson's ratio versus strain plots obtained from the finite element simulation and experiments, which illustrate the intermediate buckling strain ranges, are shown in Figure 8.18(a). The stress-strain plots obtained from the finite element simulation and the experiments are in good agreement, as shown in Figure 8.18(b). The stress-strain plots obtained from numerical simulations, shown in Figure 8.18(c), demonstrate the comparison of energy absorption ability and ZPR strain limit along with the densification strain (DS) and ZPR strain limit (ZSL) of the optimized structure with that of tubular structures having highest energy absorption ability (H-EAA) and highest strain limit (H-ZSL).

The energy absorption ability of the optimized structure was initially calculated till the buckling strain, i.e. 24.75% in finite element simulation and 21.1% in the experiment (Table 8.8). However, the buckling disappeared with further deformation and the ZPR effect was retained, as shown in Figure 8.17 and Figure 8.18(a). During this period, the structure continued to absorb energy until the self-contact of the struts occurred at a strain of ≈ 34%. Thus, the energy absorption ability can be calculated for the optimized structure until the self-contact of the struts, and it increased from 0.385 J/cm^3 to 0.59 J/cm^3, which was higher than 0.409 J/cm^3 calculated for the H-EAA tubular lattice (Table 8.8 and Figure 8.18(c)).

Table 8.8. Comparison of energy absorption ability and ZPR strain limit of the optimized SR-SRH-1 lattice obtained from DoE, numerical simulation and experiments.

	DoE	**FEM**	**Experiment**
Energy Absorption up to ZPR strain limit (J/cm^3)	0.408	0.385	0.328 ± 0.015
Energy Absorption up to densification (J/cm^3)	–	0.590	0.547 ± 0.018
ZPR strain limit (%)	24.86	24.75	21.1 ± 0.2

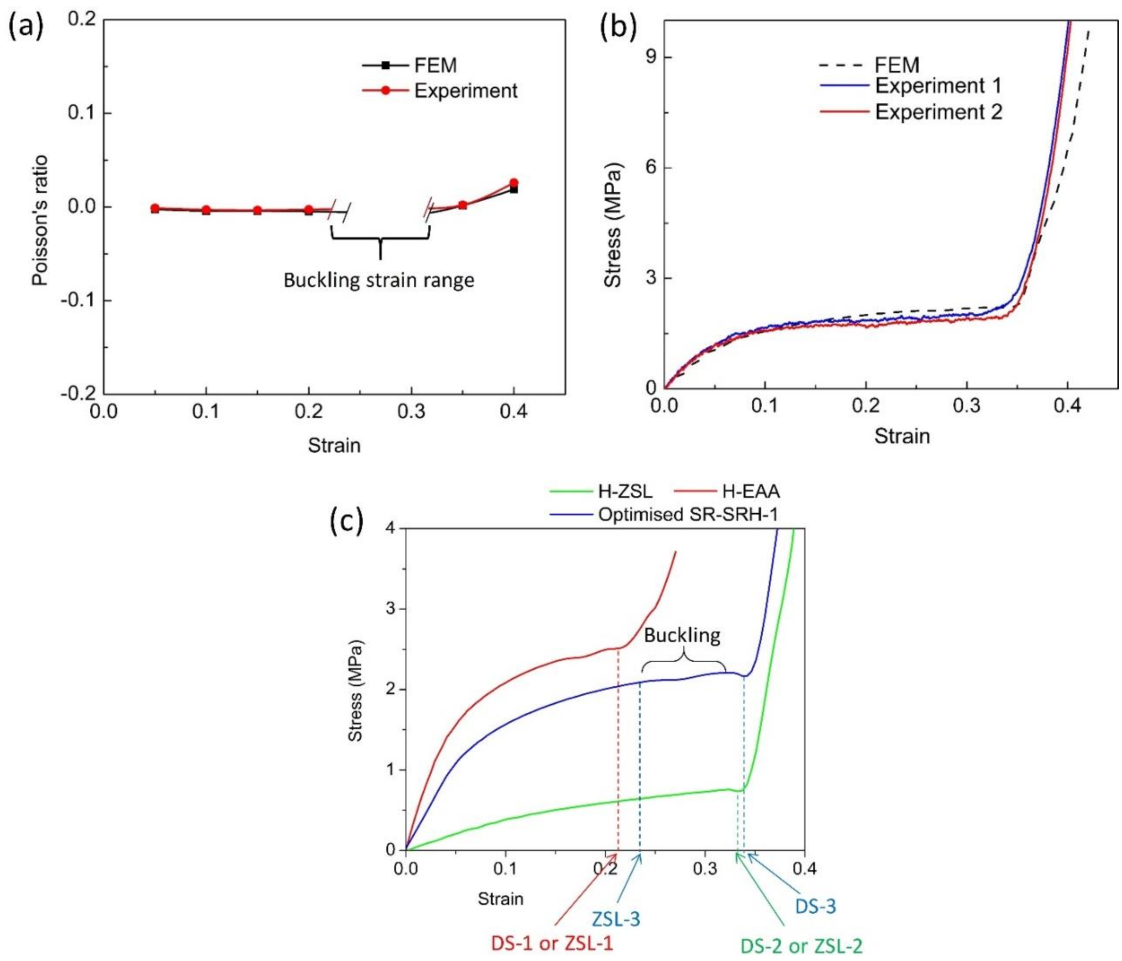

Figure 8.18. (a) Poisson's ratio vs. strain plot and (b) stress-strain plots of the optimized ZPR tubular lattice structure obtained from experiments and numerical simulation, and (c) comparison of energy absorption ability and ZPR strain limit obtained from finite element (FE) simulation of the optimized structure with that of the tubular structures having highest energy absorption ability (H-EAA) and highest strain limit (H-ZSL).

8.6 Optimized structure for highest compressive strength and elastic modulus

Another optimized structure based on SR-SRH-2 tubular lattice structure was determined using the DoE technique to maximize the compressive strength and the elastic modulus considering the input variables within the range mentioned in Equations 8.17 to 8.19. This optimized structure was also fabricated using 3D printing, and the results obtained from the experiments were compared with the numerical simulations (Table 8.9). The deformation behaviour and stress-strain response obtained from the numerical simulations and the experiments are shown in Figure 8.19. At a very low strain, the optimized tubular structure was deformed by global buckling, and the ZPR effect was lost. The deformation behaviour was similar in both finite element simulation and experiment [Figure 8.19 (a) and (b)]. In Table 8.10, the compressive strength and the elastic modulus of the SR-SRH-2 optimized structure were compared with that of the structures having the highest peak compressive strength (H-PCS), *i.e.* sample no. 16, and highest elastic modulus (H-E), *i.e.* sample no. 20, mentioned in Table 8.3. Thus, optimized structures can be made that are useful for high-strength and high-stiffness applications.

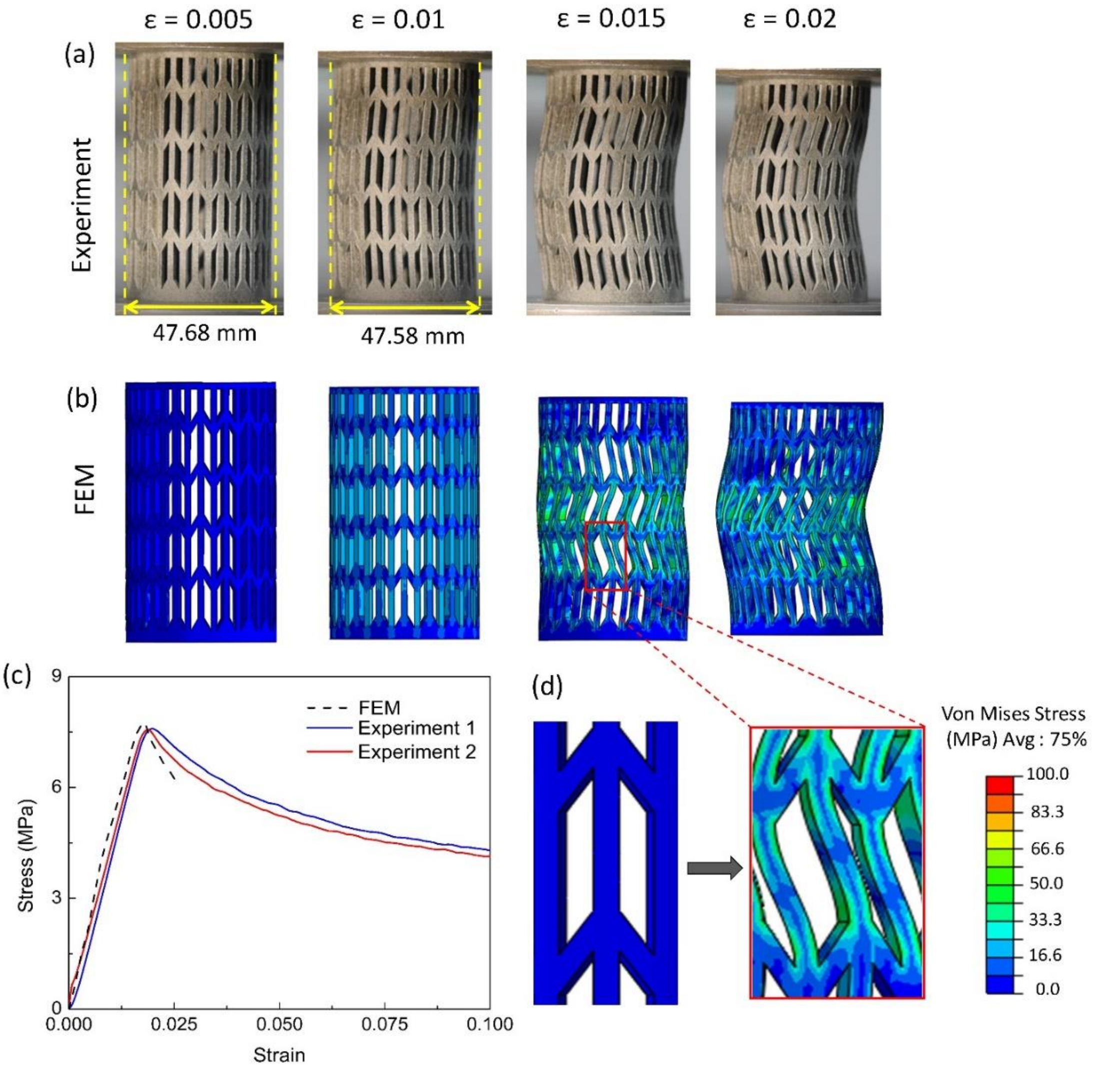

Figure 8.19. Deformation behaviour of optimized SR-SRH-2 tubular lattice obtained from (a) experiment and (b) finite element simulation, (c) stress-strain plots of the optimized SR-SRH-2 tubular lattice, and (d) zoomed image showing the deformation of the tubular lattice by buckling of the vertical struts.

Table 8.9. Comparison of compressive strengths and elastic moduli obtained for the optimized SR-SRH-2 structure from DoE, finite element simulation and experiments.

	DoE	FE simulation	Experiment
Compressive strength (MPa)	8.74	7.97	7.57 ± 0.02
Elastic modulus (MPa)	510.89	504.94	447.1 ± 18.1

Table 8.10. Comparison of the compressive strengths and elastic moduli for the highest peak compressive strength (H-PCS) structure, highest elastic modulus (H-E) structure and the optimized structure of the SR-SRH-2 design obtained from finite element simulations.

	H-PCS	H-E	Optimized SR-SRH-2
Compressive strength (MPa)	8.74	4.00	7.97
Elastic modulus (MPa)	463.8	540.6	504.9

8.7 Summary

This study aimed to design and develop novel ZPR tubular lattice structure to achieve high energy absorption ability or high-strength and high-stiffness. The quasi-static compressive mechanical properties of the tubular structures were studied by numerical simulations using Abaqus/Explicit. The effects of unit cell parameters, i.e., the ratio of the length of struts, the angle between the struts and the tube thickness, on the compressive strength, elastic modulus, extent of zero Poisson's ratio deformation and energy absorption ability of the tubular structures were studied using a Response Surface Method (RSM) based Design of Experiments (DoE) technique. Analysis of Variance (ANOVA) was used to evaluate the efficacy of the regression models developed by DoE. Based on the DoE analyses, the unit cell parameters of the tubes were optimized such that the cylindrical tubes can exhibit high energy absorption ability and high zero Poisson's ratio deformation range. Another design of the proposed ZPR tubular lattice structure was optimized to attain high compressive strength and elastic modulus. The optimized tubular lattice structures were fabricated with Polyamide 12 (PA12) using the HP Multi-Jet Fusion 3D-printing technique, and quasi-static compression tests were performed to validate the numerical results.

CHAPTER 9. CONCLUSIONS AND SCOPE FOR FUTURE WORK

9.1 Conclusions

In this thesis, different techniques to improve the mechanical properties of the negative and zero Poisson's ratio lattice structures were investigated. The lattices structures were fabricated by metallic or polymeric additive manufacturing techniques. The metallic lattices were fabricated by Selective Laser Melting using AlSi10Mg as the parent material, and the polymeric lattices were fabricated by HP Multi Jet Fusion using polyamide-12 (PA12) as the parent material. The in-plane mechanical properties of the metallic lattices were studied at both quasi-static and high-strain rate loading conditions, while the in-plane mechanical properties of the polymeric lattices were studied at only quasi-static loading. Finite element simulations were conducted to investigate the deformation mechanisms and study the effect of geometric parameters of the lattice unit cells on the mechanical properties. The results obtained from numerical simulations were corroborated with the experiments. The effectiveness of the modified lattices were confirmed by comparing them with the commonly-studied lattice structures as benchmarks. The main conclusions drawn from this thesis are discussed in a chapter-wise manner as follows:

9.1.1 Quasi-static and dynamic behaviour of varying cross-section metallic 3D-reentrant lattice

The 3D-reentrant lattice structures with uniform and tapered struts were investigated at quasi-static and dynamic loading conditions. The AlSi10Mg based lattices were successfully fabricated by laser powder bed fusion process. The major conclusions from this study are:

- In both the quasi-static and high strain rate loading, it was observed that up to a certain degree of taper in the cross-section of the struts of the 3D-reentrant lattice, the mechanical properties improved, and with further increase in the degree of taper, the mechanical properties decreased.

- It was confirmed from the numerical simulations that the stress concentration sites disappeared from the uniform strut 3D-reentrant lattice when the struts were tapered to a certain degree, and they reappeared with further increase in the degree of taper.
- The Poisson's ratio of the tapered 3D-reentrant structures decreased with the increase in the degree of taper, which was because with the increase in the degree of taper, the effective length of the oblique struts decreased.

It can be concluded from this study that a certain degree of tapered in the cross-section of the 3D-reentrant structures can led to improvement in the mechanical properties in both quasi-static and dynamic loading conditions. These tapered 3D-reentrant lattices can be used for applications requiring high-strength and high-stiffness, along with negative Poisson's ratio characteristics.

9.1.2 Composite-inspired auxetic multilattice structures with improved strength and energy absorption

In this study, the mechanical properties of the auxetic 3D-reentrant lattice structure were enhanced by mimicking structures of composite materials. The 3D-reentrant lattice, which was considered as the base lattice of the composite structure, possesses negative Poisson's ratio characteristic with lower strength and lower energy absorption. The BCTZ lattice having high strength and energy absorption ability were used as reinforcements in the matrix of 3D-reentrant lattice to improve the energy absorption ability and strength, without compromising the negative Poisson's ratio characteristic. Three different multilattice composite structures having the same relative density as pure 3D-reentrant lattice were fabricated by the HP Multi Jet Fusion technique, and quasi-static compression tests were performed to study the mechanical properties of the lattice structures.

The conclusions drawn from the experimental and numerical studies are as follows:

- With a 10% volume fraction of BCTZ lattice as reinforcements, the CFRM structure exhibited 40.0% increase in strength and 21.3% increase in elastic modulus compared with the pure 3D-reentrant lattice. The strength to stiffness ratio, a higher value of which is desired for potential biomedical bone implant applications, is found to be 13% higher for the CFRM structure than the pure 3D-reentrant lattice.

- The PRM structure demonstrated the highest energy absorption ability among the three multilattice composite structures having a 10% volume fraction of reinforcements, while the peak stress attained by the PRM structure was less as compared to the other two multilattice structures. The increase in energy absorption for the PRM structure was 81.3% compared to the pure 3D-reentrant lattice, while the peak stress attained by the PRM structure was 13.3% less than that of the CFRM structure. The high energy absorption ability of the PRM structure was due to its high densification strain and a strain hardening effect that was not observed in the pure 3D-reentrant structure.
- It was found that the elastic moduli and Poisson's ratios of the multilattice structures can be predicted by the conventional rule of mixture used for composite materials. The elastic moduli and Poisson's ratios of the CFRM and the PRM structures with 10% and 25% reinforcements and those of the DFRM structure with 10% reinforcements showed good agreement with the elastic moduli and the Poisson's ratios predicted by the rule of mixtures for composite materials. The elastic modulus improved from 32.25 MPa for 3D-reentrant lattice to 40.10 MPa and 51.20 MPa for CFRM structures with 10% and 25% reinforcements, respectively. However, the auxetic effect decreased as the Poisson's ratio increased from −0.37 for the pure 3D-reentrant lattice to −0.32 and −0.19 for the CFRM structures having 10% and 25% reinforcements, respectively. Similarly, the elastic moduli and Poisson's ratios of the PRM and the DFRM structures were also in good agreement with the rule of mixture for composite materials. This study demonstrates that using a multilattice structure instead of a single lattice is not only a technique to tailor the elastic modulus but also useful to customize the Poison's ratio of the metamaterial for a specific application.
- The CFRM and the PRM structures with 25% reinforcements exhibited significant post-yield strain hardening compared to the CFRM and the PRM structures with 10% reinforcements. The densification strain for both the multilattice structures did not vary much with the increase in volume fraction of reinforcements. However, the energy absorption abilities of the two multilattice structures with

25% reinforcements were almost double than that of the respective multilattice structures with 10% reinforcements.

Thus, an auxetic multilattice composite with continuous fibre reinforcements can be useful for fully-porous heavy-load-bearing orthopaedic implants, in which high strength to stiffness ratio is recommended, while the particle reinforced auxetic multilattice composite can be used for high-energy absorbing applications.

9.1.3 A novel strategy to design lattice structures with zero Poisson's ratio

A new method of designing lattice structures exhibiting zero-Poisson's-ratio was proposed in this study. The strategy combines a positive and a negative Poisson's ratio exhibiting lattice to achieve zero Poisson's ratio of the resulting lattice using classical composite rule of mixture. Two different composite lattice structures, P-ZPR and F-ZPR, were developed by imitating the particle-reinforced and the fiber-reinforced composite materials, respectively. The major conclusions drawn from this work are summarized as follows:

- Near-zero Poisson's ratio for both P-ZPR and F-ZPR structures was achieved at a volume fraction of 42.8% of the BCTZ lattice reinforcements.
- Both the proposed ZPR structures exhibited superior mechanical properties than the original 3D-reentrant lattice due to BCTZ lattice reinforcements. The F-ZPR and the P-ZPR structures exhibited nearly equal compressive strength. However, the F-ZPR structure displayed a higher elastic modulus than the P-ZPR structure as the long fiber-like BCTZ reinforcements in the F-ZPR structure satisfied the isostrain condition.
- The proposed ZPR structures outperformed three other previously-studied hexagonal honeycomb based ZPR structures, namely SRE, RSRE and AuxHex, in terms of compressive strength, elastic modulus and particularly energy-absorbing ability. Moreover, the P-ZPR structure maintained zero Poisson's ratio effect for the largest value of strain among all the ZPR structures.
- The mechanical properties of the proposed ZPR structures can be further improved by the following methods: (1) using a reinforcement lattice that has higher strength and elastic modulus than the BCTZ lattice and/or (2) increasing the volume fraction of the reinforcement lattice.

The proposed strategy of improving the mechanical properties of ZPR lattice structures using a reinforcement lattice can be more promising than the conventional method of tailoring the unit cell geometry of a ZPR lattice. Thus, the composite-materials inspired ZPR lattice structures can be an excellent choice in aerospace, bio-medical and automobile industry due to the ease of design and improved mechanical properties.

9.1.4 A high energy absorbing lattice exhibiting zero Poisson's ratio up to large strain

The Strut Reinforced- Semi Reentrant Honeycomb (SR-SRH) lattice was designed to exhibit zero Poisson's ratio with enhanced stability during deformation. Numerical simulations were conducted to understand the mechanical behaviour of the ZPR structure, which was corroborated by experiments. Bending of oblique struts was the dominant deformation mechanism, and the structure exhibited zero Poisson's ratio behaviour during deformation. The additional struts in the SR-SRH lattice provided stability during deformation, and improved the ZPR strain range to 0.45, which was 0.24 for the original SRH lattice. Along with the ZPR strain range, the energy absorption ability and the specific energy absorption ability of the SR-SRH lattice were also doubled than the original SRH lattice during the quasi-static compression.

9.1.5 A high-performance design of tubular lattice structure having zero Poisson's ratio

The strut-reinforced semi-reentrant honeycomb (SR-SRH) tubular lattices were proposed in this work. Finite element simulations of the quasi-static compression of the tubular lattices were used to determine an optimized tubular structure for desired mechanical properties using the Design of Experiments technique. The optimized tubular structures were designed and fabricated by HP Multi Jet Fusion and quasi-static tests were performed to validate the numerical simulations. The major conclusions drawn from this work are:

- The SR-SRH-1 tubular lattice exhibited zero Poisson's ratio behaviour to a remarkably higher strain with a maximum value of 34% compared to 15.7% of the original SRH-1 structure. This high ZPR strain limit (ZSL) of the SR-SRH-1 structure was due to delayed buckling.

- Another configuration of the SR-SRH-1 tubular lattice exhibited the highest energy absorption ability of 0.409 J/cm^3 among all the tubular lattices studied in this work. The unit cell parameter θ had the highest effect on the energy absorption ability.
- Among all the tubular lattices investigated in this study, one configuration of the SR-SRH-2 tubular lattice exhibited the highest compressive strength of 8.74 MPa, and another SR-SRH-2 lattice exhibited the highest elastic modulus of 540.6 MPa.
- An optimized SR-SRH-1 tubular lattice for a high ZPR strain limit and high energy absorption ability was designed using the DoE technique. The significantly high energy absorption ability of the optimized lattice structure was attributed to the intermediate buckling of the SR-SRH-1 lattice during compression. Another optimized SR-SRH-2 structure was designed to achieve high strength and elastic modulus.

Thus, for applications requiring zero Poisson's ratio deformation behaviour in bio-medical and automobile industries, the proposed tubular lattice structures can be tailored to achieve a combination of desired mechanical properties. The SR-SRH-1 tubular lattices can be used for high energy absorbing applications that require a high ZPR strain limit, and the SR-SRH-2 lattice can be used for applications requiring high compressive strength and high elastic modulus.

9.2 Scope for future work

This thesis is an attempt to study different techniques to improve the mechanical properties of the negative and zero Poisson's ratio lattice structures. Although this work can open a new door to design auxetic and ZPR lattices for enhanced performance, but some more studies need to be carried out such that these lattice structures can be used in commercial applications. The following studies can be conducted in future:

- The behaviour of the tubular lattices at high strain rate needs to be studied for their potential applications in crash-worthiness.
- Studies on implementing the proposed lattices in different fields of applications are required.

LIST OF PUBLICATIONS

List of Journal articles from the thesis

1. **Sahariah BJ**, Baishya MJ, Namdeo A, Khanikar P. A novel strategy to design lattice structures with zero Poisson's ratio. ***Engineering Structures*** **(2023)**, 288, 116214.
2. **Sahariah BJ**, Dalakoti M, Khanikar P. A high-performance design of tubular lattice structure having zero Poisson's ratio. ***Mechanics of Advanced Materials and Structures*** **(2023)**, 1–21.
3. **Sahariah BJ**, Namdeo A, Khanikar P. Composite-inspired multilattice metamaterial structure: An auxetic lattice design with improved strength and energy absorption. ***Materials Today Communications*** **(2022)**, *30*, 103159.
4. **Sahariah BJ**, Namdeo A, Venkitanarayanan P, Khanikar P. Quasi-static and dynamic mechanical properties of modified varying cross-section 3D-reentrant lattice with negative Poisson's ratio *(Under preparation).*
5. **Sahariah BJ**, Khanikar P. A high energy absorbing lattice exhibiting zero Poisson's ratio for large strain *(Under preparation).*

List of conferences

1. **Sahariah BJ**, Khanikar P. Paper presentation at The 13th International Symposium on Plasticity and Impact Mechanics (IMPLAST 2022), IIT Madras, India.
2. **Sahariah BJ**, Khanikar P. Paper presentation at The 8th Asian Conference on Mechanics of Functional Materials and Structures (ACMFMS 2022), IIT Guwahati, India.
3. **Sahariah BJ**, Namdeo A, Khanikar P. Poster Presentation at Additive Manufacturing: Materials Design and Alloy Development III - Super Materials and Extreme Environments, TMS (2021), USA.

REFERENCES

[1] Gibson LJ, Ashby MF. Cellular Solids: Structure and Properties. 2nd ed. Cambridge University Press; 1997. https://doi.org/10.1017/CBO9781139878326.

[2] Nazir A, Abate KM, Kumar A, Jeng J-Y. A state-of-the-art review on types, design, optimization, and additive manufacturing of cellular structures. Int J Adv Manuf Technol 2019;104:3489–510. https://doi.org/10.1007/s00170-019-04085-3.

[3] Ashby MF. The properties of foams and lattices. Phil Trans R Soc A 2006;364:15–30. https://doi.org/10.1098/rsta.2005.1678.

[4] Xiong J, Mines R, Ghosh R, Vaziri A, Ma L, Ohrndorf A, et al. Advanced Micro-Lattice Materials: Advanced Micro-Lattice Materials. Adv Eng Mater 2015;17:1253–64. https://doi.org/10.1002/adem.201400471.

[5] Habib FN, Iovenitti P, Masood SH, Nikzad M. In-plane energy absorption evaluation of 3D printed polymeric honeycombs. Virtual and Physical Prototyping 2017;12:117–31. https://doi.org/10.1080/17452759.2017.1291354.

[6] Rashed MG, Ashraf M, Mines RAW, Hazell PJ. Metallic microlattice materials: A current state of the art on manufacturing, mechanical properties and applications. Materials & Design 2016;95:518–33. https://doi.org/10.1016/j.matdes.2016.01.146.

[7] Smith M, Guan Z, Cantwell WJ. Finite element modelling of the compressive response of lattice structures manufactured using the selective laser melting technique. International Journal of Mechanical Sciences 2013;67:28–41. https://doi.org/10.1016/j.ijmecsci.2012.12.004.

[8] Li P, Wang Z, Petrinic N, Siviour CR. Deformation behaviour of stainless steel microlattice structures by selective laser melting. Materials Science and Engineering: A 2014;614:116–21. https://doi.org/10.1016/j.msea.2014.07.015.

[9] Dong L, Deshpande V, Wadley H. Mechanical response of Ti–6Al–4V octet-truss lattice structures. International Journal of Solids and Structures 2015;60–61:107–24. https://doi.org/10.1016/j.ijsolstr.2015.02.020.

[10] Li Y, Gu H, Pavier M, Coules H. Compressive behaviours of octet-truss lattices. Proceedings of the Institution of Mechanical Engineers, Part C: Journal of Mechanical Engineering Science 2020;234:3257–69. https://doi.org/10.1177/0954406220913586.

[11] Beharic A, Rodriguez Egui R, Yang L. Drop-weight impact characteristics of additively manufactured sandwich structures with different cellular designs. Materials & Design 2018;145:122–34. https://doi.org/10.1016/j.matdes.2018.02.066.

[12] Greaves GN, Greer AL, Lakes RS, Rouxel T. Poisson's ratio and modern materials. Nature Mater 2011;10:823–37. https://doi.org/10.1038/nmat3134.

[13] Prawoto Y. Seeing auxetic materials from the mechanics point of view: A structural review on the negative Poisson's ratio. Computational Materials Science 2012;58:140–53. https://doi.org/10.1016/j.commatsci.2012.02.012.

[14] Lakes R. Foam Structures with a Negative Poisson's Ratio. Science 1987;235:1038–40. https://doi.org/10.1126/science.235.4792.1038.

[15] Evans KE, Nkansah MA, Hutchinson IJ. Auxetic foams: Modelling negative Poisson's ratios. Acta Metallurgica et Materialia 1994;42:1289–94. https://doi.org/10.1016/0956-7151(94)90145-7.

[16] Kolken HMA, Zadpoor AA. Auxetic mechanical metamaterials. RSC Adv 2017;7:5111–29. https://doi.org/10.1039/C6RA27333E.

[17] Saxena KK, Das R, Calius EP. Three Decades of Auxetics Research − Materials with Negative Poisson's Ratio: A Review: Three Decades of Auxetics Research…. Adv Eng Mater 2016;18:1847–70. https://doi.org/10.1002/adem.201600053.

[18] Novak N, Vesenjak M, Ren Z. Auxetic Cellular Materials - a Review. SV-JME 2016;62:485–93. https://doi.org/10.5545/sv-jme.2016.3656.

[19] Ren X, Das R, Tran P, Ngo TD, Xie YM. Auxetic metamaterials and structures: a review. Smart Mater Struct 2018;27:023001. https://doi.org/10.1088/1361-665X/aaa61c.

[20] Yu X, Zhou J, Liang H, Jiang Z, Wu L. Mechanical metamaterials associated with stiffness, rigidity and compressibility: A brief review. Progress in Materials Science 2018;94:114–73. https://doi.org/10.1016/j.pmatsci.2017.12.003.

[21] Olympio KR, Gandhi F. Zero Poisson's Ratio Cellular Honeycombs for Flex Skins Undergoing One-Dimensional Morphing. Journal of Intelligent Material Systems and Structures 2010;21:1737–53. https://doi.org/10.1177/1045389X09355664.

[22] Soman P, Fozdar DY, Lee JW, Phadke A, Varghese S, Chen S. A three-dimensional polymer scaffolding material exhibiting a zero Poisson's ratio. Soft Matter 2012;8:4946. https://doi.org/10.1039/c2sm07354d.

[23] Huang J, Liu W, Tang A. Effects of fine-scale features on the elastic properties of zero Poisson's ratio honeycombs. Materials Science and Engineering: B 2018;236–237:95–103. https://doi.org/10.1016/j.mseb.2018.11.005.

[24] Grima JN, Oliveri L, Attard D, Ellul B, Gatt R, Cicala G, et al. Hexagonal Honeycombs with Zero Poisson's Ratios and Enhanced Stiffness. Adv Eng Mater 2010;12:855–62. https://doi.org/10.1002/adem.201000140.

[25] Del Broccolo S, Laurenzi S, Scarpa F. AUXHEX – A Kirigami inspired zero Poisson's ratio cellular structure. Composite Structures 2017;176:433–41. https://doi.org/10.1016/j.compstruct.2017.05.050.

[26] Liu K, Han L, Hu W, Ji L, Zhu S, Wan Z, et al. 4D printed zero Poisson's ratio metamaterial with switching function of mechanical and vibration isolation performance. Materials & Design 2020;196:109153. https://doi.org/10.1016/j.matdes.2020.109153.

[27] Virk K, Monti A, Trehard T, Marsh M, Hazra K, Boba K, et al. SILICOMB PEEK Kirigami cellular structures: mechanical response and energy dissipation through zero and negative stiffness. Smart Mater Struct 2013;22:084014. https://doi.org/10.1088/0964-1726/22/8/084014.

[28] Gibson I, Rosen DW, Stucker B. Additive manufacturing technologies: 3D printing, rapid prototyping and direct digital manufacturing. 2nd edition. New York London: Springer; 2015.

[29] Saleh Alghamdi S, John S, Roy Choudhury N, Dutta NK. Additive Manufacturing of Polymer Materials: Progress, Promise and Challenges. Polymers 2021;13:753. https://doi.org/10.3390/polym13050753.

[30] Habib FN, Iovenitti P, Masood SH, Nikzad M. Fabrication of polymeric lattice structures for optimum energy absorption using Multi Jet Fusion technology. Materials & Design 2018;155:86–98. https://doi.org/10.1016/j.matdes.2018.05.059.

[31] Xiao L, Xu X, Song W, Hu M. A Multi-Cell Hybrid Approach to Elevate the Energy Absorption of Micro-Lattice Materials. Materials 2020;13:4083. https://doi.org/10.3390/ma13184083.

[32] Carneiro VH, Puga H, Meireles J. Positive, zero and negative Poisson's ratio non-stochastic metallic cellular solids: Dependence between static and dynamic mechanical properties. Composite Structures 2019;226:111239. https://doi.org/10.1016/j.compstruct.2019.111239.

[33] The mechanics of two-dimensional cellular materials. Proc R Soc Lond A 1982;382:25–42. https://doi.org/10.1098/rspa.1982.0087.

[34] Carneiro VH, Meireles J, Puga H. Auxetic materials — A review. Mater Sci-Pol 2013;31:561–71. https://doi.org/10.2478/s13536-013-0140-6.

[35] Smith CW, Grima JN, Evans KE. A novel mechanism for generating auxetic behaviour in reticulated foams: missing rib foam model. Acta Materialia 2000;48:4349–56. https://doi.org/10.1016/S1359-6454(00)00269-X.

[36] Liu W, Wang N, Luo T, Lin Z. In-plane dynamic crushing of re-entrant auxetic cellular structure. Materials & Design 2016;100:84–91. https://doi.org/10.1016/j.matdes.2016.03.086.

[37] Wu X, Su Y, Shi J. In-plane impact resistance enhancement with a graded cell-wall angle design for auxetic metamaterials. Composite Structures 2020;247:112451. https://doi.org/10.1016/j.compstruct.2020.112451.

[38] Zhang J, Lu G, Wang Z, Ruan D, Alomarah A, Durandet Y. Large deformation of an auxetic structure in tension: Experiments and finite element analysis. Composite Structures 2018;184:92–101. https://doi.org/10.1016/j.compstruct.2017.09.076.

[39] Dong Z, Li Y, Zhao T, Wu W, Xiao D, Liang J. Experimental and numerical studies on the compressive mechanical properties of the metallic auxetic reentrant honeycomb. Materials & Design 2019;182:108036. https://doi.org/10.1016/j.matdes.2019.108036.

[40] Xue Y, Wang X, Wang W, Zhong X, Han F. Compressive property of Al-based auxetic lattice structures fabricated by 3-D printing combined with investment casting. Materials Science and Engineering: A 2018;722:255–62. https://doi.org/10.1016/j.msea.2018.02.105.

[41] Yang L, Harrysson O, West H, Cormier D. Mechanical properties of 3D re-entrant honeycomb auxetic structures realized via additive manufacturing. International Journal of Solids and Structures 2015;69–70:475–90. https://doi.org/10.1016/j.ijsolstr.2015.05.005.

[42] Yang L, Harrysson O, West H, Cormier D. Compressive properties of Ti–6Al–4V auxetic mesh structures made by electron beam melting. Acta Materialia 2012;60:3370–9. https://doi.org/10.1016/j.actamat.2012.03.015.

[43] Geng L, Wu W, Sun L, Fang D. Damage characterizations and simulation of selective laser melting fabricated 3D re-entrant lattices based on in-situ CT testing and geometric reconstruction. International Journal of Mechanical Sciences 2019;157–158:231–42. https://doi.org/10.1016/j.ijmecsci.2019.04.054.

[44] Novak N, Hokamoto K, Vesenjak M, Ren Z. Mechanical behaviour of auxetic cellular structures built from inverted tetrapods at high strain rates. International Journal of Impact Engineering 2018;122:83–90. https://doi.org/10.1016/j.ijimpeng.2018.08.001.

[45] Logakannan KP, Ramachandran V, Rengaswamy J, Ruan D. Dynamic Performance of a 3D Re-entrant Structure. Mechanics of Materials 2020;148:103503. https://doi.org/10.1016/j.mechmat.2020.103503.

[46] Prall D, Lakes RS. Properties of a chiral honeycomb with a poisson's ratio of — 1. International Journal of Mechanical Sciences 1997;39:305–14. https://doi.org/10.1016/S0020-7403(96)00025-2.

[47] Alderson A, Alderson KL, Attard D, Evans KE, Gatt R, Grima JN, et al. Elastic constants of 3-, 4- and 6-connected chiral and anti-chiral honeycombs subject to uniaxial in-plane loading. Composites Science and Technology 2010;70:1042–8. https://doi.org/10.1016/j.compscitech.2009.07.009.

[48] Wu W, Qi D, Liao H, Qian G, Geng L, Niu Y, et al. Deformation mechanism of innovative 3D chiral metamaterials. Sci Rep 2018;8:12575. https://doi.org/10.1038/s41598-018-30737-7.

[49] Grima JN, Evans KE. [No title found]. Journal of Materials Science Letters 2000;19:1563–5. https://doi.org/10.1023/A:1006781224002.

[50] Mir M, Ali MN, Sami J, Ansari U. Review of Mechanics and Applications of Auxetic Structures. Advances in Materials Science and Engineering 2014;2014:1–17. https://doi.org/10.1155/2014/753496.

[51] Shukla S, Behera BK. Auxetic fibrous structures and their composites: A review. Composite Structures 2022;290:115530. https://doi.org/10.1016/j.compstruct.2022.115530.

[52] Donoghue JP, Alderson KL, Evans KE. The fracture toughness of composite laminates with a negative Poisson's ratio: Fracture toughness of composite laminates with negative Poisson's ratio. Phys Stat Sol (b) 2009;246:2011–7. https://doi.org/10.1002/pssb.200982031.

[53] Yang S, Chalivendra VB, Kim YK. Fracture and impact characterization of novel auxetic Kevlar®/Epoxy laminated composites. Composite Structures 2017;168:120–9. https://doi.org/10.1016/j.compstruct.2017.02.034.

[54] Alderson A, Alderson KL, Chirima G, Ravirala N, Zied KM. The in-plane linear elastic constants and out-of-plane bending of 3-coordinated ligament and cylinder-ligament honeycombs. Composites Science and Technology 2010;70:1034–41. https://doi.org/10.1016/j.compscitech.2009.07.010.

[55] Alderson A, Rasburn J, Evans KE, Grima JN. Auxetic polymeric filters display enhanced de-fouling and pressure compensation properties. Membrane Technology 2001;2001:6–8. https://doi.org/10.1016/S0958-2118(01)80299-8.

[56] Alderson A, Rasburn J, Evans KE. Mass transport properties of auxetic (negative Poisson's ratio) foams. Phys Stat Sol (b) 2007;244:817–27. https://doi.org/10.1002/pssb.200572701.

[57] Imbalzano G, Tran P, Ngo TD, Lee PV. Three-dimensional modelling of auxetic sandwich panels for localised impact resistance. Jnl of Sandwich Structures & Materials 2017;19:291–316. https://doi.org/10.1177/1099636215618539.

[58] Sun Y, Li QM. Dynamic compressive behaviour of cellular materials: A review of phenomenon, mechanism and modelling. International Journal of Impact Engineering 2018;112:74–115. https://doi.org/10.1016/j.ijimpeng.2017.10.006.

[59] Steffens F, Rana S, Fangueiro R. Development of novel auxetic textile structures using high performance fibres. Materials & Design 2016;106:81–9. https://doi.org/10.1016/j.matdes.2016.05.063.

[60] Yang C, Vora HD, Chang YB. Application of Auxetic Polymeric Structures for Body Protection. Volume 1: Multifunctional Materials; Mechanics and Behaviour of Active Materials; Integrated System Design and Implementation; Structural Health Monitoring, Stowe, Vermont, USA: American Society of Mechanical Engineers; 2016, p. V001T01A018. https://doi.org/10.1115/SMASIS2016-9208.

[61] Sanami M, Ravirala N, Alderson K, Alderson A. Auxetic Materials for Sports Applications. Procedia Engineering 2014;72:453–8. https://doi.org/10.1016/j.proeng.2014.06.079.

[62] Duncan O, Shepherd T, Moroney C, Foster L, Venkatraman P, Winwood K, et al. Review of Auxetic Materials for Sports Applications: Expanding Options in Comfort and Protection. Applied Sciences 2018;8:941. https://doi.org/10.3390/app8060941.

[63] Gao Q, Zhao X, Wang C, Wang L, Ma Z. Multi-objective crashworthiness optimization for an auxetic cylindrical structure under axial impact loading. Materials & Design 2018;143:120–30. https://doi.org/10.1016/j.matdes.2018.01.063.

[64] Lee W, Jeong Y, Yoo J, Huh H, Park S-J, Park SH, et al. Effect of auxetic structures on crash behaviour of cylindrical tube. Composite Structures 2019;208:836–46. https://doi.org/10.1016/j.compstruct.2018.10.068.

[65] Luo C, Han CZ, Zhang XY, Zhang XG, Ren X, Xie YM. Design, manufacturing and applications of auxetic tubular structures: A review. Thin-Walled Structures 2021;163:107682. https://doi.org/10.1016/j.tws.2021.107682.

[66] Bhullar SK. Influence of Negative Poisson′s Ratio on Stent Applications. AM 2013;2:42. https://doi.org/10.11648/j.am.20130203.14.

[67] Kuribayashi K, Tsuchiya K, You Z, Tomus D, Umemoto M, Ito T, et al. Self-deployable origami stent grafts as a biomedical application of Ni-rich TiNi shape memory alloy foil. Materials Science and Engineering: A 2006;419:131–7. https://doi.org/10.1016/j.msea.2005.12.016.

[68] Bhullar SK, Ko J, Cho Y, Jun MBG. Fabrication and Characterization of Nonwoven Auxetic Polymer Stent. Polymer-Plastics Technology and Engineering 2015;54:1553–9. https://doi.org/10.1080/03602559.2014.986812.

[69] Wu W, Song X, Liang J, Xia R, Qian G, Fang D. Mechanical properties of anti-tetrachiral auxetic stents. Composite Structures 2018;185:381–92. https://doi.org/10.1016/j.compstruct.2017.11.048.

[70] Ruan XL, Li JJ, Song XK, Zhou HJ, Yuan WX, Wu WW, et al. Mechanical Design of Antichiral-Reentrant Hybrid Intravascular Stent. Int J Appl Mechanics 2018;10:1850105. https://doi.org/10.1142/S1758825118501053.

[71] Ali MN, Rehman IU. An Auxetic structure configured as oesophageal stent with potential to be used for palliative treatment of oesophageal cancer; development and

in vitro mechanical analysis. J Mater Sci: Mater Med 2011;22:2573–81. https://doi.org/10.1007/s10856-011-4436-y.

[72] Ali MN, Busfield JJC, Rehman IU. Auxetic oesophageal stents: structure and mechanical properties. J Mater Sci: Mater Med 2014;25:527–53. https://doi.org/10.1007/s10856-013-5067-2.

[73] S. K. Bhullar, J. Ko, F. Ahmed, M. B. G. Jun. Design And Fabrication Of Stent With Negative Poisson’S Ratio 2014. https://doi.org/10.5281/ZENODO.1091366.

[74] Kolken HMA, Janbaz S, Leeflang SMA, Lietaert K, Weinans HH, Zadpoor AA. Rationally designed meta-implants: a combination of auxetic and conventional meta-biomaterials. Mater Horiz 2018;5:28–35. https://doi.org/10.1039/C7MH00699C.

[75] Attard D, Grima JN. Modelling of hexagonal honeycombs exhibiting zero Poisson’s ratio. Phys Stat Sol (b) 2011;248:52–9. https://doi.org/10.1002/pssb.201083980.

[76] Chen Y, Fu M-H. Mechanical Properties of a Novel Zero Poisson’s Ratio Honeycomb. Adv Eng Mater 2018;20:1700452. https://doi.org/10.1002/adem.201700452.

[77] Wang N, Liu W, Tang A, Huang J, Lin Z, Lei S. Strain isolation: A simple mechanism for understanding and detecting structures of zero Poisson’s ratio: Strain isolation and structures of zero Poisson’s ratio. Phys Status Solidi B 2014;251:2239–46. https://doi.org/10.1002/pssb.201451376.

[78] Wang C, Zhang L, Fang Y, Sun W. Design, Characterization, and 3D Printing of Cardiovascular Stents with Zero Poisson’s Ratio in Longitudinal Deformation. Engineering 2021;7:979–90. https://doi.org/10.1016/j.eng.2020.02.013.

[79] Guo M-F, Yang H, Ma L. Design and characterization of 3D AuxHex lattice structures. International Journal of Mechanical Sciences 2020;181:105700. https://doi.org/10.1016/j.ijmecsci.2020.105700.

[80] Chen Y, Scarpa F, Remillat C, Farrow I, Liu Y, Leng J. Curved Kirigami SILICOMB cellular structures with zero Poisson’s ratio for large deformations and morphing. Journal of Intelligent Material Systems and Structures 2014;25:731–43. https://doi.org/10.1177/1045389X13502852.

[81] Chen Y, Zheng B-B, Fu M-H, Lan L-H, Zhang W-Z. Doubly unusual 3D lattice honeycomb displaying simultaneous negative and zero Poisson’s ratio properties. Smart Mater Struct 2018;27:045003. https://doi.org/10.1088/1361-665X/aaae2b.

[82] Hamzehei R, Zolfagharian A, Dariushi S, Bodaghi M. 3D-printed bio-inspired zero Poisson’s ratio graded metamaterials with high energy absorption performance. Smart Mater Struct 2022;31:035001. https://doi.org/10.1088/1361-665X/ac47d6.

[83] Naghavi Zadeh M, Dayyani I, Yasaee M. Fish Cells, a new zero Poisson’s ratio metamaterial—Part I: Design and experiment. Journal of Intelligent Material

Systems and Structures 2020;31:1617–37. https://doi.org/10.1177/1045389X20930079.

[84] Zadeh MN, Dayyani I, Yasaee M. Fish Cells, a new zero Poisson's ratio metamaterial—part II: Elastic properties. Journal of Intelligent Material Systems and Structures 2020;31:2196–210. https://doi.org/10.1177/1045389X20942576.

[85] Qin Q, Dayyani I, Webb P. Structural Mechanics of cylindrical fish-cell zero Poisson's ratio metamaterials. Composite Structures 2022;289:115455. https://doi.org/10.1016/j.compstruct.2022.115455.

[86] Feng N, Wang S, Tie Y, Liu W, Zhao Z, Guo J. Elastic deformability and zero Poisson's ratio within a novel structure inspired by the gardenia from nature. Mechanics of Advanced Materials and Structures 2022:1–13. https://doi.org/10.1080/15376494.2022.2135052.

[87] Mao A, Zhao N, Liang Y, Bai H. Mechanically Efficient Cellular Materials Inspired by Cuttlebone. Adv Mater 2021;33:2007348. https://doi.org/10.1002/adma.202007348.

[88] Alsaidi B, Joe WY, Akbar M. Computational Analysis of 3D Lattice Structures for Skin in Real-Scale Camber Morphing Aircraft. Aerospace 2019;6:79. https://doi.org/10.3390/aerospace6070079.

[89] Huang J, Zhang Q, Scarpa F, Liu Y, Leng J. Bending and benchmark of zero Poisson's ratio cellular structures. Composite Structures 2016;152:729–36. https://doi.org/10.1016/j.compstruct.2016.05.078.

[90] Gong X, Huang J, Scarpa F, Liu Y, Leng J. Zero Poisson's ratio cellular structure for two-dimensional morphing applications. Composite Structures 2015;134:384–92. https://doi.org/10.1016/j.compstruct.2015.08.048.

[91] Chen J, Shen X, Li J. Zero Poisson's ratio flexible skin for potential two-dimensional wing morphing. Aerospace Science and Technology 2015;45:228–41. https://doi.org/10.1016/j.ast.2015.05.011.

[92] Liu W, Li H, Zhang J, Bai Y. In-plane mechanics of a novel cellular structure for multiple morphing applications. Composite Structures 2019;207:598–611. https://doi.org/10.1016/j.compstruct.2018.08.096.

[93] Huang J, Liu W, Tang A. Effects of fine-scale features on the elastic properties of zero Poisson's ratio honeycombs. Materials Science and Engineering: B 2018;236–237:95–103. https://doi.org/10.1016/j.mseb.2018.11.005.

[94] Geng LC, Ruan XL, Wu WW, Xia R, Fang DN. Mechanical Properties of Selective Laser Sintering (SLS) Additive Manufactured Chiral Auxetic Cylindrical Stent. Exp Mech 2019;59:913–25. https://doi.org/10.1007/s11340-019-00489-0.

[95] Li Q, Yang D, Mao X. Pressure-resistant cylindrical shell structures comprising graded hybrid zero Poisson's ratio metamaterials with designated band gap

characteristics. Marine Structures 2022;84:103221. https://doi.org/10.1016/j.marstruc.2022.103221.

[96] Li Q, Wang Z, Mao X, Yang D. Underwater cylindrical sandwich meta-structures composed of graded semi re-entrant zero Poisson's ratio metamaterials with pre-strained wave propagation properties. Journal of Ocean Engineering and Science 2023:S2468013323000013. https://doi.org/10.1016/j.joes.2023.02.002.

[97] Tancogne-Dejean T, Spierings AB, Mohr D. Additively-manufactured metallic micro-lattice materials for high specific energy absorption under static and dynamic loading. Acta Materialia 2016;116:14–28. https://doi.org/10.1016/j.actamat.2016.05.054.

[98] Cao X, Duan S, Liang J, Wen W, Fang D. Mechanical properties of an improved 3D-printed rhombic dodecahedron stainless steel lattice structure of variable cross section. International Journal of Mechanical Sciences 2018;145:53–63. https://doi.org/10.1016/j.ijmecsci.2018.07.006.

[99] Qi D, Yu H, Liu M, Huang H, Xu S, Xia Y, et al. Mechanical behaviours of SLM additive manufactured octet-truss and truncated-octahedron lattice structures with uniform and taper beams. International Journal of Mechanical Sciences 2019;163:105091. https://doi.org/10.1016/j.ijmecsci.2019.105091.

[100] Alomarah A, Ruan D, Masood S. Tensile properties of an auxetic structure with re-entrant and chiral features—a finite element study. Int J Adv Manuf Technol 2018;99:2425–40. https://doi.org/10.1007/s00170-018-2637-y.

[101] Alomarah A, Ruan D, Masood S, Gao Z. Compressive properties of a novel additively manufactured 3D auxetic structure. Smart Mater Struct 2019;28:085019. https://doi.org/10.1088/1361-665X/ab0dd6.

[102] Alomarah A, Xu S, Masood SH, Ruan D. Dynamic performance of auxetic structures: experiments and simulation. Smart Mater Struct 2020;29:055031. https://doi.org/10.1088/1361-665X/ab79bb.

[103] Alomarah A, Masood SH, Sbarski I, Faisal B, Gao Z, Ruan D. Compressive properties of 3D printed auxetic structures: experimental and numerical studies. Virtual and Physical Prototyping 2020;15:1–21. https://doi.org/10.1080/17452759.2019.1644184.

[104] White BC, Garland A, Alberdi R, Boyce BL. Interpenetrating lattices with enhanced mechanical functionality. Additive Manufacturing 2021;38:101741. https://doi.org/10.1016/j.addma.2020.101741.

[105] Pham M-S, Liu C, Todd I, Lertthanasarn J. Damage-tolerant architected materials inspired by crystal microstructure. Nature 2019;565:305–11. https://doi.org/10.1038/s41586-018-0850-3.

[106] Lu Z, Yan W, Yan P, Yan B. A Novel Precipitate-Type Architected Metamaterial Strengthened via Orowan Bypass-Like Mechanism. Applied Sciences 2020;10:7525. https://doi.org/10.3390/app10217525.

[107] Xiao R, Li X, Jia H, Surjadi JU, Li J, Lin W, et al. 3D printing of dual phase-strengthened microlattices for lightweight micro aerial vehicles. Materials & Design 2021;206:109767. https://doi.org/10.1016/j.matdes.2021.109767.

[108] Chen Y, Ye L, Han X. Experimental and numerical investigation of zero Poisson's ratio structures achieved by topological design and 3D printing of SCF/PA. Composite Structures 2022;293:115717. https://doi.org/10.1016/j.compstruct.2022.115717.

[109] Maskery I, Aboulkhair NT, Aremu AO, Tuck CJ, Ashcroft IA, Wildman RD, et al. A mechanical property evaluation of graded density Al-Si10-Mg lattice structures manufactured by selective laser melting. Materials Science and Engineering: A 2016;670:264–74. https://doi.org/10.1016/j.msea.2016.06.013.

[110] Xiao D, Dong Z, Li Y, Wu W, Fang D. Compression behaviour of the graded metallic auxetic reentrant honeycomb: Experiment and finite element analysis. Materials Science and Engineering: A 2019;758:163–71. https://doi.org/10.1016/j.msea.2019.04.116.

[111] Novak N, Krstulović-Opara L, Ren Z, Vesenjak M. Compression and shear behaviour of graded chiral auxetic structures. Mechanics of Materials 2020;148:103524. https://doi.org/10.1016/j.mechmat.2020.103524.

[112] Xue Y, Wang W, Han F. Enhanced compressive mechanical properties of aluminum based auxetic lattice structures filled with polymers. Composites Part B: Engineering 2019;171:183–91. https://doi.org/10.1016/j.compositesb.2019.05.002.

[113] De Pasquale G, Sibona S. Hybrid materials based on polymers-filled AM steel lattices with energy absorption capabilities. Mechanics of Advanced Materials and Structures 2022;29:2570–80. https://doi.org/10.1080/15376494.2020.1871536.

[114] Fíla T, Zlámal P, Jiroušek O, Falta J, Koudelka P, Kytýř D, et al. Impact Testing of Polymer-filled Auxetics Using Split Hopkinson Pressure Bar: Impact Testing of Polymer-filled Auxetics…. Adv Eng Mater 2017;19:1700076. https://doi.org/10.1002/adem.201700076.

[115] Novak N, Krstulović-Opara L, Ren Z, Vesenjak M. Mechanical properties of hybrid metamaterial with auxetic chiral cellular structure and silicon filler. Composite Structures 2020;234:111718. https://doi.org/10.1016/j.compstruct.2019.111718.

[116] Ngo TD, Kashani A, Imbalzano G, Nguyen KTQ, Hui D. Additive manufacturing (3D printing): A review of materials, methods, applications and challenges. Composites Part B: Engineering 2018;143:172–96. https://doi.org/10.1016/j.compositesb.2018.02.012.

[117] Majeed A, Ahmed A, Salam A, Sheikh MZ. Surface quality improvement by parameters analysis, optimization and heat treatment of AlSi10Mg parts manufactured by SLM additive manufacturing. International Journal of Lightweight Materials and Manufacture 2019;2:288–95. https://doi.org/10.1016/j.ijlmm.2019.08.001.

[118] Maconachie T, Leary M, Zhang J, Medvedev A, Sarker A, Ruan D, et al. Effect of build orientation on the quasi-static and dynamic response of SLM AlSi10Mg. Materials Science and Engineering: A 2020;788:139445. https://doi.org/10.1016/j.msea.2020.139445.

[119] Tsopanos S, Mines RAW, McKown S, Shen Y, Cantwell WJ, Brooks W, et al. The Influence of Processing Parameters on the Mechanical Properties of Selectively Laser Melted Stainless Steel Microlattice Structures. Journal of Manufacturing Science and Engineering 2010;132:041011. https://doi.org/10.1115/1.4001743.

[120] Gu D. Laser Additive Manufacturing of High-Performance Materials. Berlin, Heidelberg: Springer Berlin Heidelberg; 2015. https://doi.org/10.1007/978-3-662-46089-4.

[121] Yap CY, Chua CK, Dong ZL, Liu ZH, Zhang DQ, Loh LE, et al. Review of selective laser melting: Materials and applications. Applied Physics Reviews 2015;2:041101. https://doi.org/10.1063/1.4935926.

[122] Al-Saedi DSJ, Masood SH, Faizan-Ur-Rab M, Alomarah A, Ponnusamy P. Mechanical properties and energy absorption capability of functionally graded F2BCC lattice fabricated by SLM. Materials & Design 2018;144:32–44. https://doi.org/10.1016/j.matdes.2018.01.059.

[123] Zhang Y, Liu T, Ren H, Maskery I, Ashcroft I. Dynamic compressive response of additively manufactured AlSi10Mg alloy hierarchical honeycomb structures. Composite Structures 2018;195:45–59. https://doi.org/10.1016/j.compstruct.2018.04.021.

[124] Louvis E, Fox P, Sutcliffe CJ. Selective laser melting of aluminium components. Journal of Materials Processing Technology 2011;211:275–84. https://doi.org/10.1016/j.jmatprotec.2010.09.019.

[125] Rubben T, Revilla RI, De Graeve I. Influence of heat treatments on the corrosion mechanism of additive manufactured AlSi10Mg. Corrosion Science 2019;147:406–15. https://doi.org/10.1016/j.corsci.2018.11.038.

[126] O’Connor HJ, Dickson AN, Dowling DP. Evaluation of the mechanical performance of polymer parts fabricated using a production scale multi jet fusion printing process. Additive Manufacturing 2018;22:381–7. https://doi.org/10.1016/j.addma.2018.05.035.

[127] Vasquez GM, Majewski CE, Haworth B, Hopkinson N. A targeted material selection process for polymers in laser sintering. Additive Manufacturing 2014;1–4:127–38. https://doi.org/10.1016/j.addma.2014.09.003.

[128] Cai C, Tey WS, Chen J, Zhu W, Liu X, Liu T, et al. Comparative study on 3D printing of polyamide 12 by selective laser sintering and multi jet fusion. Journal of Materials Processing Technology 2021;288:116882. https://doi.org/10.1016/j.jmatprotec.2020.116882.

[129] Sillani F, Kleijnen RG, Vetterli M, Schmid M, Wegener K. Selective laser sintering and multi jet fusion: Process-induced modification of the raw materials and analyses of parts performance. Additive Manufacturing 2019;27:32–41. https://doi.org/10.1016/j.addma.2019.02.004.

[130] Chen W, Song B. Split Hopkinson (Kolsky) Bar: Design, Testing and Applications. Boston, MA: Springer US; 2011. https://doi.org/10.1007/978-1-4419-7982-7.

[131] Maconachie T, Leary M, Tran P, Harris J, Liu Q, Lu G, et al. The effect of topology on the quasi-static and dynamic behaviour of SLM AlSi10Mg lattice structures. Int J Adv Manuf Technol 2022;118:4085–104. https://doi.org/10.1007/s00170-021-08203-y.

[132] Li C, Lei H, Liu Y, Zhang X, Xiong J, Zhou H, et al. Crushing behaviour of multi-layer metal lattice panel fabricated by selective laser melting. International Journal of Mechanical Sciences 2018;145:389–99. https://doi.org/10.1016/j.ijmecsci.2018.07.029.

[133] Xu Z, Wang Y, Wu D, Ananth KP, Bai J. The process and performance comparison of polyamide 12 manufactured by multi jet fusion and selective laser sintering. Journal of Manufacturing Processes 2019;47:419–26. https://doi.org/10.1016/j.jmapro.2019.07.014.

[134] Li QM, Magkiriadis I, Harrigan JJ. Compressive Strain at the Onset of Densification of Cellular Solids. Journal of Cellular Plastics 2006;42:371–92. https://doi.org/10.1177/0021955X06063519.

[135] Maiti SK, Gibson LJ, Ashby MF. Deformation and energy absorption diagrams for cellular solids. Acta Metallurgica 1984;32:1963–75. https://doi.org/10.1016/0001-6160(84)90177-9.

[136] Kaw AK. Mechanics of Composite Materials. 0 ed. CRC Press; 2005. https://doi.org/10.1201/9781420058291.

[137] Smith M, Guan Z, Cantwell WJ. Finite element modelling of the compressive response of lattice structures manufactured using the selective laser melting technique. International Journal of Mechanical Sciences 2013;67:28–41. https://doi.org/10.1016/j.ijmecsci.2012.12.004.

[138] Chen Y, Fu M-H. Mechanical Properties of a Novel Zero Poisson's Ratio Honeycomb. Adv Eng Mater 2018;20:1700452. https://doi.org/10.1002/adem.201700452.

[139] Sun G, Liu T, Huang X, Zheng G, Li Q. Topological configuration analysis and design for foam filled multi-cell tubes. Engineering Structures 2018;155:235–50. https://doi.org/10.1016/j.engstruct.2017.10.063.

[140] Farrokhabadi A, Veisi H, Gharehbaghi H, Montesano J, Behravesh AH, Hedayati SK. Investigation of the energy absorption capacity of foam-filled 3D-printed glass fiber reinforced thermoplastic auxetic honeycomb structures. Mechanics of Advanced Materials and Structures 2023;30:758–69. https://doi.org/10.1080/15376494.2021.2023919.

[141] Minhas N, Thakur A, Mehlwal S, Verma R, Sharma VS, Sharma V. Multi-variable Optimization of the Shot Blasting of Additively Manufactured AlSi10Mg Plates for Surface Roughness Using Response Surface Methodology. Arab J Sci Eng 2021;46:11671–85. https://doi.org/10.1007/s13369-021-05654-z.